

**CONTROLLING THE FLOW OF LIGHT WITH
WAVEGUIDE ENCODED SLIM POLYMER FILMS**

CONTROLLING THE FLOW OF LIGHT WITH WAVEGUIDE ENCODED SLIM POLYMER FILMS

By

Hao Lin, B. Sc.

A Thesis

Submitted to the School of Graduate Studies in Partial Fulfillment of the Requirements
for the Degree

Doctor of Philosophy in Chemistry

McMaster University

© Copyright by Hao Lin, July 2018

DOCTOR OF PHILOSOPHY (2018)

MCMASTER UNIVERSITY

(Chemistry)

Hamilton, Ontario

TITLE Controlling the Flow of Light with Waveguide Encoded Slim
Polymer Films

AUTHOR: Hao Lin, B. Sc. (Beijing Normal University, China)

SUPERVISOR: Dr. Kalaichelvi Saravanamuttu

Number of pages: 213

Abstract

Manipulating the flow of light is critical in the design and fabrication of light-based devices ranging from solar cells, smart cameras, liquid crystal display (LCD) screens, projectors and light emitting diodes (LEDs). Thin films configured with spatial patterns or modulations in refractive index exhibit strong and richly varied interactions with light beams. In this thesis, we show that embedding planar films with specific geometries of waveguide lattices allows precise control over the inflow and outflow of light. Specifically, we demonstrate the fabrication of a new class of waveguide-encoded polymer films that are generated through a single-step, room temperature technique. Here, waveguide encoded lattices with a range of symmetries are spontaneously inscribed in photopolymerizable resins by self-trapped beams of incandescent light. We describe the generation of lattices consisting of five intersecting arrays of waveguides, which confer a range of unprecedented properties including a large, panoramic field of view (FOV) infinite depth of field and multiple imaging functionalities including focusing and inversion. We have also fabricated lattices inspired by natural arthropodal compound eyes, which comprise a radial distribution of waveguide and in turn impart a continuous, enhanced FOV. We demonstrate the application of these films in controlling the beam profiles of LEDs including their divergence and convergence. Finally, we show that thin films patterned with a periodic array of planar waveguides serve as effective beam steering coatings, which deflect light away from the metallic front contacts of commercially available solar cells and in this way, increase their efficiency.

Acknowledgement

Firstly, I would like to acknowledge my supervisor, Dr. Kalaichelvi Saravanamuttu, for her patience, diligent and enlightening guidance, as well as encouragements. Her genuine enthusiasm about new ideas and results also deeply motivated my doctoral studies.

I would also like to thank my committee members Dr. Ray LaPierre and Dr. Ignacia Vargas-Baca, for providing valuable feedbacks and strong encouragements through my research. Many thanks to Dr. Jose Moran-Mirabal for allowing me to use their vinyl cutter and 3-D printer; Thank Dr. Harald Stover and Dr. Nick Burke for letting me use and giving me a detailed training on their optical microscope; and thank Dr. Cecile Fradin for providing us with “Moticam” cameras.

I would also like to thank funding agencies like Canadian Foundation for Innovation, Ontario Innovation Trust, Natural Sciences and Engineering Research Council of Canada (NSERC), Ciba Inc. and McMaster University for providing financial support for my research.

I am very lucky to work in an excellent group with great atmosphere and amazing people. Special thanks to Dr. Ian D. Hosein, a former postdoc in our group, who helped me a lot on setting up the optical assemblies, explaining related concepts and background, as well as giving me guidance on figure compiling, etc. Many thanks to Kathryn A. Benincasa, for her massive input in the project described in Chapter 5. Many thanks to Dinesh K. Basker, Alexander D. Hudson, Derek Morim, Oscar A. Herrera-Cortes, Matthew R. Ponte, Liqun Qiu, Yi Pan, Fariha Mahmood, Shaochang Song, and Kyle Kavaseri, etc. for bringing in interesting ideas and participating in

valuable discussions.

My friends such as Jing Zhao, Xiuping Ding, Weiwei Zhang, Yi Feng, Baoqin Deng, Milan Gidakovic, Sanja Gidakovic, Shuai Liang, Ri Chen, Lei Wang, Mengchen Liao, and Sijia Zheng, etc. would also be greatly acknowledged, as they provided me with a lot of companies, help and encouragements.

Last but not least, words alone cannot express my gratefulness for the endless support from my parents Yonghui Xu and Mingjian Lin, my sister Lan Lin, my grandpa Dabang Xu, my brother in law Liang Chen, my cute little nephew Yiyang Chen, and my girlfriend Yuping Cui, etc. I dedicate this work to my beloved family.

Table of Content

Chapter 1 Introduction.....	1
1.1. An introduction to nonlinear propagation of light	2
1.1.1. Self-trapping of light waves	2
1.1.2. Optical Modulation instability	5
1.2. Optical media supporting nonlinear light propagation	7
1.3. Study of optical self-written waveguides (SWWs) and complex waveguide structures in photopolymers	12
1.4. Optical self-written in photopolymerisable epoxides and acrylates	15
1.4.1. Optical self-written in photopolymerisable epoxide sol	15
1.4.1. Optical self-written in photopolymerisable acrylate sol	17
1.5. Introduction to compound eyes.....	19
1.5.1. Natural compound eyes.....	19
1.5.2. Artificial compound eyes	22
1.5.2.1. Planar artificial compound eye	22
1.5.2.2. Curved artificial compound eyes	25
1.5.3. Fabrication of compound-eye microlens arrays.....	28
1.6. Research objectives: Controlling the flow of light with waveguide encoded slim polymer films.	29
Chapter 2 Waveguide Encoded Lattices (WELs): Slim Polymer Films with Panoramic Fields of View (FOV) and Multiple Imaging Functionality	41
2.1. Introduction.....	43
2.2. Results and Discussion	46
2.2.1. Design and Operation	46
2.2.2. Assembling the WEL Lattice with Colliding Self-Trapped White Light Beams.....	48
2.2.3. The WEL Lattice Microstructure	52
2.2.4. Crosstalk-Free Guiding of Light in Mutually Independent Waveguide Arrays	55
2.2.5. The Enhanced FOV of the WEL Lattice.....	57
2.2.6. The WEL Lattice as a Versatile, Multifunctional Imaging Element	60

2.3. Conclusions and Outlook	63
2.4. Experimental Section	64
Supporting Information.....	71
Chapter 3 Slim Films with Seamless Panoramic Fields of View: The Radially Distributed Waveguide Encoded Lattice (RDWEL)	99
3.1. Introduction.....	1041
3.2. Results and Discussion	104
3.2.1. Working principles of the RDWEL	104
3.2.2. Fabrication and characterization of RDWEL microstructure	106
3.2.3. Seamless collection and waveguiding of light.....	110
3.2.4 Measuring the FOV.....	112
3.2.5. Panoramic imaging	116
3.3. Conclusions and Outlook.....	117
Supporting Information.....	124
Chapter 4 Waveguide-Imprinted Polymer Slim Films: Beam Steering Coatings for Solar Cells.....	135
4.1. Introduction.....	137
4.2. Results and Discussion	138
4.2.1. Working Principles	138
4.2.2. Fabrication and Characterization	141
4.2.3. Proof of Beam Steering.....	144
4.2.4. Enhanced EQE of Solar Cells	146
4.3. Conclusions.....	149
4.4. Materials and Methods.....	150
Supplementary Information	157
Chapter 5 Shaping LED beams with Radially Distributed Waveguide Encoded Lattices (RDWELs).....	166
5.1. Introduction.....	168

5.2. Results and Discussion	170
5.2.1. Working Principles	170
5.2.2. Fabrication and structural characterization of RDWEL	173
5.2.3. Determining the Field of View	175
5.2.4. Shaping LED beams with the RDWEL	178
5.2.5. Focal length of RDWEL _{CONV}	181
5.3. Conclusions and Outlook.....	183
5.4. Materials and Methods.....	184
Supporting Information.....	191
Chapter 6 Conclusions and Future Directions	201
6.1 General Conclusions	201
6.2 Future work.....	207

List of figures

- Figure 1.1.** Schematic illustrations of the spatial beam profiles, output phase-front, and output intensity of a propagating beam as it undergoes: (a) natural diffraction; (b) self-focusing; and (c) self-trapping. 3
- Figure 1.2.** Plot of change in refractive index versus radiation exposure. U_0 is the critical exposure required to induce photoinitiation, and E_{sat} is the energy required to achieve the maximum refractive index change Δn_s 11
- Figure 1.3.** Schematic illustration showing the mechanism for the ring opening polymerization of the epoxide based photopolymer system. The epoxide based monomers are depicted as ethylene oxide in the figure. Reprinted from 16
- Figure 1.4.** Schematic illustration showing the hydrolysis and polycondensation process of the polymer system and the subsequent photopolymerization mechanisms. Reprinted from 17
- Figure 1.5.** Schematic diagrams of (a) apposition and (b) superposition compound eyes. Here, “CL” “CC” “Rh” and “CZ” refer to corneal lens, cylindrical cone, rahbodom, and clear zone, respectively. 20
- Figure 1.6.** Principle of a natural apposition compound eye which is composed of a large number of ommatidia arranged on a curved basis with radius R_{EYE} 22
- Figure 1.7.** Schematic representations of planar compound eyes. (a) A TOMBO, (b) a APCO, (c) a Cley and (d) a WEL. 24
- Figure 1.8.** Illustration of a few curved artificial compound eyes. (a) An artificial compound eye with lens-capped waveguides, (b) an arthropod eye inspired miniature camera, and (c) a cylindrical vision sensor named “CurvACE”..... 27
- Figure 2.1.** Operating principles of the WEL lattice. a) 3D model of the WEL lattice, which consists of a stack of xz planes, each comprising five intersecting waveguide arrays oriented respectively at -30° , -15° , 0° , 15° , and 30° relative to the surface normal (z). The inset contains an individual quintet of waveguides. The color scale indicates the change in refractive index (Δn). b) Each waveguide has an acceptance angular range of $\Delta\theta_n$ where n = waveguide orientation angle. The FOV at the convergence point of a single waveguide quintet (and the entire WEL lattice) is the sum of all $\Delta\theta_n$. The FOV is quantified in c) color-coded computed plots (generated through the beam propagation method) of transmitted power at each waveguide exit versus the incidence angle. Black plots correspond to an unstructured medium without waveguides (control). The bar chart below depicts $\Delta\theta_n$ for each waveguide (solid color) and the unstructured medium (solid black); $\Delta\theta_n$ here is the curve width where power

$=1/e^2$ of maximum. $\Delta\theta_n$ values from ray optics-based calculations of waveguiding are included for comparison (dotted line)..... 48

Figure 2.2. Structural fabrication. a) Scheme of optical assembly consisting of five beams emitted by quartz-tungsten-halogen (QTH) lamps. The beams were collimated, passed through a 2D periodic amplitude mask, and launched into a b) cell containing fluid photopolymerizable epoxide. Upon irradiation, the epoxide transformed into a c) freestanding, solid, and flexible WEL (scale bar =1 cm). d) The spatial intensity profile of the central beam (0°) at the sample entrance face ($z = 0.0$ mm) at $t = 0$ s contained a strong 2D periodic modulation but diverged significantly with propagation so that it e) appeared uniform at the exit face ($z = 3.0$ mm) at $t = 0$ s. Refractive index changes due to epoxide strongly suppressed divergence and the beam transformed into a f) 2D periodic array of self-trapped beams at $t = 25$ min (scale bars in panels (d)–(f) = $160 \mu\text{m}$). 52

Figure 2.3. Structural characterization of a WEL lattice. a) A scheme of the WEL in which each waveguide array is individually extended along its axis to clearly depict its relative angular position. The inset is a simulated top-down view (xz plane); colored dotted lines guide the eye to each waveguide orientation and black circles indicate periodic points of waveguide intersections (scale bar = $160 \mu\text{m}$). b) Experimentally acquired optical transmission image of the top-down view (xz plane) of an actual WEL. Colored dotted lines guide the eye to each waveguide orientation and black circles indicate periodic points of waveguide intersections (scale bar = $160 \mu\text{m}$). c) Transmission optical image of the five waveguide arrays within a single WEL; images were acquired by monotonically tilting the WEL until the propagation axis of each waveguide array coincided with the microscope optic axis (scale bar = $160 \mu\text{m}$). d) Optical image of the yz plane shows that WEL comprises a periodic stack of planes (scale bar = $160 \mu\text{m}$). e) Photographs of the far-field output of laser light ($\lambda = 633$ nm) propagating through a WEL at -30° , -15° , 0° , 15° , and 30° . Images were acquired at $\approx 45^\circ$ from the screen, which was placed 2 m away from the WEL lattice. The input laser beam was roughly Gaussian in profile with $1/e^2$ width of $570 \mu\text{m}$ (see Movie S1 in the Supporting Information). 54

Figure 2.4. Simultaneous of multidirectional light propagation. a) Experimentally acquired spatial intensity profiles of a broad incandescent beam propagating through each of the five waveguide arrays in a WEL. Profiles were acquired at the exit face of the lattice ($z = 3.0$ mm). Scale bars of relative intensity are provided; horizontal and vertical line profiles correspond to the white dotted lines in each 2D profile (scale bars = $160 \mu\text{m}$). b) Beam propagation simulations of a Gaussian beam ($\lambda = 633$ nm) propagating through each of the five waveguide arrays in a WEL. For clarity, only the optical intensity distribution is in color while the WEL structure is in gray. c) Photograph of three different laser beams propagating simultaneously through waveguides oriented respectively at 0° (red), 15° (blue), and 30° (green) in the WEL and being projected onto a far-field screen. d) Magnified photographs of the spatial intensity profiles of each laser beam. 57

Figure 2.5. WEL exhibits enhanced field of view (FOV). a) Scheme of experimental setup to determine FOV: an object, which is a circular ring of incandescent light (the inset), was monotonically rotated about the WEL surface normal from -50° to 50° . The output of each waveguide lattice was imaged respectively at fixed angles of -44° , -22° , 0° , 22° , and 44° ; these correspond to the orientation of each waveguide array (-30° , -15° , 0° , 15° , and 30°) after refraction at the glass/air interface at the sample exit. b) 2D spatial intensity profiles of the exit of the central waveguide array (at 0°) acquired when the incidence angle of the object was varied from -6° to 6° . Identical measurements made for an unstructured medium without waveguides (control) are included. For clarity, intensity was normalized to the maximum intensity in each sequence of images. c) Plots of normalized total intensity of the image versus the angle of incidence of the object for the WEL (red) and an unstructured medium without waveguides (black). d) The complete sequence of images acquired by varying the incidence angle of the object from -50° to 50° into the WEL (top) and control (bottom). The inset is a scheme of the angular range (blue) over which images were acquire. 59

Figure 2.6. Multiple imaging configurations. a) Scheme and b) photograph of assembly to launch three illuminated objects “M,” “A,” and “C” positioned in a hemisphere with radius z into waveguide arrays oriented at 30° , 0° , and -30° , respectively, and imaged at the WEL lattice exit plane with a CCD chip. Propagation of “C” is traced in red as an example. c) Schemes of three imaging configurations achieved by varying z ($z_1 = 4.5$ mm, $z_2 = 7.5$ mm, $z_3 = 10.5$ mm). d) At z_1 , the letters propagate through waveguides that do not intersect and are projected adjacent to each other at the exit. At z_2 , the letters propagate through waveguides that intersect at the exit face and are focused onto the same area. At z_3 , the letters propagate in waveguides that intersect in the lattice and appear inverted at the exit face. e) Corresponding images of the three letters when launched individually in the respective waveguide arrays at z_1 , z_2 , and z_3 62

Figure S2.1. BPM simulations in a graded index cylindrical waveguide ($n = 1.47$, $\Delta n = 0.006$) at launch angles from 0° to 11° . The contour maps represent the xz plane; the waveguide boundaries are traced in white. 73

Figure S2.2. BPM simulations in a graded index cylindrical waveguide ($n = 1.47$, $\Delta n = 0.006$) at launch angles from 0° to 9° . The contour maps represent the xy plane at a propagation distance of 3 mm; waveguide boundaries are traced in white. 73

Figure S2.3. Optical assembly for the fabrication of WELs (a) Scheme of assembly along the beam oriented at 0° ; four beams (not shown) are arranged pairwise on either side of the optic axis at angles of -44° , -22° , 22° , 44° . (b) and (c) Photographs of assembly showing the five quartz tungsten halogen (QTH) lamps and optical components. (d) Scheme of configuration employed to fabricate the WEL. 75

Figure S2.4. Temporal evolution of the intensity concentration factor (CF) during the formation of a single waveguide array (oriented at 0° with respect to the surface

normal). CF was calculated for $\sim 22 \times \sim 20$ waveguides over an area of $1780 \times 1638 \mu\text{m}^2$ 77

Figure S2.5. Temporal evolution of optical intensity integrated over an area of $1780 \times 1638 \mu\text{m}^2$ acquired at the exit face of the sample during the formation of a single waveguide lattice. 77

Figure S2.6. Spatial intensity profiles of waveguided white light at the exit face of the waveguide array oriented at (a) $+15^\circ$ and (b) $+30^\circ$ in the WEL lattice. Scale bars = $160 \mu\text{m}$ 78

Figure S2.7. Collision situations: (a) Schematic diagram of the collision behaviors of a single 0° , -15° , and -30° waveguide with non-parallel waveguides; (b) Calculation of the collision times of the three collision situations in (a). 79

Figure S2.8. Bravais lattices formed by intersecting waveguides, based on the number of waveguides and their orientations. Lines are used to model the lattices for the lattice plane on which they intersect and black dots indicating the 2D Bravais lattice, as shown in the image(s) on the left of each panel. The 3D unit cell lattice consists of stacks of these 2D lattices perpendicular to its plane (highlighted green), as shown in the image on the right of each panel for a 3D unit cell. All lattice orientations are with respect to the vertical of the page. (a) Two lattices oriented at -15° and 15° . The 2D lattice has pl symmetry, and the 3D lattice unit cell is primitive monoclinic. (b) Two lattices oriented at -30° and 30° . The 2D lattice has pm symmetry, and the 3D lattice unit cell is hexagonal. (c) Two lattices oriented 0 plus any other symmetric combination of beams, e.g., -15° and 15° , or -30° and 30° , or -30° , -15° , 15° , 30° . Specifically, two 3 beam combinations are shown: -15° , 0° , 15° and -30° , 0° , 30° . The 2D lattice has pmm symmetry, and the 3D lattice unit cell is primitive tetragonal. The length c depends on the orientation of the beams. 79

Figure S2.9. Large scale lattices: spatial intensity profiles of white light acquired at the exit face of (a) WEL-1 $_{-30^\circ}$ (b) WEL-1 $_{-15^\circ}$ (c) WEL-1 $_{0^\circ}$ (d) WEL-1 $_{15^\circ}$ and (e) WEL-1 $_{30^\circ}$. To account for refraction at the air/sample interface, the probe beam was launched and the lattice exit face was imaged at -44° , -22° , 0° , 22° , and 44° , respectively relative to the normal of the sample entrance face. In all images, scale bar = 1 mm 80

Figure S2.10. Waveguide arrays generated with a single beam (WEL-1) oriented respectively at (a) 0° , (b) 22° and (c) 44° and (d)-(f) optical micrographs of the exit face of each lattice, imaged at 0° , 22° , and 44° , respectively, relative to the microscope optical axis. (g)-(i) Corresponding Top-down micrographs of the WEL-1 lattices in (d)-(f). In all images, scale bar = $160 \mu\text{m}$ 81

Figure S2.11. Lattices consisting of an intersecting pair of waveguide arrays (WEL-2) generated with (a) two incandescent beams with incident angles of -22° and 22° ,

relative to the surface normal. (b)-(c) Optical micrographs of the exit face of WEL-2 imaged at -22° and 22° , respectively, relative to the microscope optical axis. (d) Top-down micrograph showing that the pair of waveguide arrays intersects at an angle of $\sim 29^\circ$ in the medium. (e) WEL-2 generated with beams incident at angles of -44° and 44° relative to the surface normal. (f)-(g) Optical micrographs of the exit face of the resulting lattice imaged at -44° and 44° , respectively, relative to the microscope optical axis. (h) Top-down micrograph showing that the pair of waveguide arrays intersects at an angle of $\sim 55^\circ$ in the medium. The red rhombus in (d) and (h) indicates the unit cell of the lattice in this plane. In all images, scale bar = $160 \mu\text{m}$ 82

Figure S2.12. Lattices consisting of three intersecting waveguide arrays (WEL-3) generated with (a) three incandescent beams incident at angles of -22° , 0° and 22° respectively, relative to the surface normal. (b)-(d) Optical micrographs of the exit face of WEL-3 imaged -22° , 0° and 22° , respectively, relative to the microscope optical axis. (e) Top-down micrograph showing the intersections of the three waveguide arrays. (f) WEL-3 generated with beams at incident angles of -44° , 0° and 44° , relative to the surface normal. (g)-(i) Optical micrographs of the exit face of WEL-3 imaged at -44° , 0° and 44° , respectively relative to the microscope optical axis. (j) Top-down micrograph showing the intersections of the three waveguide arrays. The red rhombus in (e) and (j) indicates the unit cell face in this plane. In all images, scale bar = $160 \mu\text{m}$ 82

Figure S2.13. Spatial intensity profiles acquired at the exit face of (a) WEL-1 $_{0^\circ}$, (b) WEL-1 $_{15^\circ}$ and (c) WEL-1 $_{30^\circ}$, where the probe beam was launched at 0° , 22° and 44° respectively, relative to the normal of the sample entrance face. Horizontal and vertical line-scans (indicated by dotted white lines) and a color intensity scale are included. In all images, scale bar = $160 \mu\text{m}$ 83

Figure S2.14. Spatial intensity profiles of transmitted white light acquired at the exit face of (a) WEL-2 $_{(-15^\circ, 15^\circ)}$ and (b) WEL-2 $_{(-30^\circ, 30^\circ)}$. In (a), the probe beams were launched at angles of -22° and 22° , respectively whereas in (b), probe beams were launched at -44° and 44° , respectively relative to the normal of the sample entrance face. Horizontal and vertical line-scans (indicated by dotted white lines) and a color intensity scale are included. In all images, scale bar = $160 \mu\text{m}$ 83

Figure S2.15. Spatial intensity profiles of transmitted white light acquired at the exit face of (a) WEL-3 $_{(-15^\circ, 0^\circ, 15^\circ)}$ and (b) WEL-3 $_{(-30^\circ, 0^\circ, 30^\circ)}$. In (a), the probe beams were launched at angles of -22° , 0° and 22° , respectively whereas in (b) probe beams were launched at -44° , 0° and 44° , respectively relative to the normal of the sample entrance face. Horizontal and vertical line-scans (indicated by dotted white lines) and a color intensity scale are included. In all images, scale bar = $160 \mu\text{m}$ 84

Figure S2.16. Normalized power coupled from one waveguide to another as a function of their intersection angle. 85

Figure S2.17. Simultaneous and independent transmission of multiple wavelengths through the WEL lattice (a) Scheme of optical assembly showing arrangement and orientation of red, blue, and green lasers, to couple respectively into waveguide arrays oriented at 0° , 15° , and 30° . Transmitted light was projected in the far-field onto a screen. Inset is a top-down photograph showing the relative of the sample and projected transmission patterns of the red, green and blue beams. (b) Photographs of the assembly acquired along the three different propagation directions of the three beams. 85

Figure S2.18. 2-D simulations of the propagation of a Gaussian beam ($240\ \mu\text{m}$ -wide, $\lambda = 633\ \text{nm}$) in a WEL lattice. Angles of propagation in the structure are (a) -30° , (b) -15° , (c) 0° , (d) 15° , and (e) 30° , with respect to the z -axis. Transverse profiles in (a, e) were acquired at $z = 1.5\ \text{mm}$ while those in (b-d) were acquired at $z = 2.0\ \text{mm}$. These simulations correspond to those presented in Figure 2.4b of the manuscript. 87

Figure S2.19. Optical assembly for determining the field of view of the WEL-5 lattice. The WEL lattice is first rotated so that (accounting for refraction at the air/sample interface), the illuminated object “O” couples directly into one of the five waveguide arrays; transmitted light at the exit face is then imaged onto the CCD camera. A 2 mm-wide aperture was placed in front of the imaging lenses to avoid stray light. To vary the angle of incidence of the illuminated object, the WEL lattice, the imaging lenses and CCD camera are then simultaneously rotated about the optic axis over an interval of -6° to 6° with a resolution of 0.5° 89

Figure S2.20. Sequence of spatial intensity profiles of illuminated “O” object transmitted at varying angles of incidence through each of the five waveguide arrays of a WEL lattice. The angle of orientation of each waveguide array is indicated on the left. The horizontal axis indicates the angle of incidence of the illuminated “O” with respect to the normal of the entrance face. Images were acquired at the exit face of the WEL lattice. Corresponding measurements for a control sample without the lattice are provided below each sequence for comparison. In all images, scale bar = 1 mm. 90

Figure S2.21. Sequence of spatial intensity profiles of an illuminated “O” (object) transmitted at varying angles of incidence through five different WEL-1 lattices. The angle of orientation of waveguides in each array with respect to the normal of the sample entrance face is indicated on the left. The x axis indicates the angle of incidence of the illuminated “O”. Images were acquired at the exit face of the WEL lattice. Corresponding measurements for a control sample without the lattice are provided below each sequence for comparison. In all images, scale bar = 1 mm. 91

Figure S2.22. Plots of normalized total intensity of the image versus the angle of incidence of the object for five different WEL-1 lattices at different orientation angles, with respect to the surface normal. The filled red squares represent the lattice, and the filled black circles represent the control (i.e., unstructured medium). 92

Figure S2.23. 2D spatial intensity profiles of images for two WEL-2 lattices with following lattice orientations: (a) -15° and 15° , (b) -30° and 30° with respect to WEL surface normal. Scale bars = 1 mm. 93

Figure S2.24. 2D spatial intensity profiles of images for two WEL-3 Lattices with the following lattice orientations: (a) -15° , 0° and 15° , (b) -30° , 0° and 30° , with respect to WEL surface normal. Scale bars = 1 mm. 93

Figure S2.25. Plots of normalized total intensity of the image versus the angle of incidence of the object for two WEL-2 lattices and two WEL-3 lattices with different lattice orientations. The red plots represent the angular acceptance performance of the lattices, while black curves represent that of the control (i.e., unstructured medium). Lattice combinations are: (a) -15° and 15° ; (b) -30° and 30° ; (c) -15° , 0° and 15° ; (d) -30° , 0° and 30° 94

Figure S2.26. Calculated normalized intensity versus angle of incidence curves that match the experimental data shown in Figure 2.5c with $\Delta n=0.001$ 97

Figure S2.27. Setup for the simultaneous capture of multiple images at different angular positions. (a) Schematic showing the orientation of the images on the CCD chip. Light propagates in the $+z$ direction. The perspective view of the captured images is looking down the $+z$ axis, as indicated by the eye. (b) Photo showing the paper template containing the cut out letters, the arrangement of the letters ‘M’, ‘A’, and ‘C’ are indicated. (c) Close up view of the cut out letters mounted onto the piece of paper, which is bent at two points so as to orient the letters ‘M’ and ‘C’ perpendicular to their respective beams. 97

Figure S2.28. Simultaneous image collection transmission of two objects from the WEL-3(-30° , 0° , 30°) lattices. Scale bar = 1 mm. 97

Figure S2.29. (a) Schematic diagram of assembly to study the multifunctional imaging behaviors of the WEL lattice. Propagation of ‘C’ is traced in red as an example. (b) A phenomenological equation generalizing and describing the conditions required for each imaging operation of the WEL lattice. 98

Figure 3.1. Operating principles of the RDWLs. (a) Comparison of angular collection range of identical waveguides with the same θ_{wg} but with a curved and (right) planar surface, respectively. (b) Scheme of a single layer (xz plane) comprising a radial distribution of waveguides. The FOV corresponds to the sum of collection angular ranges of all the waveguides. (c) Scheme of the yz cross-section and corresponding FOV (d) Scheme of RDWEL depicting a seamless, panoramic FOV at the exit face (xy plane). 106

Figure 3.2. Fabrication and microstructural characterization of RDWEL. (a) Optical assembly employed to construct the RDWEL consists of a broad incandescent beam

emitted by a quartz-tungsten-halogen (QTH) lamp, which is collimated by a plano-convex lens, focused by a linear Fresnel lens and patterned by an amplitude mask before entering a sample cell containing photopolymerisable epoxide fluid. The spatial intensity profile of the beam at the exit face of the sample was imaged through plano-convex lenses onto a CCD camera. The inset contains a magnified image of the converging light beams entering the sample. (b) Scheme of 3-D RDWEL with color-coded boxes that correspond to transmission optical micrographs of (c) longitudinal and (d) transverse cross-sections. Scale bar in (c) and (d) = 160 μm ... 109

Figure 3.3. Seamless light collection in RDWEL. (a) Scheme of optical assembly employed to characterize light propagation through the RDWEL as a function of incidence angle. Light emitted by a QTH lamp is collimated by a planoconvex lens (L_1) and launched onto the entrance face of the RDWEL sample (S), which is placed on a rotation stage (R) and rotated about its central axis (along y axis) at 5° intervals from -55° to $+55^\circ$ with respect to the surface normal (z axis). The spatial intensity profiles at the exit face are imaged through a planoconvex lens pair (L_2 and L_3) onto a CCD camera. (b) Spatial profiles of the RDWEL exit face ($z = 2$ mm) acquired at probe beam incidence angles = 0° , -10° , -20° , -30° , -40° and -50° , respectively. 1-D traces along the x and y axes are provided. For all images, intensity color bars are provided together with scale bar = 160 μm 112

Figure 3.4. The seamless FOV of the RDWEL. (a) optical assembly employed to measure the FOV of the RDWEL; Light emitted by a QTH lamp is collimated by a planoconvex lens (L_1) before entering the RDWEL sample (S), which is mounted on a rotation stage (R). For measurements, S is rotated about its central axis (along y axis) to locate a specific sub-population of waveguides; S and all imaging components are then simultaneously rotated over an arc of $\pm 8^\circ$ at 0.5° intervals. Spatial intensity profiles at the exit face are imaged through a planoconvex lens pair (L_2 and L_3) onto a CCD camera. (b) Intensity profiles of the RDWEL exit face and control (bottom row) at different incidence angles of the probe beam. Results correspond to waveguide sub-population with $\theta_{\text{wg}} = 0^\circ$. Intensity color scale is provided. Magnified images within the inset show tight confinement of light within waveguides in the RDWEL. (c) Plots of integrated intensity versus probe incidence angle for RDWEL (red) and control (black). (d) A representation of the panoramic FOV determined by the cumulative, experimentally determined acceptance ranges of the 23 waveguide sub-populations (red) of the RDWEL. Equivalent plots for the control are provided (black). θ_{wg} of each sub-population is indicated in blue. 115

Figure 3.5. Panoramic imaging by RDWEL. (a) Scheme and (b) photograph of optical assembly for simultaneous panoramic imaging of five shapes. The inset shows the masks employed to generate the five shapes. Images of the five shapes that were (c) simultaneously and (d) sequentially recorded by the CCD chip at the RDWEL exit face. (Scale bar = 1 mm). 117

Figure S3.1. Schematic diagram showing the ray tracing method used to indicate the

angular directions of the waveguides in the RDWELs. Blue lines depict the transmission traces of the normal incident light through a bare Fresnel lens. The red ones indicate the transmission traces through the Fresnel lens, a photomask and the photopolymerisable sample..... 125

Figure S3.2. Plots showing the refraction angles of the beam before (red curve) and after (black curve) refracting into the photopolymer versus the off-centered distance of their starting point at the entrance face of the RDWEL..... 126

Figure S3.3. A schematic diagram of ray tracing in a slant waveguide with flat surface. 129

Figure S3.4. Transverse micrographs of all the 23 waveguide sub-populations of the RDWEL. The tilting angle are labeled. Scale bar = 250 μm 132

Figure 4.1. Working principles of the beam steering coating. (a) Schematic diagram of employing slanted slab waveguides as beam steering elements for solar cells. The waveguide slabs are oriented at small slants relative to the surface normal. The inset shows the geometry and orientation of a single slab waveguide. Beam Propagation Method (BPM) simulations of the propagation of a Gaussian beam (633 nm) launched along the surface normal (z) of a 3000 μm -thick polymer film containing a planar waveguide ($\Delta n = 0.002$) oriented at 0.00°, 0.66°, 1.33°, 1.99°, 2.65°, and 3.31° with respect to z . (b) Longitudinal (xz) and (c) transverse (xy) cross-sections are presented. The intensity scale bar is provided. (d) Plot showing the physical orientation and boundaries of waveguides and the resulting displacement from the normal at the exit face (in black). Peak intensity of light (in red) launched along the surface normal at the waveguide exit. (e) Plot of optical power at waveguide exit versus waveguide orientation. 140

Figure 4.2. (a) Scheme of optical assembly employed to fabricate beam steering coatings: incandescent light emitted by a quartz-tungsten-halogen (QTH) lamp is collimated (L_1) and launched through an amplitude mask into a transparent cell containing photopolymerizable epoxide fluid (S) mounted on a rotation stage (R, resolution = 1°). Spatial intensity profiles of the exit face of S are imaged through a plano-convex lens pair (L_2 and L_3) onto a CCD camera. Inset shows amplitude mask patterned with a periodic ($\Lambda = 2.4$ mm) array of stripes (thickness = 300 μm) placed flush with the entrance face of S. Dark orange stripes correspond to waveguides induced by stripes. (b) Spatial intensity profiles acquired at the exit face ($z = 3000$ μm) of S before (top) and after (down) inscription of waveguides (scale bar = 500 μm ; colour bars provide relative intensity). Insets are magnified images of individual stripes with corresponding 1-D profiles (scale bar = 100 μm). (c) Photographs (left) and corresponding optical micrographs of transverse and longitudinal cross-sections of a beam steering coating; in these samples, planar waveguides possess $\theta = 2.7^\circ$ 143

Figure 4.3. (a) Scheme of optical assembly employed to characterize beam steering behaviour. A 633 nm laser beam was attenuated by a neutral density (ND) filter and

focused through a plano-convex lens (L) onto the beam steering coating (S), which was mounted on a translation station (resolution $\pm 10 \mu\text{m}$). The spatial intensity profile of the beam at the exit face of S was imaged onto a CCD chip. (b) Images in the first column trace the incident position (x) of the input beam (in red) to a single planar waveguide (dark orange) in the coating; black dotted line indicates $x = 0 \mu\text{m}$. Corresponding spatial intensity profiles of the beam at the exit face of S are provided in the second column. Images (1) to (10) correspond to $x = 750 \mu\text{m}$, $250 \mu\text{m}$, $200 \mu\text{m}$, $175 \mu\text{m}$, $50 \mu\text{m}$, $0 \mu\text{m}$, $-50 \mu\text{m}$, $-100 \mu\text{m}$, $-500 \mu\text{m}$, and $-750 \mu\text{m}$, respectively, where the “-” refers to the laser beam entering the film from the left side of the waveguide. Dotted white lines in the spatial intensity profiles trace the trajectory of the beam in the absence of a waveguide. Scale bar = $200 \mu\text{m}$. (c) Plot of the displacement (Δx) of the incident beam (relative to its trajectory in the absence of a waveguide) at the exit face of the sample. 146

Figure 4.4. Beam steering coatings enhance the EQE of a Si solar cell. Incident light, which would be (a) scattered and reflected is (b) steered away from the metal contact by a waveguide with $\theta = 2.7^\circ$. Corresponding photographs show the marked decrease in scattering in the latter. (c) External quantum efficiency (EQE) plots of solar cells coated with unpatterned (control) and waveguide-imprinted polymer films. The inset is the magnified region from 500 nm to 1000 nm. (d) Plot of average EQE of control and polymer films imprinted with waveguides with varying θ . (e) Scheme of relative orientation of waveguides with respect to a single metal contact. The displacement of waveguided light away from the metal contact increases with θ . Regions of the incident beam that propagate directly through the sample are indicated in green; yellow corresponds to light that will reach the metal contact while red corresponds to light coupled into the waveguide..... 149

Figure S4.1. Beam propagation simulation of longitudinal (a) and transverse (b) cross-sections of slanted channel waveguides when a 532 nm Gaussian beam is launched with normal incidence into these waveguides. The labels refer to the refraction angle of the waveguide angles. The intensity bar is provided, with red color refer to intensity of 1, while white color refer to intensity higher than 1. 159

Figure S4.2. A schematic diagram of a slant waveguide. The red and black lines show how light incident at the boundary of the acceptance cone is transmitting inside the waveguide. 160

Figure S4.3. UV-Vis absorption (a) and transmission (b) spectra of the epoxide based polymer system. 161

Figure S4.4. CCD images of the laser beam when it is launched at varied positions. The samples are shifted perpendicular to the laser beam with an interval of 25 μm . #47 is the one when waveguide exit face overlaps with the laser beam, and is defined as 0 μm . Images 1-90 correspond to the intensity profiles when laser beam is launched at -1150 μm , -1125 μm , etc., till 1100 μm , away from the position of #47..... 163

Figure S4.5. Corresponding CCD images to that shown in Figure S4.4 when backlight is turned off. 164

Figure S4.6. Total integrated (red) and normalized (blue) beam intensity of the He-Ne laser beam as a function of entrance positions..... 165

Figure 5.1. Operating principles of the RDWEL (a) Scheme of the RDWEL, which consists of a periodic stack of radially distributed waveguide arrays (b) Beam propagation (BPM) simulations of a laser beam propagating through a waveguide oriented at θ_{wg} with respect to the normal of a 2000 μm -thick film. Control results for the same film without a waveguide are provided in the bottom row. Longitudinal (xz plane) intensity profiles are shown with the corresponding colour intensity scale; refractive indices of the different layers and angles associated with the trajectory of the beam are provided. For clarity, boundaries of the waveguides are indicated in white while the trajectory of the beam upon exiting the film is indicated by a red arrow. Ray tracing diagrams of light propagating through (c) RDWELDIV and (d) RDWELCONV. 173

Figure 5.2. The RDWEL was fabricated with (a) incandescent light emitted by a quartz-tungsten-halogen (QTH) lamp, which was collimated by a plano-convex lens (L_1), focused through a cylindrical condenser lens and passed through an amplitude mask and launched onto the optically flat entrance face of a cylindrical cell containing photopolymer fluid. A plano-convex lens pair (L_2 , L_3) imaged the cross-sectional spatial intensity profiles at the sample exit face onto a CCD camera. The inset traces the convergence of the patterned beam of light within the sample. (b) A scheme of the RDWEL containing colour-coded rectangular regions, which were characterized through (c-d) transmission optical microscopy. Scale bar in (c-d) = 200 μm 175

Figure 5.3. Field of view (FOV) of the RDWEL was characterized with (a) probe incandescent beam (PB), which red-filtered (F), collimated (L_1) and launched onto the entrance face of RDWEL_{CONV} (S), which was mounted on a rotatory stage (R). Spatial intensity profiles of a specific waveguide sub-population were imaged by a plano-convex lens pair (L_2 , L_3) equipped with an aperture (A) onto a CCD camera. For each waveguide sub-population, the spatial intensity profile was acquired by varying the incidence angle of the probe beam over $\pm 10^\circ$. (b) Angle-dependent spatial intensity profiles of the $\theta_{wg} = 0^\circ$ waveguide subpopulation (top-row) and control (bottom-row). Scale bar = 300 μm . A colour intensity scale is provided. Inset shows well-defined, discrete spots corresponding to the output of individual waveguides. (c) Plots of normalized intensity vs. incidence angle of the probe beam for the $\theta_{wg} = 0^\circ$ waveguide subpopulation (red) and control (black). (d) The seamless FOV of the RDWEL corresponds to the overlapping angular acceptance ranges of all 13 waveguide sub-populations (red). Corresponding measurements for the control are provided in black. θ_{wg} of the central waveguide in each waveguide subpopulation is indicated for each plot. 177

Figure 5.4. Shaping LED beams with RDWEL was demonstrated by (a) launching a blue LED beam, which was first passed through a pinhole onto the entrance face of the RDWEL_{DIV} or RDWEL_{CONV} sample. The spatial intensity profile of the beam in the xz plane was projected onto a white board and imaged with a camera. Corresponding top-down photographs of the beam after propagating through (b) a control (top), RDWEL_{CONV} (central) and RDWEL_{DIV} (bottom) samples. Scale bar = 2 cm. (c-d) 1-D transverse intensity profiles of the beam after propagating through the three different samples acquired at 2 cm and 6 cm from the exit face (indicated in (b) by dotted red and white lines, respectively). 180

Figure 5.5. The focal length of RDWEL_{CONV} was determined by (a) imaging the cross-sectional spatial intensity profile of a red LED beam at different distances from the exit face of the RDWEL_{CONV}. (b) Corresponding spatial intensity profiles acquired from $z = 0$ mm (exit face) to $z = 8$. Scale bar = 1 mm. Colour intensity scale is provided. The integrated intensity of a sub-population of waveguides contained in red rectangle was (c) plotted against z to determine the focal length of RDWEL_{CONV}. Measurements were normalized to integrated intensity at $z = 0$ 182

Figure S5.1. Schematic diagram showing the ray tracing method used to determine the angular directions of the waveguides in the RDWEL. Blue lines depict the transmission traces of the normal incident light through the cylindrical condenser lens, the photomask into the photopolymerisable sample. 192

Figure S5.2. Plots showing the refraction angles of the beam into the photopolymer versus the off-centered distance of their starting point at the entrance face of the RDWEL. 193

Figure S5.3. Schematic diagram of employing RDWEL with converging orientation (a) and diverging orientation (b) to a LED beam. z is the optical axis, L is the distance between the RDWEL and the LED, and θ_{ic} and θ_{id} refer to refer to the incident angle of the LED when the RDWEL_{CONV} and RDWEL_{DIV} are employed respectively. ... 195

Figure S5.4. Optical transmission micrograph of the longitudinal cross-section of the entire RDWEL. Scale bar = 1 mm. 199

List of tables

Table 1.1 Selected parameters of a few typical planar compound eyes	25
Table 1.2 Selected parameters of a few typical curved artificial compound eyes.....	28
Table S2.1 Lattice constants of single waveguide lattices	80
Table S2.2 Lattice parameters of 3D lattices.....	80
Table S2.3 Experimental configuration of variable-angle imaging in the WEL lattice	90
Table S2.4 Angular acceptance ranges for the WEL lattice structure	91
Table S2.5 Angular acceptance ranges for five WEL-1 different lattices	92
Table S2.6 Angular acceptance ranges for WEL-2 _(-15°, 15°) lattices	95
Table S2.7 Angular acceptance ranges for WEL-2 _(-30°, 30°) lattices	95
Table S2.8 Angular acceptance ranges for WEL-3 _(-15°, 0°, 15°) lattices	95
Table S2.9 Angular acceptance ranges for WEL-3 _(-30°, 0°, 30°) lattices	95
Table S2.10 Incident and refracted angles as determined from samples made from 2, 3 and 5 beams, and the calculated refractive index of the polymer	96
Table S3.1 Summary of the angles of all the waveguides in the RDWEL.....	127
Table S3.2 Acceptance ranges (in the form of boundary angles) of waveguides with different slant angles but flat entrance faces	129
Table S3.3 Summary of the FOVs of the 23 waveguide sub-populations in the RDWEL	133
Table S4.1 Acceptance ranges of slanted waveguides via ray-tracing calculation ...	161
Table S4.2 Comparison of the total EQE and EQE enhancement among slanted slab waveguides over the different waveguide ranges	165
Table S5.1 Summary of the angles of all waveguides in the RDWEL.....	194
Table S5.2 Summary of waveguide off-centered distances (d'), waveguide angles (θ_{wg}),	

waveguide acceptance cones (θ_1, θ_2), waveguide refraction angles (θ_{rwg}) and incident angle of the LED when employing REWEL_{CONV} (θ_{ic}) 197

Table S3 Summary of waveguide off-centered distances (p_d), waveguide angles (θ_{wg}), waveguide acceptance cones (θ_1, θ_2), waveguide refraction angles (θ_{rwg}) and incident angle of the LED when employing RDWEL_{DIV} (θ_{id})..... 198

List of Abbreviations

<i>cw</i>	Continuous wave
Δn	Refractive index change
NLS	Nonlinear Schrödinger
NIR	Near infrared
<i>fs</i>	Femtosecond
<i>ms</i>	Millisecond
MI	Modulation instability
PI	Photoinitiator
SWW(s)	Self-written waveguide(s)
SMF	Single mode fibers
LCD	Liquid crystal display
LEDs	Light emitting diodes
BCC	Body-centered cubic
WEL(s)	Waveguide encoded lattice(s)
FOV	Field(s) of view
FWHM	Full width at half maximum
MLA	Microlens array
TOMBO	Thin observation module by bound optics
APCO	Apposition compound eye objective
ACE	Artificial compound eye
CurvACE	Curved artificial compound eye

PBC	Printed circuit board
MEMS	Micro-electromechanical systems
RDWEL(s)	Radially distributed waveguide encoded lattice(s)
QTH	Quartz-tungsten-halogen
CCD	Charged-coupled device
BPM	Beam propagation method
NA	Numerical aperture
CF	Concentration factor
PTFE	Polytetrafluoroethylene
TIR	Total internal reflection
EQE	External quantum efficiency
J_{sc}	Short circuit current
RDWEL_{CONV}	RDWEL with converging orientation
RDWEL_{DIV}	RDWEL with diverging orientation
MAPTMS	3-(Trimethoxysilyl)propyl methacrylate

Chapter 1 Introduction

Optical fields transmitting in nonlinear media induces changes to the physical or chemical properties of the media, which in turn change the propagation behaviors of the optical field. These reciprocal light-matter actions lead to various interesting nonlinear optical phenomena, which may applied in a wide range of applications.

In the first part of this introduction chapter, a general description of nonlinear light propagation relevant to the studies is presented, which includes optical self-trapping and optical modulation instability. Thereafter, conventional optical media include Kerr media and photorefractive crystals and nonconventional photopolymer media which support the nonlinear light propagation is presented. The third part talks about the study of self-written waveguide structures in photopolymer systems, followed by a section describing two specific photopolymer systems – epoxide and acrylate based systems - which are employed in the following projects. The next section gives a brief introduction on natural and artificial compound eyes, as most of the waveguide structures studied in this thesis are inspired by the compound eyes. Finally, the research objectives and chapter arrangement of this thesis are presented.

1.1. An introduction to nonlinear propagation of light

1.1.1. Self-trapping of light waves

A continuous wave (*cw*) light beam propagating through most dielectric media (dispersive linear materials) suffers spatial broadening, due to natural diffraction. This can be understood by treating the beam as a linear superposition of plane-waves, each propagating along slightly different directions, thus having different phase velocities relative to the propagation axis. However, when travelling through a nonlinear medium, the light beam induces a structural change to the medium and modifies the property of the material, which in turn changes the propagation behavior of the original input light beam.

For instance, when a Gaussian-profile beam is propagating along z axis in a linear medium, the phase fronts undergo slight angular deviation thus propagate at different phase velocities with respect to z axis, which leads to a curved phase front acting similar to a concave lens and causes the beam to broaden in diameter and weaken in intensity (**Figure 1.1a**).¹ When this beam travels through a medium that leads to intensity-dependent change in refractive index (Δn), it induces a refractive index change which mirrors its intensity profile (Gaussian) along its path. This is essentially a positive lens, which causes the beam to self-focus along its propagation axis (**Figure 1.1b**). Under certain conditions, the self-focusing effect would exactly counterbalance the divergence of the beam, leaving the beam to propagate in the material over long distance (\gg Rayleigh length) without broadening and retain its original spatial intensity profile (**Figure 1.1c**). This unperturbed beam is called a “self-trapped” beam, or a spatial soliton.²

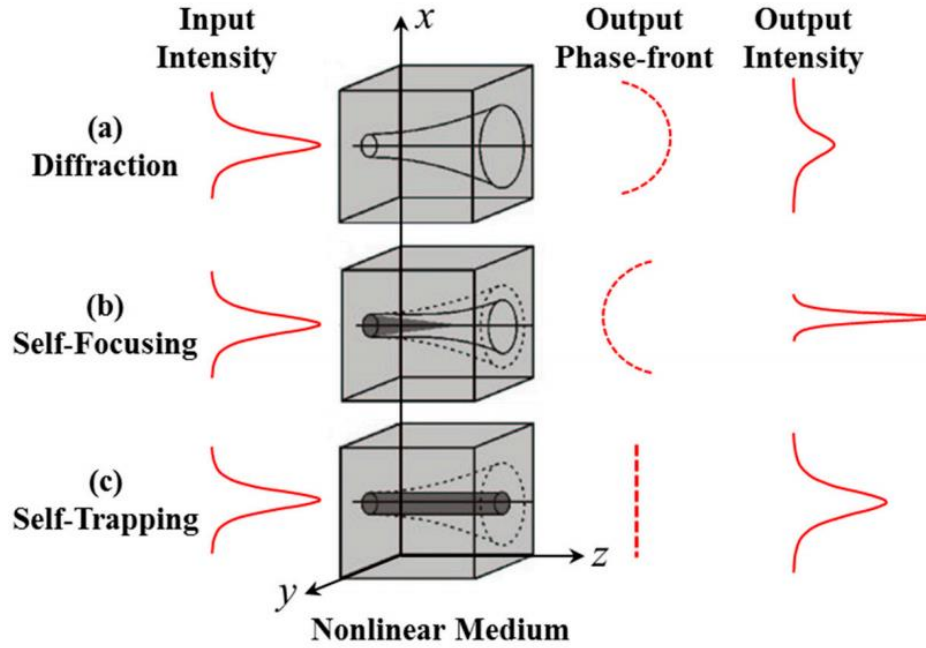


Figure 1.1. Schematic illustrations of the spatial beam profiles, output phase-front, and output intensity of a propagating beam as it undergoes: (a) natural diffraction; (b) self-focusing; and (c) self-trapping. Reproduced with permission from Ra’ed Malallah, Haoyu Li, Damien P. Kelly, John J. Healy and John T. Sheridan, A review of hologram storage and self-written waveguides formation in photopolymer media; published by MDPI, 2018.¹

The propagation of an optical beam in photoresponsive materials can be described using the nonlinear Schrödinger (NLS) equation:^{3,4}

$$2ikn_0(\partial\Psi/\partial z) + \nabla^2_{\perp}\Psi + k^2(n^2 - n_0^2)\Psi = 0 \quad (1-1)$$

Where Ψ is the amplitude of the electric field $E = \Psi e^{ikn_0z}$, z is the propagation direction, $k = 2\pi/\lambda$ is the angular wave vector, n and n_0 refer to the refractive index of the exposed and non-exposed region, respectively. The first term $2ikn_0(\partial\Psi/\partial z)$, describes the propagation of light in a photo responsive medium, while the second term $\nabla^2_{\perp}\Psi$ (where $\nabla^2_{\perp} = (\partial^2/\partial x^2) + (\partial^2/\partial y^2)$) describes the natural diffraction of the beam, and the third term: $k^2(n^2 - n_0^2)\Psi$, indicates the self-focusing of the beam due to the self-induced refractive index changes $(n - n_0)$ along the propagation path. The

self-trapped beam or soliton can be obtained by solving the Schrödinger equation presented above.

Self-trapping has been well studied in coherent laser light over 50 years.⁵ Kerr media (vide infra) provides an ideal platform for conducting theoretical studies on solitons. However, experimental demonstration of solitons is restricted to one dimensional beam in a slab waveguide,⁶ as beams self-trapping of a (2+1) dimensional (written as “(2+1) D” in the following content) beam in Kerr media is unstable, which eventually breaks into filaments.^{7,8}

The first experimental demonstration of spatial soliton was reported in 1974 by Ashkin and Bjorkholm, who launched a circularly symmetric laser into a sodium vapor (a nonlinear medium).⁹ It took over 10 years for the next experimental demonstration of self-trapped beam – a 1-D spatial soliton, when Barthelemy *et al.* irradiated a reorientational CS₂ liquid crystal with a coherent light source.¹⁰ It took nearly another 10 years until the first stable 2-D solitons was observed in a photorefractive crystal.¹¹ For a long period of time, spatial solitons are considered exclusive to coherent optical fields.

The self-trapping of incoherent light was first discovered in 1996 when *Mitchell et al.* passed a partially spatially incoherent laser light into a photorefractive crystal.¹² Soon after, self-trapping of incoherent white light was observed when an incandescent beam was launched into the photorefractive crystal.¹³ An incandescent beam, unlike a coherent laser beam, is a chaotic¹⁴ entity of visible and near infrared (NIR) waves, which are poorly correlated in phase and amplitude (in other words: both spatially and temporally incoherent). Consequently, the beam is an entirety of intensity speckles,

which fluctuate randomly in space at the femtosecond (fs) timescale.¹³

To achieve self-trapped beam in incoherent optical fields, three prerequisites^{2,13} must be obeyed. Firstly, a non-instantaneous photoresponse is required that is delayed as compared to the fs fluctuation of the irradiation. Under this condition, changes in refractive index are induced by the time-averaged intensity of the beam, thus random phase fluctuations are effectively cancelled out. Secondly, the optical power should be conserved, which requires that the waveguides induced during self-trapping must be multimoded to support the multiple optical modes constituting white light. Thirdly, the white light beam should be always confined to the self-induced waveguide, and the total intensity resulting from the time-averaged distribution of waveguide modes (intensity at waveguide exit face) must correspond to the time-averaged intensity of the white light beam (intensity at the waveguide entrance face).

Self-trapping of incoherent light has also been observed in systems other than photorefractive crystals, such as in photopolymers.^{1,15-17}

1.1.2. Optical Modulation instability

Another nonlinear phenomenon closely related to self-trapping is modulation instability (MI). MI is a wide-reaching mechanism that describes the spontaneous emergence of patterns in diverse systems including plasma waves¹⁸⁻²⁰, water waves²¹⁻²³, and electromagnetic waves²⁴⁻²⁶, etc. and over very large length scales (from the galactic scale to atomic scale).²⁷ During this process, noise – negligible amplitude and phase perturbations in the otherwise homogeneous system - becomes greatly amplified due to the integrated effects of nonlinearity and diffraction/dispersion²⁸. In the spatial

optical regime, MI particularly refers to the phenomenon when a broad and uniform beam passing through a photo responsive medium spontaneously breaks into large population of microscopic light filaments to stabilize the amplified perturbation of the optical field.^{29,30} Each of these light filaments is a self-trapped light beam (vide supra), which propagates without changing in shape or intensity and inscribes a permanent waveguide along its path. Because they originate from adventitious noise – uncorrelated decay of excited states in the white light source, the MI-induced filaments (as well as the resulting waveguides) are positioned randomly in space, while possessing statistically identical diameters;²⁹ such amplification of a select frequency or length-scale is characteristic of MI.²

Same as the case of self-trapping, MI was firstly predicted and observed in coherent beams^{31–34}, thus has been believed for a time to only occur in coherent optical field, until Soljagic *et al.* theoretically demonstrated the existence of the incoherent MI in 2000, by solving the nonlinear paraxial wave equation of an incoherent beam in a non-instantaneous medium.²⁸ The growth rate $g(\alpha)$ of incoherent MI was proposed in this study, which is given as:^{28,35}

$$\frac{g(\alpha)}{k_0} = -(k_{x0}/k_0)(|\alpha|/k_0) + (|\alpha|/k_0)\sqrt{\frac{\kappa I_0}{n_0} - \left(\frac{\alpha}{2k_0}\right)^2} \quad (1-2)$$

Where k is the wave vector, α is the spatial wave vector of the perturbation, I_0 is the intensity of the incident beam, $\kappa = d(\Delta n)/dI$ represents the marginal nonlinear refractive change affected by the optical intensity I_0 ; and (k_{x0}/k) refers to the width of the angular power spectrum, and describes the spatial incoherence of the beam. This equation indicates that for a given degree of coherence, incoherent MI occurs only

when the nonlinear refractive index change κI_0 exceeds a specific threshold: $n_0 \times (k_{x0}/k)^2$. It also indicates that at a fixed value of the coherence and nonlinearity, the incoherent MI has a maximum growth rate at a preferred perturbation period (or spatial frequency), which leads to the formation of ordered patterns.³⁵

The first experimental evidence of incoherent MI was given shortly by the same group, who passed a partially spatially incoherent but temporally coherent laser light into a strontium-barium-niobate crystal – a non-instantaneous nonlinear medium.³⁶ Several prerequisites³⁶ of incoherent MI were proposed in this study including: (1) non-instantaneous media with much slower response versus the fs phase fluctuation of the optical wavefront is inevitable for the MI to occur; (2) a sharp threshold nonlinearity should present above which quasi-periodic patterns would form and below which the perturbations would decay; (3) the threshold is defined by the correlation distance of the input source; and (4) the growth rate of MI is restricted only by the saturation of the nonlinearity.

This experimental verification paved the way for the proposed prerequisites to become the guidelines for all the future incoherent MI works, and since then, MI of partially spatially incoherent beam has been widely reported.^{35,37–39} MIs of both spatially and temporally incoherent light (such as white incandescent light) were also predicted via theoretic studies⁴⁰ and experimentally observed in photorefractive crystals⁴¹ and soft matters including such as in photopolymer media^{4,29,30,42–45}, etc.

1.2. Optical media supporting nonlinear light propagation

An optical field travelling through a nonlinear medium induces change to the

property of the medium, which in turn modifies the propagation behavior of the optical field. The behavior of the beam after the light-medium reciprocal action is dependent on the on the polarization density vector $P(r, t)$ of the medium and the electric field vector $E(r, t)$ associated with optical field travelling through the medium.⁴⁶ In general, in a bulk dielectric medium, the relationship between P and E can be expressed using the Taylor series expansion as follows,⁴⁶

$$P = \epsilon_0(\chi^{(1)}E + \chi^{(2)}EE + \chi^{(3)}|E|^2E + \dots) \quad (1-3)$$

Where ϵ_0 is the dielectric constant of the medium in vacuum and χ is the electric susceptibility of the medium. For a linear medium, the polarization has a linear relationship with the optical field, namely, $P = \epsilon_0\chi^{(1)}E$. For Kerr media and photorefractive crystals mentioned above, P is related to the nonlinear terms of the expansion, and the change in refractive index arises from the higher order susceptibilities $\chi^{(n)}$ (where $n > 1$).

Kerr media provides an ideal platform for conducting theoretical study on self-trapping and solitons. In this type of materials, the nonlinearity arises from the drifting of bound electrons induced by the electric field associated with the externally applied optical field. This nonlinearity is represented by the 3rd term of **1-3**. The refractive index of Kerr media under nonlinear polarization is then given as⁵

$$n = n_0 + \Delta n = n_0 + 2n_2|E|^2 \quad (1-4)$$

Where n_0 is the linear refractive index of the media, and Δn is the optically induced refractive index change, which is proportional to the Kerr nonlinear refractive index coefficient n_2 and the optical intensity $|E|^2$.

Kerr media has several unique characteristics including (1) ultrafast response time

(in *fs* timescale); (2) ultra-small nonlinear refractive index coefficient (eg: $n_2 \approx 2 \times 10^{-13}$ cm² W⁻¹ for AlGaAs) which requires ultra-large optical intensity (in the order of GW cm⁻²) to realize efficient nonlinear light propagation;^{5,7} (3) nonsaturable refractive index changes which increase infinitely with increasing optical intensity until the media is damaged, which hinders the stability of (2+1) D solitons;^{7,8} (4) nonpermanent refractive index changes which disappear once the external optical field is removed.

Photorefractive crystals are typically dielectric or semiconductor crystals doped with low-concentration photo-excitabile impurities. The electrical/optical polarization in these materials is represented by the 2nd term of **1-3**. This nonlinearity arises from the redistribution of the non-equilibrium charge carriers (electrons and holes) induced from the impurities by the electric field associated with the optical field. The stabilization of the charge separation results in the formation of the internal space charge field, which leads to the refractive index change of the crystals.⁴⁶ The change in refractive index in photorefractive crystals induced by an electrical/optical field is expressed as:⁴⁶

$$\Delta n = -\frac{1}{2} n_0^3 r_{eff} E \quad (1-5)$$

Where n_0 is the linear refractive index of the photorefractive crystal and r_{eff} is the effective electro-optic tensor.

Compared with Kerr media, the photoresponse process in photorefractive crystals is non-instantaneous (response time varies from nanoseconds to minutes, which is in negative correlation to the applied optical intensity).⁴⁷ These materials therefore only see the time-averaged intensity profile of the optical beam, allowing the occurrence of the self-trapping and modulation instability of beams with low-level coherence.¹³ The optical intensity required to achieve efficient nonlinear light propagation is much lower,

usually in the range from mW cm^{-2} to MW cm^{-2} , which is easily experimentally realizable.⁴⁷ The change in refractive index in photorefractive crystals is saturable, which renders the stabilities of (2+1) D self-trapped beams or solitons. Similar to that in Kerr media, the refractive index changes in photorefractive crystals are reversible, which disappear after the removal of the external optical field.

Photopolymers is another type of materials which supports the nonlinear propagation of light. Unlike that in Kerr media and photorefractive crystals in which the optical nonlinearity results from the photo-induced physical changes, the nonlinearity in photopolymers arises from chemical changes, specifically photochemical reactions called photopolymerization. In a photopolymerization, photoinitiators (PI) absorb light with particular wavelength(s) to generate reactive species (free-radicals and ions), which attack the monomers and transfer their reactive sites to the monomers. The monomers with reactive ending groups then attack other monomers to continue the transfer of the reactive sites. The bonding of the monomers and propagation of the polymer chains results in cumulative increase in local density and corresponding refractive index. The evolution of refractive index changes in a photopolymer system is shown in **Figure 1.2**,⁴⁸ which is the plot of an empirically derived expression:⁴⁹

$$\Delta n(x, y, z, t) = \Delta n_s \left\{ 1 - \exp \left[-\frac{1}{U_0} \int_0^{t-\tau} |E(x, y, z, t)|^2 dt \right] \right\} \quad (1-6)$$

Where Δn_s refers to the saturated refractive index change in the polymer system, U_0 is the critical exposure below which the initiation of the polymerization reaction would not occur, t is the irradiation time, τ is the lifetime of the monomers, and $E(x, y, z, t)$ corresponds to the optical field amplitude at a particular point in time and space.

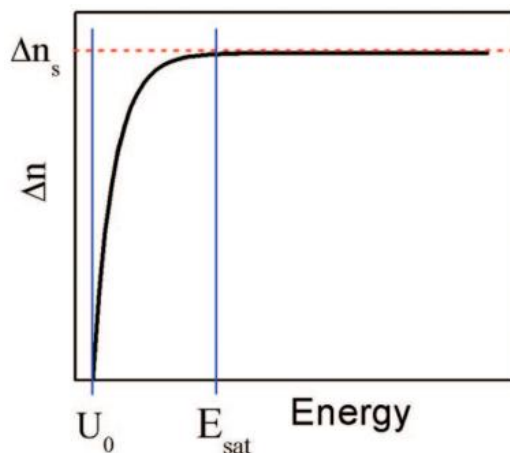


Figure 1.2. Plot of change in refractive index versus radiation exposure. U_0 is the critical exposure required to induce photoinitiation, and E_{sat} is the energy required to achieve the maximum refractive index change Δn_s . Reprinted with permission from.⁴⁸ Copyright © 2008, American chemistry society.

The photoresponse time is slow (milliseconds to seconds) in photopolymer systems, determined by the rate-determining step (either initiation step or propagation step depending on the types of active species (free-radicals, cations, and anions) inducing the chain propagation of the polymerization) and varies from one polymer system to another. It is this fundamental property of noninstantaneity that facilitates self-trapping and MI of incoherent beams in the photopolymer systems. The optical intensity required to trigger nonlinear light propagation in photopolymers can be extremely low, as low as tens of $\mu\text{W cm}^{-2}$.⁴⁸ The saturable refractive index changes (vide supra) in photopolymers renders the stabilities of (2+1) D self-trapped beams or solitons. Particularly, as induced by irreversible photochemical reactions, the refractive index changes in polymer system are retained after the removal of the external optical field. This unique property of nonlinear light propagation in photopolymers opens a door for the fabrication of self-written optical structures (waveguides) and application of the

these structures in a wide range of fields in which controlling the flow of light is critical.

1.3. Study of optical self-written waveguides (SWWs) and complex waveguide structures in photopolymers

Optical self-written technique is significantly different from other techniques such as holographic lithography and mask-based photolithography, in which the structural fabrication is driven by interference of mutually coherent beams and light induced transfer of the geometric pattern of the mask, respectively. This technique harnesses the nonlinear propagation of light in photoresponsive materials such as photopolymers, and generates self-written waveguides with permanent change in refractive index over a relatively long distances (\gg Rayleigh length).

Optical self-written waveguides has been studied in varies photopolymer systems.^{16,30,49–60} Initially, coherent or partially coherent/incoherent laser beams were employed to generate self-written waveguides. The first self-written waveguide was fabricated in a UV-cured epoxy by Frisken in 1993 using a 532 nm *cw* laser beam.⁶¹ A couple years later, Kewitsch and Yariv fabricated waveguides with pathlength up to >10 mm in a acrylate-based photopolymer mediums using a 325 nm laser beam and proposed the empirically derived equation (1-6) describing the polymerization-induced refractive index changes.⁶² In 1999, Shoji *et al.* examined the interactions between the fiber-like patterns optically-induced in a urethane acrylate based photoresist and observed that two of such fibers could merge to form a single fiber (Y junction structure) under a critical angle of 9° .⁶³ A numerical model was proposed a few years later to describe the growth and interactions of multi-channel self-written waveguides and an

intensity threshold was predicted for the polymerization to occur.⁵⁸ In 2000, Eldada and Lawrence fabricated single-mode, multimode, and micrometer-sized waveguide structures with planar geometry in different photopolymer fluids, which exhibited transmission losses as low as 0.01 dB/cm.⁶⁴ This opens the door for the potential application of a variety of optical waveguide devices, such as straight waveguides, bends, splitters, light couplers, band-pass filters, and waveguide arrays etc. In 2001, Kagami *et al.* fabricated a ≥ 20 mm 3D optical waveguide by laser induced polymerization and phase separation in a mixture consisting of a radical-type acrylate (as the high-index core) and a cationic-type epoxy (as the low-index cladding).⁵⁶ Dorkenoo *et al.* examined intensity-dependent waveguide formation in 2002 and observed that low intensity from a single mode fiber led to a uniform-channel fiber, whereas high intensity led to filamentation of the propagating beam and subsequent formation of multi channels.⁵⁷ In 2006, Zhang *et al.* observed the self-trapping of an incoherent white light in a methacrylate substituent organosiloxane gel,^{16,17} which leads to a variety of subsequent studies (*vide infra*). In 2009, Kashin *et al.* developed a numerical model to describe the propagation of self-trapped laser beams in a polymethylmethacrylate matrix doped with phenanthrenequinone.⁶⁵ This model investigated the diffusion theory in the system and combined with the physical paraxial wave model to give a more accurate description of the evolution of self-written waveguides induced optically in photopolymers.

Self-written photopolymer waveguides have potential applications in the fields of integrated optical circuits and optoelectronic devices for optical sensing and optical telecommunication applications. To date, self-written photopolymer waveguides have

been fabricated and acting as optical interconnects to couple light from laser diodes to optical fibers or between optical fibers.⁶⁶⁻⁶⁹ For instance, Missinne *et al.* employed a self-written waveguide fabricated from a UV curable adhesive to interconnect two telecom single mode fibers (SMF), and exhibited total insertion losses below 0.3 dB for SMF-SWW-SMF transition at 1550 nm.⁶⁸ Self-written polymer waveguides have also been applied as building blocks for complex 3-D structures such as open-cellular structures^{55,70,71} and artificial compound eye⁷²⁻⁷⁷, for mechanical processing and bio-inspired sensing applications. For instance, Jacobson *et al.* fabricated cellular truss architectures with controlled and predictable mechanical properties from self-propagating intersecting waveguide arrays by adopting mask assisted self-trapping of light in a UV resin.⁵⁵ Kim *et al.*^{72,74} proposed to use self-written waveguides capped with microlenses as artificial rhabdoms, and fabricated and patterned these waveguides in both 2-D⁷⁷ and 3-D geometries^{73,75,76} in UV-polymerizable resins. Self-written polymer waveguides have also been encoded in thin films^{78,79} which would enhance, spatially modulate and precisely control the flow of light in optoelectronics systems and optical devices such as solar cells, smart cameras, liquid crystal display (LCD) screens, projectors and light emitting diodes (LEDs) (See Chapter 2–5 for details).

1.4. Optical self-written in photopolymerisable epoxides and acrylates

In this thesis, two photopolymer systems, which based on a cycloaliphatic epoxide fluid and an organosiloxane substituted methacrylate medium, are employed for different studies. Below is a brief summary of the study about self-written waveguides in these two systems.

1.4.1. Optical self-written in photopolymerisable epoxide sol

The photopolymerisable epoxide system used in this thesis is based on the dye-sensitized photoinitiation system exploited for cationic polymerization of wide range of epoxides under visible light.⁸⁰ Basker *et al.*^{30,81} modified this system by introducing epoxide terminated organosiloxane to improve the toughness and flexibility of the final structures. **Figure 1.3** shows the mechanism for the polymerization of the epoxide system. Briefly, in presence of suitable nonbasic hydrogen donor polybutanediol, the photosensitizer camphorquinone absorbs visible light and generates radicals (Figure 1.3, reaction 1). The α -hydroxypolybutanediol radical reacts with the photoinitiator bis(4-butylphenyl) iodonium hexafluoroantimonate to form a α -hydroxypolybutanediol cation, which then undergoes deprotonation to form a Bronsted acid H^+SbF_6^- (Figure 1.3, reaction 2 and 3). The Bronsted acid then initiates the cationic ring opening polymerization and chain propagation of the epoxide monomers (Figure 1.3, reaction 5 and 6). Other reactions exist in this system. For instance, the decomposition reaction depicted in (Figure 1.3, reaction 4) generates an aryl radical, which can attract hydrogen from polybutanediol and contribute to the initiation (nonphotochemical process) of the cationic polymerization. A rapid propagation mechanism called “activated monomer mechanism”⁸² depicted by (Figure

1.3, reaction 7 and 8) shows the alcohol (polybutanediol) promoted propagation reactions, which accelerate the consumption of the epoxide monomers and the whole polymerization process.

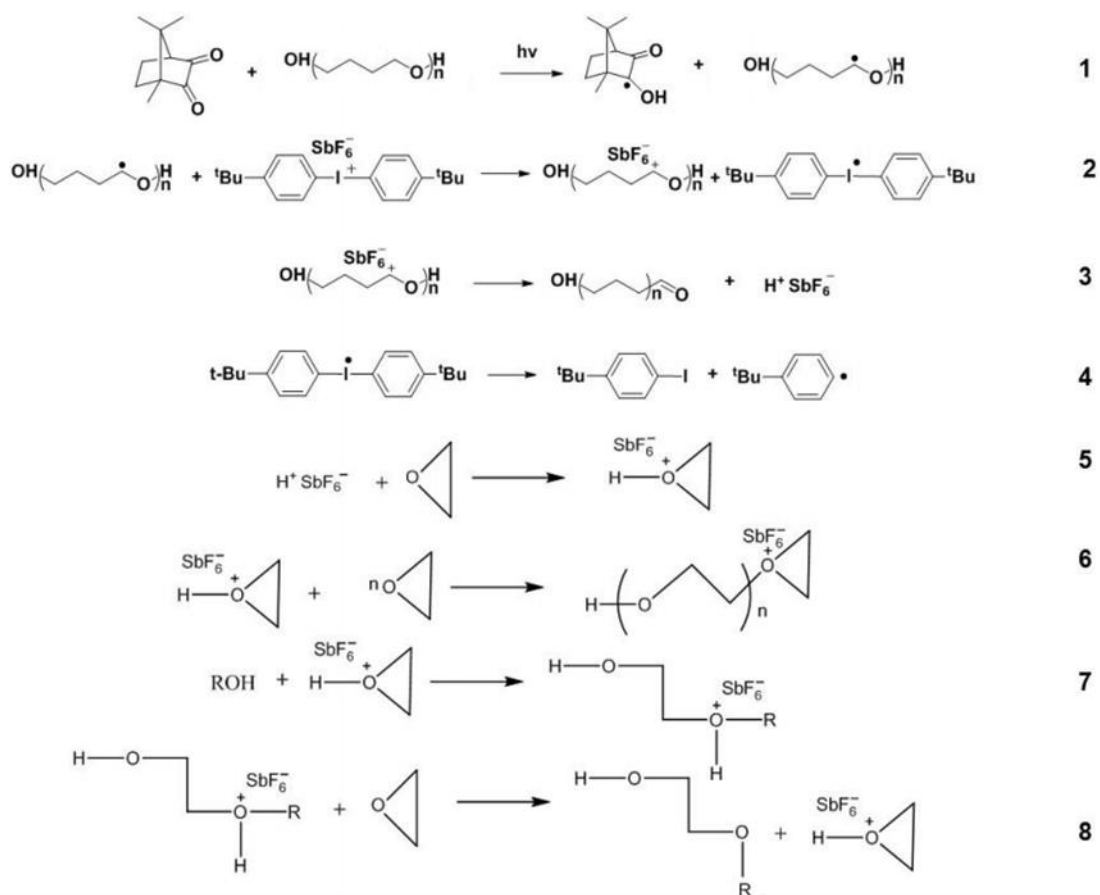


Figure 1.3. Schematic illustration showing the mechanism for the ring opening polymerization of the epoxide based photopolymer system. The epoxide based monomers are depicted as ethylene oxide in the figure. Reprinted from (81).

This photopolymer system has been employed to examine the modulation instability and spontaneous pattern formation of white incandescent light.³⁰ It's also employed to fabricate ordered lattices of self-written waveguides which have potential application in light harvesting and bio-inspired sensing.⁷⁹ The change of refractive index in this photopolymer system can be tuned by changing its composition. The

system containing 50% epoxide monomer and 26% epoxide terminated organosiloxane was found to give a refractive index change of $\Delta n \approx 0.001$.⁷⁹ Employing this system as nonlinear optical matrix for the 3-D print of functional dielectric and metallodielectric polymer structures (self-written waveguides) has also been reported.⁸³

1.4.1. Optical self-written in photopolymerisable acrylate sol

Another photopolymer system is based on the free radical polymerization of an organosiloxane substituted methacrylate, the mechanism of which is depicted in **Figure 1.4**. Prior to the illumination, the medium is hydrolyzed with dilute HCl which leads to the condensation of the acrylate monomers. During illumination, the optically induced free radicals from the photoinitiator (Irgacure 784) attack the C=C double bonds of the acrylates, and force them to cross-link to form polymer chains. Based on the previous study by Saravanamuttu *et al.*, the maximum change in refractive index optically induced in this system is $\Delta n_s \approx 0.006$.⁸⁴

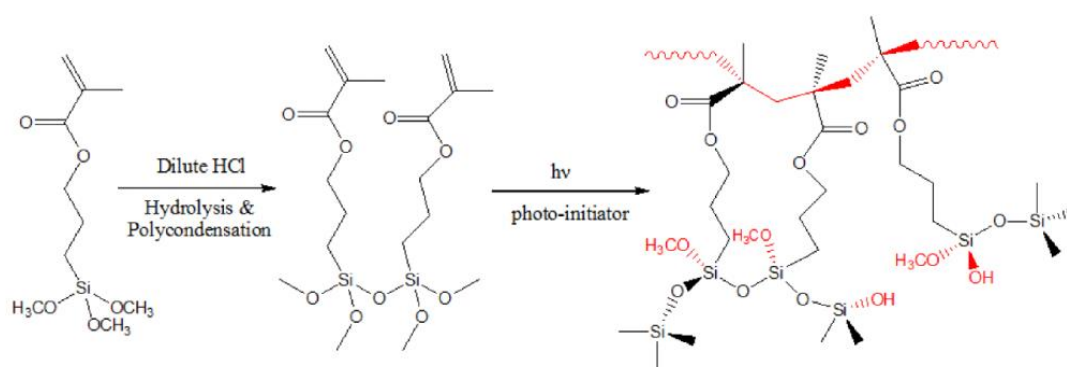


Figure 1.4. Schematic illustration showing the hydrolysis and polycondensation process of the polymer system and the subsequent photopolymerization mechanisms. Reprinted from (85).

Optical self-written in this system was first observed by Saravanamuttu *et al.*, who

coupled a laser beam into a solgel-derived silica methacrylate hybrid thin film and demonstrated that self-focusing occurs over a distance up to 120 mm.⁸⁶ Villafranca and Saravanamuttu conducted a series of experimental and theoretical studies to examine the dynamics of nonlinear propagation of coherent light in this system, and observed a rich diversity of dynamic phenomena in different intensity regimes.^{48,87–89} For instance, in the low intensity regime ($3.2 \times 10^{-5} \sim 1.6 \times 10^{-2}$ W/cm), the beam self-traps in the photopolymer and generates a waveguide capable of guiding multiple high order modes; In the medium intensity regime ($0.19 \sim 16$ W/cm²), concentric self-diffraction rings are formed owing to spatial self-phase modulation^{87–89}; At high intensities ($159 \sim 12732$ W/cm²), the beam splits into filaments, which self-trap individually, through a mechanism similar to modulation instability^{29,42} of broad, uniform beams. Qiu and Saravanamuttu extended the system to a hybrid system by introducing silver nanoparticles, and studied the self-trapping of laser beam and the inscription of metallodielectric waveguides.⁹⁰

Owing to the noninstantaneity of this material, optical self-trappings of incoherent white light are also observed in this photopolymer system. For instance, Zhang *et al.* gave the first experimental evidence of self-trapping of incoherent white light in this photopolymerizable system in 2006 and demonstrated the dynamics.^{16,17} Kasala and Saravanamuttu studied the interactions of self-trapped white light filaments¹⁵, and the self-trapping of dark⁹¹ and hybrid⁹² incandescent beams, which give insights about a variety of incoherent light propagation in this polymer system. Motivated by the self-trapping of a narrow incoherent light, Burguss *et al.* demonstrated the modulation instability of a broad, uniform white light beams in the photopolymerizable medium

and inscribed a 2-D periodic array of polymer waveguides by imposing a 1-D weak, periodic modulation to the beam.²⁹ Qiu and Saravanamuttu demonstrated later on that this polymer system doped with silver nanoparticles also supported the modulation instability of white incandescent light.⁴² By extending the modulation instability of incoherent white light beams to multiple beams, the Saravanamuttu group generated a diverse range of microscopic patterns – 2-D and 3-D polymer waveguide lattices - with square,^{29,44} near cubic,⁴ cubic,^{44,93} body-centered cubic (BCC) symmetries and woodpile arrangements⁴⁵ as well as a new class of “black and bright polymer lattices”.⁴³

1.5. Introduction to compound eyes

As three chapters in this thesis deal with waveguide encoded lattices (WELs) inspired by compound eye, the structures of natural and artificial compound eyes are briefly summarized in the following section.

1.5.1. Natural compound eyes

There are two kinds of animal eyes, single aperture eyes like vertebrate eyes and compound eyes found in arthropods. The vertebrate eyes only have a single lens to collect and focus light onto their retina, whereas in compound eyes, there are numerous (up to tens of thousands) independent and omnidirectional photoreception units called ommatidia, each focusing light onto a small number of retinula cells. The images perceive by vertebrate eyes are usually highly resolved, the fields of view (FOV), however, are always small. To see the entire surrounding, eye and head movement are needed. The images perceived by a compound eye is mosaic-like images, and each ommatidium contributes only one “pixel”. The spatial resolution of such images is very

low as compared to that perceived by single aperture eyes. However, this lack of high resolution in arthropod eyes is often counterbalanced by other advantages such as wide FOV, fast panoramic motion perception, and high sensitivity to light intensity even polarization^{94,95}. The hemispherical and compact arrangement of the ommatidia allows compound eyes to have a large FOV within small volume, leaving the remaining main volume of the head for signal processing without overloading the brains.

Based on the structure, natural compound eyes can be classified into two types: apposition compound eyes and superposition compound eyes. In natural apposition compound eyes, light passing through each ommatidium is only received by a single corresponding photoreceptor; whereas in the superposition compound eyes, each photoreceptor is able to perceive light from multiple ommatidia (**Figure 1.5**).^{96,97} The structures of arthropods' eyes are closely-linked to the habitats in which they live, as well as the behavioral tasks they must fulfill to survive. Superposition compound eyes are more light-sensitive, therefore are usually found in deep-water crustaceans and nocturnal insects, such as moths. Whereas apposition compound eyes are most commonly seen in diurnal insects such as flies.

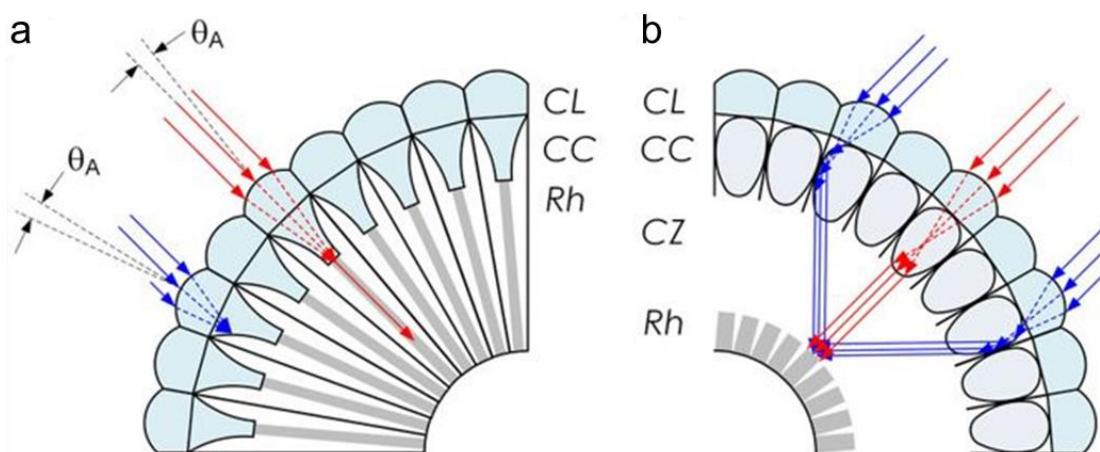


Figure 1.5. Schematic diagrams of (a) apposition and (b) superposition compound eyes.

Here, “CL” “CC” “Rh” and “CZ” refer to corneal lens, cylindrical cone, rhabdom, and clear zone, respectively. Reprinted with permission from Springer Nature.⁹⁸

Since the superposition eyes usually lead to high optical aberrations, artificial compound eyes (vide infra) are mostly in apposition type. Therefore, the operation principle of only apposition compound eye is discussed. **Figure 1.6** shows the schematic diagram of an apposition compound eye. The total FOV of this eye is determined by the angular range of the curved surface. The inter-ommatidial angle ($\Delta\Phi$), which gives the angular offset between the adjacent ommatidia is given as:⁹⁷

$$\Delta\Phi = D/R_{EYE} \quad (1-7)$$

Where D and R_{EYE} correspond to the diameter of the corneal lens and the radius of the curved eye. One very important parameter of compound eye is the acceptance angle ($\Delta\varphi$) of a single ommatidium, which is defined as the full width at half maximum (FWHM) of the angular range over which the photoreceptor in each ommatidium accepts. $\Delta\varphi$ is expressed as:⁹⁷

$$\Delta\varphi = \sqrt{\left(\frac{d}{f}\right)^2 + \left(\frac{\lambda}{D}\right)^2} \quad (1-8)$$

Where d , λ , f , and D refer to the diameter of the photoreceptor, the sampling wavelength, the focal length and diameter of the corneal lens, respectively. The term d/f corresponds to the geometry contribution of $\Delta\varphi$ determined by the photoreceptor diameter projected into the object space (via the focal length f). Term λ/D correlates to the diffraction at the microlens aperture D for the wavelength λ .

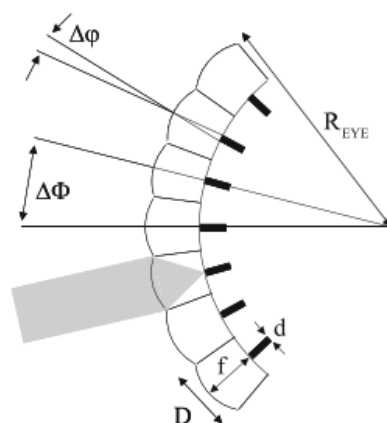


Figure 1.6. Principle of a natural apposition compound eye which is composed of a large number of ommatidia arranged on a curved basis with radius R_{EYE} . Reprinted with permission from IOP Publishing.⁹⁷

1.5.2. Artificial compound eyes

Due to the superior characteristics inherited from their natural counterparts, artificial compound eyes, which aim to transcribe arthropodal vision into imaging devices, hold promise as next-generation compact imaging systems. These imaging systems may find potential application in various fields such as medical imaging,^{99,100} security and surveillance,^{101,102} precision navigation,^{103,104} motion detection,^{105,106} and displaces,^{107,108} etc.

Based on the structural geometry, artificial compound eyes are divided into two types: planar artificial compound eyes and curved artificial compound eyes.

1.5.2.1. Planar artificial compound eye

The first artificial compound eye is initiated in the 1990s. Due to the limitation of the fabrication (eg: photodetectors are intrinsically on rigid planar substrates) technologies, the eyes in early research are all in planar geometry. To date, a lot of planar artificial compound eyes have been fabricated.^{79,109–117} One typical example is

“TOMBO” (thin observation module by bound optics),^{109,110} inspired by the dragonfly’s apposition compound eye (**Figure 1.7a**). This imaging system consists of a microlens array (MLA), a separation array and a photodetector array. Each microlens covers an open channel (separated by the separation layer) and multiple photosensitive cells on the photodetector board to form a small imaging unit. This imaging system is thin, easy to fabricate and its components are dismountable for future upgrades. However, its FOV is very small.

Another type of eye named “APCO” (apposition compound eye objective)^{111,112} was proposed later on, which comprises a MLA, a spacing substrate, a pinhole arrays at the focal plane of the MAL, and a sensor array (Figure 1.7b). The pitch difference ($\Delta P = P_L - P_K$) between the pinhole array and the MLA enables the gradual tilting of the viewing angles to obtain wider FOV. This type of eye is also very thin (a few hundred micrometers) and easy to construct, but the FOV is usually small, and the image resolution is poor.

The third representative of planar artificial compound eye is called cluster eye.^{113–115} This type of eye is completely comprised of multiple lenslet arrays, without other components such as pinholes, separation layers and opaque walls. An eye named “Cley” is shown in Figure 1.7c, which has three MLAs to focus the object onto the imaging plane. The FOV of the whole imaging system is achieved by adjusting the periodicities between the microlens arrays. This eye system has possibility of obtaining large FOV, the imaging resolution and distortion are also improved from the APCO. However, its fabrication process is quite complicated, and it suffers astigmatism at large incident angles. Several other members in this Clay family were reported later on, including clay

with elliptical microlens, oCley¹¹⁵ and eCley¹¹⁴, etc., which exhibited improved astigmatism, FOV and imaging resolution.

A new type of planar film inspired by the collective behavior of ommatidial elements of compound eye was proposed recently. It is called WELs (Waveguide encoded lattices).⁷⁹ This system is a thin polymer film comprising multidirectional self-written waveguides (Figure 1.7d). The FOV of the film is dependent on the orientation and acceptance cone of the constituent waveguide subpopulations, and the spatial resolution is determined by the width of the waveguides (a few tens of micrometers). The film has several advantages such as ease of fabrication, potential to have large panoramic FOV, high spatial resolution, etc.

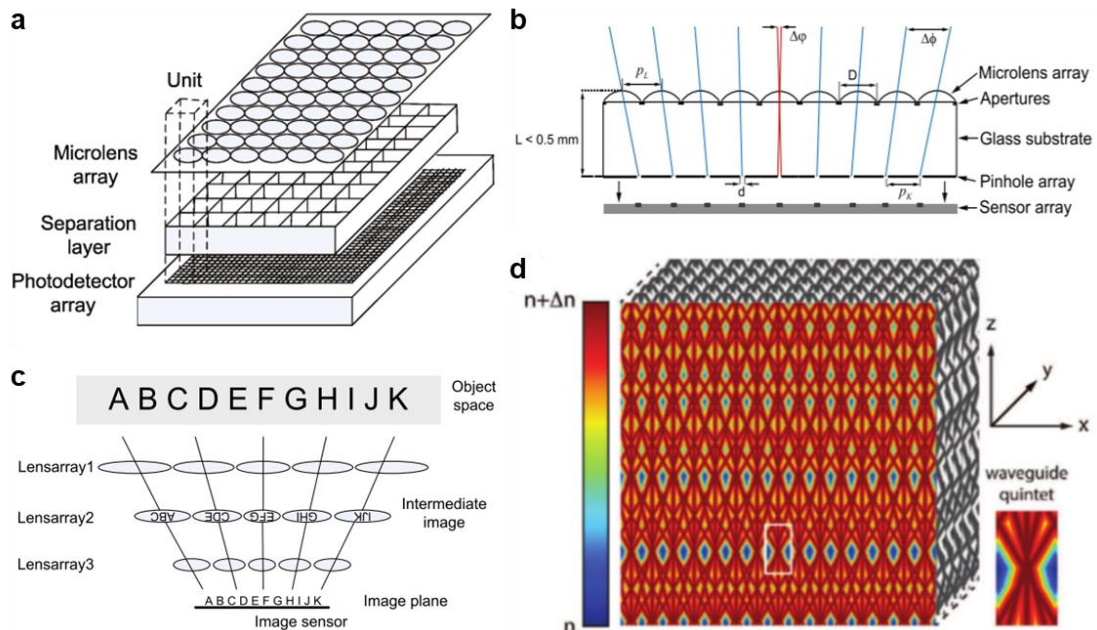


Figure 1.7. Schematic representations of planar compound eyes. (a) A TOMBO, (b) a APCO, (c) a Cley and (d) a WEL. Reprinted with permission from optical society of America^{109,111,113} and John Wiley and Sons.⁷⁹

Table 1.1 summarizes some parameters of a few typical planar artificial compound eyes. The FOV of these eyes are usually not big, but recently developed novel planar

compound eyes have potential to increase the FOV to significantly large values. Due to their compact size and good depth estimation capacity, etc., planar artificial compound eyes have been applied in medical instruments, security systems, tiny scanners and projectors, etc.

Table 1.1 Selected parameters of a few typical planar compound eyes

Compound eye type	Total FOV (°)	Size (mm)	Thickness (mm)	Pixels	Channels
TOMBO ¹⁰⁹	-	6 × 5	-	320 × 240	up to 32 × 32
APCO ¹¹¹	20 × 20	6 × 5	0.216 ~ 0.345	-	130 × 130
Chirped APCO ¹¹²	64.3	6 × 5	0.9	130 × 130	130 × 130
Cley ¹¹³	70 × 10	6 × 5	2	700 × 550	21 × 3
MULTCAM	30	-	24.8	320 × 256	5 × 5
GSL	29	2.8 × 2.8	2	156 × 156	15 × 15
eCley ¹¹⁵	58 × 46	6.5 × 5.2	1.4	700 × 500	17 × 13
oCley ¹¹⁴	53.2 × 39.9	2.2 × 2.9	1.86	640 × 480	14 × 13
Close-up imaging system	52 × 63	8.5 × 8.5	6	3280 × 2464	26, 000
WELs ⁷⁹	94	R = 8	3	-	> 15000 /cm ²
Wide-angle array camera ¹¹⁷	110	-	0.95	1350 × 810	15 × 11

“-”, “D” and “R” refer to unknown, diameter and radius, respectively.

1.5.2.2. Curved artificial compound eyes

Artificial compound eyes with curved geometry are the ones in closer proximity to their natural counterparts. As the of planar artificial compound eye cannot satisfy some application in which wide FOV is desirable, and owing to the fast development of fabrication and processing techniques, artificial eyes with curved geometry start to emerge. To date, numerous curved artificial compound eyes have been constructed, in both cylindrical^{76,104,118} and hemispherical geometries.^{73–75,102,119–121} In the following content, several typical curved artificial compound eyes are illustrated.

The first curved artificial compound eye was fabricated in 2006 by Jeong *et al.* in a hemispherical dome filled with UV-cured polymer medium (**Figure 1.8a**).⁷⁵ This eye system has 8370 artificial ommatidia, each of which consists of a polymer microlens, a light-guiding polymer cone, and a self-written waveguide, as found in its natural counterparts.^{94,122} The FOV of single artificial ommatidium is also comparable with natural compound eyes. Compound eyes consisting of such microlens-assisted waveguides are usually employed for obtaining wide FOV.

For obtaining high image definition, a new type of curved eye emerges in which the waveguides are removed and photodetectors are positioned at the focal plane of the microlenses. For instance, a miniature apposition camera inspired by arthropod eye was reported Song *et al.* in 2013, which contains a sheet of elastomeric compound optical elements (microlenses) and a deformable silicon photodetector array elastically transformed into hemispherical geometry (Figure 1.8b).¹⁰² This camera has 256 artificial ommatidia and exhibits exceptional wide FOV of 160°. It also shows nearly infinite depth of field and the images reconstructed show no without off-axis aberrations.

Another representative curved artificial compound eye is the CurvACE (curved artificial compound eye) (Figure 1.8c). This vision system consists of a microlens array, a deformable neuromorphic photodetector array, and a flexible PBC (printed circuit board), which are accurately aligned, cut and mechanically deformed into a semicylindrical shape.¹⁰⁴ This system has 630 repeating imaging units, and gives a panoramic, undistorted FOV of 180° × 60°.

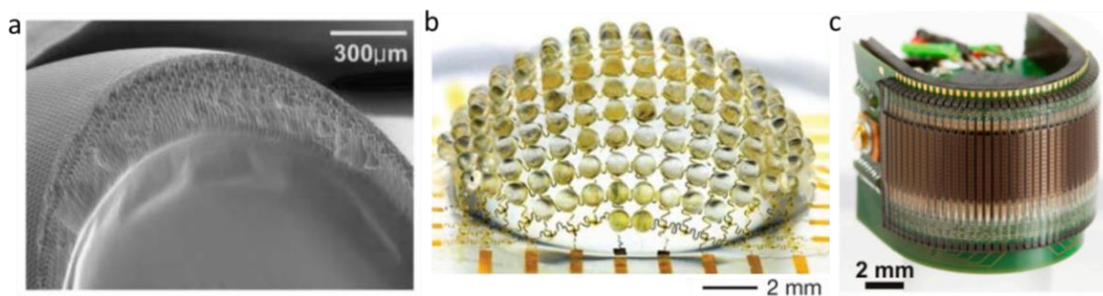


Figure 1.8. Illustration of a few curved artificial compound eyes. (a) An artificial compound eye with lens-capped waveguides, (b) an arthropod eye inspired miniature camera, and (c) a cylindrical vision sensor named “CurvACE”. Reprinted with permission from the American Association for the Advancement of Science,⁷⁵ Springer Nature,¹⁰² and National Academy of Sciences of the United States of America.¹⁰⁴

Table 1.2 summarizes some parameters of a few typical curved artificial compound eyes including the ones mentioned above. As determined by the spanning angle of the artificial ommatidia (or the curvature of the curved plane), the FOV of the entire eye systems are usually big (except the early ones), even up to 360 ° are achievable. These imaging systems may find application in wide FOV imaging and displaying, motion detection and autonomous navigation, etc. However, tremendous effort will be needed in designing novel ACE, improving the fabrication technology, developing image reconstruction models and algorithms, as well as application exploration and implementation.

Table 1.2 Selected parameters of a few typical curved artificial compound eyes

Compound eye type	Single ommatidium FOV (°)	Total FOV (°)	Size (mm)	Thickness (mm)	Channels
Hemispherical compound eye ⁷⁵	4.4	-	D = 2.5	-	8370
Spherical compound eye ⁷³	0.3	10.3 × 10.3	D = 40	-	40 × 40
3-D compound eye ¹²³	-	18.43	D = 20	2.03	601
Parabolic cluster eye camera ¹²⁴	-	102 × 90	6.12 × 4.62	2.74	59
Arthropod-inspired camera ¹⁰²	9.7	160	R = 6.96	-	180
CurvACE ¹⁰⁴	4.2	180 × 60	D = 12.8	-	630
SCECam ¹⁰¹	2.4	122.4	R = 20	80	4400
Dragonfly-eye-inspired ACE ¹²⁰	5.8	≈ 140	D = 5	≥ 2	≈ 30000

“-”, “D” and “R” refer to unknown, diameter and radius, respectively.

1.5.3. Fabrication of compound-eye microlens arrays

Artificial compound eyes, either planar or curved, usually involve microlenses. The fabrication of artificial compound eyes, therefore, mainly involves the fabrication of the microlens arrays. Several methods have been employed to fabricate microlenses, including thermal reflow methods,^{125,126} micro-plastic embossing methods,^{127,128} micro-droplet jetting methods,^{129–131} micro-electromechanical systems (MEMS) based methods,^{132–134} and ultraprecision machining methods,^{135,136} etc.⁹⁶

The first three methods are classified as direct fabrication methods, as they are based on the surface tension of the thermoplastic lens material, without the need of masks or molds with micro concave shapes. These methods are relatively simple and cost-effective, thus are suitable for mass industrial production. However, these methods face challenges on controlling microlens-uniformity over large areas and obtaining microlenses arrays with curved geometries. Deformation processes, which are usually complicated, are therefore inevitable for the fabrication of curved artificial eyes.

MEMS based methods, and ultraprecision machining methods are classified as

indirect methods, as they involve replication of 3-D molds with concave micro-lens shapes. These methods have better control on the microlens geometries, and microlens arrays with high smooth and uniform surfaces are achieved. These methods are also directly employed in fabricating curved artificial compound eyes. For instance, Bian *et al.* patterned a curved glass substrate with omnidirectional-aligned negative/concave microlenses via a femtosecond laser enhanced wet-etching process (MEMS-based method). Based on the negative microlens mold, they fabricated a distortion-free artificial compound eye which gives clear and uniform imaging capabilities.¹³⁴ Li and Yi fabricated a 3-D compound eye system consisting of a 3D microprism array, an aperture array, and a microlens array, using a few ultraprecision machining methods, including regular diamond turning^{136,137}, and micromilling^{135,138}, etc.¹²³ The main disadvantage of these indirect methods is the high cost, as multiple complex processes are usually involved.

1.6. Research objectives: Controlling the flow of light with waveguide encoded slim polymer films.

Optical waveguide based structures hold strong application potentials in integrated optical circuits, optical sensing and optical telecommunication systems. The development of these fields requires fabricating waveguide structures with facile, cost-effective and scalable approaches.

As discussed in previous sections, optical waveguides and waveguide lattices can be fabricated through self-written techniques – nonlinear propagations of light in photopolymers. The primary objective of this thesis is to employ self-written

techniques to encode slim polymer films with specific geometries of waveguide lattices, and examine their properties on spatially modulating and controlling the flow of light, then try to explore the applications of such waveguide encoded structures.

One specific goal of this thesis is to fabricate a waveguide encoded thin film which is in planar geometry but possesses large FOV so as to be applied in optical imaging and sensing. Related studies are presented in Chapter 2 and Chapter 3.

In Chapter 2, we present the fabrication of a polymer thin film comprising intersecting waveguide encoded lattices (WELs) via mask-assisted modulation instability and self-trapping of microscopic white incandescent light into an epoxide based photopolymerisable system. Detailed experiments such as fabrication dynamics, structural characterization, and optical property examination including cross-free light guiding, enhanced FOV, and multiple imaging functionalities, etc. are also presented in Chapter 2.

We present in Chapter 3 another slim polymer film fabricated in the photopolymerisable epoxide medium, which contains radially distributed waveguide encoded lattices (RDWELs). We detail the design rationale of obtaining wide seamless panoramic FOV and microstructural characterization of the RDWEL, then elucidate its optical properties and potential applications.

Another specific objective of this research work is to design a waveguide encoded thin film which increases the power output of solar cell while sustains current production costs. This is demonstrated in Chapter 4, where an array of slanted slab waveguides is encoded in an epoxide based thin polymer film, which exhibit beam steering effect to reduce optical losses when coated on solar panels.

The third specific goal is to develop a waveguide based thin film which can manipulate the output of diverging light beams. This is presented in Chapter 5, where a self-written RDWEL constructed in an acrylate-based photopolymer system is applied to the beam emitted by a LED, and exhibited precisely control on the divergence and convergence of a light beams.

Chapter 6 summarizes the work presented in the above 4 chapters, and gives suggestions for future research.

The content presented in Chapter 2 has been published in *Adv. Funct. Mater.*,⁷⁹ and is reproduced in this thesis with permissions from the publishers. The contents in Chapter 3 and Chapter 4 have been submitted to *Adv. Opt. Mater.*, and *ACS photonics*, respectively. Whereas the contents in Chapter 5 has been put up as a manuscript, which is under final edition before submission.

In this thesis, detailed literature reviews when necessary are presented in the introduction of individual chapter; the corresponding references are also self-contained within each chapter.

References

- (1) Malallah, R.; Li, H.; Kelly, D.; Healy, J.; Sheridan, J. A Review of Hologram Storage and Self-Written Waveguides Formation in Photopolymer Media. *Polymers (Basel)*. **2017**, *9* (12), 337.
- (2) Trillo, S.; Torruellas, W. *Spatial Solitons*; Trillo, S., Torruellas, W., Eds.; Springer Series in Optical Sciences; Springer Berlin Heidelberg: Berlin, Heidelberg, 2001; Vol. 82.
- (3) Snyder, A. W. Accessible Solitons. *Science (80-.)*. **1997**, *276* (5318), 1538–1541.
- (4) Burgess, I. B.; Ponte, M. R.; Saravanamuttu, K. Spontaneous Formation of 3-D Optical and Structural Lattices from Two Orthogonal and Mutually Incoherent Beams of White Light Propagating in a Photopolymerisable Material. *J. Mater. Chem.* **2008**, *18* (35), 4133–4139.
- (5) Chiao, R. Y.; Garmire, E.; Townes, C. H. Self-Trapping of Optical Beams. *Phys. Rev. Lett.* **1964**, *13* (15), 479–482.
- (6) Aitchison, J. S.; Weiner, A. M.; Silberberg, Y.; Oliver, M. K.; Jackel, J. L.; Leaird, D. E.; Vogel, E. M.; Smith, P. W. E. Observation of Spatial Optical Solitons in a Nonlinear Glass Waveguide. *Opt. Lett.* **1990**, *15* (9), 471–473.
- (7) Luther-Davies, B.; Stegeman, G. I. *Materials for Spatial Solitons*; 2001; pp 19–35.
- (8) Kelley, P. L. Self-Focusing of Optical Beams. *Phys. Rev. Lett.* **1965**, *15* (26), 1005–1008.
- (9) Bjorkholm, J. E.; Ashkin, A. A. Cw Self-Focusing and Self-Trapping of Light in Sodium Vapor. *Phys. Rev. Lett.* **1974**, *32* (4), 129–132.
- (10) Barthelemy, A.; Maneuf, S.; Froehly, C. Propagation Soliton et Auto-Confinement de Faisceaux Laser Par Non Linearité Optique de Kerr. *Opt. Commun.* **1985**, *55* (3), 201–206.
- (11) Duree, G. C.; Shultz, J. L.; Salamo, G. J.; Segev, M.; Yariv, A.; Crosignani, B.; Di Porto, P.; Sharp, E. J.; Neurgaonkar, R. R. Observation of Self-Trapping of an Optical Beam due to the Photorefractive Effect. *Phys. Rev. Lett.* **1993**, *71* (4), 533–536.
- (12) Mitchell, M.; Chen, Z.; Shih, M.; Segev, M. Self-Trapping of Partially Spatially Incoherent Light. *Phys. Rev. Lett.* **1996**, *77* (3), 490–493.
- (13) Mitchell, M.; Segev, M. Self-Trapping of Incoherent White Light. *Nature* **1997**, *387* (6636), 880–883.
- (14) Goodman, J. W. *Statistical Optics*; Wiley, 1985.
- (15) Kasala, K.; Saravanamuttu, K. An Experimental Study of the Interactions of Self-Trapped White Light Beams in a Photopolymer. *Appl. Phys. Lett.* **2008**, *93* (5), 051111–051113.
- (16) Zhang, J.; Kasala, K.; Rewari, A.; Saravanamuttu, K. Self-Trapping of Spatially and Temporally Incoherent White Light in a Photochemical Medium. *J. Am. Chem. Soc.* **2006**, *128* (2), 406–407.

- (17) Zhang, J.; Saravanamuttu, K. The Dynamics of Self-Trapped Beams of Incoherent White Light in a Free-Radical Photopolymerizable Medium. *J. Am. Chem. Soc.* **2006**, *128* (46), 14913–14923.
- (18) Guo, S.; Mei, L.; He, Y.-L.; Ma, C.; Sun, Y. Modulation Instability and Dissipative Ion-Acoustic Structures in Collisional Nonthermal Electron-Positron-Ion Plasma: Solitary and Shock Waves. *Plasma Sources Sci. Technol.* **2016**, *25* (5), 055006.
- (19) H. Ichikawa, Y.; Suzuki, T.; Taniuti, T. Modulation Instability of Electron Plasma Wave. *J. Phys. Soc. Japan* **1973**, *34* (4), 1089–1092.
- (20) Ghosh, B.; Das, K. P. Modulational Instability of Electron Plasma Waves in a Cylindrical Wave Guide. *Plasma Phys. Control. Fusion* **1985**, *27* (9), 969–982.
- (21) Onorato, M.; Osborne, A. R.; Serio, M.; Cavaleri, L. Modulational Instability and Non-Gaussian Statistics in Experimental Random Water-Wave Trains. *Phys. Fluids* **2005**, *17* (7), 078101.
- (22) Dold, J. W.; Peregrine, D. H. Water-Wave Modulation. In *Coastal Engineering 1986*; American Society of Civil Engineers: New York, NY, 1987; pp 163–175.
- (23) Shukla, P. K.; Kourakis, I.; Eliasson, B.; Marklund, M.; Stenflo, L. Instability and Evolution of Nonlinearly Interacting Water Waves. *Phys. Rev. Lett.* **2006**, *97* (9), 094501.
- (24) Abdullaev, F. K.; Darmanyan, S. A.; Bischoff, S.; Sørensen, M. P. Modulational Instability of Electromagnetic Waves in Media with Varying Nonlinearity. *J. Opt. Soc. Am. B* **1997**, *14* (1), 27–33.
- (25) Abdullaev, F. K.; Darmanyan, S. A.; Garnier, J. Modulational Instability of Electromagnetic Waves in Inhomogeneous and in Discrete Media. *Prog. Opt.* **2002**, *44*, 303–365.
- (26) Niknam, A. R.; Rastbood, E.; Bafandeh, F.; Khorashadizadeh, S. M. Modulational Instability of Electromagnetic Waves in a Collisional Quantum Magnetoplasma. *Phys. Plasmas* **2014**, *21* (4), 042307.
- (27) Marcuse, D.; American Telephone and Telegraph Company. *Theory of Dielectric Optical Waveguides*; Academic Press, 1991.
- (28) Soljacic, M.; Segev, M.; Coskun, T.; Christodoulides, D. N.; Vishwanath, A. Modulation Instability of Incoherent Beams in Noninstantaneous Nonlinear Media. *Phys. Rev. Lett.* **2000**, *84* (3), 467–470.
- (29) Ian B. Burgess; Whitney E. Shimmell, A.; Saravanamuttu*, K. Spontaneous Pattern Formation Due to Modulation Instability of Incoherent White Light in a Photopolymerizable Medium. **2007**, *129*, 4738–4764.
- (30) Basker, D. K.; Brook, M. A.; Saravanamuttu, K. Spontaneous Emergence of Nonlinear Light Waves and Self-Inscribed Waveguide Microstructure during the Cationic Polymerization of Epoxides. *J. Phys. Chem. C* **2015**, *119* (35), 20606–20617.
- (31) Peccianti, M.; Conti, C.; Assanto, G.; De Luca, A.; Umeton, C. Routing of Anisotropic Spatial Solitons and Modulational Instability in Liquid Crystals. *Nature* **2004**, *432* (7018), 733–737.
- (32) Iturbe-Castillo, M. D.; Torres-Cisneros, M.; Sánchez-Mondragón, J. J.; Chávez-Cerda, S.; Stepanov, S. I.; Vysloukh, V. A.; Torres-Cisneros, G. E.

- Experimental Evidence of Modulation Instability in a Photorefractive Bi₁₂TiO₂₀ Crystal. *Opt. Lett.* **1995**, *20* (18), 1853.
- (33) Shih, M.-F.; Jeng, C.-C.; Sheu, F.-W.; Lin, C.-Y. Spatiotemporal Optical Modulation Instability of Coherent Light in Noninstantaneous Nonlinear Media. *Phys. Rev. Lett.* **2002**, *88* (13), 133902.
- (34) Mamaev; Saffman; Anderson; Zozulya. Propagation of Light Beams in Anisotropic Nonlinear Media: From Symmetry Breaking to Spatial Turbulence. *Phys. Rev. A, At. Mol. Opt. Phys.* **1996**, *54* (1), 870–879.
- (35) Chen, Z.; Klinger, J.; Christodoulides, D. N. Induced Modulation Instability of Partially Spatially Incoherent Light with Varying Perturbation Periods. *Phys. Rev. E* **2002**, *66* (6), 066601.
- (36) Kip, D.; Soljacic, M.; Segev, M.; Eugenieva, E.; Christodoulides, D. N. Modulation Instability and Pattern Formation in Spatially Incoherent Light Beams. *Science* **2000**, *290* (5491), 495–498.
- (37) Klinger, J.; Martin, H.; Chen, Z. Experiments on Induced Modulational Instability of an Incoherent Optical Beam. *Opt. Lett.* **2001**, *26* (5), 271–273.
- (38) Kip, D.; Soljačić, M.; Segev, M.; Sears, S. M.; Christodoulides, D. N. (1+1)-Dimensional Modulation Instability of Spatially Incoherent Light. *J. Opt. Soc. Am. B* **2002**, *19* (3), 502–512.
- (39) Dylov, D. V.; Fleischer, J. W. Modulation Instability of a Coherent–incoherent Mixture. *Opt. Lett.* **2010**, *35* (13), 2149–2151.
- (40) Buljan, H.; Šiber, A.; Soljačić, M.; Segev, M. Propagation of Incoherent “white” Light and Modulation Instability in Noninstantaneous Nonlinear Media. *Phys. Rev. E* **2002**, *66* (3), 035601.
- (41) Schwartz, T.; Carmon, T.; Buljan, H.; Segev, M. Spontaneous Pattern Formation with Incoherent White Light. *Phys. Rev. Lett.* **2004**, *93* (22), 223901.
- (42) Qiu, L.; Saravanamuttu, K. Modulation Instability of Incandescent Light in a Photopolymer Doped with Ag Nanoparticles. *J. Opt.* **2012**, *14* (12), 125202.
- (43) Kasala, K.; Saravanamuttu, K. Optochemical Organization in a Spatially Modulated Incandescent Field: A Single-Step Route to Black and Bright Polymer Lattices. *Langmuir* **2013**, *29* (4), 1221–1227.
- (44) Ponte, M. R.; Hudson, A. D.; Saravanamuttu, K. Self-Organized Lattices of Nonlinear Optochemical Waves in Photopolymerizable Fluids: The Spontaneous Emergence of 3-D Order in a Weakly Correlated System. *J. Phys. Chem. Lett.* **2018**, *9* (5), 1146–1155.
- (45) Kasala, K.; Saravanamuttu, K. Optochemical Self-Organisation of White Light in a Photopolymerisable Gel: A Single-Step Route to Intersecting and Interleaving 3-D Optical and Waveguide Lattices. *J. Mater. Chem.* **2012**, *22* (24), 12281–12287.
- (46) Boyd, R. W. *Nonlinear Optics*; Academic Press, 2008.
- (47) Segev, M.; Shih, M.; Valley, G. C. Photorefractive Screening Solitons of High and Low Intensity. *J. Opt. Soc. Am. B* **1996**, *13* (4), 706–718.
- (48) Villafranca, A. B.; Saravanamuttu, K. An Experimental Study of the Dynamics and Temporal Evolution of Self-Trapped Laser Beams in a Photopolymerizable Organosiloxane. *J. Phys. Chem. C* **2008**, *112* (44), 17388–17396.

- (49) Kewitsch, A. S.; Yariv, A. Self-Focusing and Self-Trapping of Optical Beams upon Photopolymerization. *Opt. Lett.* **1996**, *21* (1), 24–26.
- (50) Tolstik, E.; Romanov, O.; Matusevich, V.; Tolstik, A.; Kowarschik, R. Formation of Self-Trapping Waveguides in Bulk PMMA Media Doped with Phenanthrenequinone. *Opt. Express* **2014**, *22* (3), 3228–3233.
- (51) Jisha, C. P.; Kishore, V. C.; John, B. M.; Kuriakose, V. C.; Porsezian, K.; Kartha, C. S. Self-Written Waveguide in Methylene Blue Sensitized Poly(vinyl Alcohol)/acrylamide Photopolymer Material. *Appl. Opt.* **2008**, *47* (35), 6502–6507.
- (52) Monro, T. M.; Poladian, L.; de Sterke, C. M. Analysis of Self-Written Waveguides in Photopolymers and Photosensitive Materials. *Phys. Rev. E* **1998**, *57* (1), 1104–1113.
- (53) Li, H.; Qi, Y.; Ryle, J. P.; Sheridan, J. T. Self-Written Waveguides in a Dry Acrylamide/polyvinyl Alcohol Photopolymer Material. *Appl. Opt.* **2014**, *53* (34), 8086–8094.
- (54) Malallah, R.; Cassidy, D.; Muniraj, I.; Ryle, J. P.; Healy, J. J.; Sheridan, J. T. Self-Written Waveguides in Photopolymer. *Appl. Opt.* **2018**, *57* (22), E80–E88.
- (55) Jacobsen, A. J.; Barvosa-Carter, W.; Nutt, S. Micro-Scale Truss Structures Formed from Self-Propagating Photopolymer Waveguides. *Adv. Mater.* **2007**, *19* (22), 3892–3896.
- (56) Kagami, M.; Yamashita, T.; Ito, H. Light-Induced Self-Written Three-Dimensional Optical Waveguide. *Appl. Phys. Lett.* **2001**, *79* (8), 1079–1081.
- (57) Dorkenoo, K.; Crégut, O.; Mager, L.; Gillot, F.; Carre, C.; Fort, A. Quasi-Solitonic Behavior of Self-Written Waveguides Created by Photopolymerization. *Opt. Lett.* **2002**, *27* (20), 1782–1784.
- (58) Shoji, S.; Kawata, S.; Sukhorukov, A. A.; Kivshar, Y. S. Self-Written Waveguides in Photopolymerizable Resins. *Opt. Lett.* **2002**, *27* (3), 185–187.
- (59) Biria, S.; Malley, P. P. A.; Kahan, T. F.; Hosein, I. D. Optical Autocatalysis Establishes Novel Spatial Dynamics in Phase Separation of Polymer Blends during Photocuring. *ACS Macro Lett.* **2016**, *5* (11), 1237–1241.
- (60) Biria, S.; Hosein, I. D. Control of Morphology in Polymer Blends through Light Self-Trapping: An *in Situ* Study of Structure Evolution, Reaction Kinetics, and Phase Separation. *Macromolecules* **2017**, *50* (9), 3617–3626.
- (61) Frisken, S. J. Light-Induced Optical Waveguide Uptapers. *Opt. Lett.* **1993**, *18* (13), 1035–1037.
- (62) Kewitsch, A. S.; Yariv, A. Nonlinear Optical Properties of Photoresists for Projection Lithography. *Appl. Phys. Lett.* **1998**, *68* (4), 455–457.
- (63) Shoji, S.; Kawata, S. Optically-Induced Growth of Fiber Patterns into a Photopolymerizable Resin. *Appl. Phys. Lett.* **1999**, *75* (5), 737–739.
- (64) Eldada, L.; Shacklette, L. W. Advances in Polymer Integrated Optics. *IEEE J. Sel. Top. Quantum Electron.* **2000**, *6* (1), 54–68.
- (65) Kashin, O.; Tolstik, E.; Matusevich, V.; Kowarschik, R. Numerical Investigation of the (1+1)D Self-Trapping of Laser Beams in Polymeric Films Based on Polymethylmethacrylate and Phenanthrenequinone. *J. Opt. Soc. Am. B* **2009**, *26*

- (11), 2152–2156.
- (66) Bachelot, R.; Fares, A.; Fikri, R.; Barchiesi, D.; Lerondel, G.; Royer, P. Coupling Semiconductor Lasers into Single-Mode Optical Fibers by Use of Tips Grown by Photopolymerization. *Opt. Lett.* **2004**, *29* (17), 1971–1973.
- (67) Xiao, L.; Jin, W.; Demokan, M. S.; Ho, H. L.; Tam, H.; Ju, J.; Yu, J. Photopolymer Microtips for Efficient Light Coupling between Single-Mode Fibers and Photonic Crystal Fibers. *Opt. Lett.* **2006**, *31* (12), 1791–1793.
- (68) Missinne, J.; Beri, S.; Dash, M.; Samal, S. K.; Dubruel, P.; Watt   J.; Van Steenberge, G. Curing Kinetics of Step-Index and Graded-Index Single Mode Polymer Self-Written Waveguides. *Opt. Mater. Express* **2014**, *4* (7), 1324–1335.
- (69) Burrell, D.; Middlebrook, C. Comparison of Self-Written Waveguide Techniques and Bulk Index Matching for Low-Loss Polymer Waveguide Interconnects; Schr  der, H., Chen, R. T., Eds.; International Society for Optics and Photonics, 2016; Vol. 9753, p 975306.
- (70) Jacobsen, A. J.; Barvosa-Carter, W.; Nutt, S. Shear Behavior of Polymer Micro-Scale Truss Structures Formed from Self-Propagating Polymer Waveguides. *Acta Mater.* **2008**, *56* (6), 1209–1218.
- (71) Jacobsen, A. J.; Barvosa-Carter, W.; Nutt, S. Compression Behavior of Micro-Scale Truss Structures Formed from Self-Propagating Polymer Waveguides. *Acta Mater.* **2007**, *55* (20), 6724–6733.
- (72) Kim, J.; Jeong, K.-H.; Lee, L. P. Artificial Ommatidia by Self-Aligned Microlenses and Waveguides. *Opt. Lett.* **2005**, *30* (1), 5–7.
- (73) Radtke, D.; Duparr   J.; Zeitner, U. D.; T  nnermann, A. Laser Lithographic Fabrication and Characterization of a Spherical Artificial Compound Eye. *Opt. Express* **2007**, *15* (6), 3067–3077.
- (74) Jung, H.; Jeong, K.-H. Microfabricated Ommatidia Using a Laser Induced Self-Writing Process for High Resolution Artificial Compound Eye Optical Systems. *Opt. Express* **2009**, *17* (17), 14761–14766.
- (75) Jeong, K.-H.; Kim, J.; Lee, L. P. Biologically Inspired Artificial Compound Eyes. *Science* **2006**, *312* (5773), 557–561.
- (76) Keum, D.; Jung, H.; Jeong, K. H. Planar Emulation of Natural Compound Eyes. *Small* **2012**, *8* (14), 2169–2173.
- (77) Jun, B. M.; Serra, F.; Xia, Y.; Kang, H. S.; Yang, S. Fabrication of Free-Standing, Self-Aligned, High-Aspect-Ratio Synthetic Ommatidia. *ACS Appl. Mater. Interfaces* **2016**, *8* (45), 30671–30676.
- (78) Biria, S.; Chen, F. H.; Pathreker, S.; Hosein, I. D. Polymer Encapsulants Incorporating Light-Guiding Architectures to Increase Optical Energy Conversion in Solar Cells. *Adv. Mater.* **2018**, *30* (8), 1705382.
- (79) Hosein, I. D.; Lin, H.; Ponte, M. R.; Basker, D. K.; Brook, M. A.; Saravanamuttu, K. Waveguide Encoded Lattices (WELs): Slim Polymer Films with Panoramic Fields of View (FOV) and Multiple Imaging Functionality. *Adv. Funct. Mater.* **2017**, *27* (40), 1702242.
- (80) Crivello, J. V. A New Visible Light Sensitive Photoinitiator System for the Cationic Polymerization of Epoxides. *J. Polym. Sci. Part A Polym. Chem.* **2009**, *47* (3), 866–875.

- (81) Basker, D. Nonlinear Optical Waves in Cationic Polymerization Systems: Facile Route to 3-D Polymer and Metallodielectric Functional Microstructures, McMaster University, 2016.
- (82) Kubisa, P. Activated Monomer Mechanism in the Cationic Polymerization of Cyclic Ethers. *Makromol. Chemie. Macromol. Symp.* **1988**, 13-14 (1), 203–210.
- (83) Basker, D. K.; Cortes, O. A. H.; Brook, M. A.; Saravanamuttu, K. 3D Nonlinear Inscription of Complex Microcomponents (3D NSCRIPT): Printing Functional Dielectric and Metallodielectric Polymer Structures with Nonlinear Waves of Blue LED Light. *Adv. Mater. Technol.* **2017**, 2 (5), 1600236.
- (84) Saravanamuttu, K.; Du, M.; Najafi, S. I.; Andrews, M. P. Photoinduced Structural Relaxation and Densification in Sol-Gel-Derived Nanocomposite Thin Films: Implications for Integrated Optics Device Fabrication. *Can. J. Chem.* **1998**, 76, 1717–1729.
- (85) Qiu, L. Nonlinear Light Propagation and Self-Inscription Processes in a Photopolymer Doped with Ag Nanoparticles, McMaster University, 2012.
- (86) Saravanamuttu, K.; Andrews, M. P. Visible Laser Self-Focusing in Hybrid Glass Planar Waveguides. *Opt. Lett.* **2002**, 27 (15), 1342–1344.
- (87) Villafranca, A. B.; Saravanamuttu, K. Diversity and Slow Dynamics of Diffraction Rings: A Comprehensive Study of Spatial Self-Phase Modulation in a Photopolymer. *J. Opt. Soc. Am. B* **2012**, 29 (9), 2357–2372.
- (88) Villafranca, A. B.; Saravanamuttu, K. Diffraction Rings due to Spatial Self-Phase Modulation in a Photopolymerizable Medium. *J. Opt. A Pure Appl. Opt.* **2009**, 11 (12), 125202.
- (89) Villafranca, A. B.; Saravanamuttu, K. Spontaneous and Sequential Transitions of a Gaussian Beam into Diffraction Rings, Single Ring and Circular Array of Filaments in a Photopolymer. *Opt. Express* **2011**, 19 (16), 15560–15573.
- (90) Qiu, L.; Saravanamuttu, K. Optical Self-Trapping in a Photopolymer Doped with Ag Nanoparticles: A Single-Step Route to Metallodielectric Cylindrical Waveguides. *J. Opt. Soc. Am. B* **2012**, 29 (5), 1085–1093.
- (91) Kasala, K.; Saravanamuttu, K. A Black Beam Borne by an Incandescent Field Self-Traps in a Photopolymerizing Medium. *J. Am. Chem. Soc.* **2012**, 134 (34), 14195–14200.
- (92) Kasala, K.; Saravanamuttu, K. Coaxial Self-Trapping of White and Gray Regions of an Incandescent Field: A Bright Core with a Dark Cladding. *Phys. Res. Int.* **2012**, 2012, 1–5.
- (93) Ponte, M. R.; Welch, R.; Saravanamuttu, K. An Optochemically Organized Nonlinear Waveguide Lattice with Primitive Cubic Symmetry. *Opt. Express* **2013**, 21 (4), 4205–4214.
- (94) Marshall, N. J.; Land, M. F.; King, C. a.; Cronin, T. W. The Compound Eyes of Mantis Shrimps (Crustacea, Hoplocarida, Stomatopoda). I. Compound Eye Structure: The Detection of Polarized Light. *Philos. Trans. R. Soc. B Biol. Sci.* **1991**, 334 (1269), 33–56.
- (95) Nilsson, D.-E.; Kelber, A. A Functional Analysis of Compound Eye Evolution. *Arthropod Struct. Dev.* **2007**, 36 (4), 373–385.
- (96) Yuan, W.; Li, L.-H.; Lee, W.-B.; Chan, C.-Y. Fabrication of Microlens Array

- and Its Application: A Review. *Chinese J. Mech. Eng.* **2018**, *31* (1), 16.
- (97) Duparré J. W.; Wippermann, F. C. Micro-Optical Artificial Compound Eyes. *Bioinspir. Biomim.* **2006**, *1* (1), R1–R16.
- (98) Kim, J. Absorption-Assisted Mode Transformation in Butterfly Compound Eyes. *Sci. Rep.* **2015**, *4* (1), 6291.
- (99) Tanida, J.; Akiyama, H.; Kagawa, K.; Ogata, C.; Umeda, M. A Stick-Shaped Multi-Aperture Camera for Intra-Oral Diagnosis; Mahalanobis, A., Ashok, A., Tian, L., Petrucci, J. C., Kubala, K. S., Eds.; International Society for Optics and Photonics, 2017; Vol. 10222, p 102220L.
- (100) Kagawa, K.; Yamada, K.; Tanaka, E.; Tanida, J. A Three-Dimensional Multifunctional Compound-Eye Endoscopic System with Extended Depth of Field. *Electron. Commun. Japan* **2012**, *95* (11), 14–27.
- (101) Shi, C.; Wang, Y.; Liu, C.; Wang, T.; Zhang, H.; Liao, W.; Xu, Z.; Yu, W. SCECam: A Spherical Compound Eye Camera for Fast Location and Recognition of Objects at a Large Field of View. *Opt. Express* **2017**, *25* (26), 32333–32345.
- (102) Song, Y. M.; Xie, Y.; Malyarchuk, V.; Xiao, J.; Jung, I.; Choi, K. J.; Liu, Z.; Park, H.; Lu, C.; Kim, R. H.; et al. Digital Cameras with Designs Inspired by the Arthropod Eye. *Nature* **2013**, *497* (7447), 95–99.
- (103) Leitel, R.; Brückner, A.; Buß, W.; Viollet, S.; Pericet-Camara, R.; Mallot, H.; Bräuer, A. Curved Artificial Compound-Eyes for Autonomous Navigation; Thienpont, H., Mohr, J., Zappe, H., Nakajima, H., Eds.; International Society for Optics and Photonics, 2014; Vol. 9130, p 91300H. .
- (104) Floreano, D.; Pericet-Camara, R.; Viollet, S.; Ruffier, F.; Brückner, A.; Leitel, R.; Buss, W.; Menouni, M.; Expert, F.; Juston, R.; et al. Miniature Curved Artificial Compound Eyes. *Proc. Natl. Acad. Sci. U. S. A.* **2013**, *110* (23), 9267–9272.
- (105) Franceschini, N. Small Brains, Smart Machines: From Fly Vision to Robot Vision and Back Again. *Proc. IEEE* **2014**, *102* (5), 751–781.
- (106) Pang, K.; Fang, F.; Song, L.; Zhang, Y.; Zhang, H. Bionic Compound Eye for 3D Motion Detection Using an Optical Freeform Surface. *J. Opt. Soc. Am. B* **2017**, *34* (5), B28–B35.
- (107) Sieler, M.; Schreiber, P.; Dannberg, P.; Bräuer, A.; Tünnermann, A. Ultrathin Fixed Pattern Projectors with Inherent Homogenization of Illumination. *Appl. Opt.* **2012**, *51* (1), 64–74.
- (108) Horisaki, R.; Tanida, J. Compact Compound-Eye Projector Using Superresolved Projection. *Opt. Lett.* **2011**, *36* (2), 121–123.
- (109) Tanida, J.; Kumagai, T.; Yamada, K.; Miyatake, S.; Ishida, K.; Morimoto, T.; Kondou, N.; Miyazaki, D.; Ichioka, Y. Thin Observation Module by Bound Optics (TOMBO): An Optoelectronic Image Capturing System. International Society for Optics and Photonics, 2000; Vol. 4089, pp 1030–1036.
- (110) Tanida, J.; Kumagai, T.; Yamada, K.; Miyatake, S.; Ishida, K.; Morimoto, T.; Kondou, N.; Miyazaki, D.; Ichioka, Y. Thin Observation Module by Bound Optics (TOMBO): Concept and Experimental Verification. *Appl. Opt.* **2001**, *40* (11), 1806–1813.
- (111) Duparré J.; Dannberg, P.; Schreiber, P.; Bräuer, A.; Tünnermann, A. Artificial

- Apposition Compound Eye Fabricated by Micro-Optics Technology. *Appl. Opt.* **2004**, *43* (22), 4303–4310.
- (112) Duparré J.; Wippermann, F.; Dannberg, P.; Reimann, A. Chirped Arrays of Refractive Ellipsoidal Microlenses for Aberration Correction under Oblique Incidence. *Opt. Express* **2005**, *13* (26), 10539–10551.
- (113) Duparré J.; Schreiber, P.; Matthes, A.; Pshenay-Severin, E.; Bräuer, A.; Tünnemann, A.; Vökel, R.; Eisner, M.; Scharf, T. Microoptical Telescope Compound Eye. *Opt. Express* **2005**, *13* (3), 889–503.
- (114) Brueckner, A.; Duparré J.; Leitel, R.; Dannberg, P.; Bräuer, A.; Tünnemann, A. Thin Wafer-Level Camera Lenses Inspired by Insect Compound Eyes. *Opt. Express* **2010**, *18* (24), 24379–24394.
- (115) Meyer, J.; Brückner, A.; Leitel, R.; Dannberg, P.; Bräuer, A.; Tünnemann, A. Optical Cluster Eye Fabricated on Wafer-Level. *Opt. Express* **2011**, *19* (18), 17506–17519.
- (116) Deng, H.; Gao, X.; Ma, M.; Li, Y.; Li, H.; Zhang, J.; Zhong, X. Catadioptric Planar Compound Eye with Large Field of View. *Opt. Express* **2018**, *26* (10), 12455–12468.
- (117) Gassner, C.; Dunkel, J.; Oberdörster, A.; Brückner, A. Compact Wide-Angle Array Camera for Presence Detection. In *MOEMS and Miniaturized Systems XVII*; Piyawattanametha, W., Park, Y.-H., Zappe, H., Eds.; SPIE, 2018; Vol. 10545, p 10.
- (118) Huang, C.-C.; Jiang, H. Bio-Inspired Wide-Angle Broad-Spectrum Cylindrical Lens Based on Reflections from Micro-Mirror Array on a Cylindrical Elastomeric Membrane. *Micromachines* **2014**, *5* (2), 373–384.
- (119) Huang, C. C.; Wu, X.; Liu, H.; Aldalali, B.; Rogers, J. A.; Jiang, H. Large-Field-of-View Wide-Spectrum Artificial Reflecting Superposition Compound Eyes. *Small* **2014**, *10* (15), 3050–3057.
- (120) Deng, Z.; Chen, F.; Yang, Q.; Bian, H.; Du, G.; Yong, J.; Shan, C.; Hou, X. Dragonfly-Eye-Inspired Artificial Compound Eyes with Sophisticated Imaging. *Adv. Funct. Mater.* **2016**, *26* (12), 1995–2001.
- (121) Wu, S.; Jiang, T.; Zhang, G.; Schoenemann, B.; Neri, F.; Zhu, M.; Bu, C.; Han, J.; Kuhnert, K.-D. Artificial Compound Eye: A Survey of the State-of-the-Art. *Artif. Intell. Rev.* **2017**, *48* (4), 573–603.
- (122) Varela, F. G.; Wiitanen, W. The Optics of the Compound Eye of the Honeybee (*Apis Mellifera*). *J. Gen. Physiol.* **1970**, *55*, 336–358.
- (123) Li, L.; Yi, A. Y. Development of a 3D Artificial Compound Eye. *Opt. Express* **2010**, *18* (17), 18125–18137.
- (124) Shen, H.-K.; Su, G.-D. J. Cluster Eye Camera Using Microlenses on Parabolic Surface; Gregory, G. G., Davis, A. J., Eds.; 2013; p 884202.
- (125) Roy, E.; Voisin, B.; Gravel, J.-F.; Peytavi, R.; Boudreau, D.; Veres, T. Microlens Array Fabrication by Enhanced Thermal Reflow Process: Towards Efficient Collection of Fluorescence Light from Microarrays. *Microelectron. Eng.* **2009**, *86* (11), 2255–2261.
- (126) Wang, M.; Yu, W.; Wang, T.; Han, X.; Gu, E.; Li, X. A Novel Thermal Reflow Method for the Fabrication of Microlenses with an Ultrahigh Focal Number.

- RSC Adv.* **2015**, 5 (44), 35311–35316.
- (127) Pan, L.-W.; Shen, X.; Lin, L. Microplastic Lens Array Fabricated by a Hot Intrusion Process. *J. Microelectromechanical Syst.* **2004**, 13 (6), 1063–1071.
- (128) Shen, X.-J.; Lin, L. Micro Plastic Embossing Process: Experimental and Theoretical Characterizations. In *Transducers '01 Eurosensors XV*; Springer Berlin Heidelberg: Berlin, Heidelberg, 2001; pp 1612–1615.
- (129) Kim, J. Y.; Pfeiffer, K.; Voigt, A.; Gruetzner, G.; Brugger, J. Directly Fabricated Multi-Scale Microlens Arrays on a Hydrophobic Flat Surface by a Simple Ink-Jet Printing Technique. *J. Mater. Chem.* **2012**, 22 (7), 3053–3058.
- (130) Luo, Y.; Wang, L.; Ding, Y.; Wei, H.; Hao, X.; Wang, D.; Dai, Y.; Shi, J. Direct Fabrication of Microlens Arrays with High Numerical Aperture by Ink-Jetting on Nanotextured Surface. *Appl. Surf. Sci.* **2013**, 279, 36–40.
- (131) Kim, J. Y.; Brauer, N. B.; Fakhfour, V.; Boiko, D. L.; Charbon, E.; Grutzner, G.; Brugger, J. Hybrid Polymer Microlens Arrays with High Numerical Apertures Fabricated Using Simple Ink-Jet Printing Technique. *Opt. Mater. Express* **2011**, 1 (2), 259–262.
- (132) Yi, X.; Zhang, X.; Li, Y.; Zhao, X.-R. Microlens Arrays Formed by Melting Photoresist and Ion Beam Milling; Motamedi, M. E., Goering, R., Eds.; International Society for Optics and Photonics, 1998; Vol. 3276, pp 249–253.
- (133) Albero, J.; Nieradko, L.; Gorecki, C.; Ottevaere, H.; Gomez, V.; Thienpont, H.; Pietarinen, J.; P ä v änranta, B.; Passilly, N. Fabrication of Spherical Microlenses by a Combination of Isotropic Wet Etching of Silicon and Molding Techniques. *Opt. Express* **2009**, 17 (8), 6283–6292.
- (134) Bian, H.; Wei, Y.; Yang, Q.; Chen, F.; Zhang, F.; Du, G.; Yong, J.; Hou, X. Direct Fabrication of Compound-Eye Microlens Array on Curved Surfaces by a Facile Femtosecond Laser Enhanced Wet Etching Process. *Appl. Phys. Lett.* **2016**, 109 (22), 221109.
- (135) Zhang, P.; Du, Y.; Wang, B.; Shan, D. Fabrication of Micro-Lens Array on Convex Surface by Meaning of Micro-Milling; Yang, L., Ruch, E., Li, S., Eds.; International Society for Optics and Photonics, 2014; Vol. 9281, p 928106.
- (136) Liu, X.; Zhang, X.; Fang, F.; Zeng, Z.; Gao, H.; Hu, X. Influence of Machining Errors on Form Errors of Microlens Arrays in Ultra-Precision Turning. *Int. J. Mach. Tools Manuf.* **2015**, 96, 80–93.
- (137) Yu, D. P.; Hong, G. S.; Wong, Y. S. Profile Error Compensation in Fast Tool Servo Diamond Turning of Micro-Structured Surfaces. *Int. J. Mach. Tools Manuf.* **2012**, 52 (1), 13–23.
- (138) Chen, P.-C.; Chang, Y.-P.; Zhang, R.-H.; Wu, C.-C.; Tang, G.-R. Microfabricated Microfluidic Platforms for Creating Microlens Array. *Opt. Express* **2017**, 25 (14), 16101–16115.

Chapter 2

Waveguide Encoded Lattices (WELs): Slim Polymer Films with Panoramic Fields of View (FOV) and Multiple Imaging Functionality

Ian D. Hosein⁺, Hao Lin⁺, Matthew R. Ponte, Dinesh K. Basker, Michael A. Brook, and Kalaichelvi Saravanamuttu*

Reprinted with permission from John Wiley and Sons.

Adv. Funct. Mater. **2017**, 27, 1702242, DOI: 10.1002/adfm.20170224

Copyright © 2017 Wiley-VCH Verlag GmbH & Co. KGaA, Weinheim.

HL and IDH contributed equally to this work. KS, IDH, HL and MRP conceived the project. HL, IDH and MRP carried out experiments and data analysis. IDH performed calculations and simulations. DKB provided the photopolymerizable resins. MAB made valuable suggestions. KS, IDH and HL wrote the manuscript.

Abstract

When encoded with a 3D network of interconnected and pentadirectional waveguides, an otherwise passive polymer film transforms into an intelligent optical element – a waveguide encoded lattice (WEL) - that combines a panoramic field of view, infinite depth of field and powerful capacity to perform multiple imaging operations such as divergence-free transmission, focusing, and inversion. The lattices are moreover operable with coherent and incoherent light at all visible wavelengths, both individually (e.g., narrow band sources such as lasers, light-emitting diodes) and collectively (e.g., incandescent sources). This combination of properties is unprecedented in single-component films and the WEL structures represent a new class of flexible, slim films that could confer advanced optical functionalities when integrated with light-based technologies (e.g., solar panels, smart phone cameras, and smart screens) and are amenable to the design and fabrication of new miniaturized optical and optoelectronic devices.

Key words

Bioinspired compound eyes, nonlinear waves, panoramic field of view, smart optical films, waveguide structures

2.1. Introduction

Optical fields exhibit strong and richly varied interactions with planar films that are configured with spatial patterns or modulations in refractive index. Natural and synthetic photonic crystals,^[1,2] metamaterials,^[3] nanohole arrays,^[4] roughened metal surfaces,^[5,6] and chiral films^[7,8] are examples of plane-faced microstructures that reflect, refract, transmit, resonate with, scatter or rotate the polarization plane of light with extraordinary selectivity and sensitivity. These nonclassical mechanisms create pathways to precisely control and manipulate light flow within micron-scaled architectures^[3,9–12] and therefore hold significant promise in the design and fabrication of miniaturized photonics and optoelectronics devices. Here, we introduce a fundamentally new class of intelligent optical films – WELs (waveguide encoded lattices) - that are encoded with a dense 3D network of intersecting cylindrical waveguides, which confer a panoramic field of view (FOV) and enable multiple imaging operations such as focusing and inversion that would typically require bulky optical elements. Because it is assembled from polychromatic, multimode waveguides, the WEL lattice functions at all visible wavelengths ranging from the broad spectrum of incoherent light^[13,14] emitted by incandescent sources (including sunlight) to the narrow wavelength ranges emitted by lasers and light-emitting diodes (LEDs).

The WEL lattice design draws inspiration from the collective behavior of light-harvesting ommatidia – biological waveguides composed of a lens, crystalline cone, and rhabdom - that constitute the compound eyes of arthropods.^[15–17] Light beams naturally diverge and weaken in intensity as they travel through boundless, homogeneous media but when confined to a waveguide, propagate over long distances

(>>Rayleigh range) as optical modes that retain their original spatial profiles. When packed into a hemisphere, the discrete light-collection ranges of individual ommatidia impart a cumulative FOV of $\approx 180^\circ$. Elegant replicas of compound eyes, which aim to transcribe arthropodal vision to imaging devices^[18,19] have been fabricated in planar, primarily lens-based configurations^[20–24] as well as in curved configurations with panoramic^[25] and near-hemispherical^[26–29] FOVs. While these processes typically involve rigid components and multiple fabrication steps, eyes have also been constructed from soft materials by inducing lens-capped waveguides in UV-polymerizable resins in 3D,^[30] and 2D hemispherical geometries,^[16] embossing densely packed microlenses on polymethylmethacrylate hemispheres^[31] and in an elastomeric monolith, which is first embedded with lens-like posts, each interfaced with a Si photodetector, and then deliberately deformed into a hemispherical dome.^[32]

We fabricate WELs from single-component epoxide films that are freestanding, flexible, and thermomechanically robust.^[33] In contrast to the finite number of omnidirectional ommatidia, which pack adjacent to each other into the small-volumed, curved geometries of natural and most artificial compound eyes, the WEL structure is a thin, flexible, and optically flat film that is assembled from five pentadirectional and intersecting arrays of lens-free cylindrical waveguides. While the large FOV of the most artificial compound eyes originates from lenses positioned over a hemispherical surface,^[30–32] the panoramic FOV of the optically flat and lens-free WEL corresponds to the cumulative angular collection ranges of its constituent wave-guides. This arrangement of waveguides also confers discrete translational symmetry to the WEL lattice, enabling it – unlike curved architectures - to be limitlessly extended to large

areas without losing optical functionality. The WEL lattice surface is densely patterned with an extremely large population of wave-guide elements ($>15\ 000\ \text{cm}^{-2}$ per waveguide array), which significantly exceeds the absolute number of ommatidial elements in artificial eyes including those in photopolymer (8370 in a hemispherical dome with base diameter =2.5 cm),^[30] elastomer (180 functional ommatidia over a $1.472\ \text{cm} \times 1.472\ \text{cm}$ area) systems^[32] and is commensurate with the tightly packed microlens populations embossed on a polymer dome ($\approx 30\ 000$ in a hemispherical dome with base diameter =5 mm).^[31] The WEL lattice waveguides collectively capture light from a wide, panoramic space and guide it without loss of intensity through the film. The micron-scale diameter ($\approx 80\ \mu\text{m}$) of these wave-guides and in particular, their intersecting geometry allow the WEL lattice to collect, image, and most significantly, manipulate all forms of visible light from large panoramic spaces with excellent spatial resolution. This combination of properties distinguishes the WEL lattice from compound eyes, which boast larger, nearly hemispherical FOVs but due to their small volumes and finite number of ommatidia, have characteristically poor imaging range and resolution. We detail below the design rationale and fabrication of the WEL lattice, which is impossible to construct through conventional lithographic techniques.^[34,35] We generate its complex 3D microstructure in a single, low-energy, room temperature process by launching and eliciting collisions between large populations of nonlinear incandescent waves in a photopolymerizable medium.^[33,36–39] We then elucidate its microstructure and optical properties through a series of studies including control experiments.

2.2. Results and Discussion

2.2.1. Design and Operation

Simulations in **Figure 2.1** describe the microstructure and working principles of the WEL lattice, which consists of identical xz planes stacked along the y axis (Figure 2.1a); its optically flat entrance (top) and exit (bottom) faces correspond to xy planes and light propagates along z . Each xz slice contains five intersecting rows of ≈ 70 – 80 μm wide and ≈ 3000 – 3460 μm long cylindrical waveguides (in red), each with a gradient refractive index profile and maximum index change (Δn_{max}) of 0.006 relative to its surroundings where $n = 1.47$. We selected these waveguides to model the WEL lattice as we know from previous studies that they guide incandescent white light – which is critical for imaging and vision-based applications - and by extension, visible laser and LED light.^[40,41] Four waveguide rows in the xz plane are oriented at $\pm 30^\circ$ and $\pm 15^\circ$, respectively, about the central row of waveguides, which runs normal to the lattice faces along the z axis. Each waveguide suffers multiple inter-sections with nonparallel neighbors; for example, a waveguide oriented along 0° intersects its nearest neighbors oriented along $\pm 15^\circ$ every 299 μm , and those along $\pm 30^\circ$, every 139 μm .

The WEL entrance (xy) face contains the input faces of periodically arranged waveguide quintets – individual sets of pentadirectional waveguides oriented respectively at $\pm 30^\circ$, $\pm 15^\circ$, and 0° - that together “see” and collect light over a panoramic space (Figure 2.1a,b). The panoramic FOV of the WEL lattice (along the x direction) is the same as the cumulative angular acceptance ranges of a single waveguide quintet (Figure 2.1b). Plots of optical power at the waveguide exit computed through the beam propagation method versus the incidence angle of a Gaussian beam (λ

= 633 nm) yield respective acceptance ranges ($1/e^2$) of 21 °, 22 °, and 28 ° (Figure 2.1c; see the details in Section S2.1 in the Supporting Information) imparting an overall FOV of 120 ° to the lattice. Because the waveguides are multimoded (e.g., they guide ≈ 13 modes at 633 nm; see Section S2.2 in the Supporting Information), light incident at any angle within the acceptance cone propagates as a guided (loss-free) mode. The angular acceptance ranges of the five waveguides do not overlap (Figure 2.1c), which prevents mixing of light incident from different directions and the consequent distortion of images transmitted through the lattice. Simulations showed a significantly diminished FOV for a control sample where light propagates through refraction alone: a film that does not contain wave-guides but is otherwise identical to the WEL lattice possesses effective acceptance ranges of only $\approx 5^\circ$ in each of the directions corresponding to the five waveguide arrays (Figure 2.1c).

Its repeat motif of intersecting waveguide-quintets (i.e., discrete translational symmetry in the x and y directions) combined with a planar geometry allows the WEL lattice to be easily extended to infinitely large areas. The lattice moreover has an extremely high density of light-harvesting waveguide elements oriented along each of the five orientations ($>15\,000\text{ cm}^{-2}$ (vide infra)) so that the absolute angular space that can be sampled as well the spatial resolution of transmitted images (determined by waveguide diameter ($\approx 80\ \mu\text{m}$)) is vastly increased compared to an unstructured film and hemispherical waveguide constructs.

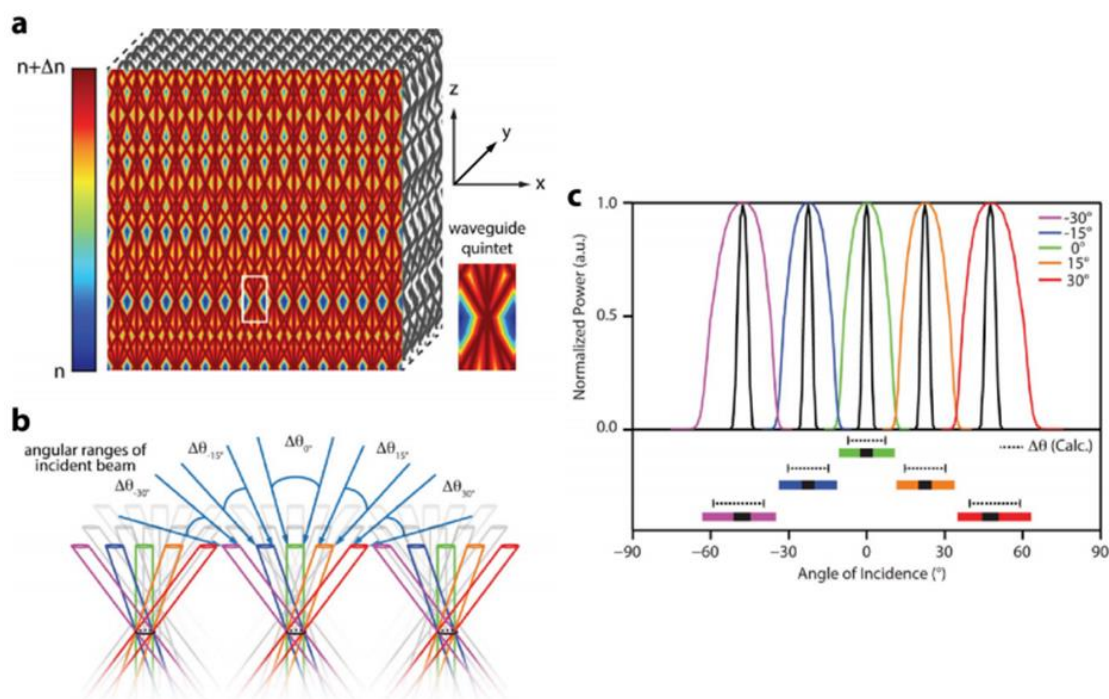


Figure 2.1. Operating principles of the WEL lattice. a) 3D model of the WEL lattice, which consists of a stack of xz planes, each comprising five intersecting waveguide arrays oriented respectively at -30° , -15° , 0° , 15° , and 30° relative to the surface normal (z). The inset contains an individual quintet of waveguides. The color scale indicates the change in refractive index (Δn). b) Each waveguide has an acceptance angular range of $\Delta\theta_n$ where $n =$ waveguide orientation angle. The FOV at the convergence point of a single waveguide quintet (and the entire WEL lattice) is the sum of all $\Delta\theta_n$. The FOV is quantified in c) color-coded computed plots (generated through the beam propagation method) of transmitted power at each waveguide exit versus the incidence angle. Black plots correspond to an unstructured medium without waveguides (control). The bar chart below depicts $\Delta\theta_n$ for each waveguide (solid color) and the unstructured medium (solid black); $\Delta\theta_n$ here is the curve width where power $=1/e^2$ of maximum. $\Delta\theta_n$ values from ray optics-based calculations of waveguiding are included for comparison (dotted line).

2.2.2. Assembling the WEL Lattice with Colliding Self-Trapped White Light Beams

To fabricate the WEL lattice, we generate a 3D lattice^[36–39] of microscopic self-trapped incandescent beams (**Figure 2.2a**), which permanently inscribes the corresponding structure of cylindrical waveguides in a photopolymerizable epoxide

medium. Under the nonlinear conditions created by photopolymerizing systems, incandescent beams become entrapped within self-induced waveguides and propagate without diverging through the medium. By launching large populations of multidirectional self-trapped beams, it is possible to generate 3D wave-guide architectures with a variety of symmetries,^[36–39] similarly, intersecting polymer waveguides induced by self-trapped UV beams have been used to generate 3D microscopic trusses.^[42,43] Such 3D structures are inaccessible to conventional, mask-based lithographic techniques that are limited by the natural divergence of light and can only inscribe 2D structures.^[44] Our nonlinear technique also differs from holographic lithography – the only other route to 3D optical lattices - which relies on the interference of four mutually coherent laser beams.^[45,46] By contrast, the incandescent lattice is generated with five quartz-tungsten-halogen (QTH) lamps – low intensity, white light bulbs - which emit a broad range of wavelengths (400–800 nm) and being mutually incoherent, do not produce periodic interference patterns when they coincide in space.

The cycloaliphatic epoxide sol^[33] selected for lattice fabrication polymerizes into thermomechanically robust, flexible, and transparent monoliths (Figure 2.2b,c) and importantly, satisfies the rigorous prerequisites for self-trapping of incandescent light.^[13,14,47–49] Composed of a broad spectrum and originating from the poorly correlated relaxation of excited states, incandescent light suffers phase and amplitude fluctuations – it is spatially and temporally incoherent - at the *fs* timescale.^[14] While self-trap-ping of this chaotic^[50] wavepacket would be impossible in most nonlinear media with virtually instantaneous photoresponse,^[14] the relatively slow evolution of

epoxide polymerization^[33] (*ms* to minutes) renders the system insensitive to *fs* fluctuations. It responds only to the time-averaged (smoothed) optical field, which allows an incandescent beam to self-trap.^[13,14,47–49] Equally importantly, Δn in the epoxide system is saturable and relatively large (0.001) (see Section S2.8 in the Supporting Information for details), which enables waveguides induced by self-trapped beams to self-consistently guide the large modal population and multiple wavelengths of incandescent light.^[13,14,49]

The lattice is generated by five incandescent beams ($\lambda = 400\text{--}800\text{ nm}$), which are each collimated, modulated by a 2D periodic mask ($A = 80\ \mu\text{m}$) and launched at $\pm 44^\circ$, $\pm 22^\circ$, 0° , respectively into a cell containing epoxide sol (Figure 2.2a; see Figure S2.3 in the Supporting Information for details). Upon refraction at the air/sample interface, the beams travel through the medium at $\pm 30^\circ$, $\pm 15^\circ$, 0° , respectively, each bearing a 2D pattern of bright spots. Due to the particularly large divergence of incandescent light,^[47] the spots blur and disappear with propagation distance so that the beams appear uniform at the sample exit (Figure 2.2e is the 0° beam profile). However, when the intensity is increased above the photoinitiation threshold, each spot initiates epoxide polymerization and associated refractive index changes (Δn) along its path.^[33] Δn strongly suppresses the divergence of each spot, enabling it to propagate as a self-trapped beam so that at the sample exit face ($z = 3.0\text{ mm}$), the initially uniform beam profile spontaneously transforms into a 2D array of bright, tightly focused spots (Figure 2.2f). The concentration of incandescent light into self-trapped beams is an efficient process in which the fraction of light redistributed to bright spots increases even as the total power of transmitted light remains effectively constant (see Figure

S2.4 and S2.5 in the Supporting Information). Because the five beams are modulated by the same mask, a single bright spot at the sample entrance face seeds the growth of five self-trapped beams propagating along $\pm 30^\circ$, $\pm 15^\circ$, and 0° . In this way, the incandescent beams transform into five, intersecting 2D arrays of self-trapped beams, each with a density of $>15\,000$ waveguides cm^{-2} .

Intersections in the incandescent lattice are formed by colliding self-trapped beams, which pass through each other without altering their trajectories or intensity profiles;^[36–39,42,43] remarkably, the self-trapped beams oriented at 0° , $\pm 15^\circ$, and $\pm 30^\circ$ undergo as many as 62, 72, and 106 collisions, respectively, with nonparallel neighbors as they propagate through the 3 mm long sample (see Figure S2.7 in the Supporting Information for details). Similar to the spatial soliton, a pair of self-trapped beams undergoes seemingly elastic collisions when separated by angles exceeding the critical waveguiding angle of their respective waveguides—i.e., when the beams cannot couple into each other's waveguides.^[51–53] During lattice formation, nonparallel self-trapped beams are separated by a minimum of 15° , which exceeds the angular acceptance range of their respective waveguides (vide infra).

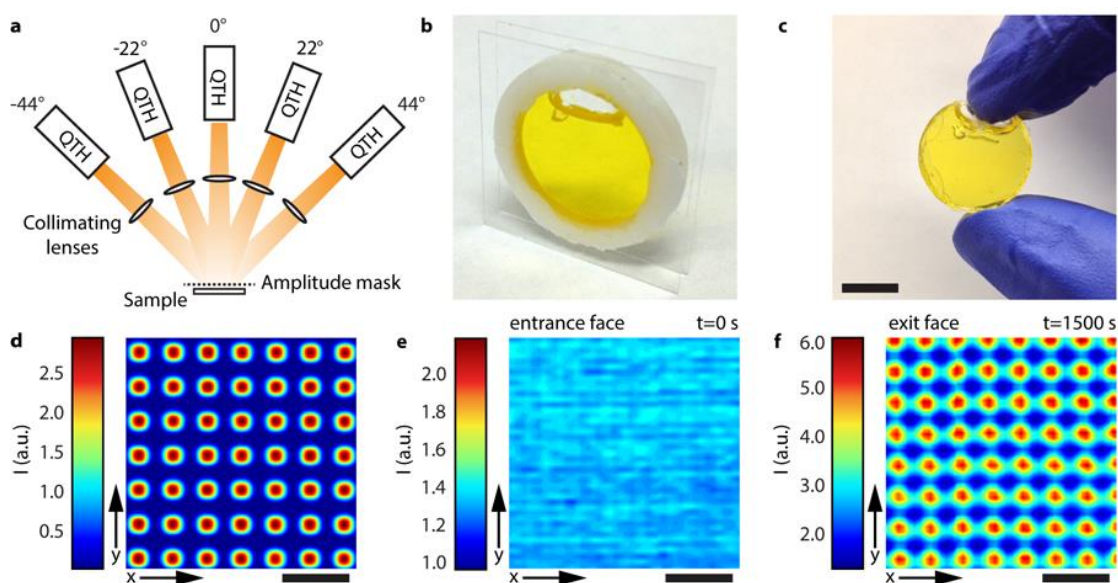


Figure 2.2. Structural fabrication. a) Scheme of optical assembly consisting of five beams emitted by quartz-tungsten-halogen (QTH) lamps. The beams were collimated, passed through a 2D periodic amplitude mask, and launched into a b) cell containing fluid photopolymerizable epoxide. Upon irradiation, the epoxide transformed into a c) freestanding, solid, and flexible WEL (scale bar = 1 cm). d) The spatial intensity profile of the central beam (0°) at the sample entrance face ($z = 0.0$ mm) at $t = 0$ s contained a strong 2D periodic modulation but diverged significantly with propagation so that it e) appeared uniform at the exit face ($z = 3.0$ mm) at $t = 0$ s. Refractive index changes due to epoxide strongly suppressed divergence and the beam transformed into a f) 2D periodic array of self-trapped beams at $t = 25$ min (scale bars in panels (d)–(f) = $160 \mu\text{m}$).

2.2.3. The WEL Lattice Microstructure

The 3D incandescent lattice inscribes the corresponding lattice of waveguides in the epoxide medium. Figure 2.3a and the inset are illustrations of the expected WEL lattice microstructure and respectively depict the relative orientation of its five wave-guide arrays and top-down view of their densely intersecting paths. These closely match transmission optical images of the fabricated microstructure: the top-down (xz) image shows the multidirectional waveguide arrays and the periodic intersection points where they collide and penetrate each other. xy cross-sectional images acquired by

monotonically tilting the lattice with respect to the microscope optic axis reveal each input faces of the five waveguide arrays. The yz cross-section (Figure 2.3d) shows a periodic stack of layers, each with a thickness of $\approx 74 \mu\text{m}$, which is commensurate with the average waveguide diameter of $\approx 80 \mu\text{m}$. Each waveguide propagating along 0° intersects its nearest neighbors at $\pm 15^\circ$ every $302 \mu\text{m}$ and those at $\pm 30^\circ$, every $147 \mu\text{m}$, which are comparable to the calculated values of 299 and $139 \mu\text{m}$, respectively (vide supra). The waveguide density in the 0° , $\pm 15^\circ$, and $\pm 30^\circ$ arrays is $\approx 15\,625$, $\approx 16\,749$, and $\approx 20\,800 \text{ cm}^{-2}$, respectively (see Section S2.4 in the Supporting Information).

We fabricated a family of lattices with increasing numbers of waveguide arrays (WEL-1, WEL-2, and WEL-3) to systematically trace and deconvolute their increasing complexity and elucidate the symmetry of the WEL lattice (see Section S2.5 in the Supporting Information for detailed characterization of each lattice type). The WEL-1 lattice induced by the 0° beam possesses square symmetry while WEL-1 lattices induced by single beams at $\pm 15^\circ$ or $\pm 30^\circ$ are rectangular. (This is because these non- 0° beams project the 2D mask pattern onto the sample entrance by $\cos(\alpha)$, where $\alpha = 22^\circ$ and 44° ; see Figure 2.2a and Figure S2.3 in the Supporting Information for details). 3D lattices are generated with multiple beams; we determined their symmetry by considering the stacking of the WEL-2s induced by a symmetric pair of beams (propagating at -22° and 22° or -44° and 44°) to be monoclinic and hexagonal, respectively. When a third central beam propagating at 0° was introduced, the two resulting types of WEL-3s (-22° , 0° , 22° , and -44° , 0° , 44°) were tetragonal in symmetry. Finally, we determined that the WEL lattices possess tetragonal symmetry (Figure S2.8 and Table S2.1 and S2.2, Supporting Information).

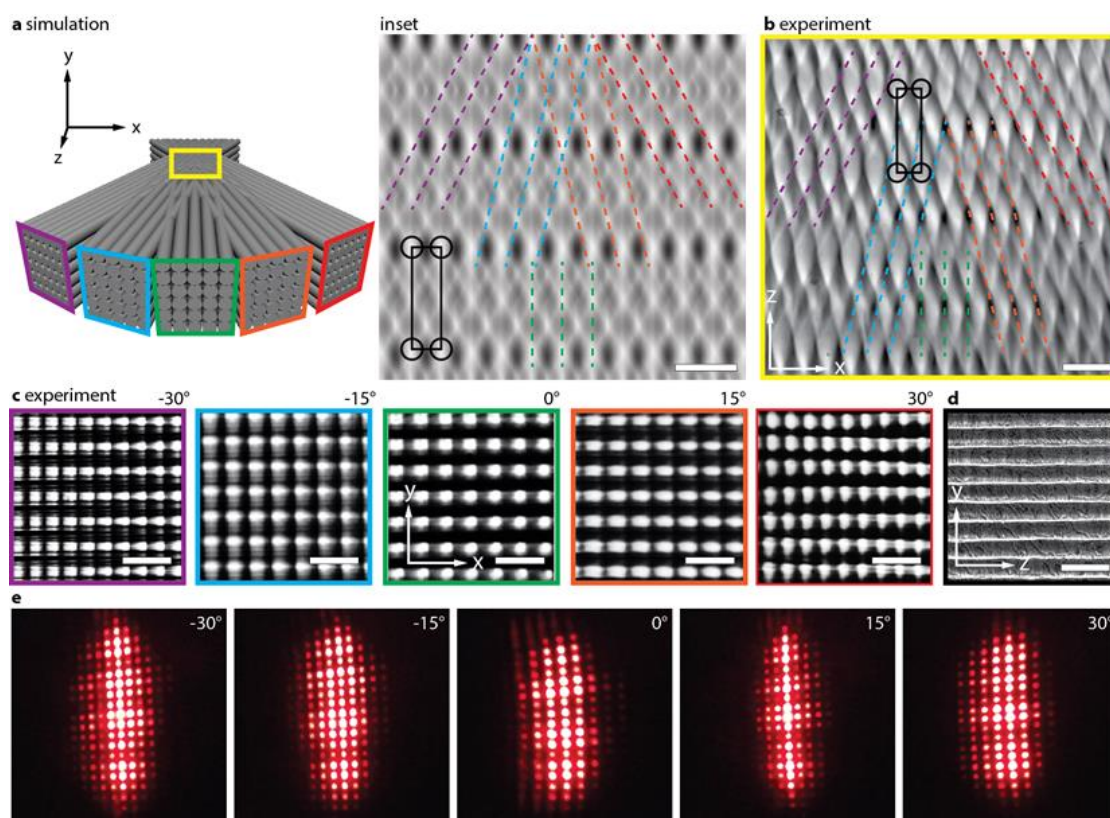


Figure 2.3. Structural characterization of a WEL lattice. a) A scheme of the WEL in which each waveguide array is individually extended along its axis to clearly depict its relative angular position. The inset is a simulated top-down view (xz plane); colored dotted lines guide the eye to each waveguide orientation and black circles indicate periodic points of waveguide intersections (scale bar = 160 μm). b) Experimentally acquired optical transmission image of the top-down view (xz plane) of an actual WEL. Colored dotted lines guide the eye to each waveguide orientation and black circles indicate periodic points of waveguide intersections (scale bar = 160 μm). c) Transmission optical image of the five waveguide arrays within a single WEL; images were acquired by monotonically tilting the WEL until the propagation axis of each waveguide array coincided with the microscope optic axis (scale bar = 160 μm). d) Optical image of the yz plane shows that WEL comprises a periodic stack of planes (scale bar = 160 μm). e) Photographs of the far-field output of laser light ($\lambda = 633 \text{ nm}$) propagating through a WEL at -30° , -15° , 0° , 15° , and 30° . Images were acquired at $\approx 45^\circ$ from the screen, which was placed 2 m away from the WEL lattice. The input laser beam was roughly Gaussian in profile with $1/e^2$ width of 570 μm (see Movie S1 in the Supporting Information).

2.2.4. Crosstalk-Free Guiding of Light in Mutually Independent Waveguide

Arrays

The WEL lattice captures, confines, and guides incandescent and laser light through its five waveguide arrays. There is no leakage of light between the five waveguide arrays – a critical requirement for vision - based applications where such cross-talk would scramble and distort the transmitted image. Equally importantly, light does not leak even between parallel-propagating waveguides within the same array. As a result, each waveguide effectively serves as a discrete pixel, with its diameter ($\approx 80 \mu\text{m}$) determining the excellent spatial resolution of the resulting image.

When we launched a continuous wave, laser beam ($\lambda = 632.9 \text{ nm}$) and monotonically varied its angle with respect to the lattice normal, the five waveguide arrays “lit up” in sequence when the laser incidence angle fell within their respective acceptance ranges (see Movie S1 in the Supporting Information). Far-field photographs of the lattice exit face show 2D arrays of bright spots, which correspond to laser modes propagating within individual waveguide elements (Figure 2.3e). Similarly, all five waveguide arrays exhibit strong guiding of incandescent light: spatial profiles and corresponding 1D traces acquired at the lattice exit face confirmed that optical intensity was tightly confined to waveguides and did not leak into surrounding regions, which were black (Figure 2.4a). While for clarity, we present only a selected area of the lattice ($550 \mu\text{m} \times 550 \mu\text{m}$) containing $\approx (7 \text{ to } 10) \times 7$ waveguides, waveguiding occurs throughout the WEL lattice ($\approx 200 \text{ mm}^2$) an area limited only by sample cell size (see Figure S2.9 in the Supporting Information). While both natural and artificial compound eyes employ highly absorbing pigments to prevent light leakage between

ommatidia^[15,17,32] the large contrast in refractive index relative to their surroundings (0.001) alone ensures that light remains confined to wave-guides in the WEL lattice (see Section S2.8 in the Supporting Information for details).

Waveguided light also does not leak between nonparallel waveguides within different arrays – even though they structurally intersect each other hundreds of times. This is consistent with simulations in Figure 2.4b, which show that a Gaussian beam coupled into any of the five waveguide arrays of the WEL lattice does not leak into neighboring nonparallel waveguides (further details are provided in Figure S2.18 in the Supporting Information). We quantified this behavior by calculating the power transferred between a pair of waveguides as a function of angular separation; results confirmed that power transfer is negligible when separation was $\geq 15^\circ$ (Figure S2.16, Supporting Information). The mutual independence of waveguide arrays was strikingly evident when we launched three different colored laser beams ($\lambda = 632.9, 488,$ and 532 nm) into arrays oriented along $0^\circ, 15^\circ, 30^\circ$, respectively, in the WEL lattice. Far-field images of the lattice output showed no mixing of colors despite structural overlap of their waveguide arrays; each colored beam remained confined to its array throughout propagation (Figure 2.4c; see also Figure S2.17 in the Supporting Information). The mutually independent yet intersecting wave-guide arrays of the WEL lattice are an elegant consequence of elastic collisions between self-trapped beams. These traverse through each other unimpeded when their separation angle exceeds the critical waveguiding angle of their respective wave-guides (otherwise, the colliding beams would couple into each other's waveguides and fuse; vide supra).^[51–53] Even under passive conditions, optical modes propagating in the intersecting waveguides

induced by intersecting self-trapped beams cannot couple into each other's waveguides as neither falls within the other's angular acceptance range – the result is that the non-parallel waveguides are effectively invisible to each other in the WEL lattice.

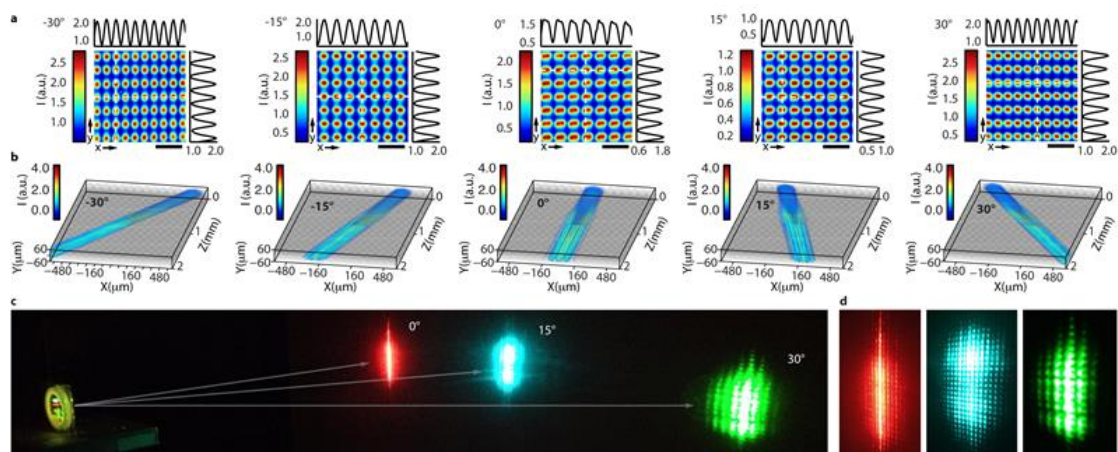


Figure 2.4. Simultaneous of multidirectional light propagation. a) Experimentally acquired spatial intensity profiles of a broad incandescent beam propagating through each of the five waveguide arrays in a WEL. Profiles were acquired at the exit face of the lattice ($z = 3.0$ mm). Scale bars of relative intensity are provided; horizontal and vertical line profiles correspond to the white dotted lines in each 2D profile (scale bars = $160 \mu\text{m}$). b) Beam propagation simulations of a Gaussian beam ($\lambda = 633$ nm) propagating through each of the five waveguide arrays in a WEL. For clarity, only the optical intensity distribution is in color while the WEL structure is in gray. c) Photograph of three different laser beams propagating simultaneously through waveguides oriented respectively at 0° (red), 15° (blue), and 30° (green) in the WEL and being projected onto a far-field screen. d) Magnified photographs of the spatial intensity profiles of each laser beam.

2.2.5. The Enhanced FOV of the WEL Lattice

The FOV of the WEL lattice is 66% greater compared to a sample that does not contain waveguides. To quantify its FOV, we measured the angular range over which incandescent light from an illuminated object – a stencilled letter “O” - is collected, waveguided, and deposited at the lattice exit face (Figure 2.5a; see Section S2.7 in the Supporting Information for details). The “O” was first launched into the central waveguide array (0°) of the lattice; its incidence angle was varied with a resolution of

$\pm 0.5^\circ$ from -6° to $+6^\circ$ centered about the array axis and its image at the lattice exit imaged by a CCD camera, which was always positioned normal to the array axis. The transmitted “O” is crisp and well resolved, being composed of bright, tightly focused pixel-like spots, each corresponding to the output of an individual waveguide (Figure 2.5b). The “O” is detected over an incidence angular range ($1/e^2$) of 5.5° ; it is detected over 3.3° in the control. Identical measurements carried out for each of the five waveguide arrays (see Figure S2.20 in the Supporting Information) showed that the quality of the “O” at the exit face, i.e., its intensity distribution and spatial definition, did not change with waveguide array; the image remained focused without the blurring or aberration observed in off-axis lens configurations. Plots of integrated intensity of the “O” image at the lattice exit versus their angle of incidence (Figure 2.5c; Table S2.4, Supporting Information) yielded angular acceptance ranges ($1/e^2$) of 5.9° , 5.6° , 5.5° , 5.3° , and 5.5° for arrays oriented at -30° , -15° , 0° , $+15^\circ$, and $+30^\circ$, respectively. (Corresponding values for the control sample were 3.3° , 3.3° , 3.4° , 3.3° , and 3.3° , respectively.) The angular acceptance ranges in the WEL lattice exceed equivalent values (angular sensitivity functions) of individual ommatidia (1.1° – 4.4°) in polymer compound eyes;^[18] equally significantly, our measurements in the WEL lattice correspond to entire populations of waveguides and not individual ommatidia as in the above case.

The FOV of the WEL lattice for the entire visible spectrum spans -47° to 47° with a 66% increase in the sampled angular range compared to an unstructured but otherwise identical film. The WEL model in Figure 2.1 possesses a FOV of 120° , as its organosiloxane waveguides possess a refractive index difference of 0.006 relative to

their surroundings. For our experiments, we selected the considerably more flexible, thermomechanically stable epoxide photopolymer, which has an index difference of 0.001 that still generates a significantly increased FOV but is also compatible with the widely employed epoxide photoresists and coatings.^[54]

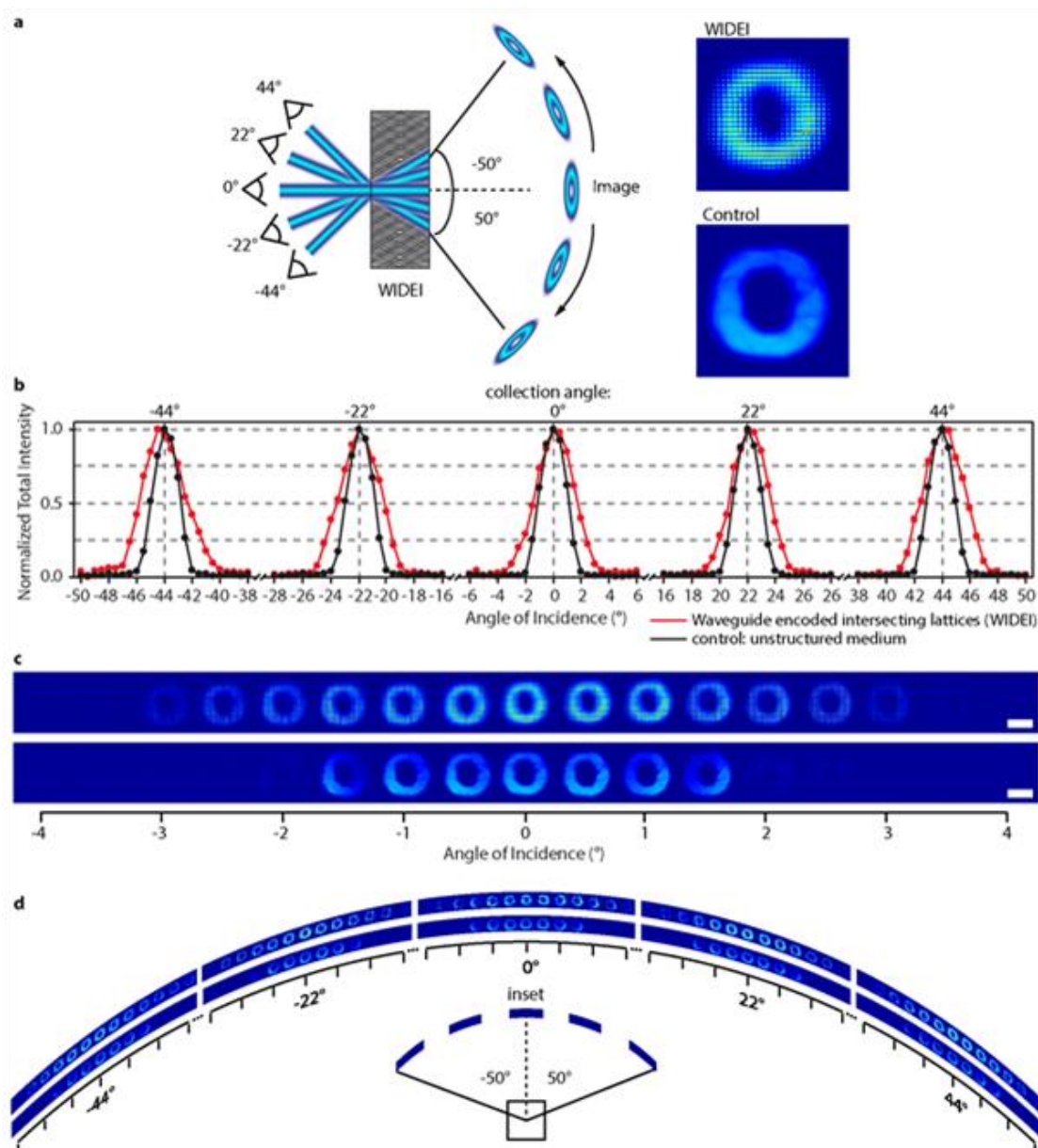


Figure 2.5. WEL exhibits enhanced field of view (FOV). a) Scheme of experimental setup to determine FOV: an object, which is a circular ring of incandescent light (the inset), was monotonically rotated about the WEL surface normal from -50° to 50° . The output of each waveguide lattice was imaged respectively at fixed angles of -44° , -22° , 0° , 22° , and 44° ; these correspond to the orientation of each waveguide array (-30° ,

-15° , 0° , 15° , and 30°) after refraction at the glass/air interface at the sample exit. b) 2D spatial intensity profiles of the exit of the central waveguide array (at 0°) acquired when the incidence angle of the object was varied from -6° to 6° . Identical measurements made for an unstructured medium without waveguides (control) are included. For clarity, intensity was normalized to the maximum intensity in each sequence of images. c) Plots of normalized total intensity of the image versus the angle of incidence of the object for the WEL (red) and an unstructured medium without waveguides (black). d) The complete sequence of images acquired by varying the incidence angle of the object from -50° to 50° into the WEL (top) and control (bottom). The inset is a scheme of the angular range (blue) over which images were acquire.

2.2.6. The WEL Lattice as a Versatile, Multifunctional Imaging Element

The intersecting arrangement of cylindrical waveguides enables the WEL lattice to perform imaging operations, which are not possible with hemispherical constructs. To demonstrate, we created a camera by placing a planar CCD chip flush with the WEL lattice exit. Three letters “M,” “A,” and “C” illuminated by incandescent light and positioned respectively at -44° , 0° , $+44^\circ$ relative to the normal, were launched into the lattice face (Figure 2.6a–c). Depending on the distance of its entrance face from the illuminated object, the WEL lattice can (i) simultaneously collect light from objects positioned over a hemispherical space and project the resulting images without loss of integrity onto a flat plane, (ii) focus images from the same hemispherical space onto a narrow area or (iii) invert the positions of images (Figure 2.6c). The spatial resolution for each of these operations is defined by the $\approx 80 \mu\text{m}$ width of each waveguide. In case (i), the planar chip simultaneously records images of all three letters; the images retain their clarity and are well-defined regardless of their angle of incidence at the WEL entrance face (Figure 2.6d). (Experiments with illuminated shapes produced equivalent results; see Section S2.9 in the Supporting Information.) For configurations (ii) and (iii), the relative angular orientations of letters were kept the same as in case (i) but their

distance from the lattice entrance face was increased. In case (ii), each letter propagated through waveguides with outputs that coincided within a narrow area at the lattice exit face; in this case, all three sets of waveguides delivered their respective “letters” and focused their intensity onto the same area of the detector. When the distance of the objects from the entrance face was increased even further (case (iii)), the letters propagated through waveguides, which intersected midway through the lattice so that their output faces now fell on the opposite side of the lattice normal; in this case, the letter “A” that propagated through 0° waveguides remained in the centre while the positions of “M” and “C” switched positions, resulting in image inversion. A phenomenological equation generalizing and describing the conditions required for each imaging operation of the WEL lattice is presented in Figure S2.30 in the Supporting Information.

We note that while refraction at the exit and entrance faces alone could change which gives rise to similar behavior in unstructured films, the WEL lattice waveguides ensure that the images retain their integrity and spatial definition. Images propagated through an unstructured, uniform medium would suffer considerable blurring, mixing, and loss of definition – especially due to the significant divergence associated with incandescent light.

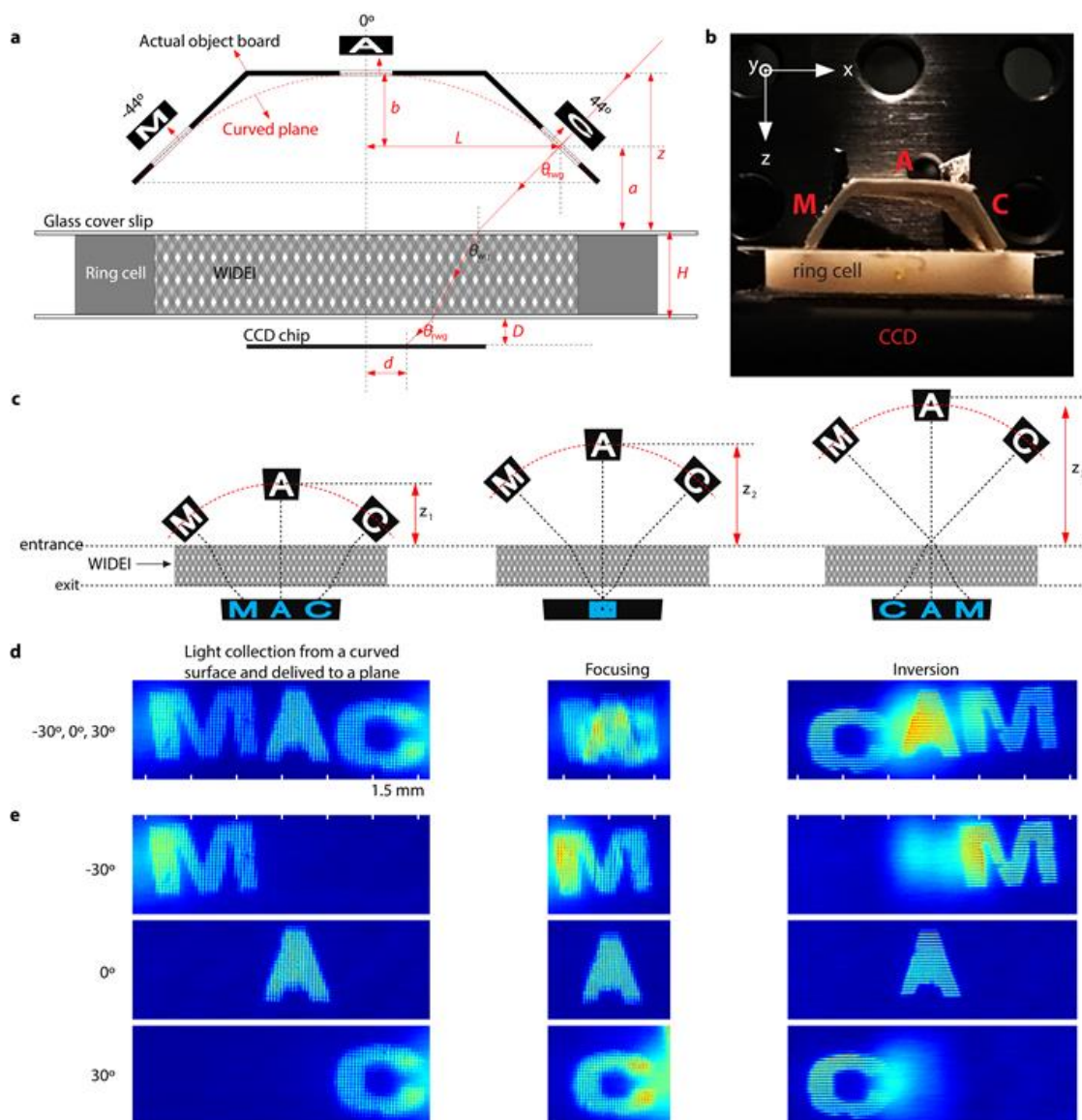


Figure 2.6. Multiple imaging configurations. a) Scheme and b) photograph of assembly to launch three illuminated objects “M,” “A,” and “C” positioned in a hemisphere with radius z into waveguide arrays oriented at 30° , 0° , and -30° , respectively, and imaged at the WEL lattice exit plane with a CCD chip. Propagation of “C” is traced in red as an example. c) Schemes of three imaging configurations achieved by varying z ($z_1 = 4.5$ mm, $z_2 = 7.5$ mm, $z_3 = 10.5$ mm). d) At z_1 , the letters propagate through waveguides that do not intersect and are projected adjacent to each other at the exit. At z_2 , the letters propagate through waveguides that intersect at the exit face and are focused onto the same area. At z_3 , the letters propagate in waveguides that intersect in the lattice and appear inverted at the exit face. e) Corresponding images of the three letters when launched individually in the respective waveguide arrays at z_1 , z_2 , and z_3 .

2.3. Conclusions and Outlook

The WEL lattice does not seek to solely mimic the visual configuration of arthropods but inspired by the collective behavior of ommatidial elements, combines a 66% enhancement in panoramic FOV, an infinite depth of field, excellent imaging resolution and range – and fundamentally different from hemi-spherical compound eyes - the powerful capacity to focus and invert images. Based entirely on waveguiding, the imaging operations of the WEL lattice are independent of the incidence angle of incoming light and – in contrast to lenses based on paraxial optics - free from aberration. Because its constituent waveguides, which are induced by incandescent light, are necessarily polychromatic and multimoded, the lattice can function at all visible wavelengths emitted by sources ranging from incandescent lamps, lasers to LEDs.

The intersecting, long-pathed waveguides of the WEL lattice, which are impossible to construct through conventional, divergence-limited photolithographic techniques, are induced by nondivergent, nonlinear incandescent waves and their solitonic interactions.^[36–39,42,43] This low-cost, room temperature technique requiring only incandescent sources and commercially available epoxide photoresists is adaptable to roll-to-roll manufacturing processes; the discrete translational symmetry of the WEL lattice ensures that its optical properties are retained over infinitely large areas. The planar geometry, transparency, flexibility, and scalability of the WEL lattices would allow seamless integration as intelligent conformal coatings and encapsulants that enhance and manipulate light-collection in solar panels, switchable windows and increase the FOV of endoscopic probes and other imaging systems such as microscopes and cameras. The WEL lattices also open meaningful and valuable opportunities as

smart slim films in phone cameras and smart screens, where enhancing imaging functionality, minimizing bulk, and optimizing flexibility are critical parameters for next-generation devices.^[18,19,55–57]

2.4. Experimental Section

Photopolymerizable Epoxide Sols: WEL lattices were fabricated from sols consisting of a mixture of 3,4-epoxycyclohexylmethyl-3,4-epoxycyclohexanecarboxylate (Sigma-Aldrich, Canada), epoxypropoxypropyl-terminated polydimethylsiloxane (Gelest, USA), polytetrahydrofuran (Sigma-Aldrich, Canada) in 50%, 26%, and 20%, respectively, by weight. The photoinitiator bis(4-tert-butylphenyl) iodonium hexafluoroantimonite (Hampford Research Inc., USA) and photosensitizer camphorquinone ($\lambda_{\text{max}} = 468 \text{ nm}$) were added in 2.5% and 1.5% by weight, respectively.^[33,58] The mixture was stirred vigorously for two days and filtered through a polytetrafluoroethylene membrane (0.2 μm pore size, Pall Corporation USA) before use. Sols were protected from exposure to ambient light at all times.

Optical Assembly for the Fabrication of the WEL Lattices: The assembly consisted of five QTH lamps (Cole-Parmer, USA), each of which emitted a broad beam of incandescent white light (400–800 nm) (Figure S2.3, Supporting Information). Each beam was collimated with a planoconvex lens (F. L. = 250 mm, $d = 25.4 \text{ mm}$) and passed through a 2D periodic amplitude mask ($\Lambda = 80 \mu\text{m}$) before being launched at angles -44° , -22° , 0° , 22° , and 44° with respect to the surface normal of a sample cell (diameter = 16 mm, path length = 3 mm) containing the photopolymerizable epoxide medium. Upon refraction at the air/sample interface, the beams propagated at angles of

-30° , -15° , 0° , 15° , and 30° within the epoxide medium (refractive index of $n = 1.51$). After transmission through the mask, each beam irradiated the entire entrance face of the sample cell ($z = 0.0$ mm) with an intensity of $12.93\text{--}16.91$ mW cm^{-2} . The spatial intensity profile at the exit face of the sample cell ($z = 3.0$ mm) was imaged through a pair of planoconvex lenses (F.L. = 250 mm, $d = 25.4$ mm) onto a high-resolution, progressive scan, charged-coupled device (CCD) camera (1360 (H) \times 1024 (V) of 4.65 μm square pixels; sensitivity range = 350–1150 nm; WinCamD digital camera, Data Ray Inc., USA) and monitored over time.

Structural Characterization of the WEL Lattices: Transmission optical images of WEL lattices were acquired with an Olympus BX51 microscope ($\times 10$ magnification) equipped with a digital CCD camera (Q Imaging, RETIGA EXi, Mono 12-bit, non-cooled). Transverse and longitudinal cross-sections were imaged; for the former, the WEL lattices were mounted on a goniometer stage, which was monotonically tilted until the orientation of each of the five waveguide lattices coincided with the optic axis of the microscope.

Optical Characterization of the WEL Lattices: Transmission of laser (633 nm) and incandescent white light (400–800 nm) in the WEL lattices was studied; here, the incidence angle of the probe beams was monotonically varied with a resolution of $\pm 0.5^\circ$ while the WEL lattices' output was projected onto a screen or imaged onto a CCD camera. To characterize the simultaneous propagation of multiple wavelengths in the WEL lattices, three laser beams at 633 nm He–Ne (Spectra-Physics), 488 nm (Coherent, Sapphire CDRH LP), and 532 nm (Verdi, V2) were simultaneously launched into the waveguide arrays oriented respectively at 0° , 15° , and 30° . The spatial intensity profile

at the WEL exit face was then projected onto a screen in the far-field (see Figure S2.17 in the Supporting Information).

Determining the Field of View (FOV) of the WEL Lattices: To calculate the FOV of the WEL lattice, first the angular acceptance range of each waveguide array was determined. Here, the incidence angle of the object “O” (a stenciled letter “O” illuminated with a collimated beam of incandescent light) was varied over an arch of 12° arch (i.e., $\pm 6^\circ$) centered about the propagation axis of each waveguide array. Measurements of the spatial intensity profile of the letter “O” at the exit face of the WEL lattices were acquired at intervals of 0.5° . In this way, the angular range was determined over which light could be coupled and efficiently guided through each of the five waveguide arrays. Angular ranges scanned were -50° to -38° ; -28° to -16° ; -6° to 6° ; 16° to 28° ; and 38° to 50° . The FOVs of the WEL lattices were defined as the collective angular acceptance ranges of the five waveguide arrays (see Figure S2.19 and S2.20 and Table S2.3 and S2.4 in the Supporting Information).

Characterizing Different Modes of Light Collection and Delivery to the WEL Lattices' Exit Plane: Simultaneous imaging of the transmission from several waveguide lattices in a WEL was carried out using a CCD chip (image area 8.8×6.6 mm, 1360 (H) \times 1024 (V) of $6.45 \mu\text{m}$ square pixels; sensitivity range = 350–1150 nm; WinCamD digital camera, Data Ray Inc., USA) positioned close (<1 mm) to the exit face of the sample cell. A neutral density filter (ND = 2) was placed between the sample and the chip in order to protect the latter from saturating intensities.

Simulations of Light Propagation: Simulation of light transmission in single waveguides, the unstructured control medium, and the WEL lattices employed the beam

propagation method (BPM),^[59–61] which was implemented through the BeamPROP software package (RSoft Products, Synopsys, USA). The alternating direction implicit scheme was employed for 3D simulations. Nonparaxial BPM using a Padé approximant was employed to accommodate wide-angle propagation and stronger variations in refractive index contrast ($\Delta n = 0.001–0.006$).^[60–64] The Padé order employed was (1, 1). The computational grid resolution was $\Delta(x, y, z) = (0.1, 1, 0.2)$ with units in μm . Simulations of single waveguides and the unstructured control medium shown in Figure 2.1 consisted of varying the beam propagation direction angle (see Section S2.1 in the Supporting Information). Each waveguide had a Gaussian index profile with peak index contrast of $\Delta n = 0.006$ and width of $80 \mu\text{m}$. For the WEL lattices, light propagation was simulated in a single plane consisting of five intersecting arrays of waveguides oriented at -30° , -15° , 0° , 15° , and 30° . Each waveguide had a Gaussian index profile with peak index contrast of $\Delta n = 0.001$ and width of $80 \mu\text{m}$. A single Gaussian beam was launched into each waveguide array at -30° , -15° , 0° , 15° and 30° (see Section S2.8 in the Supporting Information).

Acknowledgement

I.D.H. and H.L. contributed equally to this work. We are grateful to Prof. J. S. Preston for valuable discussions. Funding from the Natural Sciences and Engineering Research Council, Canadian Foundation for Innovation, and McMaster University is gratefully acknowledged.

References

- [1] J. D. Joannopoulos, P. R. Villeneuve, S. Fan, *Nature* **1997**, *386*, 143.
- [2] J. D. Joannopoulos, S. G. Johnson, J. N. Winn, R. D. Meade, *Photonic Crystals: Molding the Flow of Light (Second Edition)*, Princeton University Press, Princeton, NJ, USA **2008**.
- [3] D. R. Smith, J. B. Pendry, M. C. K. Wiltshire, *Science* **2004**, *305*, 788.
- [4] C. Genet, T. W. Ebbesen, *Nature* **2007**, *445*, 39.
- [5] F. J. Garcia-Vidal, J. B. Pendry, *Prog. Surf. Sci.* **1995**, *50*, 55.
- [6] D. Beaglehole, O. Hunderi, *Phys. Rev. B* **1970**, *2*, 309.
- [7] A. S. Schwanecke, A. Krasavin, D. M. Bagnall, A. Potts, a V Zayats, N. I. Zheludev, *Phys. Rev. Lett.* **2003**, *91*, 247404.
- [8] A. V. Rogacheva, V. A. Fedotov, A. S. Schwanecke, N. I. Zheludev, *Phys. Rev. Lett.* **2006**, *97*, 177401.
- [9] M. Pelton, J. Aizpurua, G. Bryant, *Laser Photonics Rev.* **2008**, *2*, 136.
- [10] A. D. Boardman, A. V. Zayats, *Handb. Surf. Sci.* **2014**, *4*, 329.
- [11] W. L. Barnes, A. Dereux, T. W. Ebbesen, *Nature* **2003**, *424*, 824.
- [12] D. Cialla, A. März, R. Böhme, F. Theil, K. Weber, M. Schmitt, J. Popp, *Anal. Bioanal. Chem.* **2012**, *403*, 27.
- [13] J. Zhang, K. Kasala, A. Rewari, K. Saravanamuttu, *J. Am. Chem. Soc.* **2006**, *128*, 406.
- [14] M. Mitchell, M. Segev, *Nature* **1997**, *387*, 880.
- [15] D. E. Nilsson, A. Kelber, *Arthropod Struct. Dev.* **2007**, *36*, 373.
- [16] D. Keum, H. Jung, K. H. Jeong, *Small* **2012**, *8*, 2169.
- [17] W. Patten, *J. Morphol.* **1887**, *1*, 67.
- [18] L. P. Lee, R. Szema, *Science* **2005**, *310*, 1148.
- [19] Compound eyes for industry and smartphone, <https://phys.org/news/2017-01-compound-eyes-industry-smartphone.html>, April, **2017**.
- [20] K. Hamanaka, H. Koshi, *Opt. Rev.* **1996**, *3*, 264.
- [21] J. Duparré P. Dannberg, P. Schreiber, A. Bräuer, A. Tünnermann, *Appl. Opt.* **2005**, *44*, 2949.
- [22] J. W. Duparre, P. Schreiber, P. Dannberg, T. Scharf, P. Pelli, R. Voelkel, H.-P. Herzig, A. Braeuer, In *Proc. SPIE*, Vol. 5346, MOEMS and Miniaturized Systems IV, San Jose, USA **2004**, p. 89.
- [23] S. Ogata, J. Ishida, T. Sasano, *Opt. Eng.* **1994**, *33*, 3649.
- [24] A. Brueckner, J. Duparré R. Leitel, P. Dannberg, A. Bräuer, A. Tünnermann, *Opt. Express* **2010**, *18*, 24379.
- [25] D. Floreano, R. Pericet-Camara, S. Viollet, F. Ruffier, A. Brückner, R. Leitel, W. Buss, M. Menouni, F. Expert, R. Juston, M. K. Dobrzynski, G. L'Eplattenier, F. Recktenwald, H. a Mallot, N. Franceschini, *Proc. Natl. Acad. Sci. U. S. A.* **2013**, *110*, 9267.
- [26] L. Li, A. Y. Yi, *Opt. Express* **2010**, *18*, 18125.

- [27] D. Wu, J.-N. Wang, L.-G. Niu, X. L. Zhang, S. Z. Wu, Q.-D. Chen, L. P. Lee, H. B. Sun, *Adv. Opt. Mater.* **2014**, *2*, 751.
- [28] D. Radtke, J. Duparré U. D. Zeitner, A. Tünnermann, *Opt. Express* **2007**, *15*, 3067.
- [29] P. Qu, F. Chen, H. Liu, Q. Yang, J. Lu, J. Si, Y. Wang, X. Hou, *Opt. Express* **2012**, *20*, 5775.
- [30] K.-H. Jeong, J. Kim, L. P. Lee, *Science* **2006**, *312*, 557.
- [31] Y. M. Song, Y. Xie, V. Malyarchuk, J. Xiao, I. Jung, K. J. Choi, Z. Liu, H. Park, C. Lu, R. H. Kim, R. Li, K. B. Crozier, Y. Huang, J. A. Rogers, *Nature* **2013**, *497*, 95.
- [32] D. K. Baskar, M. A. Brook, K. Saravanamuttu, *J. Phys. Chem. C* **2015**, *119*, 20606.
- [33] Z. Nie, E. Kumacheva, *Nat. Mater.* **2008**, *7*, 277.
- [34] C. A. Mack, *Fundamental Principles of Optical Lithography: the Science of Microfabrication (Reprint)*, John Wiley & Sons Ltd, Hoboken, NJ, USA **2012**.
- [35] K. Kasala, K. Saravanamuttu, *J. Mater. Chem.* **2012**, *22*, 12281.
- [36] I. D. Hosein, H. Lin, M. R. Ponte, D. K. Baskar, K. Saravanamuttu, In *Proc. SPIE*, Vol. 8983, Organic photonic materials and devices XVI, San Francisco, USA **2014**, p. 89830E.
- [37] I. B. Burgess, M. R. Ponte, K. Saravanamuttu, *J. Mater. Chem.* **2008**, *18*, 4133.
- [38] M. R. Ponte, R. Welch, K. Saravanamuttu, *Opt. Express* **2013**, *21*, 4205.
- [39] K. Saravanamuttu, X. M. Du, S. I. Najafi, M. P. Andrews, *Can. J. Chem.* **1998**, *76*, 1717.
- [40] A. B. Villafranca, K. Saravanamuttu, *J. Phys. Chem. C* **2008**, *112*, 17388.
- [41] A. J. Jacobsen, W. Barvosa-Carter, S. Nutt, *Adv. Mater.* **2007**, *19*, 3892.
- [42] A. J. Jacobsen, W. Barvosa-Carter (HRL Laboratories, LLC) *US. 008197930 B1*, **2012**.
- [43] A. Pimpin, W. Srituravanich, *Eng. J.* **2012**, *16*, 37.
- [44] A. J. Turberfield, *Nature* **2000**, *404*, 53.
- [45] X. Wang, J. F. Xu, H. M. Su, Z. H. Zeng, Y. L. Chen, H. Z. Wang, Y. K. Pang, W. Y. Tam, *Appl. Phys. Lett.* **2003**, *82*, 2212.
- [46] S. Trillo, W. E. Torruellas, *Spatial Solitons*, Vol. 82 (Eds. S. Trillo, W. Torruellas), Springer, Heidelberg, Berlin, Germany **2001**, p. 87.
- [47] H. Buljan, M. Segev, M. Soljacić, N. K. Efremidis, D. N. Christodoulides, *Opt. Lett.* **2003**, *28*, 1239.
- [48] J. Zhang, K. Saravanamuttu, *J. Am. Chem. Soc.* **2006**, *128*, 14913.
- [49] Y. Li, S. Krinsky, J. W. Lewellen, K.-J. Kim, V. Sajaev, S. V. Milton, *Phys. Rev. Lett.* **2003**, *91*, 243602.
- [50] M. F. Shih, M. Segev, *Opt. Lett.* **1996**, *21*, 1538.
- [51] A. W. Snyder, *Science* **1997**, *276*, 1538.
- [52] G. I. Stegeman, M. Segev, *Science* **1999**, *286*, 1518.
- [53] C. Wang, S.-J. Cho, N.-Y. Kim, *Mater. Manuf. Process.* **2013**, *28*, 947.
- [54] An insect's eye inspires a new camera for smartphones, <https://www.economist.com/news/science-and-technology/21718859-series-eye-lets-can-make-cameras-much-smaller-insects-eye-inspires-new>, accessed: April,

2017.

- [55] Digital still cameras: the changing face of imaging, <https://www.photonics.com/EDU/Handbook.aspx?AID=25131>, accessed: April, **2017**.
- [56] C. Yuan, S. J. Daly (Sharp Laboratories Of America, Inc.) *US. 20090245696 A1*, **2009**.
- [57] J. V. Crivello, *J. Polym. Sci. Part A Polym. Chem.* **2009**, *47*, 866.
- [58] M. D. Feit, J. A. Fleck, *Appl. Opt.* **1978**, *17*, 3990.
- [59] D. Yevick, *Opt. Quantum Electron.* **1994**, *26*, S185.
- [60] R. Scarmozzino, A. Gopinath, R. Pregla, S. Helfert, *IEEE J. Sel. Top. Quantum Electron.* **2000**, *6*, 150.
- [61] G. R. Hadley, *Opt. Lett.* **1992**, *17*, 1426.
- [62] I. Ilic, R. Scarmozzino, R. M. Osgood, *J. Light. Technol.* **1996**, *14*, 2813.
- [63] H. J. W. M. Hoekstra, G. J. M. Krijnen, P. V. Lambeck, *Opt. Commun.* **1993**, *97*, 301.

Supporting Information

Table of Contents

S2.1 Simulations of light propagation in cylindrical waveguides with different orientations	72
S2.2 Calculation of the number of modes in a waveguide	74
S2.3 Fabrication of WEL lattices and analysis of evolution dynamics of WEL lattice.....	75
S2.4 Calculation of lattice spacing, waveguide density and collisions between non-parallel waveguides	78
S2.5 Characterization of WEL lattice microstructure.....	82
S2.6 Simulations of angle-dependent light coupling between a waveguide pair and beam propagation simulations in WEL lattice	85
S2.7 Optical characterization of light collection and transmission, and determination of the field of view of WEL lattices	88
S2.8 Calculation of refractive index of the epoxide medium and determination of the photo-induced change in refractive index in self-induced waveguides	96
S2.9 Study of the multifunctional imaging performances of the WEL lattice.....	97
References	98

S2.1 Simulations of light propagation in cylindrical waveguides with different orientations

The Beam Propagation Method (BPM) was employed for 2-D simulations of a Gaussian beam ($\lambda = 633$ nm) propagating in a cylindrical waveguide. The waveguide was 80 μm -wide and 3 mm long with a Gaussian profile in refractive index, maximizing at $n = 1.476$ and embedded in a medium with $n = 1.470$. (These parameters were based on self-induced waveguides generated in previous experiments^[1]). To calculate its angular acceptance range, the beam was launched into the waveguide at angles ranging from -11° and 11° with a resolution of 1° with respect to the waveguide axis. The optical power at the waveguide exit at a propagation distance (z) of 3.00 mm was determined at each angle. Figure S2.1 contains BPM simulations in the waveguide at launch angles ranging from 0° to 11° . Figure S2.2 contains corresponding transverse cross-sections of intensity profiles at the waveguide exit.

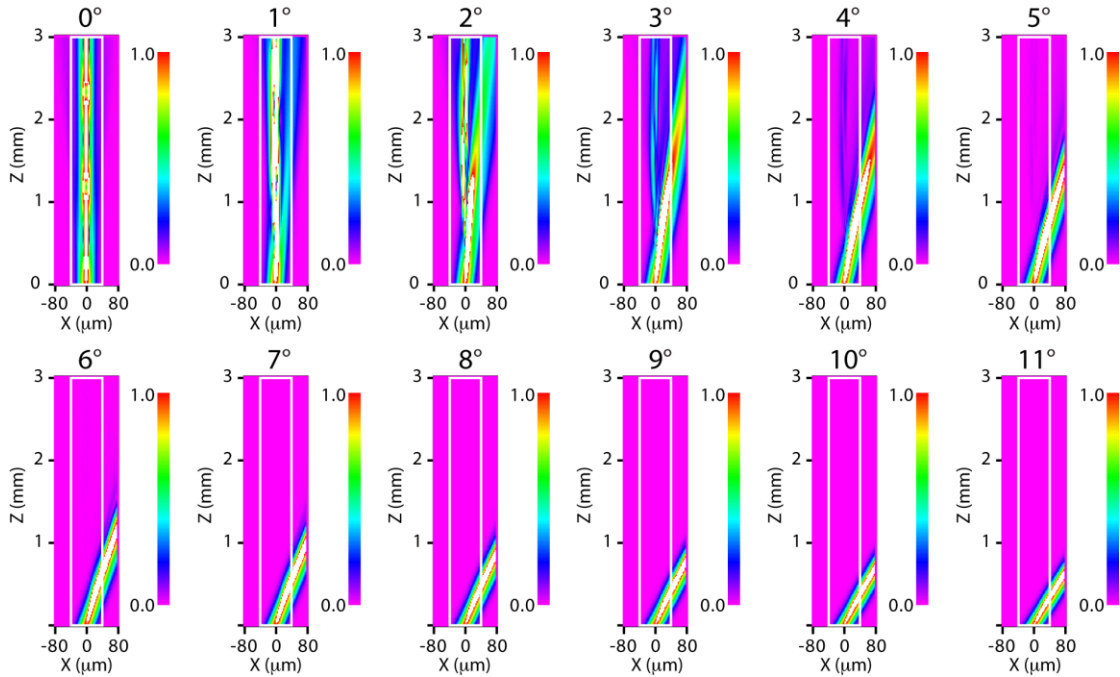


Figure S2.1. BPM simulations in a graded index cylindrical waveguide ($n = 1.47$, $\Delta n = 0.006$) at launch angles from 0° to 11° . The contour maps represent the xz plane; the waveguide boundaries are traced in white.

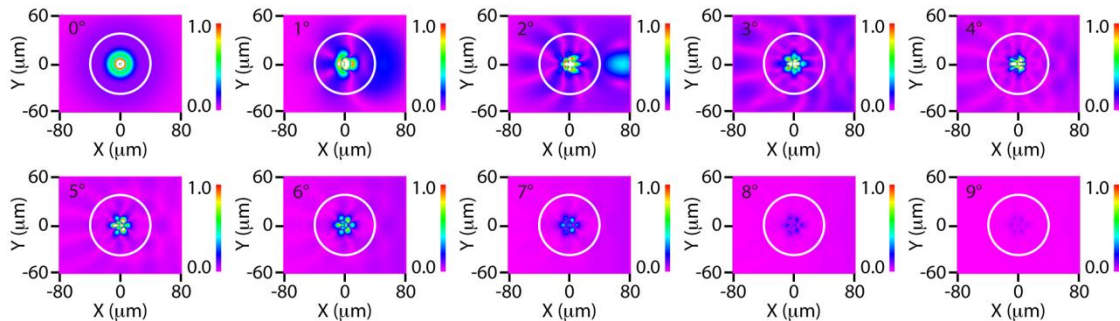


Figure S2.2. BPM simulations in a graded index cylindrical waveguide ($n = 1.47$, $\Delta n = 0.006$) at launch angles from 0° to 9° . The contour maps represent the xy plane at a propagation distance of 3 mm; waveguide boundaries are traced in white.

In Figure S2.1 and S2.2, the waveguide was parallel (oriented at 0°) to the normal of the entrance face. We then calculated angular acceptance ranges for the same waveguide oriented at different angles ($\alpha = -30^\circ, -15^\circ, 15^\circ, 30^\circ$) with respect to the entrance face normal. Because the waveguides are identical in terms of diameter and refractive index profile, their absolute range of angular acceptance remains almost the

same. To calculate the corresponding incident angles, results obtained for the 0° waveguide from the -11° to 11° range were shifted by α and corrected with Snell's law to account for refraction at the air/medium interface.

S2.2 Calculation of the number of modes in a waveguide

The number of modes in a graded index waveguide (*i.e.*, fibre of cylindrical symmetry) is half the number of modes in a step-index waveguide with the same index difference^[2] and can be approximated through:

$$N = \frac{\left(\text{Diameter of core} \times NA \times \frac{\pi}{\lambda}\right)}{4} \quad \text{[S2.1]}$$

where NA is the numerical aperture of the waveguide and λ , the wavelength of incident light. The NA can be calculated as follows^[3],

$$NA = \sqrt{n_o^2 - n_c^2} \quad \text{[S2.2]}$$

Where the refractive index of the core (polymerized waveguide) $n_o = 1.476$ and that of the cladding (unpolymerized region) $n_{\text{clad}} = 1.470$ giving $NA \approx 0.1330$. According to Equation [S2.1], this yields $N \approx 13$.

S2.3 Fabrication of WELs and analysis of evolution dynamics of WELs

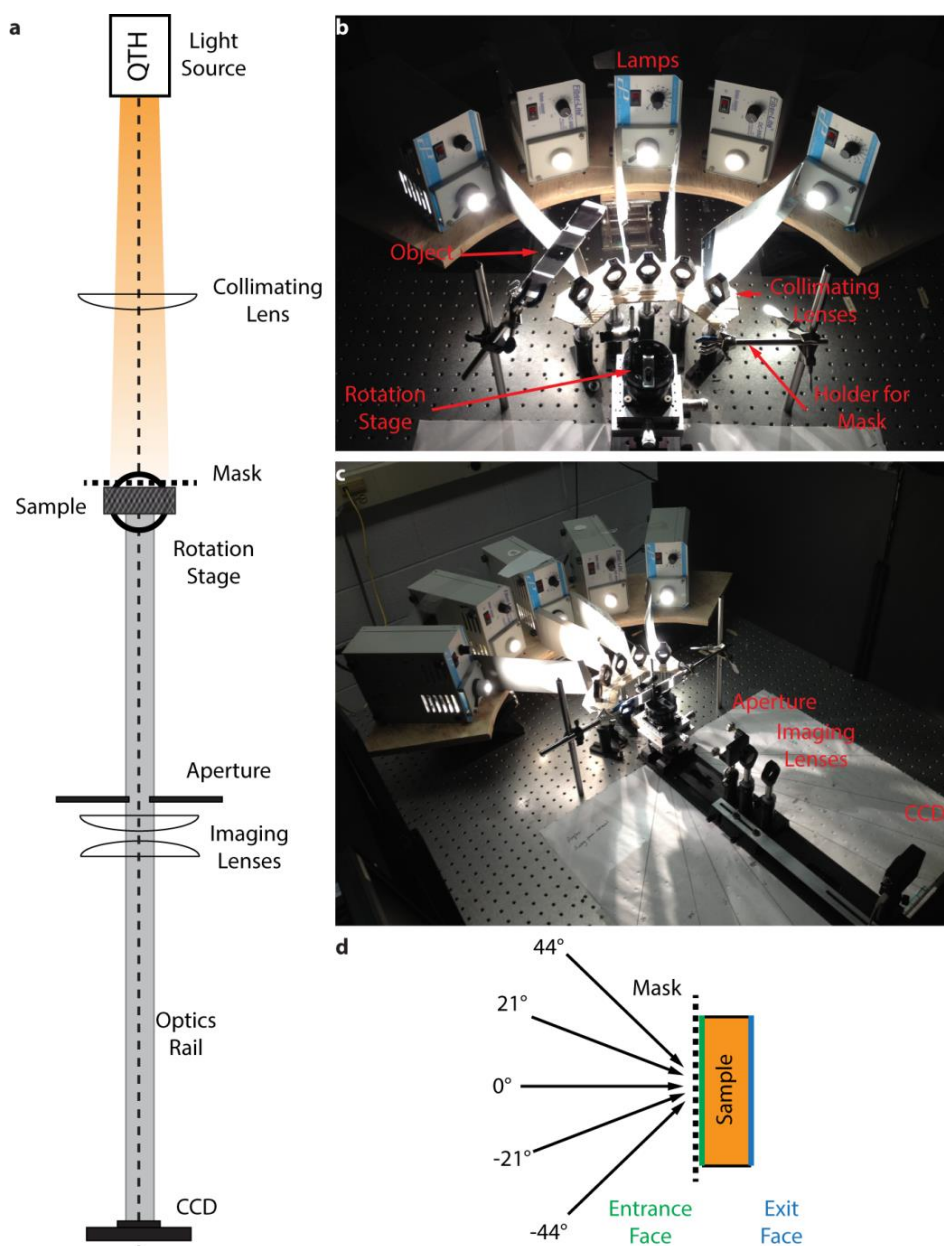


Figure S2.3. Optical assembly for the fabrication of WELs (a) Scheme of assembly along the beam oriented at 0° ; four beams (not shown) are arranged pairwise on either side of the optic axis at angles of -44° , -22° , 22° , 44° . (b) and (c) Photographs of assembly showing the five quartz tungsten halogen (QTH) lamps and optical components. (d) Scheme of configuration employed to fabricate the WEL.

During WEL formation, the initially uniform intensity profile of the optical field becomes spatially localized and confined within the emerging waveguides. We

quantified the efficiency of light confinement through the concentration factor (CF). The latter was calculated by first binarizing the spatial intensity profiles at the sample exit face at a given point in time:

$$g(pixel) = \begin{cases} 1 & I \geq I_{HM_{average}} \\ 0 & I < I_{HM_{average}} \end{cases} \quad [S2.3]$$

In [S2.3], all pixels with intensities greater than the average half maximum ($HM_{average}$) were assigned a value of 1; all other pixels were assigned 0. $I_{HM_{average}}$ is midway between the average maximum pixel intensity ($I_{max_{average}}$) and average minimum pixel intensity ($I_{min_{average}}$). For each pixel, $I_{max_{average}}$ and $I_{min_{average}}$ were determined by averaging the local maxima and minima in the image over approximately 22×20 waveguides. CF was calculated by:

$$CF = 1 - \frac{\sum_{pixels} g(pixel)}{\sum_{pixels} 1} \quad [S2.4]$$

According to [S2.4], a uniform distribution of intensity at the sample exit face gives $CF = 0$ while the confinement of all intensity to a single pixel gives $CF = 1$. In other words, the greater the value of CF, the more efficiently light is confined.

The temporal plot in Figure S2.4 shows the increase in CF that accompanies WEL formation as light becomes tightly confined within a periodic array of waveguides. The plot of intensity integrated over the same area remains relatively constant throughout the same experiment (Figure S2.5), indicating that there is negligible intensity loss or attenuation of light during lattice formation.

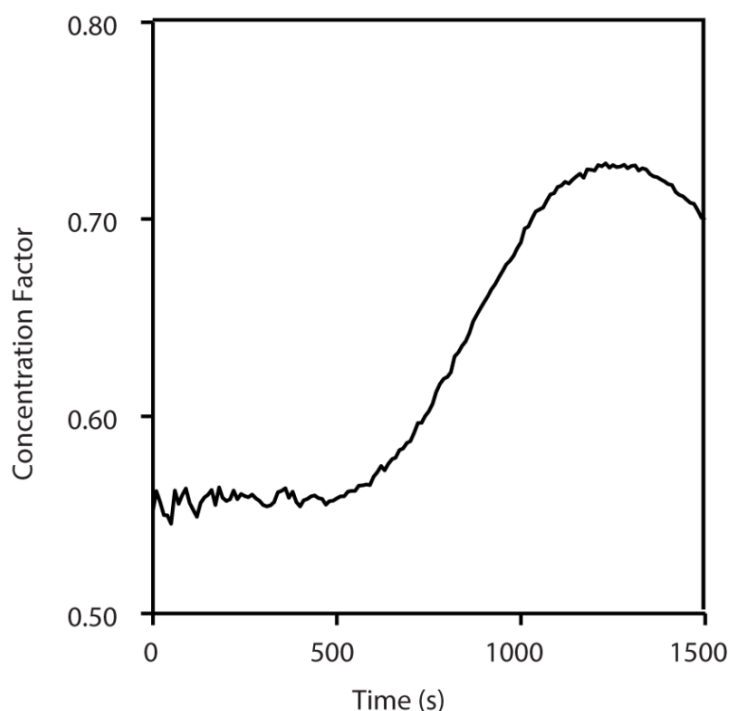


Figure S2.4. Temporal evolution of the intensity concentration factor (CF) during the formation of a single waveguide array (oriented at 0° with respect to the surface normal). CF was calculated for $\sim 22 \times \sim 20$ waveguides over an area of $1780 \times 1638 \mu\text{m}^2$.

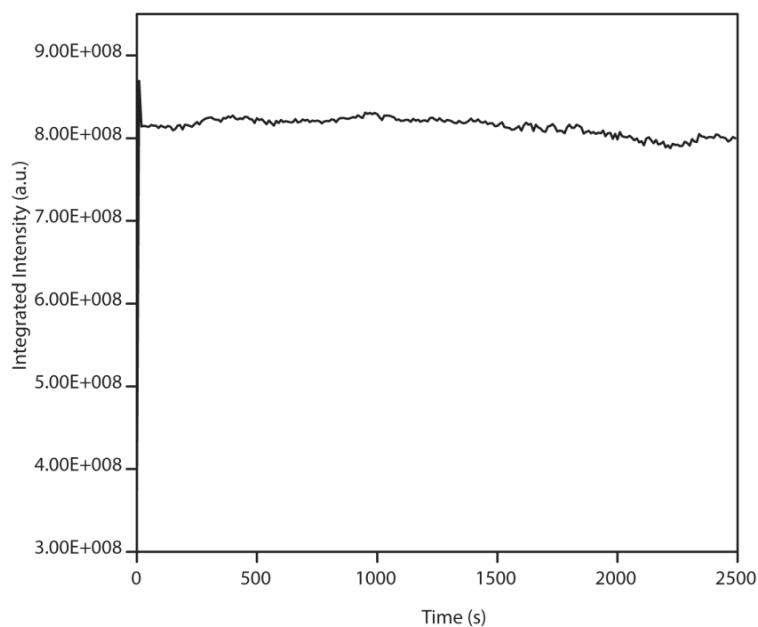


Figure S2.5. Temporal evolution of optical intensity integrated over an area of $1780 \times 1638 \mu\text{m}^2$ acquired at the exit face of the sample during the formation of a single waveguide lattice.

S2.4 Calculation of lattice spacing, waveguide density and collisions between non-parallel waveguides

The spacing between waveguides in each of the five arrays in the WEL lattice was determined from their respective output intensity profiles. The apparent decrease in waveguide spacing in arrays induced at angles other than 0° was caused by refraction at the air/sample interface (Figure S2.6). To correct for this, the waveguide spacing determined from output profiles were multiplied by $\cos(\alpha)/\cos(\theta_{\text{imaging}})$, where α is the waveguide orientation and θ_{imaging} , the angle of imaging with respect to the surface normal of the WELs. Corrected waveguide spacing (along x axis) for arrays oriented along 15° and 30° were $77.27 \mu\text{m}$ and $69.34 \mu\text{m}$, respectively. The density of waveguides in the 0° , 15° , and 30° arrays of the WEL lattice was 156 , 167 , and 208 mm^{-2} , respectively.

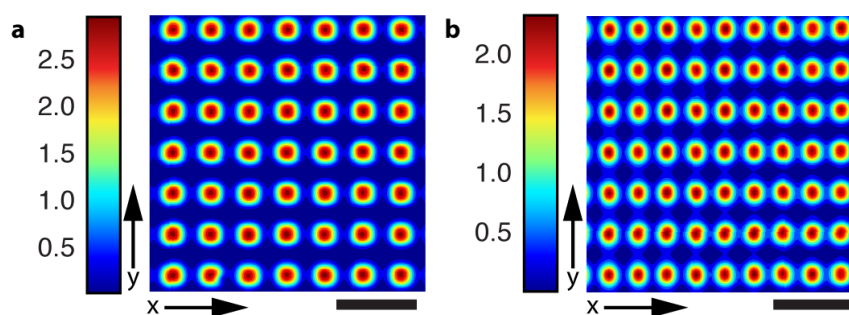


Figure S2.6. Spatial intensity profiles of waveguided white light at the exit face of the waveguide array oriented at (a) $+15^\circ$ and (b) $+30^\circ$ in the WEL lattice. Scale bars = $160 \mu\text{m}$.

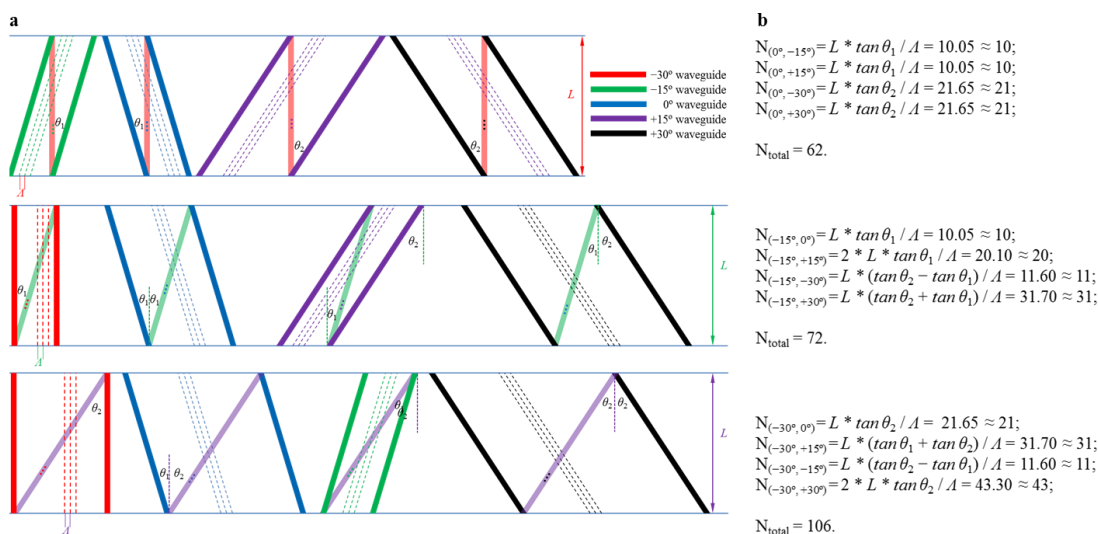


Figure S2.7. Collision situations: (a) Schematic diagram of the collision behaviors of a single 0° , -15° , and -30° waveguide with non-parallel waveguides; (b) Calculation of the collision times of the three collision situations in (a).

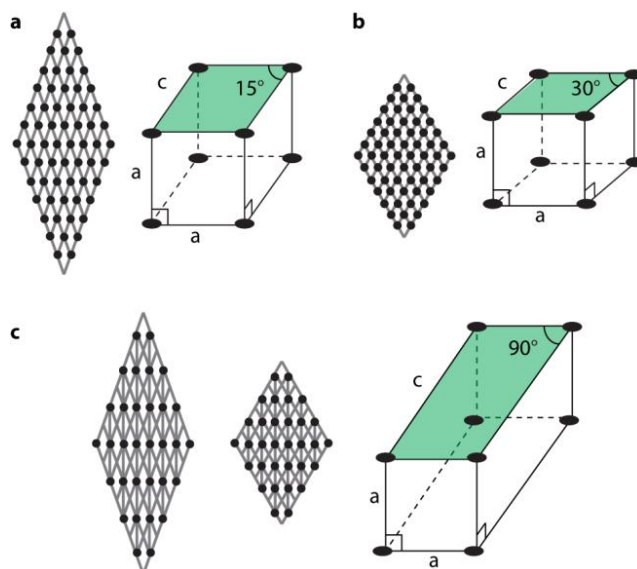


Figure S2.8. Bravais lattices formed by intersecting waveguides, based on the number of waveguides and their orientations. Lines are used to model the lattices for the lattice plane on which they intersect and black dots indicating the 2D Bravais lattice, as shown in the image(s) on the left of each panel. The 3D unit cell lattice consists of stacks of these 2D lattices perpendicular to its plane (highlighted green), as shown in the image on the right of each panel for a 3D unit cell. All lattice orientations are with respect to the vertical of the page. (a) Two lattices oriented at -15° and 15° . The 2D lattice has pl symmetry, and the 3D lattice unit cell is primitive monoclinic. (b) Two lattices oriented at -30° and 30° . The 2D lattice has pm symmetry, and the 3D lattice unit cell is hexagonal. (c) Two lattices oriented 0 plus any other symmetric combination of beams, e.g., -15° and 15° ; or -30° and 30° ; or -30° , -15° ; 15° ; 30° . Specifically, two 3 beam combinations are shown: -15° , 0° , 15° and -30° , 0° , 30° .

The 2D lattice has pmm symmetry, and the 3D lattice unit cell is primitive tetragonal. The length c depends on the orientation of the beams.

Table S2.1 Lattice constants of single waveguide lattices

Waveguide Lattice	Measured (μm)	Calculated ^a (μm)
0°	80.0	80.0
15°	76.2	74.7
30°	56.0	57.5

^a Determined by the cosine of the beam angle of incidence.

Table S2.2 Lattice parameters of 3D lattices

Waveguide Lattice	Unit Cell	Symmetry	Lattice Parameters
-15° & 15°	Monoclinic	pl	$a = 80 \mu\text{m}$, $c = 149.3 \mu\text{m}$, $\beta = 30^\circ$
-30° & 30°	Monoclinic	$P6m$	$a = 80 \mu\text{m}$, $c = 80 \mu\text{m}$, $\beta = 60^\circ$
-15° , 0° & 15°	Tetragonal	pmm	$a = 80 \mu\text{m}$, $c = 292.8 \mu\text{m}$
-30° , 0° & 30°	Tetragonal	pmm	$a = 80 \mu\text{m}$, $c = 80 \mu\text{m}$
-30° , -15° , 0° , 15° & 30°	Tetragonal	pmm	$a = 80 \mu\text{m}$, $c = 301.3 \mu\text{m}$

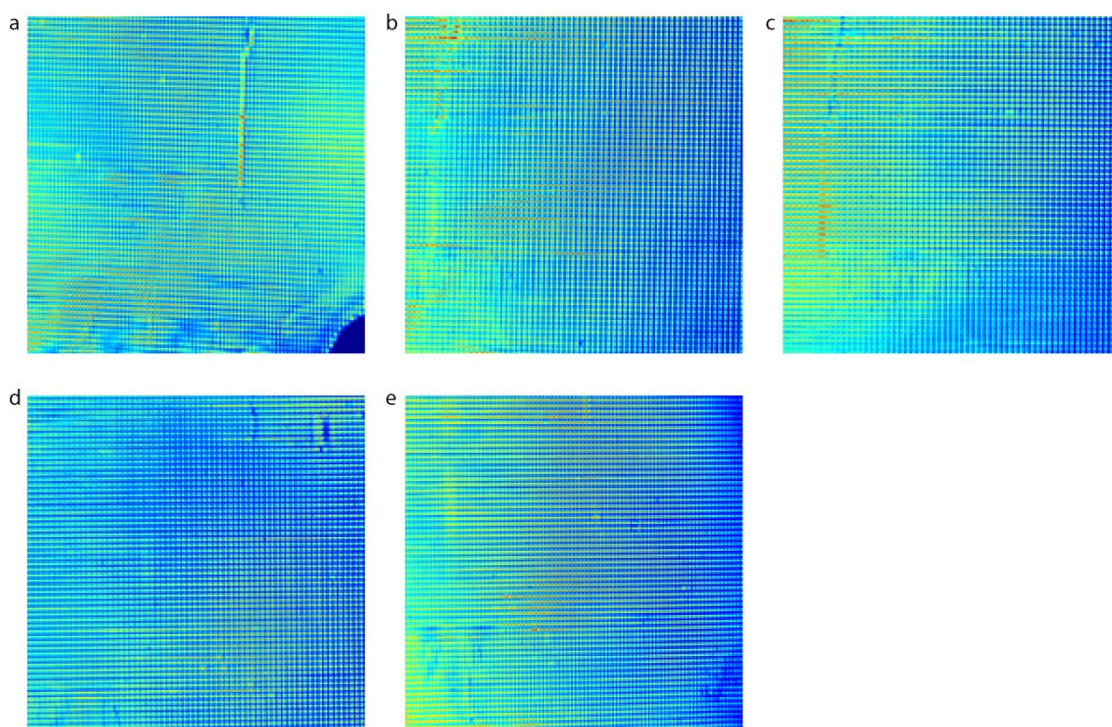


Figure S2.9. Large scale lattices: spatial intensity profiles of white light acquired at the exit face of (a) WEL-1_{-30°} (b) WEL-1_{-15°} (c) WEL-1_{0°} (d) WEL-1_{15°} and (e) WEL-1_{30°}. To account for refraction at the air/sample interface, the probe beam was launched and the lattice exit face was imaged at -44° , -22° , 0° , 22° , and 44° , respectively relative to the normal of the sample entrance face. In all images, scale bar = 1 mm.

S2.5 Characterization of WEL lattice microstructure

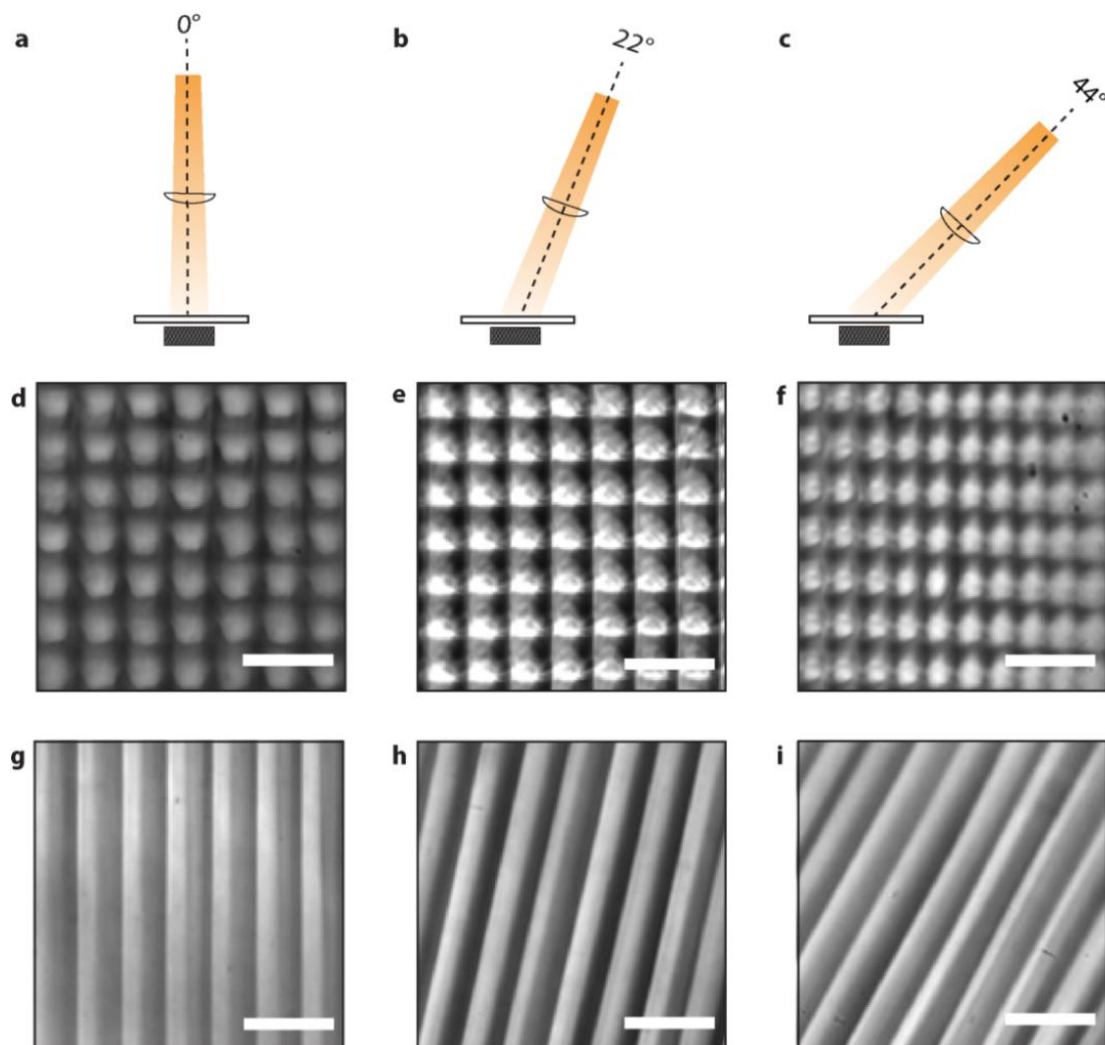


Figure S2.10. Waveguide arrays generated with a single beam (WEL-1) oriented respectively at (a) 0° , (b) 22° and (c) 44° and (d)-(f) optical micrographs of the exit face of each lattice, imaged at 0° , 22° , and 44° , respectively, relative to the microscope optical axis. (g)-(i) Corresponding Top-down micrographs of the WEL-1 lattices in (d)-(f). In all images, scale bar = $160\ \mu\text{m}$.

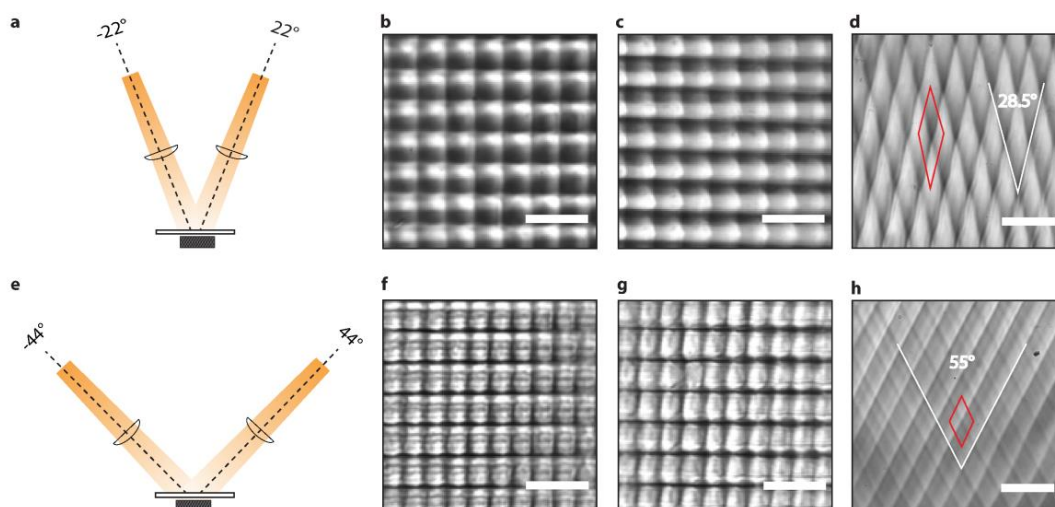


Figure S2.11. Lattices consisting of an intersecting pair of waveguide arrays (WEL-2) generated with (a) two incandescent beams with incident angles of -22° and 22° , relative to the surface normal. (b)-(c) Optical micrographs of the exit face of WEL-2 imaged at -22° and 22° , respectively, relative to the microscope optical axis. (d) Top-down micrograph showing that the pair of waveguide arrays intersects at an angle of $\sim 29^\circ$ in the medium. (e) WEL-2 generated with beams incident at angles of -44° and 44° relative to the surface normal. (f)-(g) Optical micrographs of the exit face of the resulting lattice imaged at -44° and 44° , respectively, relative to the microscope optical axis. (h) Top-down micrograph showing that the pair of waveguide arrays intersects at an angle of $\sim 55^\circ$ in the medium. The red rhombus in (d) and (h) indicates the unit cell of the lattice in this plane. In all images, scale bar = $160 \mu\text{m}$.

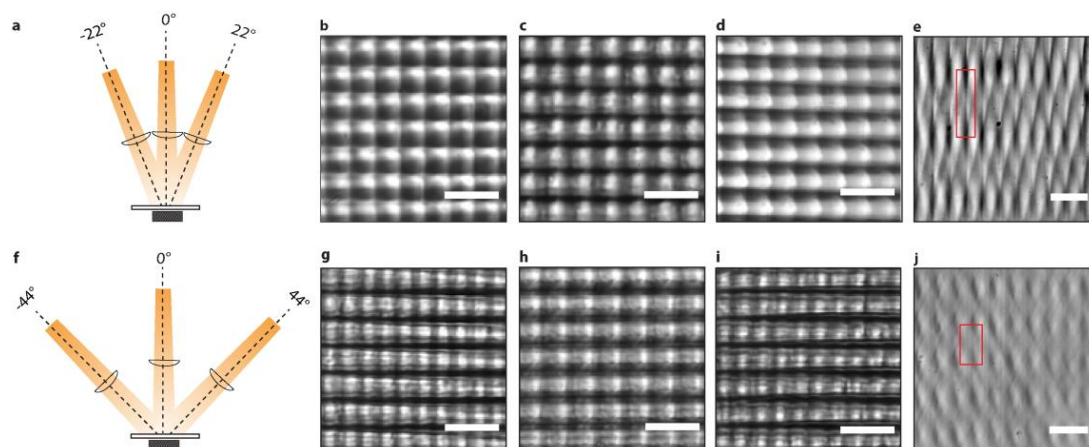


Figure S2.12. Lattices consisting of three intersecting waveguide arrays (WEL-3) generated with (a) three incandescent beams incident at angles of -22° , 0° and 22° respectively, relative to the surface normal. (b)-(d) Optical micrographs of the exit face of WEL-3 imaged -22° , 0° and 22° , respectively, relative to the microscope optical axis. (e) Top-down micrograph showing the intersections of the three waveguide arrays. (f) WEL-3 generated with beams at incident angles of -44° , 0° and 44° , relative to the surface normal. (g)-(i) Optical micrographs of the exit face of

WEL-3 imaged at -44° , 0° and 44° , respectively relative to the microscope optical axis. (j) Top-down micrograph showing the intersections of the three waveguide arrays. The red rhombus in (e) and (j) indicates the unit cell face in this plane. In all images, scale bar = $160\ \mu\text{m}$.

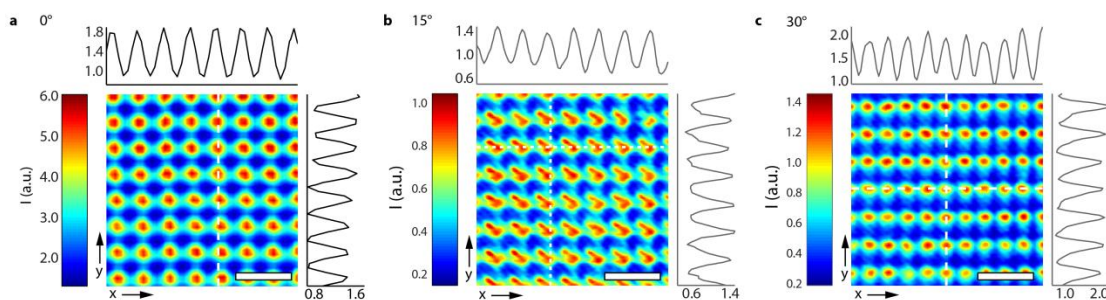


Figure S2.13. Spatial intensity profiles acquired at the exit face of (a) WEL-1 $_{0^\circ}$, (b) WEL-1 $_{15^\circ}$ and (c) WEL-1 $_{30^\circ}$, where the probe beam was launched at 0° , 22° and 44° respectively, relative to the normal of the sample entrance face. Horizontal and vertical line-scans (indicated by dotted white lines) and a color intensity scale are included. In all images, scale bar = $160\ \mu\text{m}$.

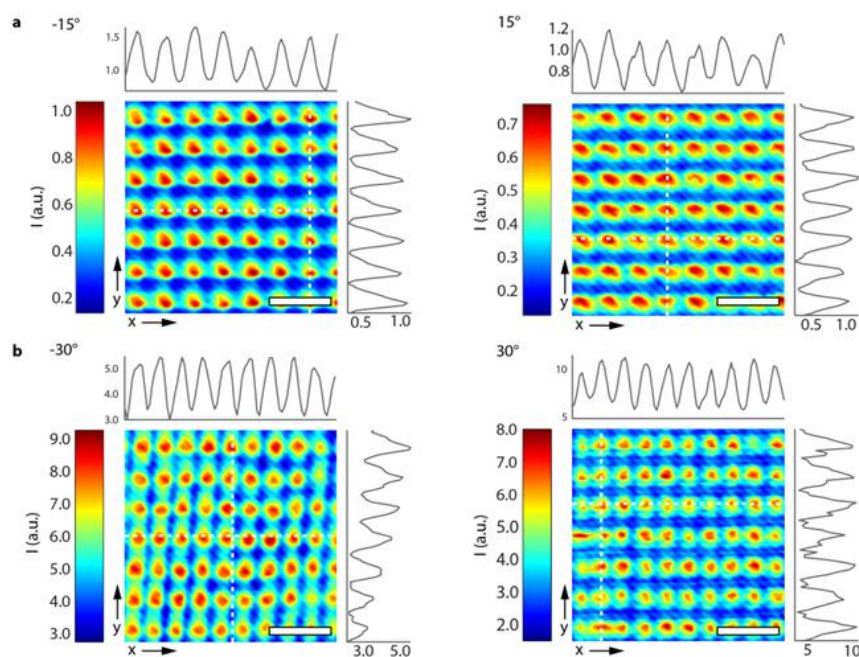


Figure S2.14. Spatial intensity profiles of transmitted white light acquired at the exit face of (a) WEL-2 $_{(-15^\circ, 15^\circ)}$ and (b) WEL-2 $_{(-30^\circ, 30^\circ)}$. In (a), the probe beams were launched at angles of -22° and 22° , respectively whereas in (b), probe beams were launched at -44° and 44° , respectively relative to the normal of the sample entrance face. Horizontal and vertical line-scans (indicated by dotted white lines) and a color intensity scale are included. In all images, scale bar = $160\ \mu\text{m}$.

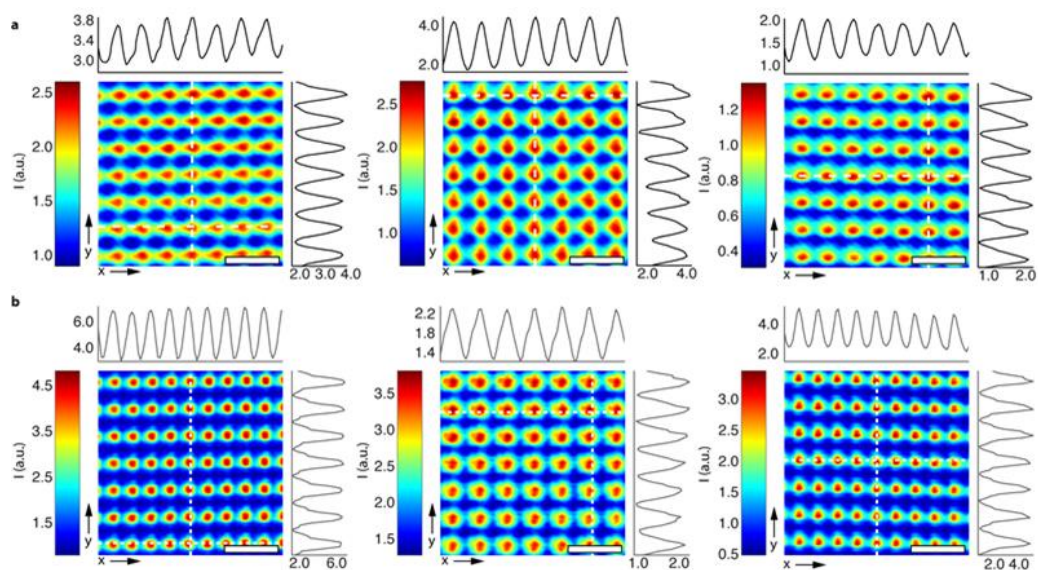


Figure S2.15. Spatial intensity profiles of transmitted white light acquired at the exit face of (a) WEL-3_(-15°; 0°; 15°) and (b) WEL-3_(-30°; 0°; 30°). In (a), the probe beams were launched at angles of -22° , 0° and 22° , respectively whereas in (b) probe beams were launched at -44° , 0° and 44° , respectively relative to the normal of the sample entrance face. Horizontal and vertical line-scans (indicated by dotted white lines) and a color intensity scale are included. In all images, scale bar = $160\ \mu\text{m}$.

S2.6 Simulations of angle-dependent light coupling between a waveguide pair and beam propagation simulations in WEL lattice

Simulations were carried out with a computational cell of two identical, gradient index waveguides ($n = 1.51$; $\Delta n = 0.001$) (See supplementary section S2.8 for details). The waveguides were each $1000\ \mu\text{m}$ long and intersected at mid-length. An $80\ \mu\text{m}$ -wide ($1/e^2$) Gaussian beam was launched into one waveguide and the optical power at the end of the other was computed; computations were carried out for waveguide intersection angles ranging from 0° to 15° .

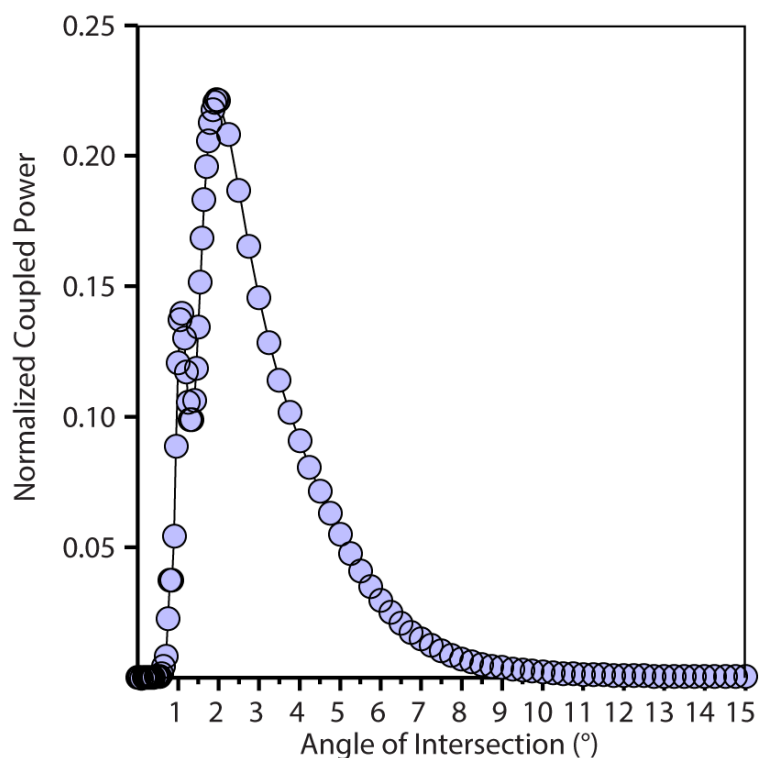


Figure S2.16. Normalized power coupled from one waveguide to another as a function of their intersection angle.

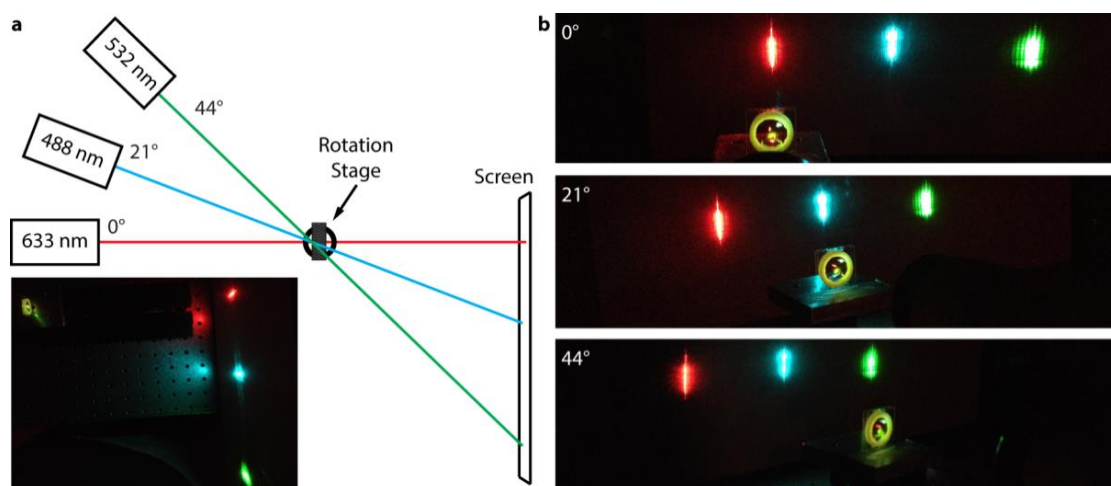


Figure S2.17. Simultaneous and independent transmission of multiple wavelengths through the WEL lattice (a) Scheme of optical assembly showing arrangement and orientation of red, blue, and green lasers, to couple respectively into waveguide arrays oriented at 0° , 15° , and 30° . Transmitted light was projected in the far-field onto a screen. Inset is a top-down photograph showing the relative of the sample and projected transmission patterns of the red, green and blue beams. (b) Photographs of the assembly acquired along the three different propagation directions of the three beams.

Light propagation in the WEL lattice was computed through the Beam Propagation Method (see Experimental, Section S2.1). The WEL model comprised five waveguide arrays oriented at -30° , -15° , 0° , 15° , and 30° with respect to the entrance face normal. The refractive index of the medium and the difference in refractive index between the polymerized waveguide and surrounding unpolymerized region (Δn) were set at 1.51 and 0.001, respectively. The dimensions of the computational cell were $x = 1200 \mu\text{m}$, $y = 120 \mu\text{m}$ and $z = 3000 \mu\text{m}$. To conserve computational time, the model WEL lattice consisted only of a single layer of waveguide arrays confined to the xz plane. For simulations, a continuous wave, Gaussian beam with a width of 3 lattice constants ($240 \mu\text{m}$) along the x axis and 1 lattice constant ($80 \mu\text{m}$) along y was launched into the WEL lattice. The beam was sequentially launched at the five different angles corresponding to the orientation of each waveguide array. To ensure that the beam propagating through the waveguide arrays oriented at $\pm 15^\circ$ and $\pm 30^\circ$ remained in the computational cell, the launch positions were offset from $x = 0$ by $\pm 4a$ and $\pm 6a$, respectively, where $a = 80 \mu\text{m}$. All simulated beams were observably converted into guided light at $2000 \mu\text{m}$.

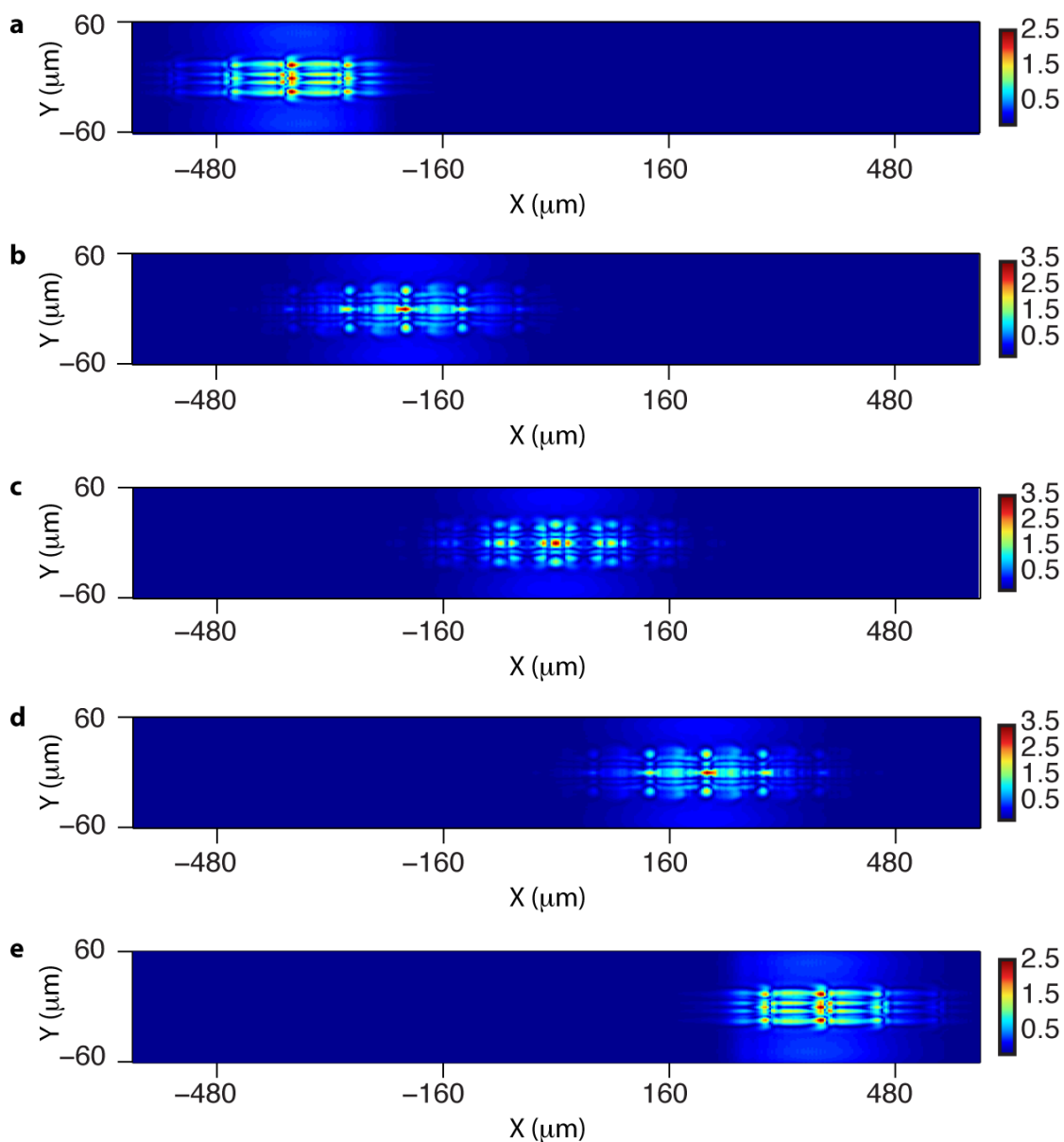


Figure S2.18. 2-D simulations of the propagation of a Gaussian beam ($240\ \mu\text{m}$ -wide, $\lambda = 633\ \text{nm}$) in a WEL lattice. Angles of propagation in the structure are (a) -30° , (b) -15° , (c) 0° , (d) 15° , and (e) 30° , with respect to the z -axis. Transverse profiles in (a, e) were acquired at $z = 1.5\ \text{mm}$ while those in (b-d) were acquired at $z = 2.0\ \text{mm}$. These simulations correspond to those presented in Figure 2.4b of the manuscript.

S2.7 Optical characterization of light collection and transmission, and determination of the field of view of WEL lattices

We used a single beam for characterizing the angle-dependent light collection and transmission in the WEL lattices. Typically, the WEL lattice was first rotated to align

one of its five waveguide arrays with the optic axis (and thus, the normal of the CCD camera chip). Figure S2.17 shows this configuration for all five waveguide arrays (oriented at -30° , -15° , 0° , 15° and 30°) in a single WEL lattice (*i.e.*, accounting for refraction at the air/sample interface, the angles of each array with respect to the optic axis was -44° , -22° , 0° , 22° and 44°). The WEL lattice, imaging lenses and CCD camera were fixed in place and then simultaneously rotated about the optic axis (indicated as the central dotted line) over an interval of -6° to 6° , in 0.5° increments. In this way, the angle of incidence of the illuminated object “O” was monotonically varied while the transmitted image at the exit of the waveguide array was monitored. Table S2.3 shows the angular ranges examined and their corresponding waveguide and central angle of incidence.

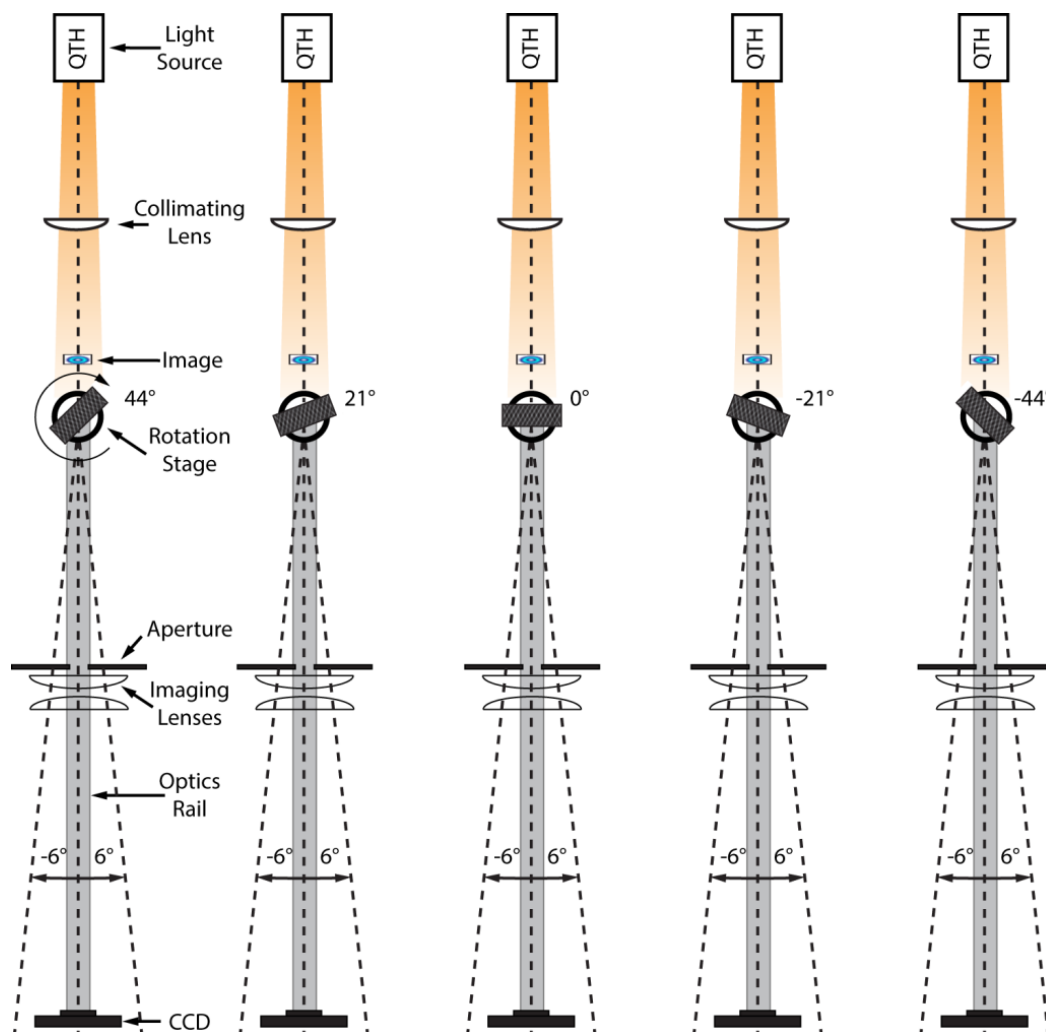


Figure S2.19. Optical assembly for determining the field of view of the WEL-5 lattice. The WEL lattice is first rotated so that (accounting for refraction at the air/sample interface), the illuminated object “O” couples directly into one of the five waveguide arrays; transmitted light at the exit face is then imaged onto the CCD camera. A 2 mm-wide aperture was placed in front of the imaging lenses to avoid stray light. To vary the angle of incidence of the illuminated object, the WEL lattice, the imaging lenses and CCD camera are then simultaneously rotated about the optic axis over an interval of -6° to 6° with a resolution of 0.5° .

The central angles of incidence coincide (after refraction at the air/sample interface) with the orientation of each waveguide array. Angles of incidence were varied over a range of -6° to 6° about each central angle of incidence. The collective incidence angles sampled therefore ranged from -50° to 50° .

Table S2.3 Experimental configuration of variable-angle imaging in the WEL lattice

Waveguide orientation in WEL lattice	Central angle of incidence	Angular range sampled
-30°	-44°	-50° to -38°
-15°	-22°	-27° to -15°
0°	0°	-6° to 6°
15°	22°	15° to 27°
30°	44°	38° to 50°

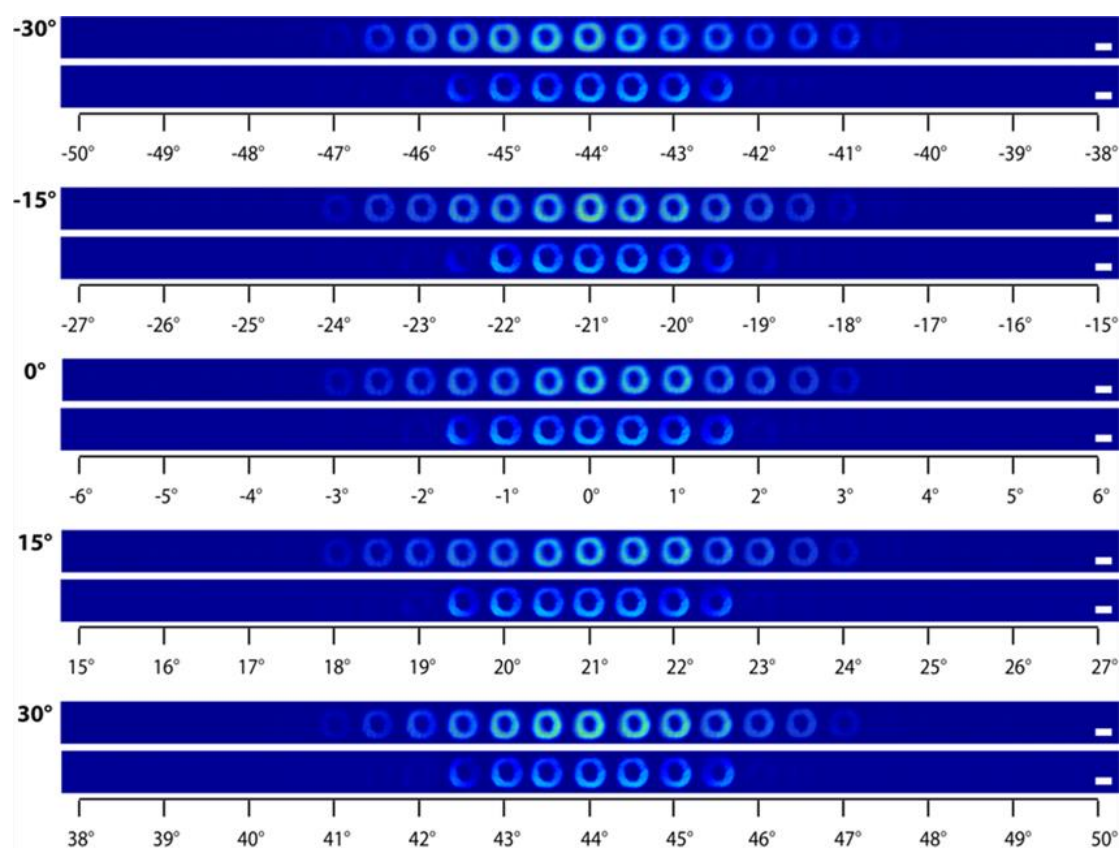


Figure S2.20. Sequence of spatial intensity profiles of illuminated “O” object transmitted at varying angles of incidence through each of the five waveguide arrays of a WEL lattice. The angle of orientation of each waveguide array is indicated on the left. The horizontal axis indicates the angle of incidence of the illuminated “O” with respect to the normal of the entrance face. Images were acquired at the exit face of the WEL lattice. Corresponding measurements for a control sample without the lattice are provided below each sequence for comparison. In all images, scale bar = 1 mm.

Table S2.4 Angular acceptance ranges for the WEL lattice structure

Waveguide Lattice		Angular Acceptance Range	Plot Width ^a
-30°	Structure	-46.7° to -40.8°	5.9°
	Control	-45.6° to -42.3°	3.3°
-15°	Structure	-23.8° to -18.2°	5.6°
	Control	-22.6° to -19.3°	3.3°
0°	Structure	-2.7° to 2.8°	5.5°
	Control	-1.7° to 1.7°	3.4°
15°	Structure	18.5° to 23.8°	5.3°
	Control	19.3° to 22.7°	3.4°
30°	Structure	41.4° to 46.9°	5.5°
	Control	42.3° to 45.6°	3.3°

^a As determined by the angle at which the total intensity was $1/e^2$ of the maximum.

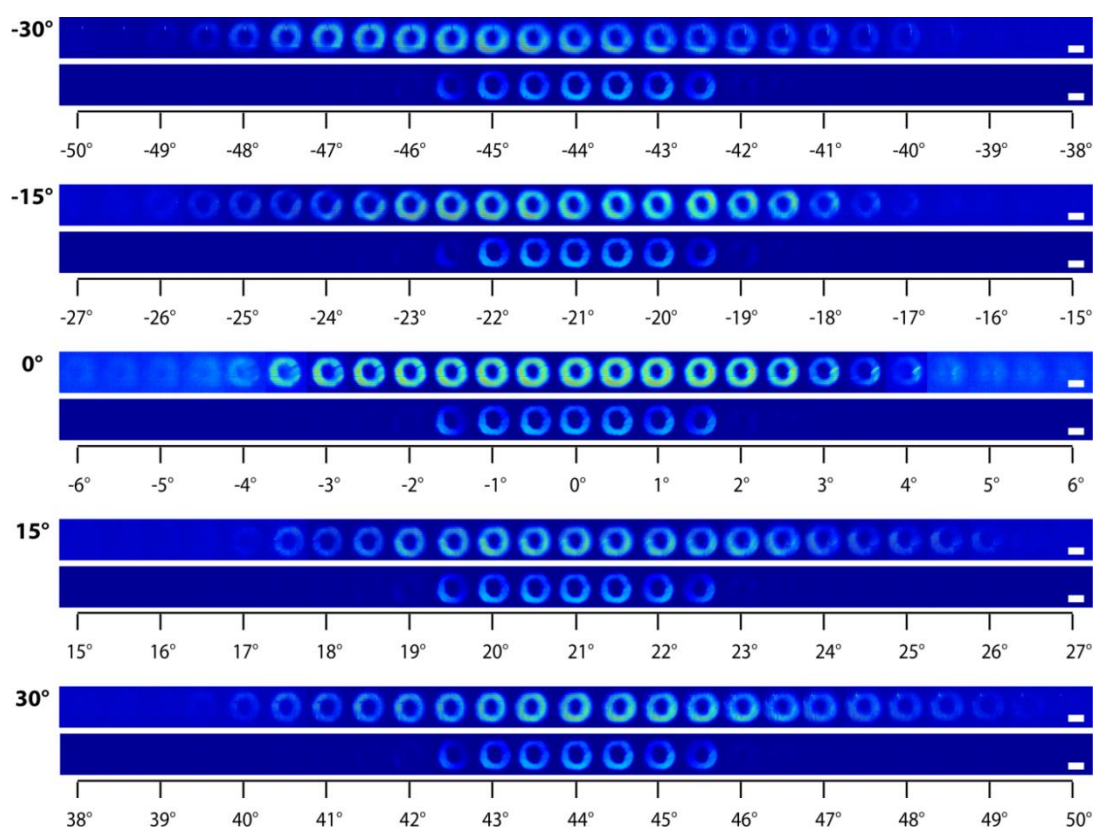


Figure S2.21. Sequence of spatial intensity profiles of an illuminated “O” (object) transmitted at varying angles of incidence through five different WEL-1 lattices. The angle of orientation of waveguides in each array with respect to the normal of the sample entrance face is indicated on the left. The x axis indicates the angle of incidence of the illuminated “O”. Images were acquired at the exit face of the WEL lattice. Corresponding measurements for a control sample without the lattice are provided below each sequence for comparison. In all images, scale bar = 1 mm.

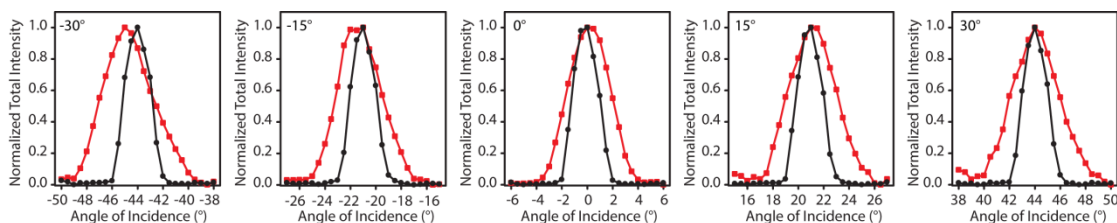


Figure S2.22. Plots of normalized total intensity of the image versus the angle of incidence of the object for five different WEL-1 lattices at different orientation angles, with respect to the surface normal. The filled red squares represent the lattice, and the filled black circles represent the control (i.e., unstructured medium).

Table S2.5 Angular acceptance ranges for five WEL-1 different lattices

Waveguide Lattice	Angular Acceptance Range	Plot Width ^a
-30°	Structure	-48.4° to -40.4°
	Control	-45.7° to -42.2°
-15°	Structure	-24.5° to -17.6°
	Control	-22.7° to -19.3°
0°	Structure	-2.9° to 3.2°
	Control	-1.7° to 1.7°
15°	Structure	17.7° to 24.8°
	Control	19.2° to 22.7°
30°	Structure	40.2° to 48°
	Control	42.4° to 45.7°

^a Determined by the angle at which the total intensity was $1/e^2$ of the maximum.

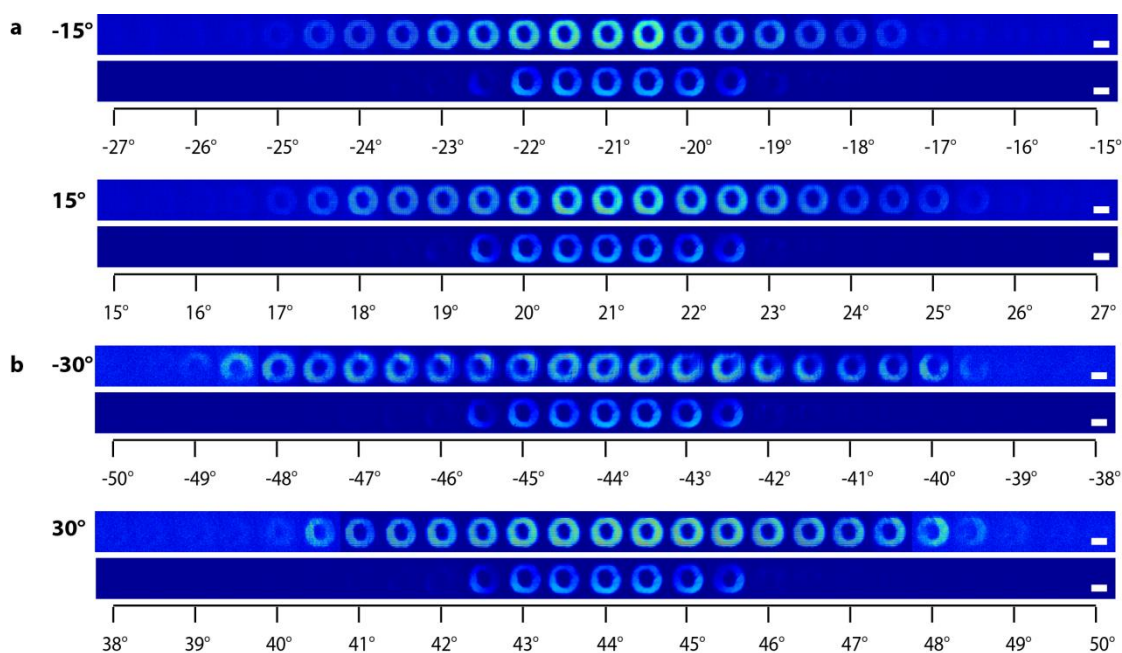


Figure S2.23. 2D spatial intensity profiles of images for two WEL-2 lattices with following lattice orientations: (a) -15° and 15° , (b) -30° and 30° with respect to WEL surface normal. Scale bars = 1 mm.

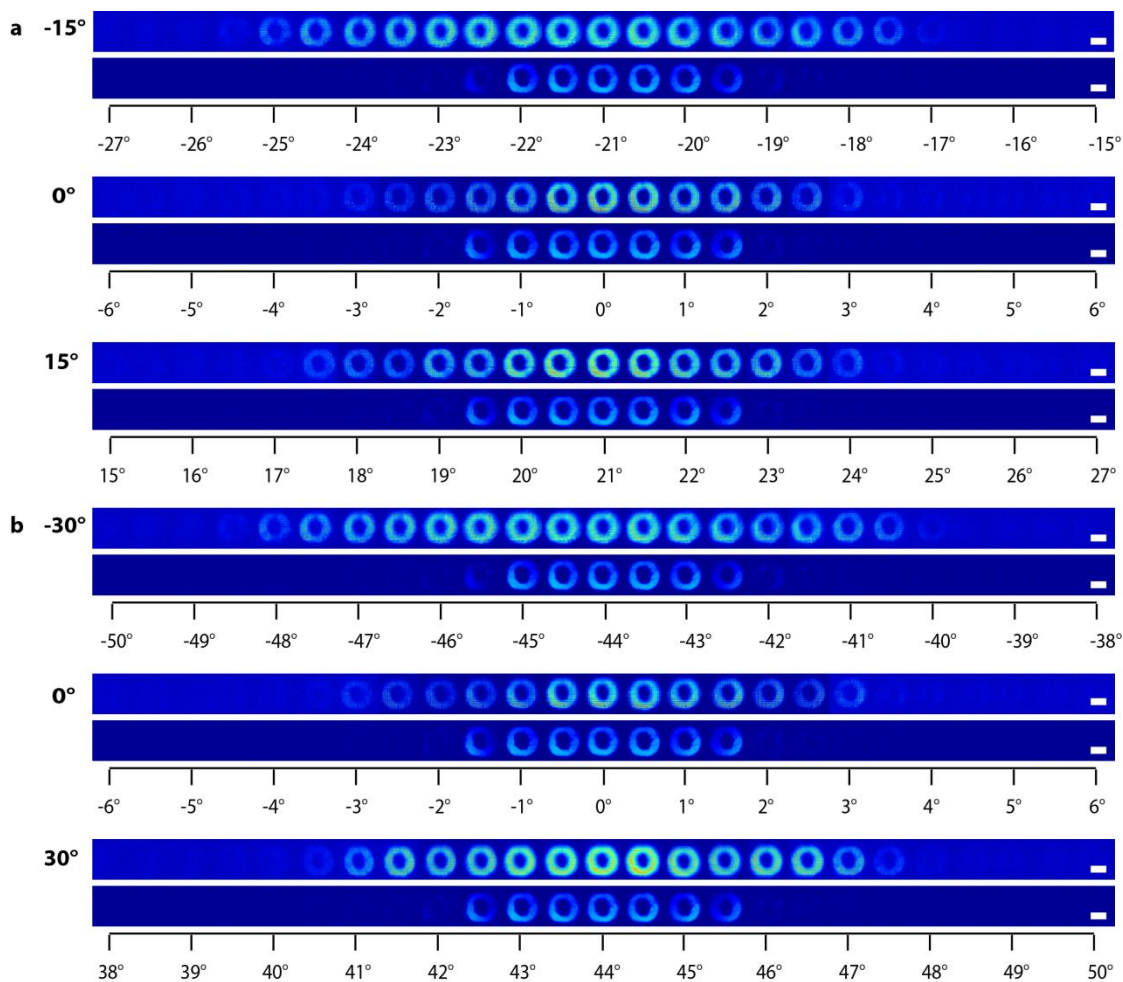


Figure S2.24. 2D spatial intensity profiles of images for two WEL-3 Lattices with the following lattice orientations: (a) -15° , 0° and 15° , (b) -30° , 0° and 30° , with respect to WEL surface normal. Scale bars = 1 mm.

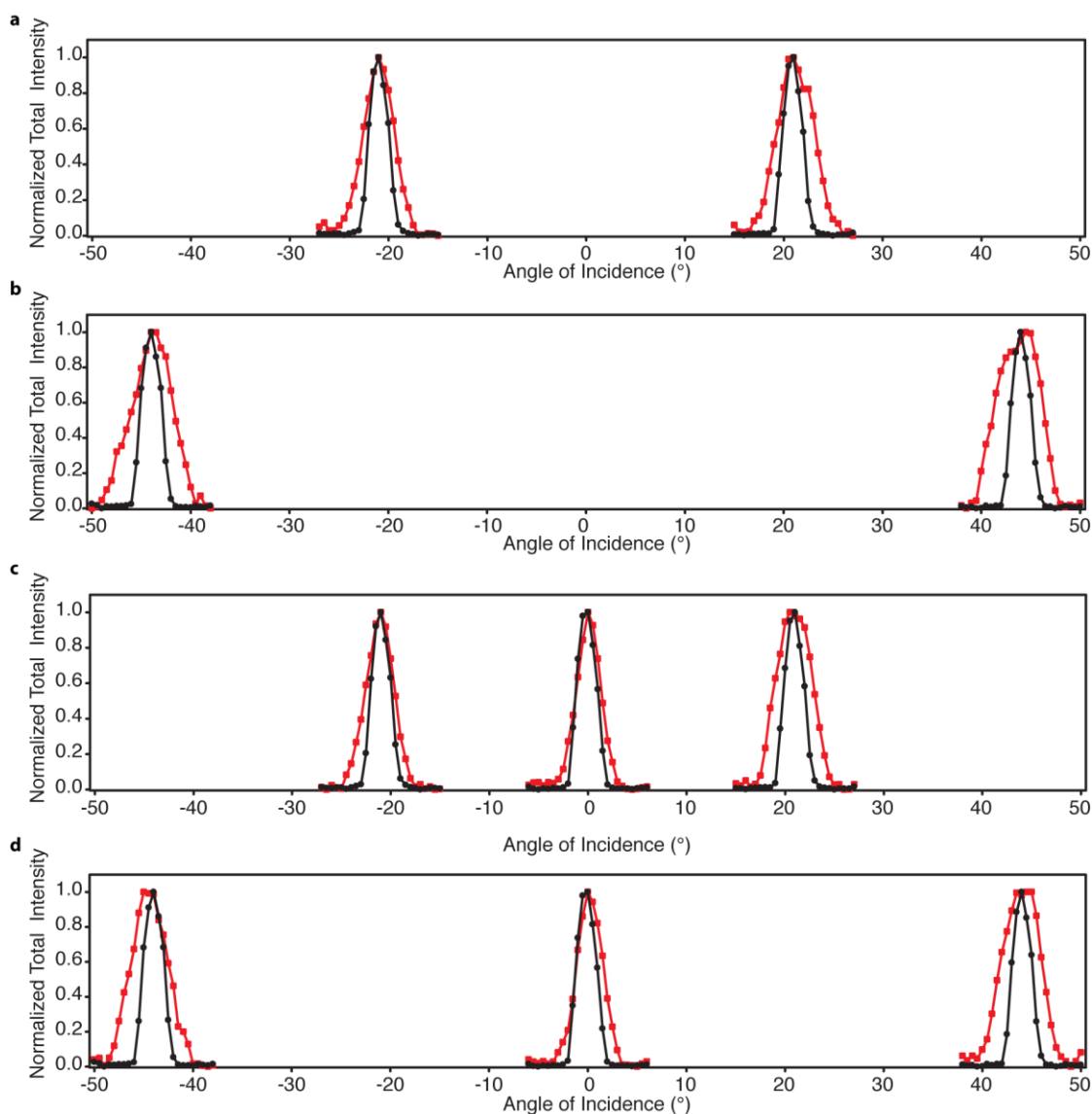


Figure S2.25. Plots of normalized total intensity of the image versus the angle of incidence of the object for two WEL-2 lattices and two WEL-3 lattices with different lattice orientations. The red plots represent the angular acceptance performance of the lattices, while black curves represent that of the control (i.e., unstructured medium). Lattice combinations are: (a) -15° and 15° ; (b) -30° and 30° ; (c) -15° , 0° and 15° ; (d) -30° , 0° and 30° .

Table S2.6 Angular acceptance ranges for WEL-2_(-15°, 15°) lattices

Waveguide Lattice		Angular Acceptance Range	Plot Width ^a
-15 °	Structure	-24.2° to -17.9°	6.3 °
	Control	-22.7° to -19.3°	3.4 °
15 °	Structure	17.7 ° to 24.7 °	7.0 °
	Control	19.2 ° to 22.7 °	3.5 °

^a Determined by the angle at which the total intensity was $1/e^2$ of the maximum.

Table S2.7 Angular acceptance ranges for WEL-2_(-30°, 30°) lattices

Waveguide Lattice		Angular Acceptance Range	Plot Width ^a
-30 °	Structure	-48.1° to -40.1°	8.0 °
	Control	-45.7° to -42.2°	3.5 °
30 °	Structure	39.8 ° to 47.4 °	7.6 °
	Control	42.4 ° to 45.7 °	3.3 °

^a Determined by the angle at which the total intensity was $1/e^2$ of the maximum.

Table S2.8 Angular acceptance ranges for WEL-3_(-15°, 0°, 15°) lattices

Waveguide Lattice		Angular Acceptance Range	Plot Width ^a
-15 °	Structure	-24.1° to -18.3°	5.8 °
	Control	-22.7° to -19.3°	3.4 °
0 °	Structure	-2.4 ° to 2.6 °	6.0 °
	Control	-1.7 ° to 1.7 °	3.4 °
15 °	Structure	17.7 ° to 24.2 °	6.5 °
	Control	19.2 ° to 22.7 °	3.5 °

^a Determined by the angle at which the total intensity was $1/e^2$ of the maximum.

Table S2.9 Angular acceptance ranges for WEL-3_(-30°, 0°, 30°) lattices

Waveguide Lattice		Angular Acceptance Range	Plot Width ^a
-30 °	Structure	-47.9° to -40.6°	7.3 °
	Control	-45.7° to -42.2°	3.5 °
0 °	Structure	-2.0 ° to 2.8 °	4.8 °
	Control	-1.7 ° to 1.7 °	3.4 °
30 °	Structure	40.4 ° to 47.4 °	7.0 °
	Control	42.4 ° to 45.7 °	3.3 °

^a Determined by the angle at which the total intensity was $1/e^2$ of the maximum.

S2.8 Calculation of refractive index of the epoxide medium and determination of the photo-induced change in refractive index in self-induced waveguides

During WEL lattice-formation, beams incident at angles that are not normal to the sample entrance face refract into the epoxide medium and induce waveguides along this direction (See Materials and Methods). The orientation of the waveguide arrays with respect to the surface normal together with the incident angles of the beams were used to estimate the refractive index of the polymerized medium n_{polymer} through Snell's Law:

$$n_{\text{air}} \sin \theta_{\text{beam}} = n_{\text{polymer}} \sin \theta_{\text{refracted beam}} \quad [\text{S2.5}]$$

Table S2.10 Incident and refracted angles as determined from samples made from 2, 3 and 5 beams, and the calculated refractive index of the polymer

Number of Beams	Beam Orientations	Beam Angle of Incidence	Waveguide Angle	Refractive Index
2 beam	-22 ° & 22 °	22 °	14.25 °	1.522
		-22 °	-14.25 °	1.522
	-44 ° & 44 °	44 °	27.5 °	1.504
		-44 °	-27.5 °	1.504
3 beam	-22 ° ; 0 ° & 22 °	22 °	14 °	1.548
		-22 °	-14 °	1.548
	-44 ° ; 0 ° & 44 °	44 °	28 °	1.480
		-44 °	-28 °	1.480
5 beam	-44 ° ; -22 ° ; 0 ° ; 22 ° & 44 °	22 °	14 °	1.548
		-22 °	-14 °	1.548
		44 °	27 °	1.530
		-44 °	-27 °	1.530

To fit the experimental intensity versus angle of incidence, single waveguide simulations (similar to those used to produce Figure 2.1c in manuscript) were run for

different values for Δn . $\Delta n = 0.001$ produced curves that best fit the experimental data in Figure 2.5c.

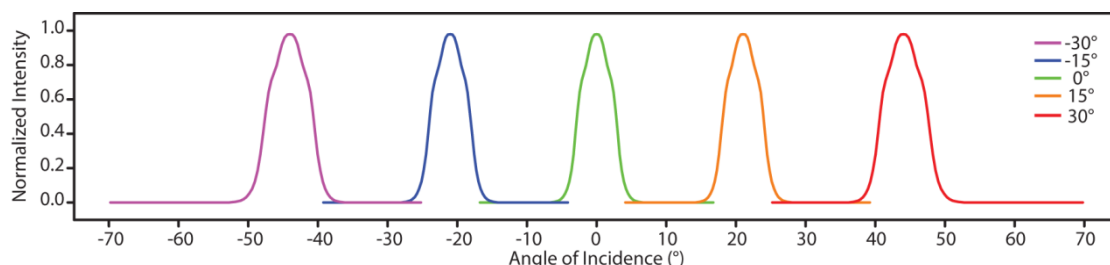


Figure S2.26. Calculated normalized intensity versus angle of incidence curves that match the experimental data shown in Figure 2.5c with $\Delta n=0.001$.

S2.9 Study of the multifunctional imaging performances of the WEL lattice

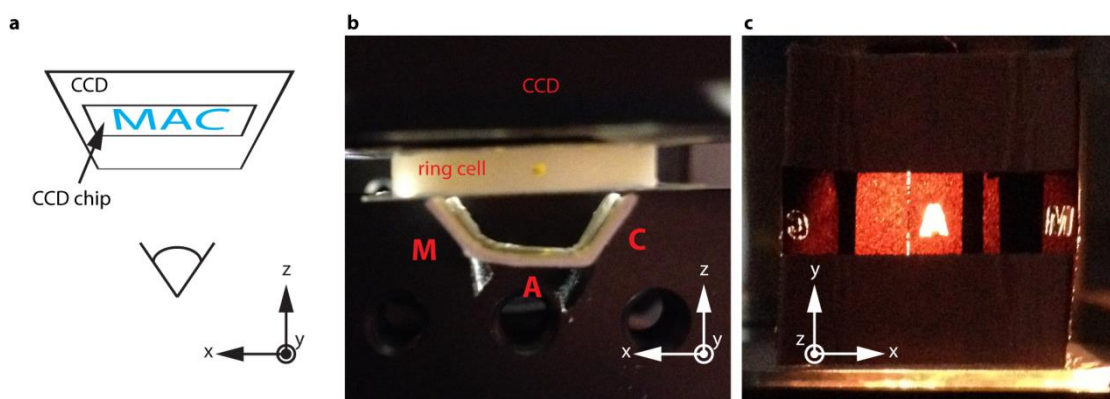
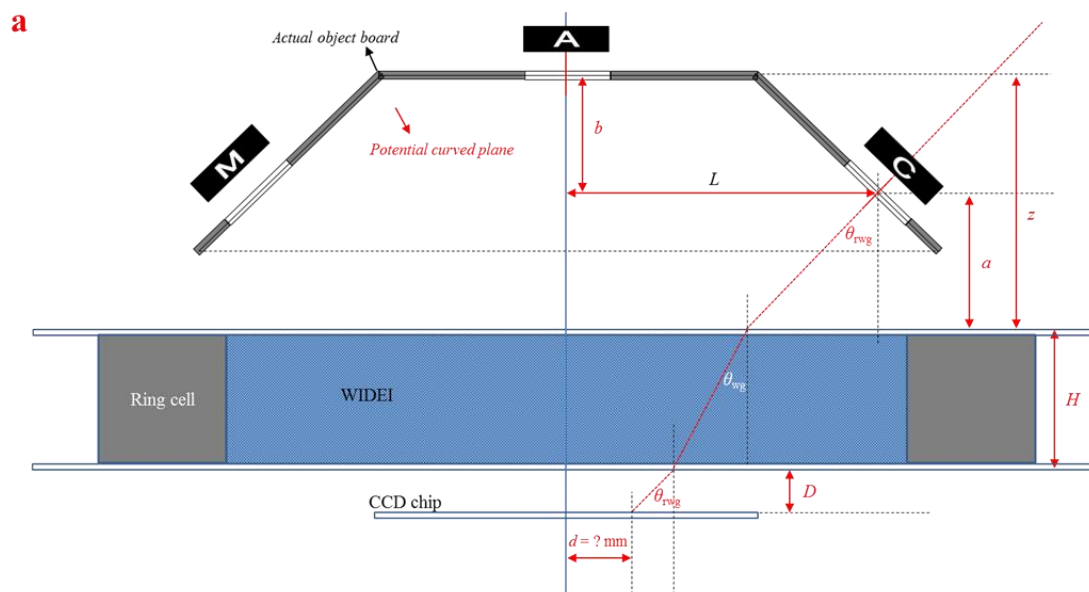


Figure S2.27. Setup for the simultaneous capture of multiple images at different angular positions. (a) Schematic showing the orientation of the images on the CCD chip. Light propagates in the $+z$ direction. The perspective view of the captured images is looking down the $+z$ axis, as indicated by the eye. (b) Photo showing the paper template containing the cut out letters, the arrangement of the letters ‘M’, ‘A’, and ‘C’ are indicated. (c) Close up view of the cut out letters mounted onto the piece of paper, which is bent at two points so as to orient the letters ‘M’ and ‘C’ perpendicular to their respective beams.



Figure S2.28. Simultaneous image collection transmission of two objects from the WEL-3_(-30°, 0°, 30°) lattices. Scale bar = 1 mm.



b

$$\begin{aligned}
 d &= L - d \times \tan\theta_{\text{rwg}} - H \times \tan\theta_{\text{wg}} - D \times \tan\theta_{\text{rwg}} \\
 &= L - (a + D) \times \tan\theta_{\text{rwg}} - H \times \tan\theta_{\text{wg}} \\
 &= L - (z - b + D) \times \tan\theta_{\text{rwg}} - H \times \tan\theta_{\text{wg}} \\
 &= 7.2 - (z - 1.8) \times \tan 44^\circ - 3.25 \times \tan 27.5^\circ
 \end{aligned}$$

Figure S2.29. (a) Schematic diagram of assembly to study the multifunctional imaging behaviors of the WEL lattice. Propagation of “C” is traced in red as an example. (b) A phenomenological equation generalizing and describing the conditions required for each imaging operation of the WEL lattice.

References

- [1] K. Saravanamuttu, X. M. Du, S. I. Najafi, M. P. Andrews, *Can. J. Chem.* **1998**, *76*, 1717.
- [2] J. Crisp, B. J. Elliott, *Introduction to fiber optics*; Newnes, **2005**.
- [3] B. E. A. Saleh, M. C. Teich, *Fundamentals of Photonics*; Wiley Series in Pure and Applied Optics; John Wiley & Sons, Inc.: New York, USA, **1991**.

Chapter 3

Slim Films with Seamless Panoramic Fields of View: The Radially Distributed Waveguide Encoded Lattice (RDWEL)

Hao Lin, Ian D. Hosein, Kathryn A. Benincasa, and Kalaichelvi Saravanamuttu

Content of this chapter has been submitted to *Advanced Optical Materials*.

HL carried out experiments and data analysis. KS, HL and IDH conceived the project. IDH proposed the employment of Fresnel lenses and KB provided valuable input. KS and HL wrote the manuscript.

Abstract

The nearly hemispherical field of view (FOV) of arthropodal compound eyes has inspired richly varied analogues ranging from curved, lens-patterned domes to planar constructs patterned with periodic arrays of micro-lenses. We report that a radial distribution of cylindrical waveguides that monotonically spans $\pm 33^\circ$ confers a FOV of 115° to a slim (≤ 3 mm) polymer film. To our knowledge, this is the greatest panoramic FOV reported for any plane-faced, single-component structure. The RDWEL waveguides are inscribed in a single, room temperature step by a large ($\approx 15,000$ cm⁻²), converging population of self-trapped incandescent beams elicited in a photopolymerizable epoxide fluid. Because the resulting waveguides are multimoded and polychromatic, the RDWEL operates at all visible wavelengths emitted by broad-band (e.g. ambient sunlight) and narrow ranged (e.g. LEDs, lasers) sources. Due to the overlap of the angular acceptance ranges between neighbouring waveguides, the structure captures light incident at any angle within its FOV. Distinct in the field, the RDWEL confers an exceptionally large, seamless FOV for all visible wavelengths to a planar, single-component, flexible and robust slim film. It therefore holds considerable potential as coatings for enhanced light capture (solar cells), beam shaping (LEDs, projectors) and imaging (smart phones, microscopes, endoscopes).

Key words

Bio-inspired optics, compound eyes, waveguide arrays, field of view, nonlinear waves

3.1. Introduction

The compound eyes of arthropods are hemispherical arrays of ommatidia – natural waveguides of ambient light - which impart exceptionally wide fields of view (FOV) and sensitivity to motion and in certain cases, to polarization.^[1,2] Efforts to fabricate replicas that mimic these properties are motivated by potential application in medical imaging,^[3–5] security and surveillance,^[6–9] displays,^[10–12] motion detection^[13,14] and autonomous navigation.^[15,16] These artificial eyes include planar configurations of micro-lenses, pinhole arrays and optoelectronic detectors^[17–20] but are predominantly curved or hemispherical constructs including micro-lens arrays interfaced to photodetectors,^[7,16] and elastomeric hemispheres patterned with lenses.^[6,21–23] While the fabrication of these architectures typically involves multiple steps and components, soft, single-component eyes have also been generated^[24,25] or proposed^[26,27] by inducing lens-capped waveguides in UV-polymerizable resins in 2-D^[24], and 3-D^[25,26] geometries.

Inspired by the collective behavior of ommatidia, we are developing new classes of multifunctional polymer films, which are inscribed with dense arrays or lattices of cylindrical waveguides.^[28] In striking contrast to the predominantly hemispherical architectures of natural and artificial compound eyes, these waveguide encoded lattices (WELs) are flexible, slim (≤ 3 mm) and optically flat, which provides ease of integration into existing light-based technologies such as solar cells, cameras and smart screens. Distinct from known examples of natural or artificial eyes, WELs also possess translational symmetry, which affords the scalability that is necessary for manufacturing (e.g. roll-to-roll) processes. We generate WELs through a single-step,

room temperature technique that employs large ensembles of nonlinear self-trapped filaments of visible light elicited in photopolymerizable media to permanently inscribe arrays of multimode, polychromatic waveguides.^[29–32] We previously fabricated a WEL consisting of a thin, epoxide film embedded with pentadirectional, intersecting arrays of multimode cylindrical waveguides, which conferred a FOV of 94°, which represented a 66 % enhancement relative to an unstructured film. The FOV of this structure corresponded to the sum of the angular acceptance ranges of waveguide arrays oriented along five discrete angles. Significantly, there was no overlap between these five ranges and the consequent discontinuities – or gaps - in the FOV prevented cross-talk between non-parallel waveguides. This in turn enabled sophisticated imaging functions such as panoramic imaging, inversion and focusing that would normally require bulky optics.^[28]

We now report a WEL that possesses a seamless and significantly enhanced panoramic FOV of 115°, which originates from a dense, radial distribution of cylindrical waveguide arrays inscribed in a thin, flexible polymer film. To the best of our knowledge, this represents the greatest panoramic FOV of any known planar system.^[33–35] We inscribe such Radially Distributed Waveguide Encoded Lattices (RDWELs) with a large, converging population of self-trapped filaments^[29–32] in a thermomechanically robust epoxide medium.^[28,36] We show that the resulting single-component microstructure retains the advantages of a planar configuration and also offers excellent imaging functionality in terms of the density, angular span and wavelength sensitivity of its constituent waveguides. Specifically, the RDWEL possesses a large density of light-collecting waveguide elements (> 31, 000 over a

circular area with $d = 1.6$ cm), which exceeds the density and absolute number of ommatidial elements of other artificial, predominantly hemispherical structures including 8370 in a polymer dome with $d = 2.5$ cm,^[25] 180 over an area of 1.472 cm \times 1.472 cm in an arthropod-inspired 3-D camera,^[7] 4400 in a dome with $d = 4$ cm^[6] and 630 in a cylindrical sensor-CurvACE (curved artificial compound eye) with $r = 6.4$ mm).^[16] Moreover, the ~ 40 μ m diameter of each waveguide imparts a high degree of spatial imaging resolution. Importantly, the RDWEL is versatile with respect to its operating wavelengths; because its waveguides are polychromatic and multimoded, the RDWEL operates both with the broad spectral range emitted by incandescent sources (such as ambient sunlight) and the discrete wavelength ranges emitted by lasers and Light Emitting Diodes (LEDs).^[28,36] We detail below the design rationale, fabrication and microstructural characterization of the RDWEL and then elucidate its optical properties.

3.2. Results and Discussion

3.2.1. Working principles of the RDWEL

Figure 3.1 is a scheme of the RDWEL, which is a periodic stack of xz planes, each containing up to 200 cylindrical waveguides that are monotonically oriented over an arc spanning $\pm 33.0^\circ$. Each waveguide is 40 μm in diameter with a refractive index contrast, $\Delta n \geq 0.001$ relative to its surroundings where $n = 1.510$.^[28] From previous studies, we know that these parameters enable waveguides to confine multimoded, polychromatic light including incandescent white light^[27, 32] with an angular acceptance range of 5.6° .^[13] Distinct from the omnidirectional ommatidia that characteristically project their output faces onto the characteristically hemispherical surface of compound eyes, the RDWEL is plane-faced and the output faces of its constituent waveguides coincide in its exit face (xy) plane.

The planar geometry of the RDWEL yields a significantly enhanced FOV compared to a curved construct with the same number and angular distribution of waveguides. Figure 3.1a compares two identical waveguides oriented along the same angle (θ_{wg}) with respect to the z axis in a curved and planar configuration, respectively. In the former, θ_{wg} always coincides with a normal to the curved surface; its angular collection range of 5.6° is therefore symmetrically distributed about θ_{wg} from $\theta_{\text{wg}} - \theta_1$ to $\theta_{\text{wg}} + \theta_2$ where $\theta_1 = \theta_2 = 2.8^\circ$. For example, for a waveguide with $\theta_{\text{wg}} = 33.0^\circ$, the angular collection range would span 31.2° to 35.8° ($33.0^\circ \pm 2.8^\circ$). For a curved construct with a radial distribution of waveguides with $\theta_{\text{wg}} = \pm 33.0^\circ$, the corresponding FOV would span $\pm 35.8^\circ$ ($\sim 72^\circ$). In the planar configuration, the normal remains constant (along z) and the angular acceptance range must account for the

refraction of incident light at the waveguide entrance faces. For $\theta_{\text{wg}} = 0^\circ$, the acceptance range remains 5.6° . However, when $\theta_{\text{wg}} \neq 0$, its acceptance range must account for refraction at the air-waveguide interface and now spans (nearly symmetrically) about an angle $\theta_{\text{r wg}}$ that corresponds to the refracted θ_{wg} , *i.e.*, $\theta_{\text{r wg}} = \arcsin(n \sin \theta_{\text{wg}})$ where $n = 1.510$ (details provided in Supplementary S3.2). Because when $\theta_{\text{wg}} > 0$, $|\theta_{\text{r wg}}| > |\theta_{\text{wg}}|$, the acceptance range of these waveguides always spans a larger range of angles and yields a greater FOV for the plane-faced structure.

The FOV of the RDWEL is the cumulative acceptance ranges of its constituent waveguides, which span $\theta_{\text{wg}} = \pm 33.0^\circ$ (Figure 3.1b). Here, the minimum collection range of an individual waveguide of 5.6° exceeds the maximum separation between waveguides of $\sim 0.6^\circ$ (details provided in Supplementary Table S3.1). As a result, there is significant overlap in the acceptance ranges of neighbouring waveguides, which in turn yields a seamlessly continuous, panoramic FOV at the exit face (*xy* plane). The FOV is easily calculated from the acceptance ranges associated with the most oblique waveguides (*i.e.*, $\theta_{\text{wg}} = \pm 33.0^\circ$) alone. The resulting FOV of $\sim \pm 60^\circ$ (spanning $\sim 120^\circ$) exceeds the FOV of $\pm 35.8^\circ$ (spanning $\sim 72^\circ$) of the equivalent curved structure by $\sim 67\%$ (details provided in Supplementary Table S3.2). The RDWEL is periodic along the *y* axis; because there is no variation of θ_{wg} along this direction, the FOV along this direction corresponds to the acceptance range of a single waveguide of 5.6° only (Figure 3.1c). The 3-D geometry and periodicity of the RDWEL along the *y* axis (Figure 3.1d) ensures that there are multiple waveguides oriented at each θ_{wg} , which increases the imaging space by the RDWEL compared to a

single-layer hemispherical constructs. Some cases of the latter only have a single waveguide oriented along a particular direction.^[24]

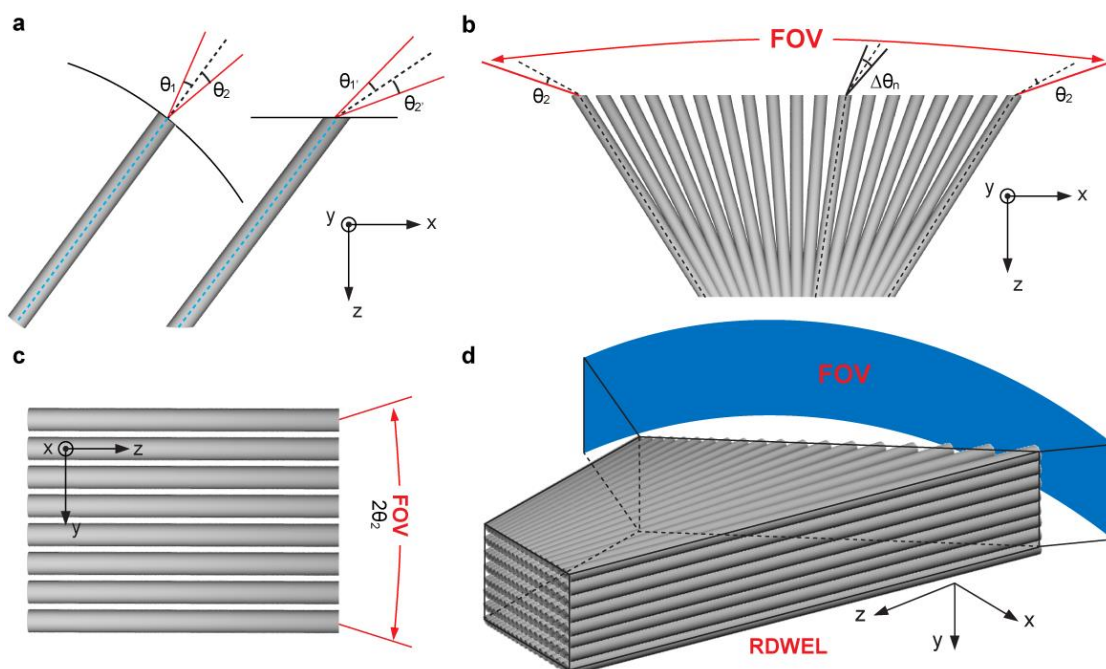


Figure 3.1. Operating principles of the RDWLs. (a) Comparison of angular collection range of identical waveguides with the same θ_{wg} but with a curved and (right) planar surface, respectively. (b) Scheme of a single layer (xz plane) comprising a radial distribution of waveguides. The FOV corresponds to the sum of collection angular ranges of all the waveguides. (c) Scheme of the yz cross-section and corresponding FOV (d) Scheme of RDWEL depicting a seamless, panoramic FOV at the exit face (xy plane).

3.2.2. Fabrication and characterization of RDWEL microstructure

Figure 3.2a is a scheme of the optical assembly employed to fabricate the RDWEL. White incandescent light is first collimated and then focused through a Fresnel lens onto the optically flat, transparent entrance face of a cell containing photopolymerizable epoxide fluid.^[28,36] An amplitude mask with a 2-D square pattern ($\lambda = 80 \mu\text{m}$) is placed flush with the entrance face so that it divides the incident beam into a square grid of individual bright spots with a density ($> 15,000 \text{ cm}^{-2}$). The

sample cell (thickness = 2 mm) was placed before the focal point of the Fresnel lens ($f = 7$ mm) so that the bright spots converged as they propagated through the epoxide fluid; the angular range of the incident light in air with respect to z spanned $\pm 56.2^\circ$. Accounting for refraction at the air-sample interface, this range became $\pm 33.4^\circ$ within the polymerizable medium (see Supplementary Figure S3.2). As it propagates, each bright spot initiates cationic polymerization of epoxide moieties; corresponding changes in refractive index along its path generate a cylindrical waveguide, which entraps light as its optical modes and guides it through the medium without diverging.^[28,36] In this way, the large population of self-trapped beams simultaneously inscribe the corresponding, converging array of cylindrical, multimode waveguides – the RDWEL - within the epoxide film (Figure 3.2b).

We selected a cycloaliphatic epoxide fluid to fabricate the RDWEL because of its optical transparency, flexibility and thermo-mechanical stability.^[28,36] Importantly and as detailed elsewhere, the photopolymerizable fluid also satisfies the strict prerequisites for the self-trapping of incandescent light,^[29–32] because its polymerization rate^[36] is relatively slow (spanning *ms* to *min.*), the epoxide system is not affected by the *fs* fluctuations in phase and amplitude that characterize incoherent incandescent light. Additionally, Δn within the medium is sufficiently large (≥ 0.001)^[28] to support the multiple modes that constitute white light and generate multimoded, polychromatic waveguides. Even under passive conditions, these structures guide both incoherent and coherent emission at all visible wavelengths, emitted both by narrow-band (lasers and LEDs) and broad-band (incandescent lamps, sunlight) sources.^[29,31]

Optical micrographs of the polymerized structure confirmed the inscription of the RDWEL in the polymer film. Longitudinal cross-sections (xz plane) comprised a single layer with a radial distribution of ~ 200 cylindrical waveguides that span $\sim \pm 33^\circ$ with respect to z (Figure 3.2c), which is consistent with the range of propagation angles of incident beams (*vide supra*). The angular spacing between waveguides decreases as the waveguide angle increases, varying from calculated values of 0.60° for $\theta_{\text{wg}} \approx 0^\circ$ to 0.12° for $\theta_{\text{wg}} \approx \pm 33^\circ$ (see Supplementary Figure S3.2, Table S3.1). Micrographs of the transverse cross-sections (xy plane) contain square arrays of discrete bright spots (Figure 3.2d), which correspond to the output of waveguides. Waveguide populations with increasing θ_{wg} appear blurred because they deviate from the microscope optic axis and no longer capture and guide its probe beam. However, focused images were obtained by tilting the RDWEL so that waveguides with $\theta_{\text{wg}} \gg 0^\circ$ now coincided with the microscope axis (Supplementary Section S3.3).

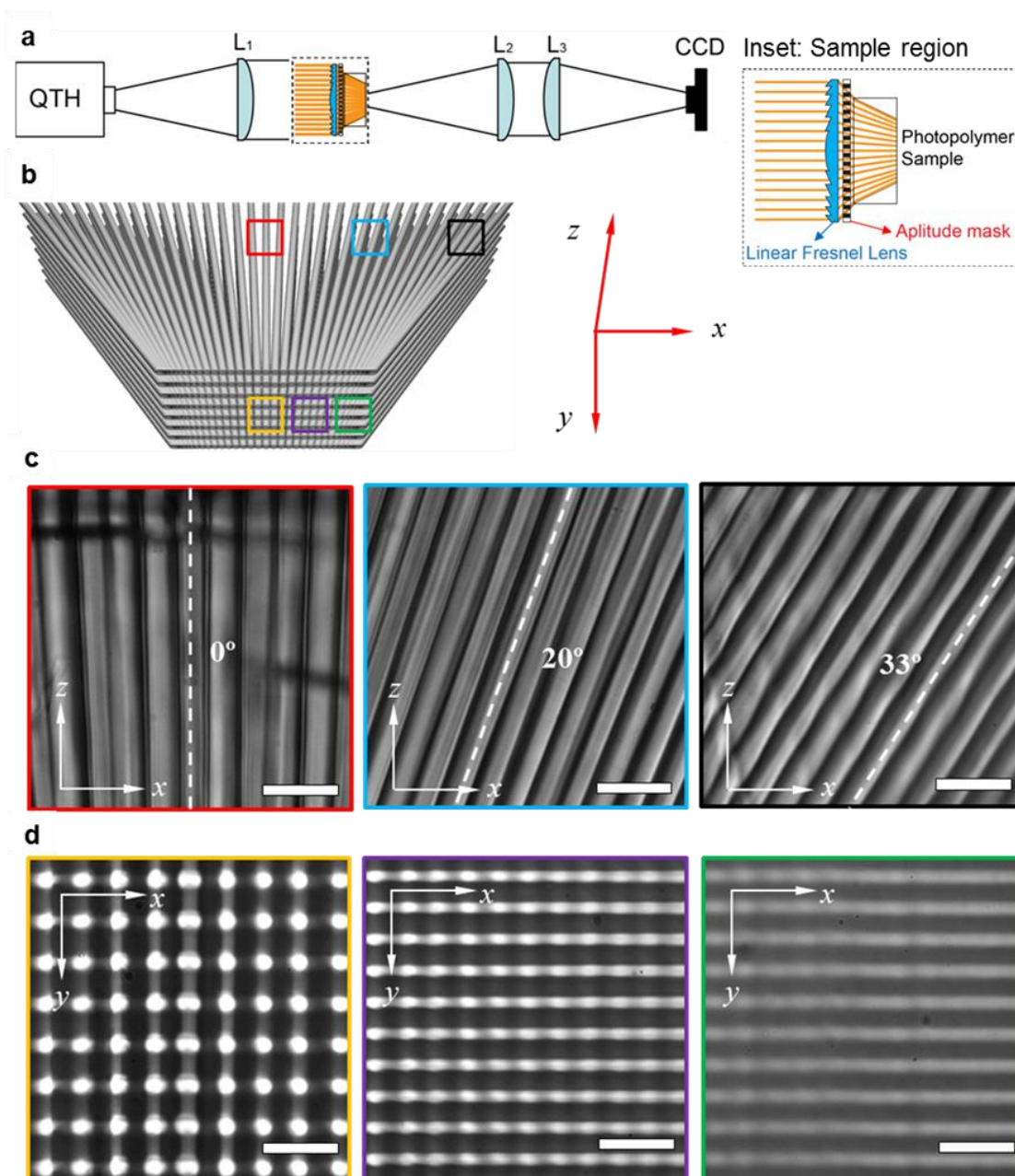


Figure 3.2. Fabrication and microstructural characterization of RDWEL. (a) Optical assembly employed to construct the RDWEL consists of a broad incandescent beam emitted by a quartz-tungsten-halogen (QTH) lamp, which is collimated by a plano-convex lens, focused by a linear Fresnel lens and patterned by an amplitude mask before entering a sample cell containing photopolymerisable epoxide fluid. The spatial intensity profile of the beam at the exit face of the sample was imaged through plano-convex lenses onto a CCD camera. The inset contains a magnified image of the converging light beams entering the sample. (b) Scheme of 3-D RDWEL with color-coded boxes that correspond to transmission optical micrographs of (c) longitudinal and (d) transverse cross-sections. Scale bar in (c) and (c) = 160 μm .

3.2.3. Seamless collection and waveguiding of light

We characterized the light collecting, guiding and transmission properties of the RDWEL with an incandescent beam, which possesses the spectral characteristics of ambient sunlight. Because they are generated by self-trapped incandescent light, the RDWEL waveguides are necessarily multimoded, polychromatic and guide incandescent light even under passive conditions. Moreover, because of their relatively large Δn (≥ 0.001)^[28] relative to the surroundings, these waveguides tightly confine optical intensity and prevent leakage into surrounding regions. Highly absorbent pigments^[37,38], which are employed to prevent light leakage between ommatidia in natural compound eyes are therefore not necessary in the RDWEL.

We first showed that light incident on the RDWEL entrance face at any angle within its FOV is always captured and waveguided to its exit face. In this experiment, we launched a broad, collimated beam of incandescent light onto the RDWEL entrance face; we then rotated the sample about its central axis an arc of $\pm 55^\circ$ (**Figure 3.3**) while acquiring intensity profiles of its exit face (at $z = 2.0$ mm) at intervals of 5° . In this way, the incidence angles of the probe beam spanned the entire FOV of the RDWEL and sampled its waveguide population with $\theta_{wg} = \pm 33^\circ$ (**Figure 3.3a**). Select images of the RDWEL exit face at probe incident angles = 0° , -10° , -20° , -30° , -40° , and -50° in **Figure 3.3b** correspond to a specific area ($1800 \mu\text{m} \times 1800 \mu\text{m}$) containing a sub-population of (~ 24 to ~ 36) (x) \times ~ 23 (y) waveguides observed as a square array of bright spots. Similar results were obtained at all incident angles, confirming that a sub-population of waveguides would always collect and efficiently guide light incident at any angle within the FOV of the RDWEL.

Light confinement is optimal in waveguides in the central region of each image in Figure 3.3b as evidenced by their discrete, well-defined spots; spots become increasingly blurred or smeared away from this region. This is because any given incidence angle of the probe beam always falls within the acceptance range of only a sub-population of waveguides. These efficiently confine and guide the beam as optical modes along their physical axes (θ_{wg}) and give rise to discrete spots at the output. For example, light incident at 0° falls within the acceptance ranges of a sub-population of ~ 7 waveguides with $\theta_{\text{wg}} \approx \pm 2^\circ$ (see Section S3.1, Supplementary Table S3.2). This is commensurate with the ~ 7 discrete spots along a single row in the leftmost image in the top row of Figure 3.3b. 1-D profiles of images in Figure 3.3b show that the waveguide density increases from ~ 7 in the vicinity of waveguides with $\theta_{\text{wg}} = 0^\circ$ to ~ 17 for $\theta_{\text{wg}} = -50^\circ$. The increase in density is accompanied by a corresponding decrease in angular separation as well as an increase in angular collection ranges of waveguides with $\theta_{\text{wg}} \gg 0^\circ$ (Section 3.1). This means that a greater number of waveguides with $\theta_{\text{wg}} \gg 0^\circ$ efficiently confine light at a given incidence angle. For example, light incident at -50° is captured by waveguides with $\theta_{\text{wg}} = -28.48^\circ$ to -2.43° (See supplementary Table S3.2), which according to calculations correspond to 25 waveguides and corresponds reasonably well with the number of discrete spots ~ 17 along a single row (x axis) in the rightmost image in the bottom row of Figure 3.3b.

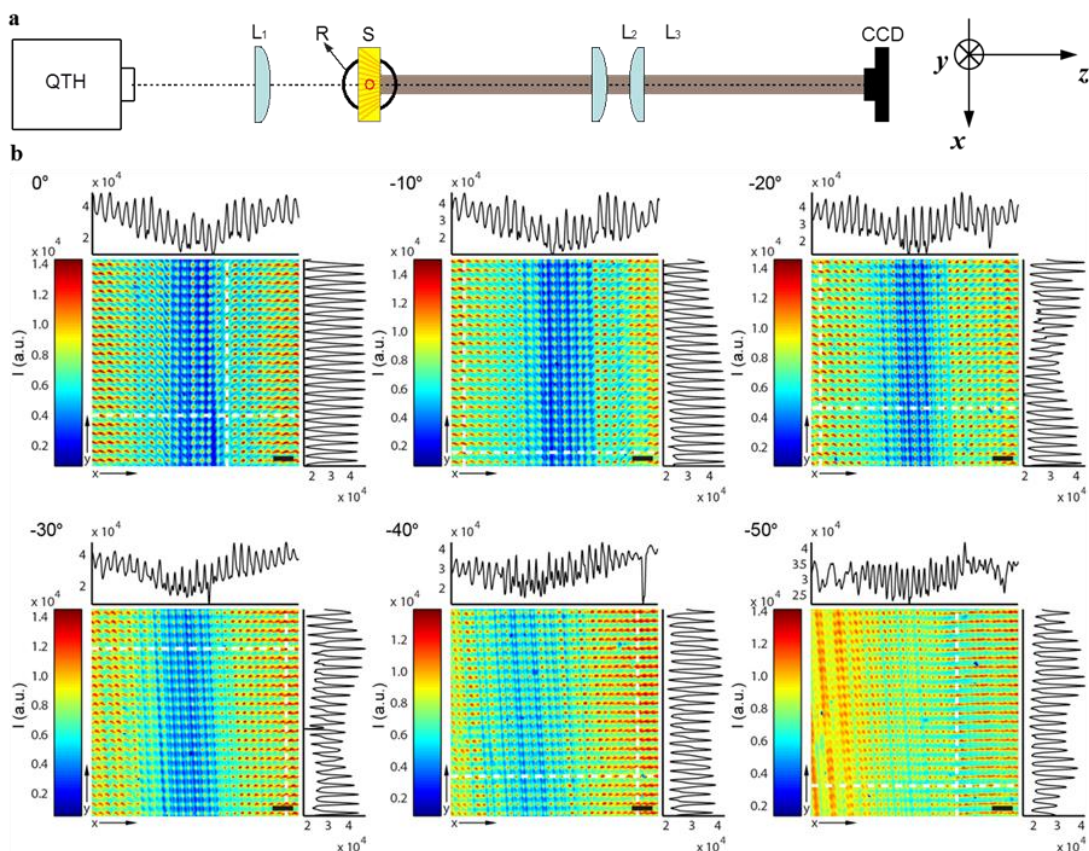


Figure 3.3. Seamless light collection in RDWEL. (a) Scheme of optical assembly employed to characterize light propagation through the RDWEL as a function of incidence angle. Light emitted by a QTH lamp is collimated by a planoconvex lens (L_1) and launched onto the entrance face of the RDWEL sample (S), which is placed on a rotation stage (R) and rotated about its central axis (along y axis) at 5° intervals from -55° to $+55^\circ$ with respect to the surface normal (z axis). The spatial intensity profiles at the exit face are imaged through a planoconvex lens pair (L_2 and L_3) onto a CCD camera. (b) Spatial profiles of the RDWEL exit face ($z = 2$ mm) acquired at probe beam incidence angles $= 0^\circ, -10^\circ, -20^\circ, -30^\circ, -40^\circ$ and -50° , respectively. 1-D traces along the x and y axes are provided. For all images, intensity color bars are provided together with scale bar $= 160 \mu\text{m}$.

3.2.4 Measuring the FOV

The FOV of the RDWEL is the cumulative angular collection ranges of its constituent waveguides. To experimentally determine this value and to confirm that it is seamless, we first divided the RDWEL waveguides into 23 sub-populations, each comprising 9 to 16 waveguides and identified by the physical axis (θ_{wg}) of the central

waveguide (**Figure 3.4**). We then measured the angular range over which the probe incandescent beam is captured by each sub-population and waveguided to the exit face. For these measurements, we rotated the RDWEL about its central axis so that the probe beam sampled only a specific subset of waveguides; for example, to probe the sub-population with $\theta_{\text{wg}} = 33^\circ$, accounting for refraction at the air-sample interface, the RDWEL was rotated about its central (y) axis by 55° . Keeping this angle fixed, the RDWEL and imaging components were simultaneously rotated over an arc of $\pm 8^\circ$. In this way, we effectively varied the incidence angle of the probe beam from 47° to 63° (*i.e.*, $55^\circ \pm 8^\circ$) while acquiring intensity profiles of the exit face at intervals of 0.5° . Measurements of acceptance ranges for the sub-population with $\theta_{\text{wg}} = 0^\circ$ are presented in Figure 3.4b; corresponding results for a control sample consisting of an unstructured but otherwise identical epoxide film are included for comparison. The images show that compared to the control, light collection and transmission occurs over a greater range of incidence angles in the RDWEL. Plots of optical intensity integrated over the waveguide sub-population against the incidence angle yielded acceptance ranges ($1/e^2$) respectively of 5.9° for the waveguide sub-population and 3.7° of the control, indicating an enhancement of 59% (Figure 3c). Identical measurements of the remaining 22 sub-populations yielded enhanced acceptance ranges from a minimum of 38% for $\theta_{\text{wg}} = -5^\circ$ to a maximum of 150% for $\theta_{\text{wg}} = -30^\circ$ (Figure 4d; additional details provided in Supplementary Table S3.3).

The cumulative acceptance ranges of the 23 sub-populations spanned -57.6° to 57.6° , yielding a continuous panoramic FOV of $\sim 115^\circ$, which corresponds to an enhancement of 83% relative to the control (Figure 3.4d). Both the absolute FOV

value and its enhancement are greater than those reported for previous WELs of $\sim 94^\circ$ and 66%, respectively.^[28] There is moreover considerable overlap between the angular collections ranges of waveguides; for example, sub-populations with $\theta_{\text{wg}} = +25^\circ$ and $+30^\circ$ possessed collection ranges from $+21.8^\circ$ to $+29.2^\circ$ and $+25.3^\circ$ to $+33.8^\circ$, respectively. As a result, the RDWEL seamlessly captures light over this continuous FOV. Significantly, the FOV of the RDWL is also much wider than all the planar artificial compound eyes ever reported, including 21° ,^[39] and 64.3° ^[40] for APCOs (Apposition compound-eye object), $70^\circ \times 10^\circ$,^[41] $58^\circ \times 46^\circ$,^[20] and $53.2^\circ \times 39.9^\circ$ ^[42] for artificial cluster eyes, and 90.4° for a catadioptric planar eye employing multiple mirrors^[34], etc. The FOV of this RDWEL also breaks the 110° latest record held by a wide-angle planar camera,^[35] and is comparable with some of the curved artificial compound eyes.^[33]

rotation stage (R). For measurements, S is rotated about its central axis (along y axis) to locate a specific sub-population of waveguides; S and all imaging components are then simultaneously rotated over an arc of $\pm 8^\circ$ at 0.5° intervals. Spatial intensity profiles at the exit face are imaged through a planoconvex lens pair (L_2 and L_3) onto a CCD camera. (b) Intensity profiles of the RDWEL exit face and control (bottom row) at different incidence angles of the probe beam. Results correspond to waveguide sub-population with $\theta_{wg} = 0^\circ$. Intensity color scale is provided. Magnified images within the inset show tight confinement of light within waveguides in the RDWEL. (c) Plots of integrated intensity versus probe incidence angle for RDWEL (red) and control (black). (d) A representation of the panoramic FOV determined by the cumulative, experimentally determined acceptance ranges of the 23 waveguide sub-populations (red) of the RDWEL. Equivalent plots for the control are provided (black). θ_{wg} of each sub-population is indicated in blue.

3.2.5. Panoramic imaging

Because of its enhanced FOV, the RDWEL is capable of panoramic imaging. To demonstrate, we made a camera by positioning a planar CCD chip flush with the RDWEL exit face (thickness = 1.5 mm) (Chip-sample spacing: ≈ 1.0 mm). Five stenciled shapes illuminated by incandescent light were then positioned over a panoramic plane at -45° , -19° , 0° , $+19^\circ$, and $+45^\circ$, respectively relative to the surface normal of the exit face of the RDWEL (**Figure 3.5a–b**). All five objects were simultaneously imaged onto the planar CCD chip (**Figure 3.5c**); regardless of their angle of incidence, all five images retained their clarity and spatial positions with a resolution of ~ 40 μm , which is determined by the diameter of each waveguide. We note that images of the objects propagated through an unstructured medium may still present on the chip, but they would suffer considerable blurring and loss of clarity due to the significant divergence associated with incandescent light as well as aberrations due to off-axis propagation.

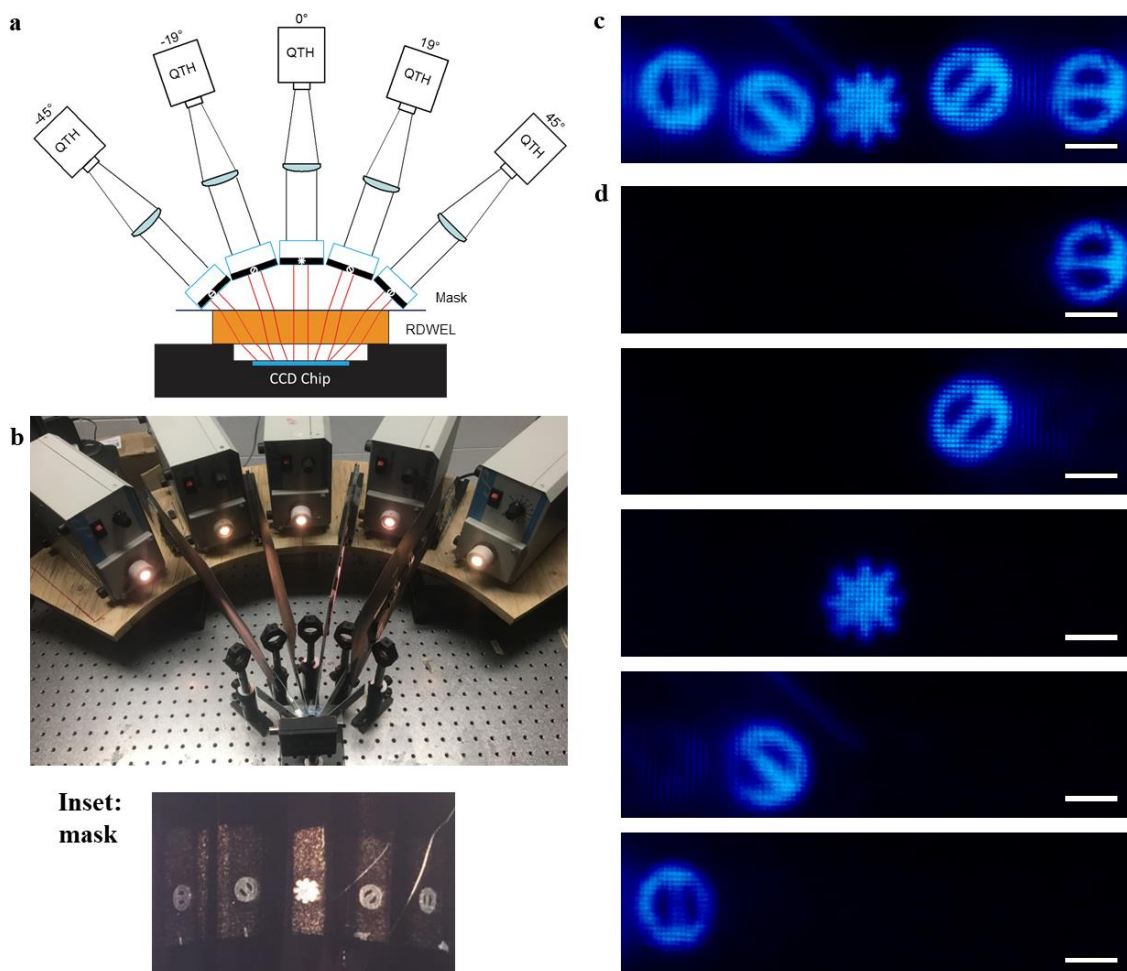


Figure 3.5. Panoramic imaging by RDWEL. (a) Scheme and (b) photograph of optical assembly for simultaneous panoramic imaging of five shapes. The inset shows the masks employed to generate the five shapes. Images of the five shapes that were (c) simultaneously and (d) sequentially recorded by the CCD chip at the RDWEL exit face. (Scale bar = 1 mm).

3.3. Conclusions and Outlook

RDWEL is a slim polymer film encoded with a radial distribution of waveguides, which confers a FOV of 115° . This corresponds to an 83 % enhancement relative to an unstructured but otherwise identical polymer film. To the best of our knowledge, the RDWEL possesses the largest known panoramic FOV for a planar structure. The overlapping acceptance angular ranges of its waveguides ensure that the FOV is

continuous and seamlessly captures light incident at any angle within this range. Distinct from other primarily lens-based, multicomponent planar eyes, the RDWEL is a single-component structure that is fabricated through a single, room-temperature technique requiring only low-energy incandescent sources in a soft, flexible polymer matrix. Equally significantly, because its waveguides are multimoded and polychromatic, the RDWEL is operable at all visible wavelengths both in the form of incandescent light (including sunlight) and narrowband sources (e.g. LEDs). Its large FOV coupled with its large density of waveguide elements (31, 000 over an area with $d = 1.6$ cm) and spatial resolution afforded by the ~ 40 μm waveguide diameter give RDWEL considerable potential in both imaging applications such as cameras, microscopes and endoscopes, as coatings in light-collection systems such as solar panels, smart windows and as conformal, beam-shaping coatings for light emitting devices. Finally, by tuning the fabrication method introduced here to generate waveguides with a range of θ_{wg} , it would be possible to further increase the FOV of the RDWEL. For example, a FOV = 180° could be obtained with θ_{wg} spanning $\pm 39.4^\circ$ in the same medium (see Supplementary Section S3.2). It would also be possible to generate RDWEL with solid-angle FOV by generating omnidirectional waveguide arrays. These studies are currently underway.

3.4. Materials and Methods

Photopolymerizable epoxide sols: The preparation of sols employed in the fabrication of the RDWELs has been detailed elsewhere.^[28,36,43] Briefly, 3, 4-epoxycyclohexylmethyl 3, 4-epoxycyclohexanecarboxylate (Sigma Aldrich,

Canada), epoxypropoxypropyl terminated polydimethylsiloxane (Gelest, USA), poly(tetrahydrofuran) (Sigma Aldrich, Canada), photosensitizer camphorquinone ($\lambda_{\text{max}} = 468 \text{ nm}$) and photoinitiator, bis (4-tert-butyl phenyl) iodoniumhexafluoro antimonite (Hampford Research Inc., USA) were added in 50.0 %, 26.0 %, 20.0 %, 2.5 %, and 1.5 % by weight, respectively. The mixture was stirred vigorously for 48 hrs. and filtered through a polytetrafluoroethylene (PTFE) membrane (0.2 μm pore size, Pall Corporation USA) before use. Sols were protected from exposure to ambient light at all times.

Optical assembly: The optical assembly employed for RDWEL fabrication is shown in Figure 3.2a. A broad beam of incandescent light ($\lambda = 320\text{--}800 \text{ nm}$) emitted by a quartz-tungsten-halogen (QTH) lamp (Cole-Parmer, USA) was first collimated by a plano-convex lens (f. l. = 250 mm, $d = 25.4 \text{ mm}$) before being focused by a linear Fresnel lens (f. l. = 7 mm, A.W.I. industries (USA) INC.) and then passed through a 2-D periodic amplitude mask ($\Lambda = 80 \mu\text{m}$). The mask was placed flush with the entrance face of an optically transparent, cylindrical cell ($d = 16 \text{ mm}$, pathlength (z) = 2.0 mm) containing the photopolymerizable epoxide sol. The 2-D spatially modulated beam irradiated the entire entrance face of the cell at an intensity of 16.9 mW cm^{-2} . The spatial intensity profile at the exit face of the sample cell ($z = 2.0 \text{ mm}$) was imaged through a pair of plano-convex lenses onto a high-resolution, progressive scan, charged-coupled device (CCD) (2040 pixels (H) x 1532 pixels (V) with a resolution of $3.2\mu\text{m pixel}^{-1}$; sensitivity range = 350 nm to 1150 nm; WinCamDTM digital camera, Data Ray Inc., USA).

Microstructural characterization: Transmission optical micrographs of longitudinal and transverse cross-sections of the RDWEL were acquired with an Olympus BX51 microscope (X5 magnification) equipped with a digital CCD camera (Q Imaging, RETIGA EXi, Mono 12-bit, non-cooled). Transverse micrographs of the 23 waveguide sub-populations in the RDWEL were acquired by mounting the sample on a self-designed micro-goniometer stage and gradually tilting it so that sub-populations of waveguides coincided in turn with the optic axis of the microscope. (See Supplementary Information S3.3).

Optical characterization of RDWEL: To demonstrate its radial distribution of waveguides and therefore its continuous, panoramic FOV, the RDWEL sample was mounted on a rotation stage with an angular resolution of $\pm 1^\circ$ (Figure 3.3a). Keeping the incident incandescent beam and imaging optics stationary, the sample was rotated from -50° to 50° with respect to the incident incandescent beam; its spatial intensity profile at the exit face (at $z = 2.0$ mm) was imaged through a plano-convex lens pair onto a CCD camera.

FOV of the RDWEL: The FOV of the whole RDWEL corresponds to the sum of the collection angular ranges of its constituent waveguides. To quantitatively determine its FOV, we divided the waveguide population of the RDWEL into 23 sub-populations, each comprising 9 to 16 waveguides, and measured their respective cumulative collection angle ranges. Each sub-population was centred about a waveguide with $\theta_{wg} = \pm 32.9^\circ, \pm 30.5^\circ, \pm 27.9^\circ, \pm 25.2^\circ, \pm 22.3^\circ, \pm 19.3^\circ, \pm 16.3^\circ, \pm 13.1^\circ, \pm 9.9^\circ, \pm 6.6^\circ, \pm 3.3^\circ$, and 0° , relative to z axis. For measurements, we rotated only the RDWEL about its central axis (Figure 3.4a) so that θ_{wg} coincided with the propagation axis (z) of the probe

incandescent beam; accounting for refraction, the RDWEL was therefore rotated by $\pm 55^\circ$, $\pm 50^\circ$, $\pm 45^\circ$, $\pm 40^\circ$, $\pm 35^\circ$, $\pm 30^\circ$, $\pm 25^\circ$, $\pm 20^\circ$, $\pm 15^\circ$, $\pm 10^\circ$, $\pm 5^\circ$ (and 0°) relative to its normal. Keeping the probe beam stationary, we then rotated the optical rail bearing the RDWEL, imaging lenses, the aperture placed before the lenses to filter stray light and CCD camera over a 16° arc (*i.e.*, $\pm 8^\circ$) about z and acquired spatial intensity profiles of the RDWEL exit face at 0.5° intervals. In this way, we determined the angular range over which each sub-population collected and waveguided light to the exit face of the RDWEL.

Panoramic imaging by the RDWELs: A set of five illuminated objects were placed along an angular range of -45° to 45° at a distance of ~ 4.5 mm from the entrance face of the RDWELs. Images of the five objects transmitted through the RDWEL both individually and simultaneously were captured with a planar CCD chip (image area 8.8×6.6 mm, 1360 (H) \times 1024 (V) of $6.45 \mu\text{m}$ square pixels; sensitivity range = 350 nm to 1150 nm; WinCamDTM digital camera, Data Ray Inc., USA), which was positioned at ~ 1 mm from its exit face. A neutral density filter (ND = 2) was placed between the sample and the chip.

Acknowledgement

Funding from the Natural Sciences and Engineering Research Council, Canadian Foundation for Innovation and McMaster University is gratefully acknowledged. We thank Mr. Idan Shmuel Yona for his assistance with FOV measurements and data processing. We are grateful to Dr. Dinesh Kumar Basker for valuable discussions.

References

- [1] N. J. Marshall, M. F. Land, C. a. King, T. W. Cronin, *Philos. Trans. R. Soc. B Biol. Sci.* **1991**, *334*, 33.
- [2] P. T. Weir, M. J. Henze, C. Bleul, F. Baumann-Klausener, T. Labhart, M. H. Dickinson, *J. Neurosci.* **2016**, *36*, 5397.
- [3] K. Kagawa, E. Tanaka, K. Yamada, S. Kawahito, J. Tanida, in (Eds.: J.-A. Conchello, C.J. Cogswell, T. Wilson, T.G. Brown), International Society For Optics And Photonics, **2012**, p. 822714.
- [4] K. Kagawa, K. Yamada, E. Tanaka, J. Tanida, *Electron. Commun. Japan* **2012**, *95*, 14.
- [5] J. Tanida, H. Akiyama, K. Kagawa, C. Ogata, M. Umeda, in (Eds.: A. Mahalanobis, A. Ashok, L. Tian, J.C. Petrucci, K.S. Kubala), International Society For Optics And Photonics, **2017**, p. 102220L.
- [6] C. Shi, Y. Wang, C. Liu, T. Wang, H. Zhang, W. Liao, Z. Xu, W. Yu, *Opt. Express* **2017**, *25*, 32333.
- [7] Y. M. Song, Y. Xie, V. Malyarchuk, J. Xiao, I. Jung, K. J. Choi, Z. Liu, H. Park, C. Lu, R. H. Kim, R. Li, K. B. Crozier, Y. Huang, J. A. Rogers, *Nature* **2013**, *497*, 95.
- [8] “Compound eyes for industry and smartphone,” can be found under <https://phys.org/news/2017-01-compound-eyes-industry-smartphone.html>, **2017**.
- [9] R. Shogenji, Y. Kitamura, K. Yamada, S. Miyatake, J. Tanida, *Appl. Opt.* **2004**, *43*, 1355.
- [10] M. Sieler, P. Schreiber, P. Dannberg, A. Br äuer, in (Eds.: H. Thienpont, P. Van Daele, J. Mohr, H. Zappe), International Society For Optics And Photonics, **2010**, p. 77161A.
- [11] M. Sieler, P. Schreiber, P. Dannberg, A. Br äuer, A. Tünnermann, *Appl. Opt.* **2012**, *51*, 64.
- [12] R. Horisaki, J. Tanida, *Opt. Lett.* **2011**, *36*, 121.
- [13] K. Pang, F. Fang, L. Song, Y. Zhang, H. Zhang, *J. Opt. Soc. Am. B* **2017**, *34*, B28.
- [14] N. Franceschini, *Proc. IEEE* **2014**, *102*, 751.
- [15] R. Leitel, A. Brückner, W. Buß S. Viollet, R. Pericet-Camara, H. Mallot, A. Br äuer, in (Eds.: H. Thienpont, J. Mohr, H. Zappe, H. Nakajima), International Society For Optics And Photonics, **2014**, p. 91300H.
- [16] D. Floreano, R. Pericet-Camara, S. Viollet, F. Ruffier, A. Brückner, R. Leitel, W. Buss, M. Menouni, F. Expert, R. Juston, M. K. Dobrzynski, G. L’Eplattenier, F. Recktenwald, H. a Mallot, N. Franceschini, *Proc. Natl. Acad. Sci. U. S. A.* **2013**, *110*, 9267.
- [17] D. Keum, D. S. Jeon, C. S. H. Hwang, E. K. Buschbeck, M. H. Kim, K.-H. Jeong, in *2016 IEEE 29th Int. Conf. Micro Electro Mech. Syst.*, IEEE, **2016**, pp. 636–639.

- [18] J. Duparré P. Dannberg, P. Schreiber, A. Bräuer, A. Tünnermann, *Appl. Opt.* **2005**, *44*, 2949.
- [19] A. Brückner, J. Duparré A. Bräuer, A. Tünnermann, *Opt. Express* **2006**, *14*, 12076.
- [20] A. Brueckner, J. Duparré R. Leitel, P. Dannberg, A. Bräuer, A. Tünnermann, *Opt. Express* **2010**, *18*, 24379.
- [21] Z. Deng, F. Chen, Q. Yang, H. Bian, G. Du, J. Yong, C. Shan, X. Hou, *Adv. Funct. Mater.* **2016**, *26*, 1995.
- [22] D. Radtke, J. Duparré U. D. Zeitner, A. Tünnermann, *Opt. Express* **2007**, *15*, 3067.
- [23] D. Wu, J.-N. Wang, L.-G. Niu, X. L. Zhang, S. Z. Wu, Q.-D. Chen, L. P. Lee, H. B. Sun, *Adv. Opt. Mater.* **2014**, *2*, 751.
- [24] D. Keum, H. Jung, K. H. Jeong, *Small* **2012**, *8*, 2169.
- [25] K.-H. Jeong, J. Kim, L. P. Lee, *Science* **2006**, *312*, 557.
- [26] H. Jung, K.-H. Jeong, *Opt. Express* **2009**, *17*, 14761.
- [27] J. Kim, K.-H. Jeong, L. P. Lee, *Opt. Lett.* **2005**, *30*, 5.
- [28] I. D. Hosein, H. Lin, M. R. Ponte, D. K. Basker, M. A. Brook, K. Saravanamuttu, *Adv. Funct. Mater.* **2017**, *27*, 1702242.
- [29] M. Mitchell, M. Segev, *Nature* **1997**, *387*, 880.
- [30] J. Zhang, K. Saravanamuttu, *J. Am. Chem. Soc.* **2006**, *128*, 14913.
- [31] J. Zhang, K. Kasala, A. Rewari, K. Saravanamuttu, *J. Am. Chem. Soc.* **2006**, *128*, 406.
- [32] S. Trillo, W. Torruellas, *Spatial Solitons*, Springer Berlin Heidelberg, Berlin, Heidelberg, **2001**.
- [33] S. Wu, T. Jiang, G. Zhang, B. Schoenemann, F. Neri, M. Zhu, C. Bu, J. Han, K.-D. Kuhnert, *Artif. Intell. Rev.* **2017**, *48*, 573.
- [34] H. Deng, X. Gao, M. Ma, Y. Li, H. Li, J. Zhang, X. Zhong, *Opt. Express* **2018**, *26*, 12455.
- [35] C. Gassner, J. Dunkel, A. Oberdörster, A. Brückner, in *MOEMS Miniaturized Syst. XVII* (Eds.: W. Piyawattanametha, Y.-H. Park, H. Zappe), SPIE, **2018**, p. 10.
- [36] D. K. Basker, M. A. Brook, K. Saravanamuttu, *J. Phys. Chem. C* **2015**, *119*, 20606.
- [37] D.-E. Nilsson, A. Kelber, *Arthropod Struct. Dev.* **2007**, *36*, 373.
- [38] D. G. Stavenga, M. F. Wehling, G. Belušič, *J. Physiol.* **2017**, *595*, 5481.
- [39] J. Duparré P. Dannberg, P. Schreiber, A. Bräuer, A. Tünnermann, *Appl. Opt.* **2004**, *43*, 4303.
- [40] J. Duparré F. Wippermann, P. Dannberg, A. Reimann, *Opt. Express* **2005**, *13*, 10539.
- [41] J. Duparré P. Schreiber, A. Matthes, E. Pshenay-Severin, A. Bräuer, A. Tünnermann, R. Völkel, M. Eisner, T. Scharf, *Opt. Express* **2005**, *13*, 889.
- [42] J. Meyer, A. Brückner, R. Leitel, P. Dannberg, A. Bräuer, A. Tünnermann, *Opt. Express* **2011**, *19*, 17506.
- [43] J. V. Crivello, *J. Polym. Sci. Part A Polym. Chem.* **2009**, *47*, 866.

Supporting Information

Table of Content

S3.1 Determination of angles of all the waveguides in the RDWEL.....	125
S3.2 Calculation of the angular acceptance ranges of waveguides with slant angle but flat entrance face.....	127
S3.3 Transverse micrographs of all the 23 waveguide sub-populations.....	131
S3.4 Clarification of the FOV measurements.....	132
S3.5 FOV summary of the waveguide sub-populations of the RDWEL	133
References.....	134

S3.1 Determination of angles of all the waveguides in the RDWEL

To find out the angle of all the waveguides in the RDWEL, we employed ray tracing as shown in Figure S3.1. The pitch curvature of the Fresnel lens is modified so that collimated light incident from normal would focus at the same point (Focal point) in air (See the blue light rays in Figure S3.1). When placing a photomask and the polymerisable sol behind the Fresnel lens, the normal incident light would refract multiple times at the interfaces (See the red traces), each time follows Snell's law.

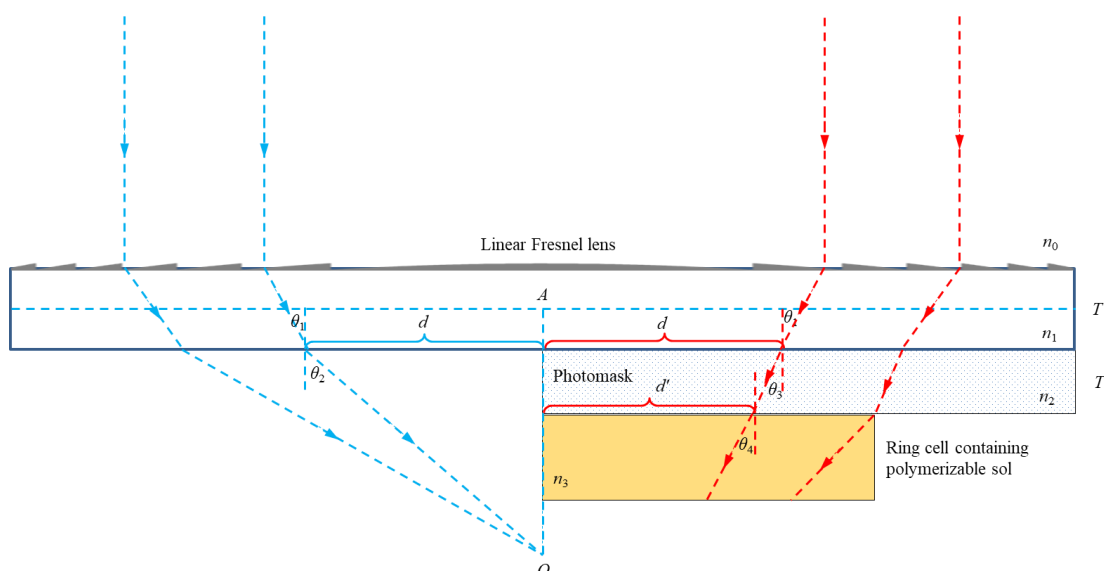


Figure S3.1. Schematic diagram showing the ray tracing method used to indicate the angular directions of the waveguides in the RDWELs. Blue lines depict the transmission traces of the normal incident light through a bare Fresnel lens. The red ones indicate the transmission traces through the Fresnel lens, a photomask and the photopolymerisable sample.

Based on the schematic diagram and the light rays, we can obtain the following formulas:

$$\begin{aligned} \tan\theta_2 &= d / (FL - T/2) & n_0 \times \sin\theta_2 &= n_1 \times \sin\theta_1 \\ n_2 \times \sin\theta_3 &= n_1 \times \sin\theta_1 & n_2 \times \sin\theta_3 &= n_3 \times \sin\theta_4 \\ d' &= d - T' \times \tan\theta_3 \end{aligned}$$

Where $n_0 = 1.00$, $n_1 = 1.46$, $n_2 = 1.55$, $n_3 = 1.51$, $FL = 7$ mm, $T = 2$ mm, and $T' = 1.5$ mm.

By assigning d with different numbers and substitute the above parameters, we can find out the angles of the beam before (in air) and after refracting into the photopolymerisable sample at different entrance points. The refraction angles versus off-centered position is plotted in Figure S3.2.

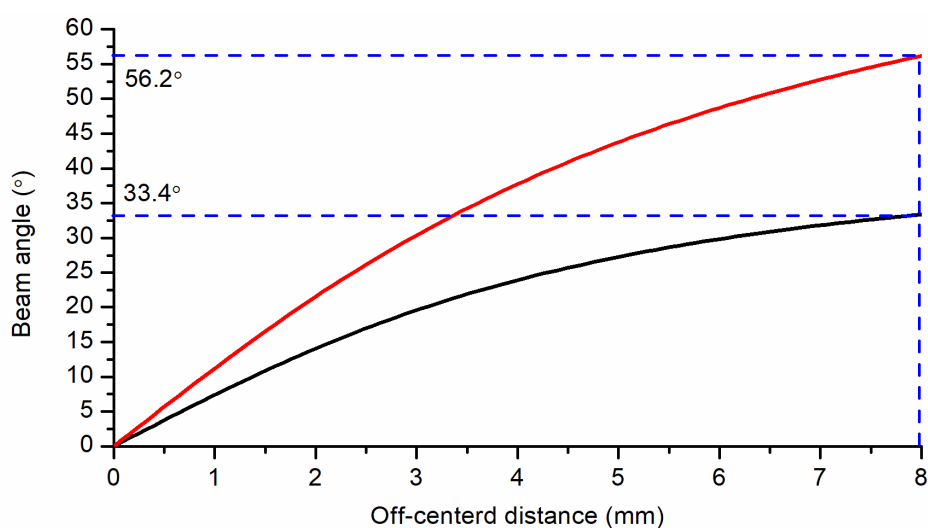


Figure S3.2. Plots showing the refraction angles of the beam before (red curve) and after (black curve) refracting into the photopolymer versus the off-centered distance of their starting point at the entrance face of the RDWEL.

Since we place a photomask in front of the sample cell, the broad beam would split into discrete microscopic light rays and subsequently inscribe the waveguides. As the photomask has a periodicity of $80 \mu\text{m}$, the off-centered positions of waveguides at the entrance face of the RDWEL are located every $80 \mu\text{m}$. Therefore, By assigning d' (off-centered distance, see Figure S3.1) with values from 0 mm to 8 mm (radius of the ring shaped sample cell) with 0.08 mm intervals, we can find out the angles of all the waveguides in the RDWEL. (As the RDWEL is symmetric, we only care about half of the waveguides).

Table S3.1 Summary of the angles of all the waveguides in the RDWEL

d' / mm	$\theta_{\text{wg}} / ^\circ$								
0.00	0.00	1.60	11.52	3.20	20.53	4.80	26.66	6.40	30.70
0.08	0.60	1.68	12.04	3.28	20.90	4.88	26.91	6.48	30.86
0.16	1.21	1.76	12.56	3.36	21.26	4.96	27.15	6.56	31.01
0.24	1.81	1.84	13.07	3.44	21.62	5.04	27.38	6.64	31.17
0.32	2.41	1.92	13.56	3.52	21.97	5.12	27.61	6.72	31.32
0.40	3.01	2.00	14.05	3.60	22.31	5.20	27.84	6.80	31.47
0.48	3.61	2.08	14.54	3.68	22.64	5.28	28.06	6.88	31.61
0.56	4.20	2.16	15.02	3.76	22.97	5.36	28.27	6.96	31.76
0.64	4.79	2.24	15.49	3.84	23.29	5.44	28.48	7.04	31.90
0.72	5.37	2.32	15.95	3.92	23.61	5.52	28.69	7.12	32.03
0.80	5.96	2.40	16.41	4.00	23.92	5.60	28.89	7.20	32.17
0.88	6.54	2.48	16.86	4.08	24.22	5.68	29.09	7.28	32.30
0.96	7.11	2.56	17.29	4.16	24.51	5.76	29.28	7.36	32.43
1.04	7.68	2.64	17.72	4.24	24.80	5.84	29.47	7.44	32.55
1.12	8.25	2.72	18.15	4.32	25.09	5.92	29.66	7.52	32.68
1.20	8.81	2.80	18.57	4.40	25.36	6.00	29.84	7.60	32.80
1.28	9.36	2.88	18.97	4.48	25.63	6.08	30.02	7.68	32.92
1.36	9.91	2.96	19.37	4.56	25.90	6.16	30.19	7.76	33.04
1.44	10.45	3.04	19.76	4.64	26.16	6.24	30.36	7.84	33.15
1.52	10.99	3.12	20.15	4.72	26.41	6.32	30.53	7.92	33.26
								8.00	33.37

S3.2 Calculation of the angular acceptance ranges of waveguides with slant angle but flat entrance face

A slanted waveguide with flat surface is depicted in Figure S3.3. The waveguide angle, the corresponding refraction angle of the waveguide angle in air, and the boundary angles of the acceptance range are written as θ_{wg} , and θ_{rwg} , α and β , respectively (relative to the z axis). The refractive indices of air, waveguide core, and waveguide cladding are recorded as n_0 , n_{core} , and n_{cladding} , respectively. The beams which incident onto the entrance face of the waveguides at the boundary angles are naturally refracted at the air-waveguide interface, then suffer total internal reflection

(TIR) at the core-cladding interface of the waveguide (See the red and black traces). The critical angle at which total internal reflection occurs is written as θ_c (relative to the normal of the waveguide wall).

To find out the angular acceptance range of a slant waveguide, we need to apply Snell's law twice - firstly at the core-cladding interface of the waveguide, secondly at air-waveguide interfaces. Therefore, we can generate the following formulas:

$$n_{\text{core}} \times \sin\theta_c = n_{\text{cladding}} \times \sin 90^\circ$$

$$n_0 \times \sin\alpha = n_{\text{core}} \times \sin[\theta_{\text{wg}} - (90^\circ - \theta_c)]$$

$$n_0 \times \sin\beta = n_{\text{core}} \times \sin[\theta_{\text{wg}} + (90^\circ - \theta_c)]$$

In our case of study, n_0 , n_{core} , and n_{cladding} are 0, 1.511, and 1.510 ($\Delta n = 0.001$)^[1] respectively. With this information, we calculated the acceptance ranges of different slanted waveguides (waveguide angle refer to that presented in Table S3.1), as shown in Table S3.2. (Note: $(\theta_{\text{rwg}} - \alpha)$ and $(\beta - \theta_{\text{rwg}})$ refer to θ_1 and θ_2 in Figure 3.1a in the manuscript).

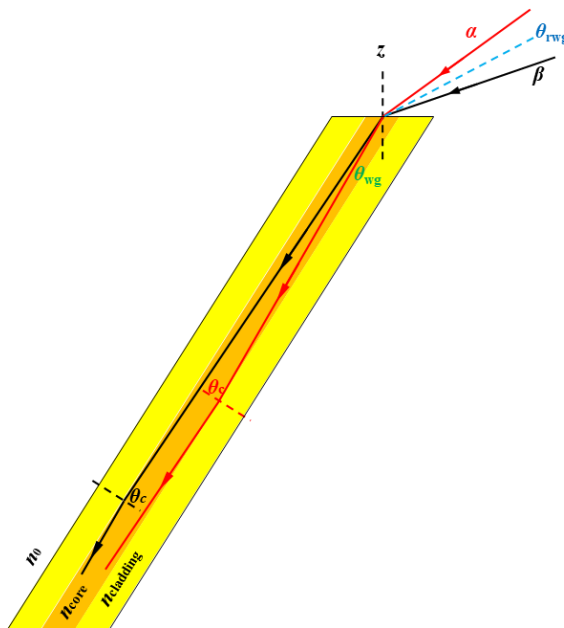


Figure S3.3. A schematic diagram of ray tracing in a slant waveguide with flat surface.

Table S3.2 Acceptance ranges (in the form of boundary angles) of waveguides with different slant angles but flat entrance faces

$\theta_{\text{wg}} / ^\circ$	$\theta_{\text{rwg}} / ^\circ$	$\alpha / ^\circ$	$\beta / ^\circ$	$(\theta_{\text{rwg}} - \alpha) / ^\circ$	$(\beta - \theta_{\text{rwg}}) / ^\circ$
0.00	0.00	-3.15	3.15	3.15	3.15
0.60	0.91	-2.24	4.06	3.15	3.15
1.21	1.82	-1.33	4.98	3.15	3.15
1.81	2.73	-0.42	5.89	3.15	3.16
2.41	3.64	0.49	6.80	3.15	3.16
3.01	4.54	1.39	7.70	3.15	3.16
3.61	5.45	2.30	8.62	3.15	3.17
4.20	6.35	3.20	9.52	3.15	3.17
4.79	7.24	4.09	10.42	3.15	3.18
5.37	8.13	4.97	11.31	3.16	3.18
5.96	9.02	5.86	12.21	3.16	3.19
6.54	9.90	6.74	13.09	3.16	3.19
7.11	10.78	7.61	13.98	3.17	3.20
7.68	11.65	8.48	14.86	3.17	3.21
8.25	12.51	9.34	15.73	3.18	3.21
8.81	13.38	10.20	16.60	3.18	3.22
9.36	14.22	11.04	17.45	3.19	3.23
9.91	15.07	11.88	18.31	3.19	3.24
10.45	15.90	12.71	19.15	3.20	3.25
10.99	16.73	13.52	19.99	3.20	3.26
11.52	17.55	14.34	20.82	3.21	3.27
12.04	18.36	15.14	21.64	3.22	3.28
12.56	19.16	15.94	22.45	3.22	3.29
13.07	19.96	16.73	23.26	3.23	3.30
13.56	20.74	17.50	24.05	3.24	3.31
14.05	21.51	18.26	24.84	3.25	3.32
14.54	22.28	19.02	25.61	3.26	3.34
15.02	23.03	19.76	26.38	3.27	3.35
15.49	23.78	20.50	27.14	3.28	3.36
15.95	24.52	21.23	27.90	3.29	3.38
16.41	25.25	21.95	28.64	3.30	3.39
16.86	25.97	22.66	29.37	3.31	3.40
17.29	26.67	23.35	30.09	3.32	3.42
17.72	27.37	24.04	30.80	3.33	3.43
18.15	28.06	24.72	31.51	3.34	3.45
18.57	28.74	25.38	32.20	3.35	3.46
18.97	29.40	26.04	32.88	3.37	3.48

19.37	30.06	26.68	33.55	3.38	3.50
19.76	30.70	27.31	34.22	3.39	3.51
20.15	31.34	27.94	34.87	3.40	3.53
20.53	31.97	28.55	35.52	3.42	3.55
20.90	32.59	29.16	36.16	3.43	3.57
21.26	33.20	29.76	36.79	3.44	3.58
21.62	33.80	30.35	37.40	3.46	3.60
21.97	34.39	30.92	38.01	3.47	3.62
22.31	34.97	31.49	38.61	3.48	3.64
22.64	35.55	32.05	39.20	3.50	3.66
22.97	36.11	32.60	39.79	3.51	3.68
23.29	36.66	33.13	40.36	3.53	3.70
23.61	37.21	33.67	40.93	3.54	3.72
23.92	37.75	34.19	41.48	3.56	3.74
24.22	38.27	34.70	42.03	3.57	3.76
24.51	38.79	35.20	42.57	3.59	3.78
24.80	39.31	35.70	43.11	3.60	3.80
25.09	39.81	36.19	43.63	3.62	3.82
25.36	40.30	36.67	44.15	3.64	3.84
25.63	40.79	37.14	44.65	3.65	3.87
25.90	41.27	37.60	45.15	3.67	3.89
26.16	41.74	38.05	45.65	3.69	3.91
26.41	42.20	38.50	46.14	3.70	3.93
26.66	42.66	38.94	46.62	3.72	3.96
26.91	43.11	39.38	47.09	3.74	3.98
27.15	43.56	39.80	47.56	3.75	4.00
27.38	43.99	40.22	48.02	3.77	4.03
27.61	44.42	40.63	48.47	3.79	4.05
27.84	44.84	41.03	48.91	3.81	4.08
28.06	45.25	41.43	49.35	3.82	4.10
28.27	45.66	41.82	49.78	3.84	4.12
28.48	46.06	42.20	50.21	3.86	4.15
28.69	46.46	42.58	50.63	3.88	4.17
28.89	46.85	42.95	51.05	3.89	4.20
29.09	47.23	43.32	51.46	3.91	4.23
29.28	47.61	43.68	51.86	3.93	4.25
29.47	47.98	44.03	52.26	3.95	4.28
29.66	48.34	44.38	52.65	3.97	4.30
29.84	48.71	44.72	53.04	3.99	4.33
30.02	49.06	45.06	53.42	4.00	4.36
30.19	49.41	45.39	53.79	4.02	4.38
30.36	49.76	45.71	54.17	4.04	4.41
30.53	50.09	46.03	54.53	4.06	4.44
30.70	50.43	46.35	54.89	4.08	4.47

30.86	50.75	46.66	55.25	4.10	4.49
31.01	51.08	46.96	55.60	4.12	4.52
31.17	51.40	47.26	55.95	4.14	4.55
31.32	51.71	47.56	56.29	4.16	4.58
31.47	52.02	47.85	56.63	4.17	4.61
31.61	52.33	48.13	56.96	4.19	4.64
31.76	52.63	48.42	57.30	4.21	4.67
31.90	52.93	48.69	57.62	4.23	4.70
32.03	53.22	48.96	57.94	4.25	4.72
32.17	53.50	49.23	58.26	4.27	4.75
32.30	53.79	49.50	58.58	4.29	4.79
32.43	54.07	49.76	58.88	4.31	4.82
32.55	54.34	50.01	59.19	4.33	4.85
32.68	54.61	50.26	59.49	4.35	4.88
32.80	54.88	50.51	59.79	4.37	4.91
32.92	55.15	50.76	60.09	4.39	4.94
33.04	55.41	51.00	60.38	4.41	4.97
33.15	55.66	51.24	60.67	4.43	5.00
33.26	55.92	51.47	60.95	4.45	5.03
33.37	56.17	51.70	61.23	4.47	5.06

As θ_{wg} increases, the outer boundary of the acceptance cone (β) also increases. By extending the table above, we obtained the $\theta_{\text{wg}} \approx 39.35^\circ$ when β is approaching 90° . Therefore, a FOV = 180° could be obtained if the peripheral waveguides of a RDWEL are oriented at $\theta_{\text{wg}} = \pm 39.35^\circ$.

S3.3 Transverse micrographs of all the 23 waveguide sub-populations

To characterize the transverse cross-sections of the entire population of radially distributed waveguides in the RDWEL, we mounted the sample on a micro-goniometer stage and monotonically tilted it so that sub-populations of waveguides coincided in turn with the optic axis of the microscope. The micrographs are shown in Figure S3.4.

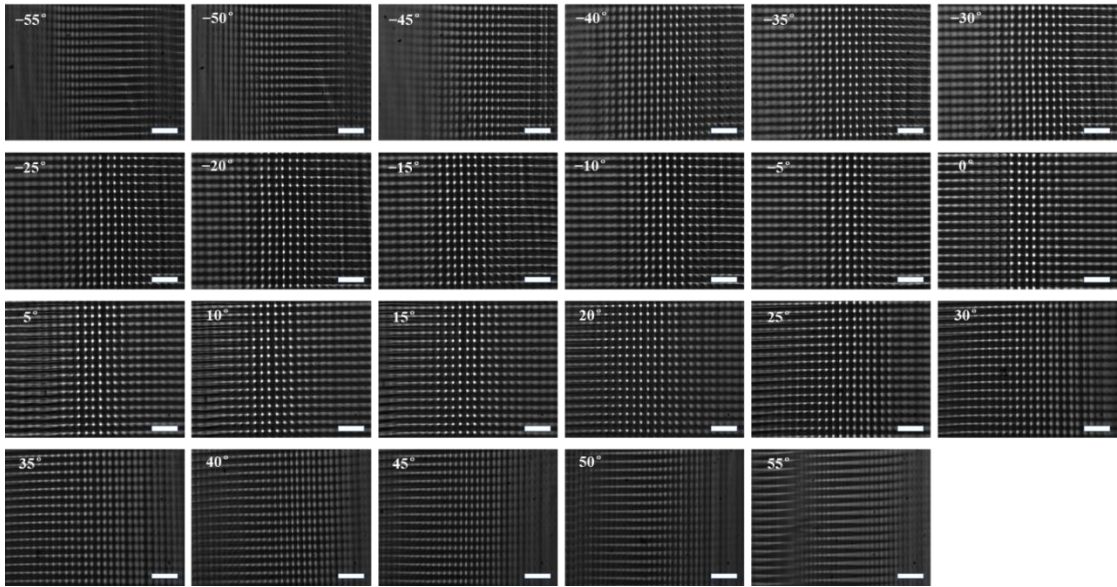


Figure S3.4. Transverse micrographs of all the 23 waveguide sub-populations of the RDWEL. The tilting angle are labeled. Scale bar = 250 μm .

S3.4 Clarification of the FOV measurements

From Table S3.2, we can see the refraction angle of a $33^\circ (\theta_{\text{wg}})$ waveguide is $55.33^\circ (\theta_{\text{rwg}})$, the corresponding boundary angles are $\alpha = 50.92^\circ$ and $\beta = 60.29^\circ$. (all angles are relative to the surface normal of the whole RDWEL sample).

During the FOV measurement, we rotated the sample by $55^\circ (\approx \theta_{\text{rwg}})$ first to probe the 33° waveguide sub-population of the RDWEL, we then rotated the whole optical assembly except the light source by -8° to 8° , so that the angular range of the incident light spans from 47° to 63° relative to the surface normal of the whole RDWEL sample, which cover the acceptance range (between 50.92° and 60.29°) of the 33° waveguide sub-populations.

Certainly we can rotate the RDWEL sample first by an angle other than the refraction angle ($\sim 55^\circ$), for instance any angle between $(60.29^\circ - 8^\circ)$ and $(50.92^\circ + 8^\circ)$, the subsequent angular range of the incident light would always cover the acceptance

range of the 33 ° waveguide sub-population, however, we used the refraction angle ($\theta_{\text{rwg}} = 55^\circ$) on the one hand for the simplicity (directly calculated from the refraction angle of the waveguide); on the other hand the refraction angle of the waveguide remains very close to the center of the boundary angles ($\theta_{\text{rwg}} = 55^\circ$, $\alpha = 50.92^\circ$ and $\beta = 60.29^\circ$) (Also see the last two columns of Table S3.2).

For the FOV measurement of other waveguide sub-populations, we can adopt the method we describe above. We first rotate the RDWEL by θ_{rwg} , where θ_{rwg} corresponds to the refraction angle of any of the 22 waveguide sub-populations (with central angle of θ_{wg}). We then rotate the optical components except the light source by -8° to 8° . The sampling angular range of the incident light would always cover the angular range of the waveguide sub-populations.

S3.5 FOV summary of the waveguide sub-populations of the RDWEL

Table S3.3 Summary of the FOVs of the 23 waveguide sub-populations in the RDWEL

Sample	FOV Range ^b / °	FOV value / °	Enhanced FOV	Sample	FOV Range ^b / °	FOV value / °	Enhanced FOV
-55 °	RDWEL	-57.6 ~ -51.6	6.0	5 °	RDWEL	1.5~9.0	7.5
	Control	-56.8 ~ -53.2	3.6		Control	3.1~6.8	3.7
-50 °	RDWEL	-53.2 ~ -46.8	6.4	10 °	RDWEL	7.3~13.0	5.7
	Control	-51.7 ~ -48.1	3.6		Control	8.2~11.9	3.7
-45 °	RDWEL	-48.2 ~ -42.1	6.1	15 °	RDWEL	11.9~17.9	6.0
	Control	-46.8 ~ -43.1	3.7		Control	13.1~16.8	3.7
-40 °	RDWEL	-43.6 ~ -36.2	7.4	20 °	RDWEL	16.6~23.9	7.3
	Control	-41.8 ~ -38.2	3.6		Control	18.2~21.8	3.6
-35 °	RDWEL	-38.4 ~ -32.1	6.3	25 °	RDWEL	21.8~29.2	7.4

	Control	-36.8 ~ -33.1	3.7		Control	23.1~26.8	3.7	
-30 °	RDWEL	-34.6 ~ -25.6	9.0	150%	RDWEL	25.3~33.8	8.5	136%
	Control	-31.8 ~ -28.2	3.6		Control	28.2~31.8	3.6	
-25 °	RDWEL	-28.9 ~ -21.7	7.2	95%	RDWEL	30.9~39.3	8.4	127%
	Control	-26.8 ~ -23.1	3.7		Control	33.2~36.9	3.7	
-20 °	RDWEL	-23.3 ~ -17.2	6.1	69%	RDWEL	35.5~43.9	8.4	133%
	Control	-21.8 ~ -18.2	3.6		Control	38.2~41.8	3.6	
-15 °	RDWEL	~18.0 ~ -12.6	5.4	46%	RDWEL	41.4~48.4	7.0	89%
	Control	-16.8 ~ -13.1	3.7		Control	43.1~46.8	3.7	
-10 °	RDWEL	-12.6 ~ -7.3	5.3	47%	RDWEL	47.3~53.0	5.7	58%
	Control	-11.8 ~ -8.2	3.6		Control	48.2~51.8	3.6	
-5 °	RDWEL	-7.4 ~ -2.3	5.1	38%	RDWEL	52.0~57.6	5.6	56%
	Control	-6.9 ~ -3.2	3.7		Control	53.2~56.8	3.6	
0 °	RDWEL	-2.9 ~ 3.0	5.9	59%				
	Control	-1.9 ~ 1.8	3.7					

^a determined at $1/e^2$ of the plots.

References

- [1] I. D. Hosein, H. Lin, M. R. Ponte, D. K. Basker, M. A. Brook, K. Saravanamuttu, *Adv. Funct. Mater.* **2017**, *27*, 1702242.

Chapter 4

Waveguide-Imprinted Polymer Slim Films: Beam Steering Coatings for Solar Cells

Hao Lin, Saeid Biria, Fu-Hao Chen, Ian D. Hosein and Kalaichelvi Saravanamuttu

Content of this chapter has been submitted to *ACS Photonics*.

HL carried out experiments and analysis. KS, HL and IDH conceived the project. IDH carried out preliminary experiments and data processing, which were later updated by HL. SB and F-H C carried out EQE measurements and some simulations. KS and HL wrote the manuscript.

Abstract

We report that transparent polymer coatings imprinted with tilted planar waveguides significantly reduce optical loss caused by scattering of incident light by the front metal contacts of solar cells. A periodic array of planar waveguides oriented at specific angles with respect to the film's surface normal efficiently captures and steers incident light away from contacts and in this way, suppresses scattering. These beam steering films are fabricated in a single, room temperature step by self-trapped incandescent beams, which inscribe multimode planar waveguides oriented at angles ranging from 0° to 2.7° in photopolymerizable epoxide resin. We characterized the microstructural and optical properties of the films and demonstrated their ability to deflect incident white light – comparable to sunlight - by as much as $180\ \mu\text{m}$ from the typically . Solar cells coated with beam steering films showed significant enhancements in external quantum efficiency (EQE) of up to 4.42 % relative to unstructured films. This first demonstration of waveguide-based deflection of light from metal contacts represents a facile, inexpensive, low energy approach to EQE enhancement, which can be integrated without disrupting the well-established solar cell manufacturing technologies.

4.1. Introduction

The extensively employed Si solar cell¹ is typically patterned with Ag contacts - referred to as “fingers” or “bus bars” - which efficiently extract photo-generated charge carriers. However, shading, reflection and scattering of light incident on these metallic top contacts lead to optical losses of up to 10%.²⁻⁴ Although losses can be reduced by tailoring the shape and size of the contacts⁵⁻⁹ or relocating them to the back surfaces of solar cells,¹⁰⁻¹² these approaches involve disrupting mature fabrication technologies. The native structure of the solar cell can be preserved by configuring deflective¹³⁻¹⁵ or diffractive¹⁶⁻¹⁸ elements within its coating or encapsulant: for example, laser-inscribed scattering and diffractive structures in an ethylene vinyl acetate encapsulant reduced optical shadowing by up to 17% with a corresponding, calculated increase of 0.7% to 1.2% in photocurrent,¹⁴ while diffractive gratings embedded in the cover yielded up to 2.8% increase in photon flux.¹⁸ In another example, a “front side diffuser” created by laser-roughening the cover regions directly above the metal contacts resulted in an increase in short circuit current (J_{SC}) of up to 3.3%,¹⁷ whereas screen-imprinted polystyrene beads in an acrylic resin coating yielded a 5.2% increase in external quantum efficiency (EQE).¹⁶ Periodic prisms within an encapsulant achieved 5.7% enhancement in J_{SC} and 5% increase in EQE;¹³ prismatic freeform surfaces exhibiting cloaking behaviour led to increases of 7.3% and 9.3%, respectively in J_{SC} and power conversion efficiency, respectively.¹⁵

We now show that slim (3 mm) polymer beam steering coatings imprinted with planar waveguides decrease the losses associated with the metal contacts of Si solar cells. Our approach relies on a periodic array of multimode, multiwavelength planar

waveguides, which confine and steer incident light away from the metal contacts onto adjacent Si surfaces (**Figure 4.1a**). The planar waveguides both decrease optical loss due to scatter but also deliver optical intensity to active regions of the solar cell and in this way, contribute to a significant increase in conversion efficiency.^{19–23} These beam steering coatings are generated in a single, room temperature technique by generating self-trapped beams of white incandescent light in an epoxide matrix, which was selected for its transparent and thermomechanical stability. Because they are self-inscribed by incandescent beams, the planar waveguides can support the multiple modes and wavelengths of these optical fields – and therefore, sunlight. We detail below the working principles, fabrication and characterization of the beam steering films and then examine their effectiveness as coatings for commercially available Si solar cells.

4.2. Results and Discussion

4.2.1. Working Principles

Figure 4.1 summarizes the working principles of the beam steering coating, which consists of a ~ 3000 μm -thick polymer film imprinted with a periodic array of slab waveguides oriented at an angle θ with respect to the surface normal ($\theta = 0^\circ$). Each waveguide is 80 μm -wide with a refractive index contrast (Δn) of 0.002 with respect to its surroundings where $n = 1.51$. We know from previous studies that waveguides with these parameters support the multimoded, polychromatic wavepackets that characterize incandescent light including sunlight (*vide infra*).^{24,25} Beam propagation simulations trace the behaviour of a Gaussian (532 nm) beam, which was launched along the

coating's surface normal into a single planar waveguide; select longitudinal (Figure 4.1b) and transverse (Figure 4.1c) cross-sections show that under these conditions, light is confined within waveguides with $\theta \leq 2.7^\circ$. In this range, the waveguide effectively steers the incident beam away from its original propagation axis of 0° by a maximum of 2.7° (please see Supplementary Figure S4.1 for entire set of simulations).

The beam steering behaviour of a single waveguide is quantified in Figure 4.1d, which plots the physical orientation (θ) against the consequent displacement of the waveguide from the surface normal. The corresponding peak intensities of the Gaussian beam launched into the waveguide along the surface normal are plotted in red. The plots reveal that for $\theta \leq 2.7^\circ$, waveguided light is confined within the boundaries of the respective waveguide and in this way, deflected from its original propagation axis along the surface normal. The plot in Figure 4.1e traces the total power of the Gaussian beam at the exit face of the waveguide; the loss of waveguiding for $\theta \leq 2.7^\circ$ is indicated by an abrupt drop in power.

The operational range of the beam deflection coating is determined by the angular acceptance range of the planar waveguides^{25,26} – light incident at angles within this range suffer total internal reflection (TIR) at the waveguide boundaries and is guided as loss-free optical modes. (Please see supplementary section S4.2 for detailed information). Based on parameters of width and Δn , the waveguides in our system possess an absolute acceptance angular range of 8.92° . For example, the waveguide with $\theta = 0^\circ$ captures and guides light with angles of incidence range from -4.46° to $+4.46^\circ$; light propagating along the surface normal (*i.e.*, with an incidence angle = 0°) is therefore efficiently guided. The acceptance ranges of waveguides with $\theta > 0^\circ$ must

now account for refraction at the waveguide entrance; corresponding calculations show that light with an incident angle $= 0^\circ$ falls within the acceptance angular ranges of waveguides with $\theta \leq 2.65^\circ$. For example, the acceptance ranges of waveguide with $\theta = 2.65^\circ$ and 3.31° span -0.45° to 8.48° and 0.55° to 9.49° , respectively. Light launched along the surface normal is therefore guided and steered by the former while it doesn't satisfy waveguiding conditions for the latter and propagates as a "lossy mode".²²

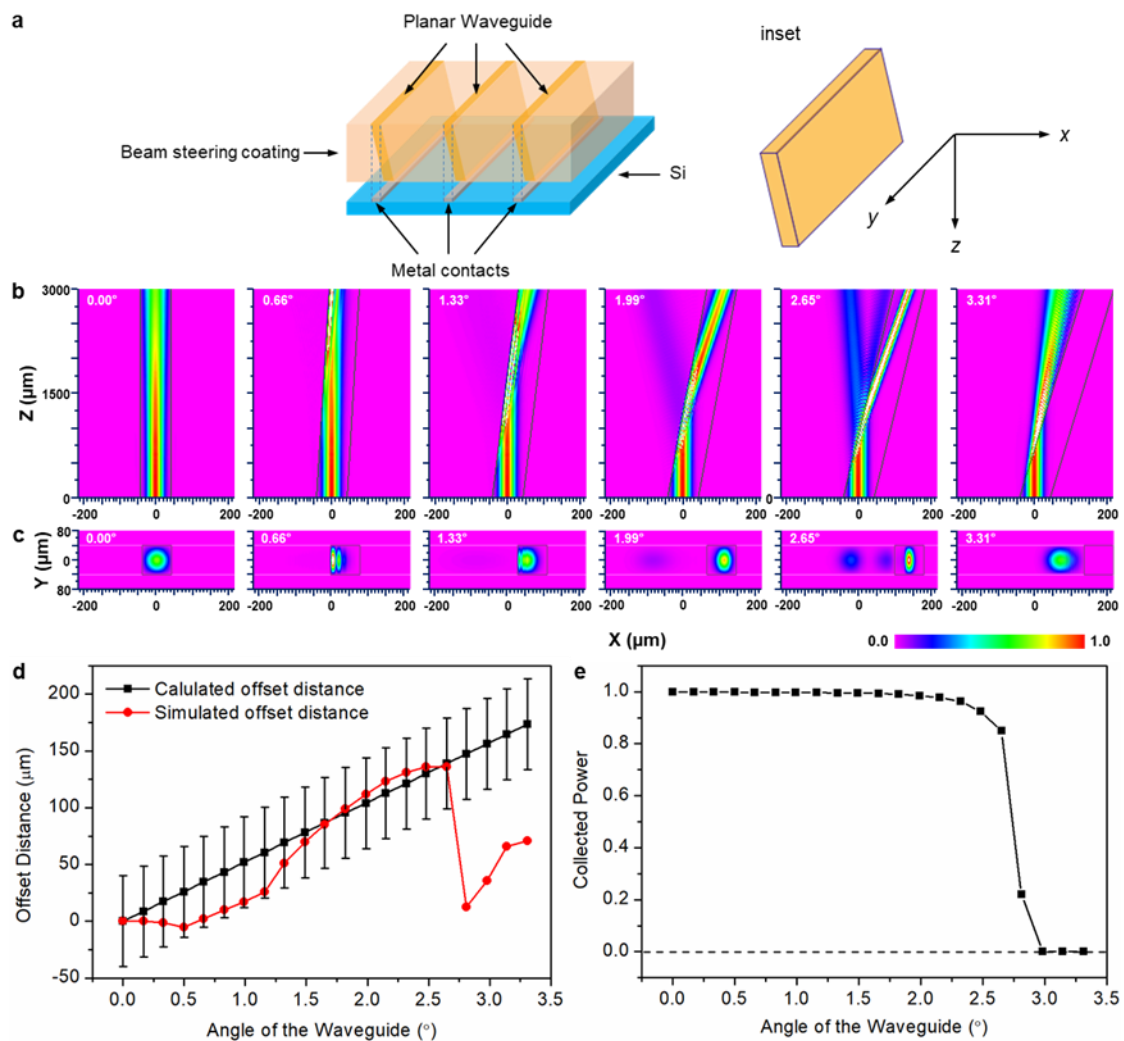


Figure 4.1. Working principles of the beam steering coating. (a) Schematic diagram of employing slanted slab waveguides as beam steering elements for solar cells. The waveguide slabs are oriented at small slants relative to the surface normal. The inset shows the geometry and orientation of a single slab waveguide. Beam Propagation Method (BPM) simulations of the propagation of a Gaussian beam (633 nm) launched along the surface normal (z) of a 3000 μm -thick polymer film containing a planar

waveguide ($\Delta n = 0.002$) oriented at 0.00° , 0.66° , 1.33° , 1.99° , 2.65° , and 3.31° with respect to z . (b) Longitudinal (xz) and (c) transverse (xy) cross-sections are presented. The intensity scale bar is provided. (d) Plot showing the physical orientation and boundaries of waveguides and the resulting displacement from the normal at the exit face (in black). Peak intensity of light (in red) launched along the surface normal at the waveguide exit. (e) Plot of optical power at waveguide exit versus waveguide orientation.

4.2.2. Fabrication and Characterization

We employed self-trapped beams of incandescent light to inscribe periodic arrays of planar waveguides in planar, 3000 μm -thick epoxy films.^{23,27} In this method, a collimated beam of incandescent light is passed through a 1-D periodic amplitude mask ($\Lambda = 2.4$ mm) (**Figure 4.2a**, INSET) and launched into the optically flat entrance face of a transparent, cylindrical cell ($d = 16$ mm, pathlength = 3000 μm) containing photopolymerizable epoxide sol. The beam, now bearing a 1-D periodic pattern of stripes, is launched at incident angles of 0° , 1° , 2° , 3° or 4° relative to the surface normal; after refraction at the air-sample interface, the striped beam propagates through the sol at 0.0° , 0.7° , 1.3° , 2.0° or 2.7° , respectively. The beam naturally diverges^{28,29} as it propagates through the 3000 μm pathlength of the sol; for example, a single stripe is ~ 300 μm ($1/e^2$) wide at the entrance and diverges to a maximum width of ~ 430 μm at the sample exit face (Figure 4.2b). However, as photopolymerization of epoxides moieties and corresponding changes in refractive index (Δn) are initiated, the system is pushed into the nonlinear regime. Under these conditions, the stripes undergo a combination of self-trapping and filamentation due to modulation instability (MI).^{27,30,31} Because of the characteristically slow evolution of the cationic polymerization reaction (ranging from *ms* to minutes), the corresponding changes in Δn

are insensitive to the *fs*-scale phase and amplitude fluctuations, which characterize incandescent light.²⁹ The polymerizing medium therefore responds only to the time-averaged, “smoothed” profile of the incandescent “stripes”, enabling them to self-trap and propagate with negligible divergence.^{24,27,29–31} This is observed as a significant narrowing of the width of each “stripe” at the sample exit face to a minimum of ~ 270 μm . In this way, each self-trapped stripe inscribes a planar waveguide along its propagation path; self-trapping is accompanied by MI-induced filamentation within each stripe, which is observed as the division of each stripe into hundreds of microscopic maxima – corresponding to individual cylindrical fibers confined within each planar waveguide. Although the bright stripes of the incident beam possess maximum intensity, the dark areas of the beam are sufficiently intense to polymerize the remainder of the epoxide medium, which transforms into a solid. However, because the extent of polymerization (and corresponding Δn) are greatest within the bright stripes, these regions serve as efficient planar waveguides.

The periodic array of planar waveguides inscribed in the epoxide film is visible to the naked eye (Figure 4.2c, left column). The yellow colour of the transparent film originates from residual blue-absorbing photosensitizer camphorquinone (see Supplementary Figure S4.3 for details). Optical micrographs of the transverse (*xy*) plane (Figure 2c, top-central and top-right) reveal the periodic array ($\Lambda \approx 2.4$ mm) of planar waveguides, each with a width of ~ 280 μm , which is consistent with CCD images (Figure 4.2b). Magnified micrograph reveals that each planar waveguide comprises a densely packed bright spots – these correspond to cylindrical waveguides inscribed by MI-induced filamentation, which entrap and guide the probe beam of the

microscope. However, these cylindrical waveguides are strictly confined within each stripe, which effectively behave as planar waveguides. The concentration of light in the central region of each planar waveguide (where Δn is greatest)³² is evident both in the spatial intensity profiles (Figure 4.2b) and corresponding micrographs (Figure 4.2c). Optical micrographs of the longitudinal (xz) cross-section of the coating confirm that the planar waveguides propagate through the 3000 μm pathlength of the sample and in this particular case, are oriented at $\sim 2.7^\circ$ with respect to the surface normal. (This is consistent with the refracted propagation angle of the incident beam, which was launched at an incident angle of 4° into the sample entrance face).

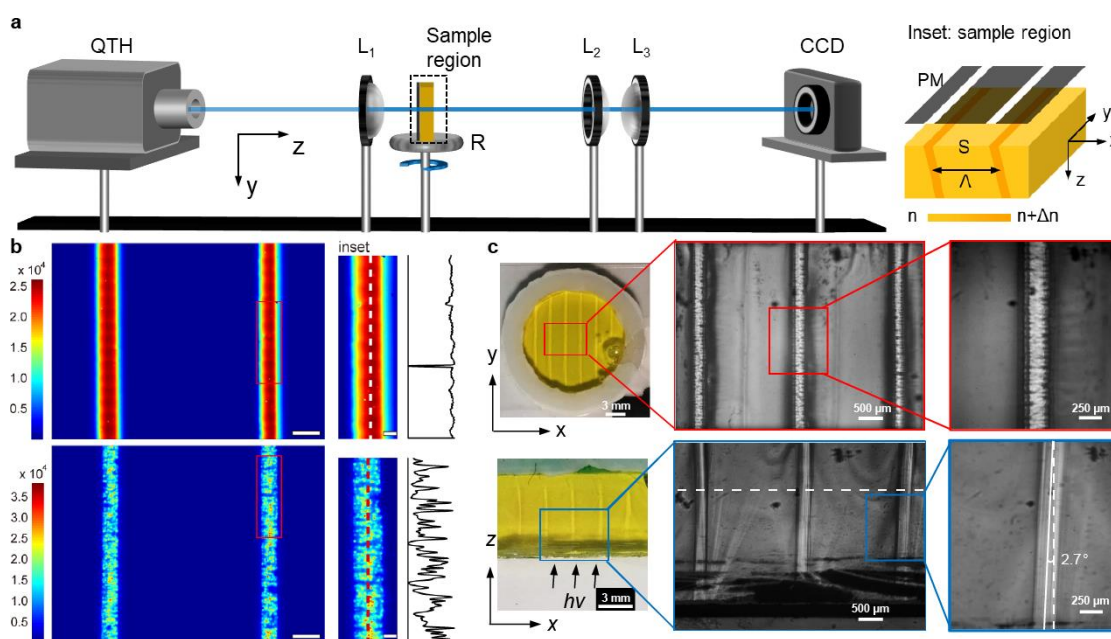


Figure 4.2. (a) Scheme of optical assembly employed to fabricate beam steering coatings: incandescent light emitted by a quartz-tungsten-halogen (QTH) lamp is collimated (L_1) and launched through an amplitude mask into a transparent cell containing photopolymerizable epoxide fluid (S) mounted on a rotation stage (R, resolution = 1°). Spatial intensity profiles of the exit face of S are imaged through a plano-convex lens pair (L_2 and L_3) onto a CCD camera. Inset shows amplitude mask patterned with a periodic ($\Lambda = 2.4$ mm) array of stripes (thickness = $300\ \mu\text{m}$) placed flush with the entrance face of S. Dark orange stripes correspond to waveguides induced by stripes. (b) Spatial intensity profiles acquired at the exit face ($z = 3000\ \mu\text{m}$) of S before (top) and after (down) inscription of waveguides (scale bar = $500\ \mu\text{m}$; colour

bars provide relative intensity). Insets are magnified images of individual stripes with corresponding 1-D profiles (scale bar = 100 μm). (c) Photographs (left) and corresponding optical micrographs of transverse and longitudinal cross-sections of a beam steering coating; in these samples, planar waveguides possess $\theta = 2.7^\circ$.

4.2.3. Proof of Beam Steering

Results in **Figure 4.3** provide evidence of beam steering by an epoxide film imprinted with planar waveguides oriented at $\theta = 2.7^\circ$. In these experiments, we launched a weak laser beam (633 nm) with diameter $\sim 190 \mu\text{m}$ ($1/e^2$) along the surface normal of the film at varying distances (along x) from the central axis ($x = 0 \mu\text{m}$) of a single planar waveguide, which had a width of $\sim 270 \mu\text{m}$ (Figure 4.3b, first column); we then monitored the spatial intensity profile of the beam at the exit face of the film with a CCD camera (Figure 4.3b, second column). The sequence of spatial intensity profiles show that the beam is steered away from its original trajectory (indicated by a dashed white light) as it approaches the vicinity of the planar waveguide. The results are quantified in a plot of displacement (Δx) at the exit face against the input position of the beam at the entrance face. Δx corresponds to the distance of the *output beam* relative to its input position along x , which is indicated by the dashed white line.

Beam steering by the planar waveguide occurs as follows (Figure 4.3b): in (1), the laser beam is incident at long distances at $x = 750 \mu\text{m}$ from the planar waveguide and propagates along the surface normal, retaining its original trajectory through the sample. Here, the displacement ($\Delta x = x_{\text{exit}} - x_{\text{entrance}}$) of the beam is $0 \mu\text{m}$. When the beam approaches the boundaries of the $\sim 270 \mu\text{m}$ -wide planar waveguide at $x = 250 \mu\text{m}$ (2) and $200 \mu\text{m}$ (3), it becomes increasingly shifted away from its original trajectory; in (3), the originally circular spatial intensity profile of the beam becomes distorted as

intensity gravitates towards the planar waveguide. When the beam is incident at $x = 175 \mu\text{m}$, a significant fraction of light suffers total internal reflection at the right boundary of the waveguide and suffers maximum deflection, $\Delta x \approx -181 \mu\text{m}$ (in (4)). The output of the beam, which is now confined within the planar boundaries of the waveguide, is no longer circular but is instead approximately rectangular shape; microscopic maxima within each rectangle correspond to light entrapped within the MI-induced cylindrical waveguides.

In (4) to (6), the beam remains entrapped within the waveguide as it is translated from $x = 175 \mu\text{m}$ to $0 \mu\text{m}$; in (6) to (8), the beam starts to reach the left boundary of the waveguide, and are thereby refracted towards the right of the dotted line. The maximum deflection of $\Delta x \approx 155 \mu\text{m}$ were found at $x = -100 \mu\text{m}$. This is commensurate with the maximum calculated deflection of $142 \mu\text{m}$ ($3000 \mu\text{m} \times \tan(2.7^\circ)$) for a waveguide with $\theta = 2.7^\circ$. At long distances, $x = -500 \mu\text{m}$ (9) and $-725 \mu\text{m}$ (10), the beam retains its original trajectory through the film. This behaviour is quantified in Figure 4.3c, which plots Δx of the beam incident from $x = -1125 \mu\text{m}$ to $1125 \mu\text{m}$ (see Supplementary Figure S4.5 for complete set of spatial intensity profiles corresponding to the points in Figure 4.3c). Importantly, the power of the beam remained constant regardless throughout the measurements and did not change significantly with the position of the incident beam (Supplementary Figure S4.6), indicating that waveguiding did not introduce significant attenuation.

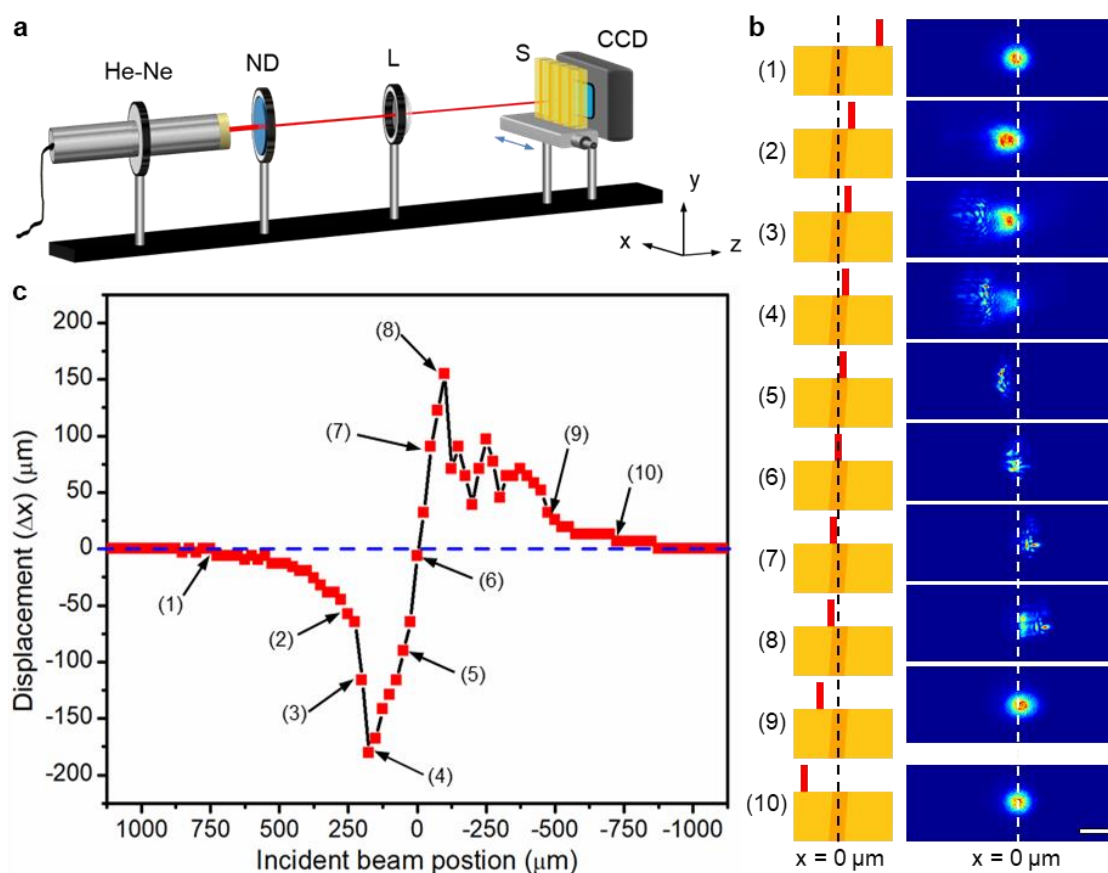


Figure 4.3. (a) Scheme of optical assembly employed to characterize beam steering behaviour. A 633 nm laser beam was attenuated by a neutral density (ND) filter and focused through a plano-convex lens (L) onto the beam steering coating (S), which was mounted on a translation station (resolution $\pm 10 \mu\text{m}$). The spatial intensity profile of the beam at the exit face of S was imaged onto a CCD chip. (b) Images in the first column trace the incident position (x) of the input beam (in red) to a single planar waveguide (dark orange) in the coating; black dotted line indicates $x = 0 \mu\text{m}$. Corresponding spatial intensity profiles of the beam at the exit face of S are provided in the second column. Images (1) to (10) correspond to $x = 750 \mu\text{m}$, $250 \mu\text{m}$, $200 \mu\text{m}$, $175 \mu\text{m}$, $50 \mu\text{m}$, $0 \mu\text{m}$, $-50 \mu\text{m}$, $-100 \mu\text{m}$, $-500 \mu\text{m}$, and $-750 \mu\text{m}$, respectively, where the “-” refers to the laser beam entering the film from the left side of the waveguide. Dotted white lines in the spatial intensity profiles trace the trajectory of the beam in the absence of a waveguide. Scale bar = $200 \mu\text{m}$. (c) Plot of the displacement (Δx) of the incident beam (relative to its trajectory in the absence of a waveguide) at the exit face of the sample.

4.2.4. Enhanced EQE of Solar Cells

The beam steering coatings deflect incident light away from the metallic contacts of solar cells and in this way, increase the EQE of a commercially available solar cell

(**Figure 4.4**). Schemes in Figure 4.4a-b show that scattering and reflection is prevented when incident light is steered by a waveguide ($\theta = 2.7^\circ$) away from the contact onto the adjacent Si surface. This is confirmed in corresponding photographs of identical solar cells coated with unpatterned and waveguide-imprinted films, respectively, which show that scattering of an incident laser beam (633 nm) is significantly suppressed in the latter.

To quantify this behaviour, we measured the relative increase in EQE of solar cells coated with films containing waveguides at varying θ . The transparent coatings were placed on the solar cells so that the entrance faces of the planar waveguides were aligned with the metal contacts; samples typically consisted of ~3 or 4 waveguide-metal contact pairs. Measurements acquired under standard solar spectral conditions are presented in Figure 4.4c; the decrease in EQE values between 400 nm and 500 nm corresponds to absorbance by residual photosensitizer in the coatings (see Supplementary Figure S4.3). Remarkably, all waveguide-imprinted coatings result in an overall increase in EQE relative to a waveguide-free but otherwise identical coating (details are provided in Supplementary Table S4.2). Results were reproducible and EQE averages (over the entire 400 nm to 1100 nm range) of thrice-repeated experiments for all samples are plotted in Figure 4.4d; these correspond to EQE enhancements relative to the control of 2.18 % ($\theta = 0^\circ$), 1.88 % ($\theta = 0.7^\circ$), 2.63 % ($\theta = 1.3^\circ$), 4.42 % ($\theta = 2.0^\circ$) and 4.33 % ($\theta = 2.65^\circ$). Employing a spectrum of 1.5 AM, the calculated short circuit currents (J_{SC}) for films imprinted with waveguides at $\theta = 0^\circ$, 0.66° , 1.33° , 1.99° and 2.65° were 279.1 Am^{-2} , 284.6 Am^{-2} , 283.6 Am^{-2} , 285.9 Am^{-2} , 290.9 Am^{-2} , respectively. For the waveguide imprinted films, these values correspond to enhancements of 1.98 %,

1.60 %, 2.45 %, 4.24 %, and 4.22 %, respectively and are commensurate with observed enhancements in total EQE.

The general increase in EQE enhancement with θ can be attributed to the orientation of the planar waveguides and the extent to which they steer light away from metal contacts (Figure 4.4e). A broad beam of light incident along the surface normal of the control – a film without waveguides - propagates without changing its trajectory through the sample; a portion of the beam that encounters the metal contact is scattered or reflected. However, light that would normally encounter the contact is steered away to the adjacent Si surface in coatings that contain slab waveguides; the extent of steering and therefore the displacement of the beam from the metal contact increases with θ . For example, waveguides with relatively small θ (0.66° , and 1.33°) deflect light to a maximum of $35\ \mu\text{m}$ and $70\ \mu\text{m}$ respectively and therefore not steer all of the light away from the contacts whereas deflection exceeding $100\ \mu\text{m}$ can be achieved when θ approaches values of 2.0° . By suppressing reflection and scattering by the metal contacts and moreover, delivering waveguided light intensity to the active regions of the solar cell,¹⁹⁻²¹ the coatings give rise to an increase in EQE and J_{SC} .

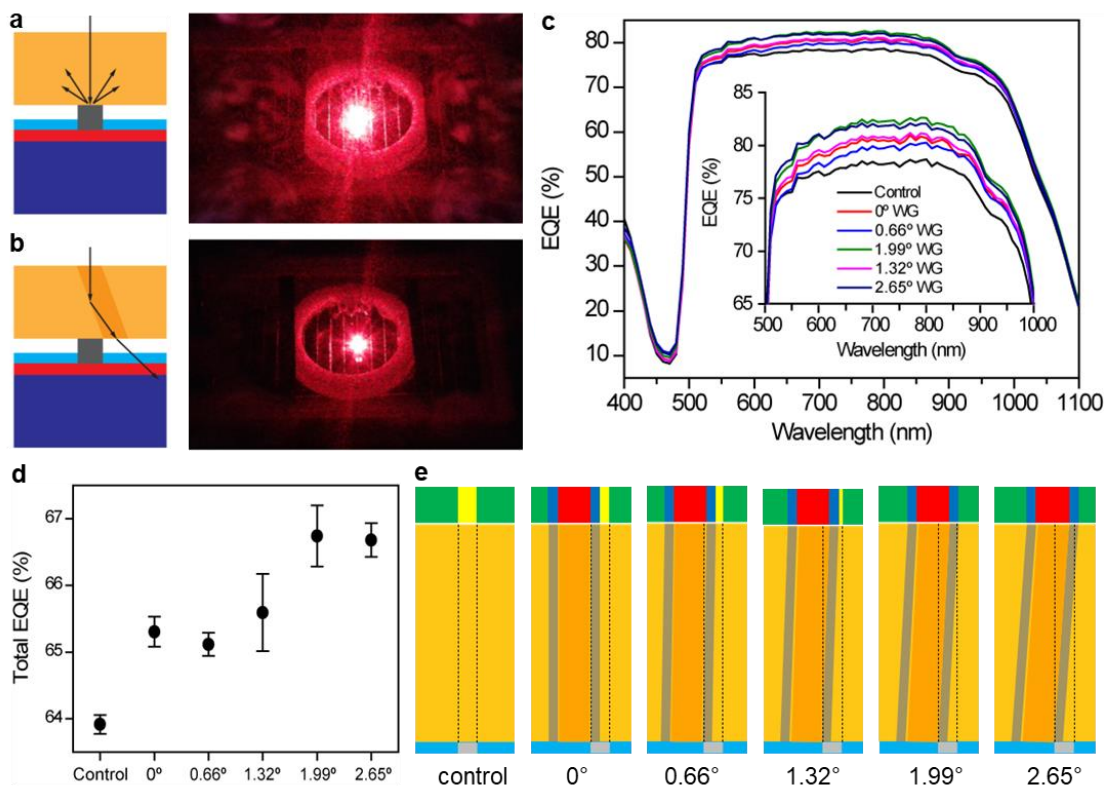


Figure 4.4. Beam steering coatings enhance the EQE of a Si solar cell. Incident light, which would be (a) scattered and reflected is (b) steered away from the metal contact by a waveguide with $\theta = 2.7^\circ$. Corresponding photographs show the marked decrease in scattering in the latter. (c) External quantum efficiency (EQE) plots of solar cells coated with unpatterned (control) and waveguide-imprinted polymer films. The inset is the magnified region from 500 nm to 1000 nm. (d) Plot of average EQE of control and polymer films imprinted with waveguides with varying θ . (e) Scheme of relative orientation of waveguides with respect to a single metal contact. The displacement of waveguided light away from the metal contact increases with θ . Regions of the incident beam that propagate directly through the sample are indicated in green; yellow corresponds to light that will reach the metal contact while red corresponds to light coupled into the waveguide.

4.3. Conclusions

Si solar cells showed an enhancement in EQE of up to 4.42 % when coated with epoxide films imprinted with a periodic array of tilted planar multimode, multiwavelength waveguides. Designed to guide incandescent light including sunlight, the waveguides serve the dual purpose of efficiently steering incident light away from

the metal contacts and delivering optical intensity to the solar cell surface.^{19–21} The resulting enhancement in EQE is significant especially in view of that the global cumulative installed PV capacity in 2016 was over 300 GW_p.¹ The beam steering coatings are fabricated in a single, room temperature step with low energy incandescent light sources. This method, which does not disrupt the native architecture of Si solar cells, would be amenable to large-scale fabrication through roll-to-roll processing for example and facile integration with existing modules. Most importantly, the beam steering films provide proof of a concept that is transferrable to other materials systems. By tuning parameters such as the width, Δn and θ of planar waveguides, it may also be possible to further enhance conversion efficiency.

4.4. Materials and Methods

Preparation of photopolymerizable epoxide has been detailed elsewhere^{25,27,33}. Briefly, 3, 4-epoxycyclohexylmethyl 3, 4-epoxycyclohexanecarboxylate (Sigma Aldrich, Canada), epoxypropoxypropyl terminated polydimethylsiloxane (Gelest, USA), and poly (tetrahydrofuran) (Sigma Aldrich, Canada) were mixed at 50 wt. %, 26 wt. % and 20 wt. %, respectively and combined with photoinitiator bis (4-tert-butyl phenyl) iodonium hexafluoro antimonite (Hampford Research Inc., USA) and photosensitizer camphorquinone ($\lambda_{\max} = 468$ nm) at 1.5 wt. %, and 2.5 wt. %, respectively. The mixture was stirred vigorously over 48 hrs and filtered through a polytetrafluoroethylene (PTFE) membrane (0.2 μm pore size, Pall Corporation USA) prior to use. Sols were protected from exposure to ambient light at all times.

Fabrication of beam steering coatings were carried out on the optical assembly in

Figure 1a. Incandescent light (300–1100 nm) emitted by a quartz-tungsten-halogen (QTH) lamp (Cole-Parmer, USA) was collimated with a planoconvex lens (f. l. = 250 mm, $d = 25.4$ mm). The beam was then passed through an amplitude mask with a 1-D periodic array of slits ($\Lambda = 2.375$ mm, linewidth = 300 μm) before being launched at 0°, 1°, 2°, 3°, and 4° with respect to the surface normal of a cylindrical sample cell ($d = 16$ mm, path-length = 3 mm) with optically transparent entrance and exit faces containing the photopolymerizable epoxide sol. Upon refraction at the air/sample interface, the beam propagated at an angle of approximately 0°, 0.7°, 1.3°, 2.0°, and 2.7°, respectively within the sol ($n = 1.51^{25}$). Samples were polymerized for 90 min. at an intensity of 16.9 mWcm^{-2} . The spatial intensity profiles at the exit face of the sample cell ($z = 3.0$ mm) were imaged through a pair of planoconvex lenses (f. l. = 250 mm, $d = 25.4$ mm) onto a high-resolution, progressive scan, charged-coupled device (CCD) camera (1360 (H) x 1024 (V) of 4.65 μm square pixels; sensitivity range = 350 nm to 1150 nm; WinCamD™ digital camera, Data Ray Inc., USA) and monitored over time.

Microscopy Transmission optical micrographs of beam steering films were acquired with a Nikon Eclipse LV100N POL epifluorescence microscope (Nikon Instruments, Mississauga, ON, Canada), equipped with x2 and x4 physiological objective lenses and a Retiga2000R cooled CCD camera (QImaging, Mono 12-bit, non-cooled, Surrey, BC, Canada).

Optical characterization of beam steering A 633 nm He-Ne (Spectra-Physics) beam was launched at normal incidence into the 3 mm-thick polymer film patterned with a periodic array of waveguides oriented at 2.7° (Figure 2a). The laser beam was monotonically translated along the film surface by a micrometer (resolution = 10 μm) at

intervals of 25 μm . The spatial intensity profile of the beam at the exit face of the film was imaged by a CCD chip (image area 8.8 x 6.6 mm, 1360 (H) x 1024 (V) of 6.45 μm square pixels; sensitivity range = 350 nm to 1150 nm; WinCamDTM digital camera, Data Ray Inc., USA), which was placed flush with the sample cell. A neutral density filter was placed between the sample and the chip.

EQE of a commercially available solar cell (planar multi-crystalline Silicon screen-printed solar cell (Sundance Solar) with a rated efficiency of 17%) that was coated with a beam steering film containing waveguides with $\theta = 2.7^\circ$ was first determined at 633 nm. Here, the beam was launched at normal incidence onto the device surface. Recording the laser power and generated photocurrent, the EQE was calculated according to:

$$EQE = \frac{\text{electrons/sec}}{\text{photons/sec}} = \frac{\text{current}/e}{\text{total photon power}/h\nu} \quad [1]$$

where e is the charge of a single electron, h , Planck's constant and ν , the frequency of the laser beam.

EQE measurements over the visible spectrum were carried out according to ASTM standards (E1021-12) by employing a commercially available measurement system (IQE 200B, Newport), which consists of an arc lamp modulated by a chopper (80 Hz), an automated monochromator system, and electronics for measuring output current. Beam steering films imprinted with waveguides with varying θ (0° , 0.7° , 1.3° , 2.0° and 2.7°) were placed on the solar cells; the entrance faces of the waveguides were carefully aligned with the metal contacts on the solar cell surface. The probe beam was always incident from normal with respect to the film surface. For comparison, films with no waveguides were also measured under the same condition. All measurements were

conducted in the same region of the solar cell in order to eliminate positional differences.

*Beam Propagation Method (BPM)*³⁴⁻³⁶ simulations of light propagation in planar waveguides were implemented through the BeamPROPTM software package (RSoft Products, Synopsys®, USA). Simulations were carried out for waveguides with θ ranging from 0° to 5° at intervals of 0.25° . All waveguides were $80\ \mu\text{m}$ -wide and possessed a step index profile with a refractive index contrast (Δn) = 0.002 with respect to their surroundings. Gaussian beam was launched with an angle of 0° (parallel to the z-axis) into the waveguides. Beam profiles in both xy and xz planes were captured, and the total powers at the waveguide exit face were recorded.

Acknowledgements

We thank Prof. John Preston for valuable discussions and the Moran-Mirabel group for access to their vinyl cutter. Funding from the Natural Sciences and Engineering Research Council (KS), Canadian Foundation for Innovation (KS), McMaster University (KS), American Chemical Society Petroleum Research Fund (IDH; Grant Agreement number PRF# 57332-DNI7) and the College and Engineering and Computer Science at Syracuse University (IDH) is gratefully acknowledged.

References

- (1) Ise, F. *Photovoltaics Report*; 2018.
- (2) Song, Y.; Gao, Z. H.; Duan, Y.; Li, Y. Z.; Yang, H. F.; Li, T.; Zhou, C. L.; Liu, Z. G.; Wang, W. J. Theoretical Analysis and Experimental Study of Optical Loss of Metal Contacts of Crystalline Silicon Solar Cells. *Acta Phys. Sin.* **2011**, *60* (9), 098801.
- (3) Blakers, A. W. Shading Losses of Solar-cell Metal Grids. *J. Appl. Phys.* **1992**, *71* (10), 5237–5241.
- (4) Stuckings, M. F.; Blakers, A. W. A Study of Shading and Resistive Loss from the Fingers of Encapsulated Solar Cells. *Sol. Energy Mater. Sol. Cells* **1999**, *59* (3), 233–242.
- (5) Schneider, J.; Rohner, P.; Thureja, D.; Schmid, M.; Galliker, P.; Poulikakos, D. Electrohydrodynamic NanoDrip Printing of High Aspect Ratio Metal Grid Transparent Electrodes. *Adv. Funct. Mater.* **2016**, *26* (6), 833–840.
- (6) Saive, R.; Atwater, H. A. Mesoscale Trumps Nanoscale: Metallic Mesoscale Contact Morphology for Improved Light Trapping, Optical Absorption and Grid Conductance in Silicon Solar Cells. *Opt. Express* **2018**, *26* (6), A275.
- (7) Atwater, H. A.; Saive, R.; Borsuk, A. M.; Emmer, H.; BUKOWSKY, C.; Yalamanchili, S. Solar Cells and Methods of Manufacturing Solar Cells Incorporating Effectively Transparent 3D Contacts, November 3, 2016.
- (8) Ou, Q.-D.; Xie, H.-J.; Chen, J.-D.; Zhou, L.; Li, Y.-Q.; Tang, J.-X. Enhanced Light Harvesting in Flexible Polymer Solar Cells: Synergistic Simulation of a Plasmonic Meta-Mirror and a Transparent Silver Mesowire Electrode. *J. Mater. Chem. A* **2016**, *4* (48), 18952–18962.
- (9) Saive, R.; Borsuk, A. M.; Emmer, H. S.; Bukowsky, C. R.; Lloyd, J. V.; Yalamanchili, S.; Atwater, H. A. Effectively Transparent Front Contacts for Optoelectronic Devices. *Adv. Opt. Mater.* **2016**, *4* (10), 1470–1474.
- (10) Schneiderlöchner, E.; Preu, R.; Lüdemann, R.; Glunz, S. W. Laser-Fired Rear Contacts for Crystalline Silicon Solar Cells. *Prog. Photovoltaics Res. Appl.* **2002**, *10* (1), 29–34.
- (11) Kerschaver, E. Van; Beaucarne, G. Back-Contact Solar Cells: A Review. *Prog. Photovoltaics Res. Appl.* **2006**, *14* (2), 107–123.
- (12) Savin, H.; Repo, P.; von Gastrow, G.; Ortega, P.; Calle, E.; Garín, M.; Alcubilla, R. Black Silicon Solar Cells with Interdigitated Back-Contacts Achieve 22.1% Efficiency. *Nat. Nanotechnol.* **2015**, *10* (7), 624–628.
- (13) Chen, F.; Pathreker, S.; Kaur, J.; Hosein, I. D. Increasing Light Capture in Silicon Solar Cells with Encapsulants Incorporating Air Prisms to Reduce Metallic Contact Losses. *Opt. Express* **2016**, *24* (22), A1419.
- (14) Kuna, L.; Eder, G. C.; Leiner, C.; Peharz, G. Reducing Shadowing Losses with Femtosecond-Laser-Written Deflective Optical Elements in the Bulk of EVA Encapsulation. *Prog. Photovoltaics Res. Appl.* **2015**, *23* (9), 1120–1130.
- (15) Schumann, M. F.; Langenhorst, M.; Smeets, M.; Ding, K.; Paetzold, U. W.;

- Wegener, M. All-Angle Invisibility Cloaking of Contact Fingers on Solar Cells by Refractive Free-Form Surfaces. *Adv. Opt. Mater.* **2017**, *5* (17), 1700164.
- (16) Chen, P.-C.; Chen, Y.-P.; Cheng, T.-D. Efficiency Improvement of Photovoltaic Module via Grid Diffusers in EVA Encapsulation Layer. *27th Eur. Photovolt. Sol. Energy Conf. Exhib.* **2012**, 333–334.
- (17) Jaus, J.; Pansar, H.; Eckert, J.; Duell, M.; Herfurth, H.; Doble, D. Light Management for Reduction of Bus Bar and Gridline Shadowing in Photovoltaic Modules. In *2010 35th IEEE Photovoltaic Specialists Conference*; IEEE, 2010; pp 000979–000983.
- (18) Mingareev, I.; Berlich, R.; Eichelkraut, T. J.; Herfurth, H.; Heinemann, S.; Richardson, M. C. Diffractive Optical Elements Utilized for Efficiency Enhancement of Photovoltaic Modules. *Opt. Express* **2011**, *19* (12), 11397.
- (19) Dalal, V. L.; Moore, A. R. Design Considerations for High-intensity Solar Cells. *J. Appl. Phys.* **1977**, *48* (3), 1244–1251.
- (20) Chegaar, M.; Hamzaoui, A.; Namoda, A.; Petit, P.; Aillerie, M.; Herguth, A. Effect of Illumination Intensity on Solar Cells Parameters. *Energy Procedia* **2013**, *36*, 722–729.
- (21) Effect of Light Intensity | PVEducation https://pveducation.org/es/fotovoltaica/effect-of-light-intensity#footnoteref1_yfn2d0a (accessed May 22, 2018).
- (22) Biria, S.; Chen, F. H.; Pathreeker, S.; Hosein, I. D. Polymer Encapsulants Incorporating Light-Guiding Architectures to Increase Optical Energy Conversion in Solar Cells. *Adv. Mater.* **2018**, *30* (8), 1705382.
- (23) Hosein, I. D.; Lin, H.; Ponte, M. R.; Baskar, D.; Saravanamuttu, K. Multidirectional Waveguide Arrays in a Planar Architecture. In *Proc. SPIE 8983; Organic photonic materials and devices XVI*, 2014; p 89830E.
- (24) Zhang, J.; Kasala, K.; Rewari, A.; Saravanamuttu, K. Self-Trapping of Spatially and Temporally Incoherent White Light in a Photochemical Medium. *J. Am. Chem. Soc.* **2006**, *128* (2), 406–407.
- (25) Hosein, I. D.; Lin, H.; Ponte, M. R.; Baskar, D. K.; Brook, M. A.; Saravanamuttu, K. Waveguide Encoded Lattices (WELs): Slim Polymer Films with Panoramic Fields of View (FOV) and Multiple Imaging Functionality. *Adv. Funct. Mater.* **2017**, *27* (40), 1702242.
- (26) Saleh, B. E. A.; Teich, M. C. *Fundamentals of Photonics*; Wiley Series in Pure and Applied Optics; John Wiley & Sons, Inc.: New York, USA, 1991.
- (27) Baskar, D. K.; Brook, M. A.; Saravanamuttu, K. Spontaneous Emergence of Nonlinear Light Waves and Self-Inscribed Waveguide Microstructure during the Cationic Polymerization of Epoxides. *J. Phys. Chem. C* **2015**, *119* (35), 20606–20617.
- (28) Buljan, H.; Segev, M.; Soljacić, M.; Efremidis, N. K.; Christodoulides, D. N. White-Light Solitons. *Opt. Lett.* **2003**, *28* (14), 1239–1241.
- (29) Mitchell, M.; Segev, M. Self-Trapping of Incoherent White Light. *Nature* **1997**, *387* (6636), 880–883.
- (30) Zhang, J.; Saravanamuttu, K. The Dynamics of Self-Trapped Beams of Incoherent White Light in a Free-Radical Photopolymerizable Medium. *J. Am.*

- Chem. Soc.* **2006**, *128* (46), 14913–14923.
- (31) Burgess, I. B.; Ponte, M. R.; Saravanamuttu, K. Spontaneous Formation of 3-D Optical and Structural Lattices from Two Orthogonal and Mutually Incoherent Beams of White Light Propagating in a Photopolymerisable Material. *J. Mater. Chem.* **2008**, *18* (35), 4133–4139.
- (32) Kasala, K.; Saravanamuttu, K. An Experimental Study of the Interactions of Self-Trapped White Light Beams in a Photopolymer. *Appl. Phys. Lett.* **2008**, *93* (5), 051111.
- (33) Crivello, J. V. A New Visible Light Sensitive Photoinitiator System for the Cationic Polymerization of Epoxides. *J. Polym. Sci. Part A Polym. Chem.* **2009**, *47* (3), 866–875.
- (34) Scarmozzino, R.; Gopinath, A.; Pregla, R.; Helfert, S. Numerical Techniques for Modeling Guided-Wave Photonic Devices. *IEEE J. Sel. Top. Quantum Electron.* **2000**, *6* (1), 150–162.
- (35) Yevick, D. A Guide to Electric Field Propagation Techniques for Guided-Wave Optics. *Opt. Quantum Electron.* **1994**, *26* (3).
- (36) Feit, M. D.; Fleck, J. A. Light Propagation in Graded-Index Optical Fibers. *Appl. Opt.* **1978**, *17* (24), 3990.

Supplementary Information

Table of Content

S4.1 Simulations of normal incident light propagation in cylindrical waveguides with different orientations	158
S4.2 Calculation of the acceptance range of slanted waveguides.....	159
S4.3 UV-Vis spectroscopy of the materials	1611
S4.4 The CCD images of beam deflecting measurement	162
S4.5 Intensity distribution of the He-Ne laser over space.....	164
S4.6 Summary of the EQE results	165

S4.1 Simulations of normal incident light propagation in cylindrical waveguides with different orientations

The Beam Propagation Method (BPM) is employed for 3-D simulations of a normal incident Gaussian beam ($\lambda = 532$ nm) propagating in channel waveguides with slanted angles. The waveguides are 80 μm -wide and 3 mm long (along z axis) with a step index profile in refractive index. The waveguide core have higher refractive index of $n = 1.512$ and surround regions have lower refractive index of $n = 1.510$ (These parameters are chosen based on previous study). The waveguide angels are 0° , 0.17° , 0.33° , 0.50° , 0.66° , 0.83° , 0.99° , 1.16° , 1.33° , 1.49° , 1.66° , 1.82° , 1.99° , 2.15° , 2.32° , 2.48° , 2.65° , 2.81° , 2.98° , 3.14° , and 3.31° respectively, which correspond to refraction angles in air of 0° to 5° with 0.25° interval. **Figure S4.1a** shows the longitudinal (xz planes) cross-sections of the simulation results, and **Figure S4.1b** shows the transverse cross-sections (xy) of intensity profiles at the exit face of the waveguides.

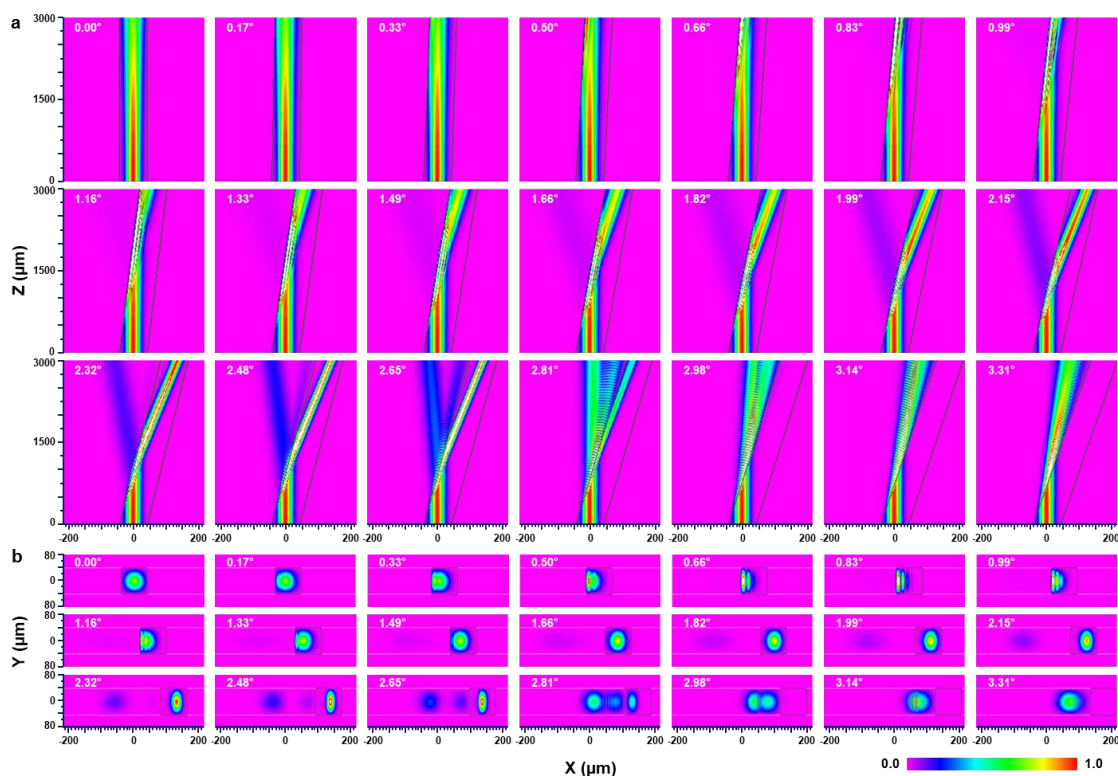


Figure S4.1. Beam propagation simulation of longitudinal (a) and transverse (b) cross-sections of slanted channel waveguides when a 532 nm Gaussian beam is launched with normal incidence into these waveguides. The labels refer to the refraction angle of the waveguide angles. The intensity bar is provided, with red color refer to intensity of 1, while white color refer to intensity higher than 1.

S4.2 Calculation of the acceptance range of slanted waveguides

The acceptance range of a waveguide is angular range over which light refractive in the waveguide encounters total internal reflection (TIR). The boundary of the acceptance range is the angles beyond which light TIR don't occur. **Figure S4.2** shows the traces of light that incident at the boundary angles of a slant waveguide. The boundary angles and can be calculated via twice application of Snell's law, specifically at air-waveguide interface and waveguide core-cladding interface.

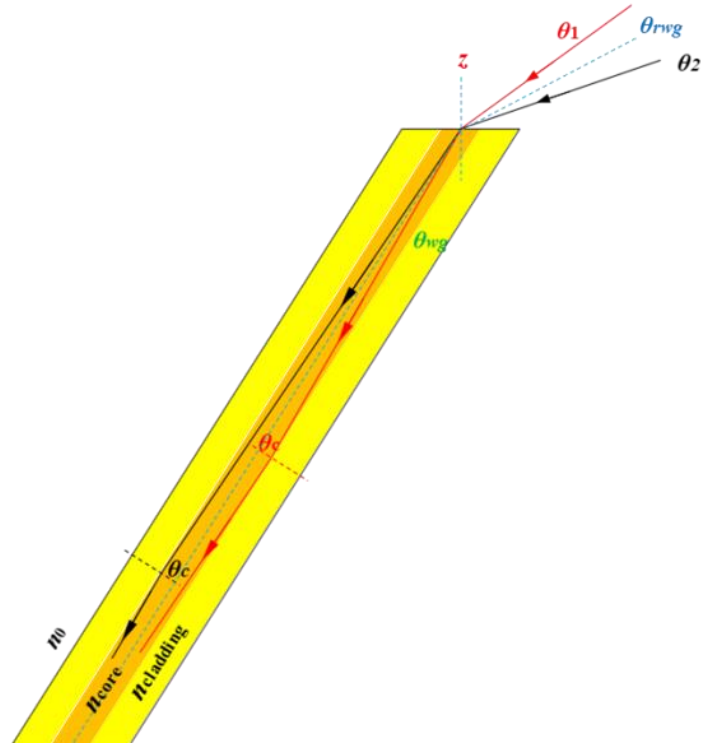


Figure S4.2. A schematic diagram of a slant waveguide. The red and black lines show how light incident at the boundary of the acceptance cone is transmitting inside the waveguide.

Base on the ray tracting depicted in Figure S4.2 and Snell's law, we can obtain the folloing formulars:

$$n_{\text{core}} \times \sin\theta_c = n_{\text{cladding}} \times \sin 90^\circ,$$

$$n_0 \times \sin\theta_1 = n_{\text{core}} \times \sin[\theta_{\text{wg}} - (90^\circ - \theta_c)],$$

$$n_0 \times \sin\theta_2 = n_{\text{core}} \times \sin[\theta_{\text{wg}} + (90^\circ - \theta_c)],$$

Where $n_0 = 1.0$, $n_{\text{core}} = 1.512$, and $n_{\text{cladding}} = 1.510$.

Therefore, the angular acceptance ranges of the slanted waveguides in our case can be calculated, which is shown in **Table S4.1**.

Table S4.1 Acceptance ranges of slanted waveguides via ray-tracing calculation

$\theta_{\text{wg}} / ^\circ$	$\theta_{\text{rwg}} / ^\circ$	$\theta_1 / ^\circ$	$\theta_2 / ^\circ$	$\theta_{\text{wg}} / ^\circ$	$\theta_{\text{rwg}} / ^\circ$	$\theta_1 / ^\circ$	$\theta_2 / ^\circ$	$\theta_{\text{wg}} / ^\circ$	$\theta_{\text{rwg}} / ^\circ$	$\theta_1 / ^\circ$	$\theta_2 / ^\circ$
0.00	0.00	-4.46	4.46	1.16	1.75	-2.70	6.22	2.32	3.51	-0.95	7.98
0.17	0.26	-4.20	4.72	1.33	2.01	-2.45	6.48	2.48	3.75	-0.71	8.22
0.33	0.50	-3.96	4.96	1.49	2.25	-2.20	6.72	2.65	4.01	-0.45	8.48
0.50	0.76	-3.70	5.22	1.66	2.51	-1.95	6.98	2.81	4.25	-0.21	8.72
0.66	1.00	-3.46	5.46	1.82	2.75	-1.70	7.22	2.98	4.51	0.05	8.98
0.83	1.26	-3.20	5.72	1.99	3.01	-1.45	7.48	3.14	4.75	0.29	9.23
0.99	1.50	-2.96	5.96	2.15	3.25	-1.21	7.72	3.31	5.01	0.55	9.49

Here, θ_{wg} refers to the angle of waveguide; θ_{rwg} is the refraction angle of the waveguide in air. θ_1 and θ_2 are the angles relative to the normal of the waveguide surface, and defines the boundary of the acceptance cone of the waveguide.

S4.3 UV-Vis spectroscopy of the materials

The absorption and transmission spectra of the epoxide based photopolymerisable sol are obtained with a Cary 50 probe UV Visible spectrometer. The sol composition is the same as described in experimental section (See section 4.4 in the main text for details) without future dilution. The path-length of the cell used for the measurement is ~2.5 mm.

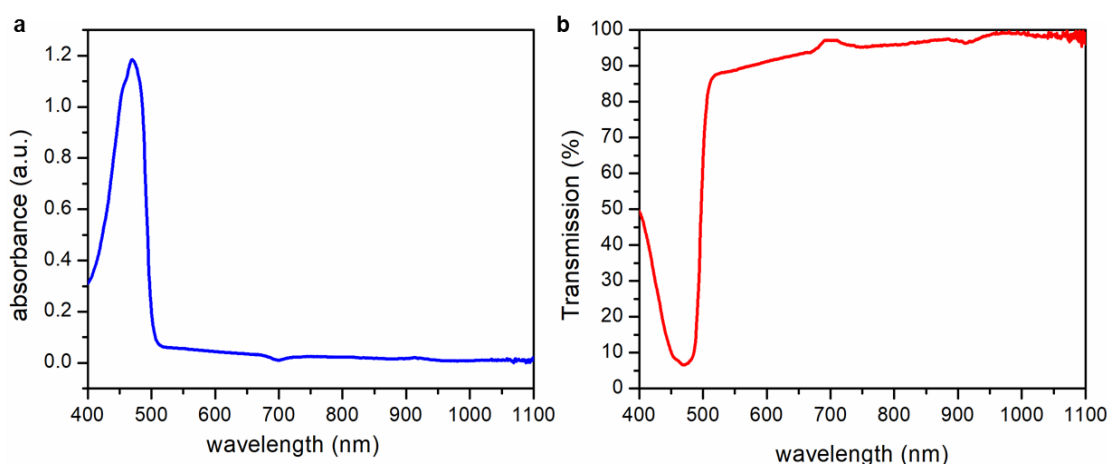


Figure S4.3. UV-Vis absorption (a) and transmission (b) spectra of the epoxide based polymer system.

S4.4 The CCD images of beam deflecting measurement

To study the beam deflection behaviors of the waveguides, a 633 nm laser beam is passed through a 3 mm thin film comprising 2.65° slab waveguides from different entrance positions and collected with a CCD chip kept flush with the exit face of the film. The intensity profiles on the CCD chip when backlight is turned on and off are both captured (**Figure S4.4** and **Figure S4.5**). The CCD images with backlight can help us clearly see the relative positions between the waveguide and the laser beam, while the ones without backlight are used for the plots in Figure 4.3c of the main text, since we can avoid the effect of the backlight as we try to locate the positions of the laser beam which has the highest pixel intensity.

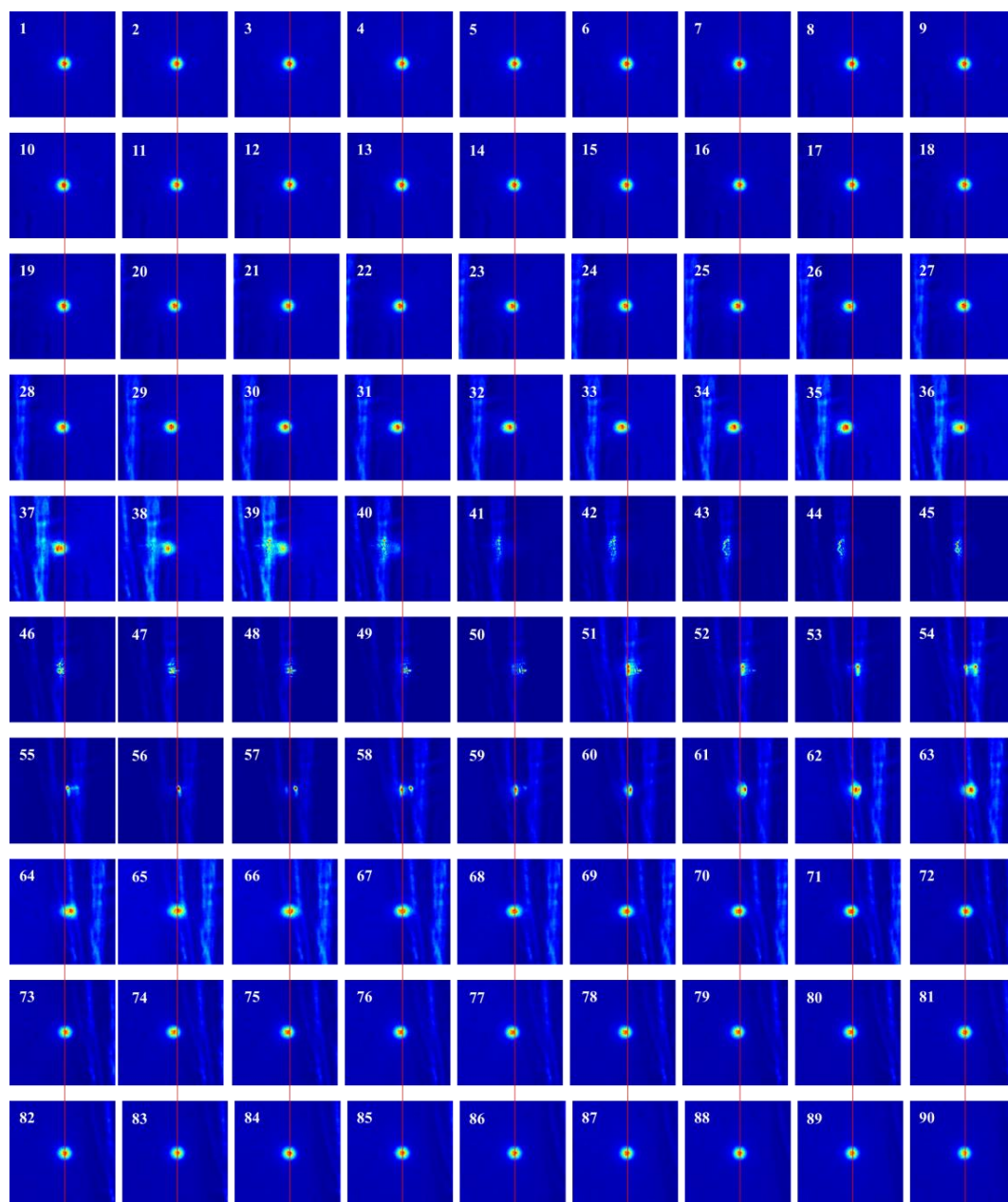


Figure S4.4. CCD images of the laser beam when it is launched at varied positions. The samples are shifted perpendicular to the laser beam with an interval of 25 μm . #47 is the one when waveguide exit face overlaps with the laser beam, and is defined as 0 μm . Images 1-90 correspond to the intensity profiles when laser beam is launched at -1150 μm , -1125 μm , etc., till 1100 μm , away from the position of #47.

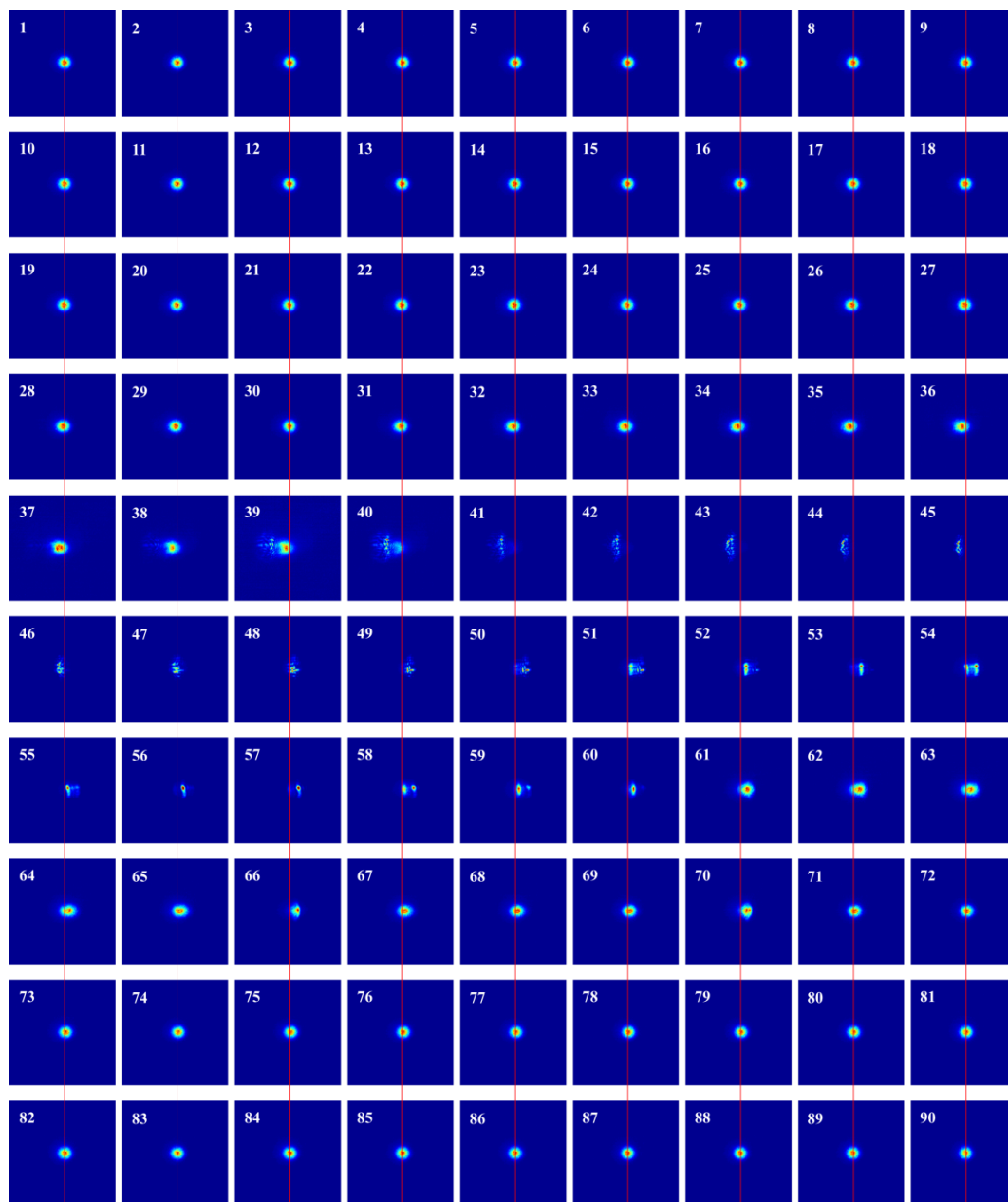


Figure S4.5. Corresponding CCD images to that shown in Figure S4.4 when backlight is turned off.

S4.5 Intensity distribution of the He-Ne laser over space

To study if the slanted slab waveguide will absorb or scatter the laser beam. The total intensity of the laser beam after passing through different positions of the waveguide comprising film is integrated and plotted in **Figure S4.6**.

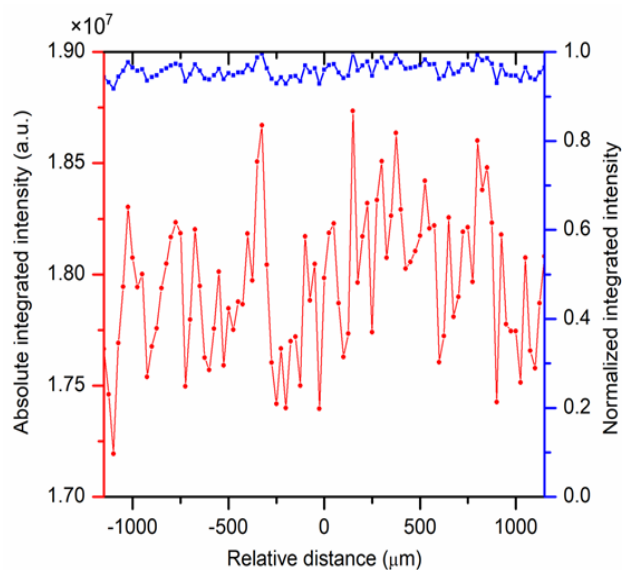


Figure S4.6. Total integrated (red) and normalized (blue) beam intensity of the He-Ne laser beam as a function of entrance positions.

S4.6. Summary of the EQE results

The total EQE is calculated by integrating the EQE values over the wavelength range followed by the average over this range. The total EQE and EQE enhancement for the slanted waveguides over the range of 400-1100 nm and 500-1000 nm are summarized in **Table S4.2**.

Table S4.2 Comparison of the total EQE and EQE enhancement among slanted slab waveguides over the different waveguide ranges

		control	0 °	0.66 °	1.32 °	1.98 °	2.65 °
400-1100 nm	Total EQE (%)	63.91	65.31	65.12	65.59	66.74	66.68
	Enhanced EQE	NA	2.18%	1.88%	2.63%	4.42%	4.33%
500-1000 nm	Total EQE (%)	77.11	78.92	78.38	79.26	80.63	80.41
	Enhanced EQE	NA	2.35%	1.65%	2.79%	4.56%	4.29%

Chapter 5

Shaping LED beams with Radially Distributed Waveguide Encoded Lattices (RDWELs)

Hao Lin⁺, Kathryn A. Benincasa⁺, Cecile Fradin, and Kalaichelvi Saravanamuttu*

HL and KB contributed equally to this work. KS, HL and KB conceived the project. HL and KB carried out experiments and data analysis. HL performed calculations and simulations. HL and KB co-wrote the manuscript.

Abstract

We demonstrate that slim, flexible polymer films imprinted with a radial distribution of cylindrical waveguides can precisely control the shape and trajectory of Light Emitting Diode (LED) beams. The radially distributed waveguide encoded lattice (RDWEL) is fabricated through a single-step, room temperature method in which a large, converging population comprising thousands of self-trapped incandescent beams induces the corresponding array of cylindrical waveguides in a photopolymerizable fluid. The self-inscribed waveguides are polychromatic, multimoded and impart a seamless field of view (FOV) of 70° – an enhancement of 320 % - to the polymer film. We show that a divergent LED beam incident on the plane-faced RDWEL efficiently couples into its constituent waveguides and – depending on their orientation - is either focused or increases in divergence. In the RDWEL_{DIV} configuration – where waveguides diverge along the propagation axis – the LED beam suffers a 45 % increase in divergence. By contrast, when the film is flipped to the RDWEL_{CONV} geometry – where waveguides converge along the propagation axis – the same beam undergoes focusing at an effective focal length of ~ 2 mm. Our findings identify a fundamentally new approach based on waveguided, beam steering to precisely tailor LED beams. By changing parameters such as the FOV, lattice geometry, refractive index contrast, it would be possible to systematically tailor the shape and propagation of LED beams. This is not possible with existing technologies.

Key words

waveguide lattices, radially distributed waveguides, field of view, light emitting diodes, beam shaping

5.1. Introduction

Light emitting diodes (LEDs) offer considerable advantages over conventional light sources including modest power consumption, high luminosity, long lifespans, miniaturization, portability and low cost and as a result, are extensively applied in lighting,^{1,2} sensing,^{3,4} displays^{5,6} and optical communication systems.^{7,8} Conformal epoxy and silicone coatings on LEDs, which are typically employed to serve both as protective sheaths and diffusers, suppress total internal reflection and in this way, enhance the external quantum efficiency (EQE) of emission. Because of the breadth and diversity of LED applications, there have been extensive efforts to shape, design and systematically modulate their characteristically Lambertian beam profiles. Approaches range from microlenses or micro-prismatic facets,^{9–12} photonic crystals^{13–15} to nanorod arrays and nanospheres;^{16,17} various radiation patterns such as a uniform intensity distribution,^{10,18} batwings,^{19,20} or beams with small divergence^{11,12} have been achieved. These technologies often require modification of the native LED die or involve multiple, complex fabrication steps. Conventional optics such as lenses or mirrors^{21,22} can also control the divergence and intensity distribution of LED beams but due to their non-planar, bulky geometries hinder the integration of these miniature light sources into optical systems and devices.

Here we show that LED beams can be modulated by a single component, plane-faced, slim polymer film embedded with a radial distribution of cylindrical

waveguides. The radially distributed waveguide encoded lattice (RDWEL)²³ is slim (≤ 2 mm) and flexible, rendering it suitable as a conformal coating that both protects and optically manipulates LED emission. Importantly, such coatings could be integrated without significantly disrupting mature LED fabrication technologies. The RDWEL is fabricated through a single-step, room-temperature self-inscription method developed in our group, which exploits the spontaneous self-trapping^{24,25} of large populations of incandescent beams in photopolymerizable acrylate²⁶⁻²⁸ and epoxide^{23,29} fluids. Each self-trapped beam elicited in these systems inscribes a multimoded, cylindrical waveguide capable of guiding all visible wavelengths including narrow-band and broadband LEDs.

Akin to the arthropodal compound eye, the RDWEL possesses an enhanced and seamless field of view (FOV).²³ As a result, a non-collimated LED beam incident on the RDWEL spontaneously partitions into the waveguide array and in this way, is guided without divergence as optical modes through the medium. By considering the FOV, orientation and geometry of the RDWEL, it is possible to precisely control both the trajectory and spatial intensity profile of visible LED light. Significantly, we show that a LED beam can be focused or made to diverge further simply by flipping the same RDWEL so that its waveguides respectively converge or diverge along the propagation axis. We detail below the operating principles, design rationale, fabrication and characterization of the RDWEL construct and its ability to modulate the output of a blue LED ($\lambda_{\text{max}} = 470$ nm) beam.

5.2. Results and Discussion

5.2.1. Working Principles

Figure 5.1a is a scheme of the RDWEL, which consists of a periodic stack of identical (xz) planes, each containing a radial distribution of cylindrical waveguides that spans $\theta_{\text{wg}} = \pm 21^\circ$, with respect to the surface normal (z); θ_{wg} represents the orientation of an individual waveguide. The maximum $\Delta\theta_{\text{wg}}$ in the radial array is $\sim 0.4^\circ$ (see Table S5.1 in the supporting information). To understand its operation, we first consider how a *single* waveguide in the RDWEL can alter the trajectory of an incident beam. 2-D beam propagation (BPM) simulations in Figure 5.1b compare the path of a beam launched at incidence angles (θ_i) = 1.5° , 4.0° and 6.5° into a film embedded with a single waveguide that is $40\ \mu\text{m}$ -wide, $\sim 2000\ \mu\text{m}$ -long ($n = 1.47$, $\Delta n_{\text{max}} = 0.006$).^{26,30} The waveguides are oriented at $\theta_{\text{wg}} = 2.5^\circ$, 5.0° and 7.5° and possess acceptance angular ranges of $[-3.9^\circ, 11.4^\circ]$, $[-0.3^\circ, 15.1^\circ]$ and $[3.4^\circ, 18.9^\circ]$ (see Section S5.2 in the supporting information), respectively; the waveguides capture and guide light incident at angles that fall within their respective acceptance ranges. Corresponding simulations for a thin film without a waveguide (control) are also presented (Figure 5.1b). In the latter, the incident beam enters and exits the sample at the same angle θ_i , after suffering refraction at both entrance and exit interfaces. By contrast, in the former case, light incident at θ_i propagates as optical modes through the waveguide and exits the film at $\arcsin(1.47 \cdot \sin \theta_{\text{wg}})$ – *i.e.*, its refraction now occurs relative to the orientation of the waveguide, θ_{wg} . As a result, a beam incident at 1.5° , 4.0° and 6.5° now exits the film at the significantly different angles θ_e of 2.2° , 5.9° and 9.6° , respectively. Equally importantly, light is tightly confined and propagates with negligible divergence in

waveguides. The same beams propagating through the control samples diverge by as much as >100% (diverged from 20 μm to over 40 μm) over the 2 mm pathlength of the film.

When assembled into the RDWEL, the overlapping angular acceptance ranges of waveguides impart a seamless, panoramic FOV (along x) of 82° (determined by the acceptance range of the waveguides with $\theta_{\text{wg}} = \pm 21^\circ$). We first consider the RDWEL_{DIV} configuration where waveguides fan out – or *diverge* - along z (Figure 5.1c); corresponding acceptance angular ranges of waveguides in this configuration are collected in Supplementary Information Sections S5.1 and S5.2 and Table S5.3. Figure 5.1c traces the behaviour of a 9.2 mm-wide beam with a divergence angle of 20° that was launched onto the entrance face of RDWEL_{DIV} (these beam parameters correspond to experimental values described below). The incident beam coincides with waveguides spanning $\theta_{\text{wg}} = \pm 14.6^\circ$. Considering the beam as a continuum of rays with $\theta_i = \pm 10^\circ$, we trace the behaviour of select rays with $\theta_i = 1.0^\circ$; 4.0° ; 7.5° ; which respectively fall within the acceptance angular ranges of vicinal waveguides with $\theta_{\text{wg}} = 1.2^\circ$; 5.1° and 10.0° . These rays are waveguided through the medium and exit at angles $\theta_e = 1.8^\circ$; 7.5° ; and 14.9° , each significantly greater than their respective θ_i . This behaviour results in an overall increase in divergence of the beam from 20.0° to 29.8° – a change of $\sim 49\%$. In an identical medium without the RDWEL, the beam's divergence would remain unchanged. Importantly, the trajectory of rays with θ_i values that do not fall within the acceptance angular range of their vicinal waveguides also remains unchanged. For example, a ray at $\theta_i = 10.0^\circ$ spatially coincides with the entrance face of the waveguide at $\theta_{\text{wg}} = 14.6^\circ$, which possesses an acceptance range of $[14.0^\circ; 30.0^\circ]$. In

this case, $\theta_i = 10.0^\circ$ does not fall within the acceptance range of its vicinal waveguide and therefore exits the RDWEL at $\theta_e = \sim 10.0^\circ$

A similar argument applies to the RDWEL_{CONV} configuration – here, the same film is flipped so that waveguides now *converge* along z (Figure 5.1d). When the 9.2 mm-wide beam with divergence of 20° is launched onto the entrance face of RDWEL_{CONV} (Figure 5.1d), the entire beam accesses waveguides spanning $\theta_{wg} = \pm 12.6^\circ$. In this case, only rays with $\theta_i \leq |2.8^\circ|$ are guided by vicinal waveguides. For example, rays with $\theta_i = 1.0^\circ$ and 2.8° couple into waveguides with $\theta_{wg} = -1.2^\circ$ and -3.2° , which possess acceptance ranges spanning $[-9.4^\circ, 5.9^\circ]$ and $[-12.4^\circ, 2.9^\circ]$, respectively. These rays then exit RDWEL_{CONV} at $\theta_e = -1.8^\circ$, and -4.7° . Because the RDWEL structure is symmetric about z , rays incident at $\theta_i = -1.0^\circ$ and -2.8° propagate through waveguides with $\theta_{wg} = 1.2^\circ$ and 3.2° and exit at $\theta_e = 1.8^\circ$ and 4.7° , respectively. These rays effectively undergo negative refraction, which results in focusing of the beam. Rays with $\theta_i > |2.8^\circ|$ are simply refracted through the sample; for example, rays with $\theta_i = 4.0^\circ$ and 10.0° cannot couple into corresponding vicinal waveguides with $\theta_{wg} = -4.7^\circ$ and -12.6° with respective acceptance ranges of $[-14.6^\circ, 0.8^\circ]$ and $[-26.8^\circ, -11.0^\circ]$. As a result, they exit the RDWEL_{CONV} at $\theta_e = 4.0^\circ$ and 10.0° - *i.e.*, without changing their trajectory.

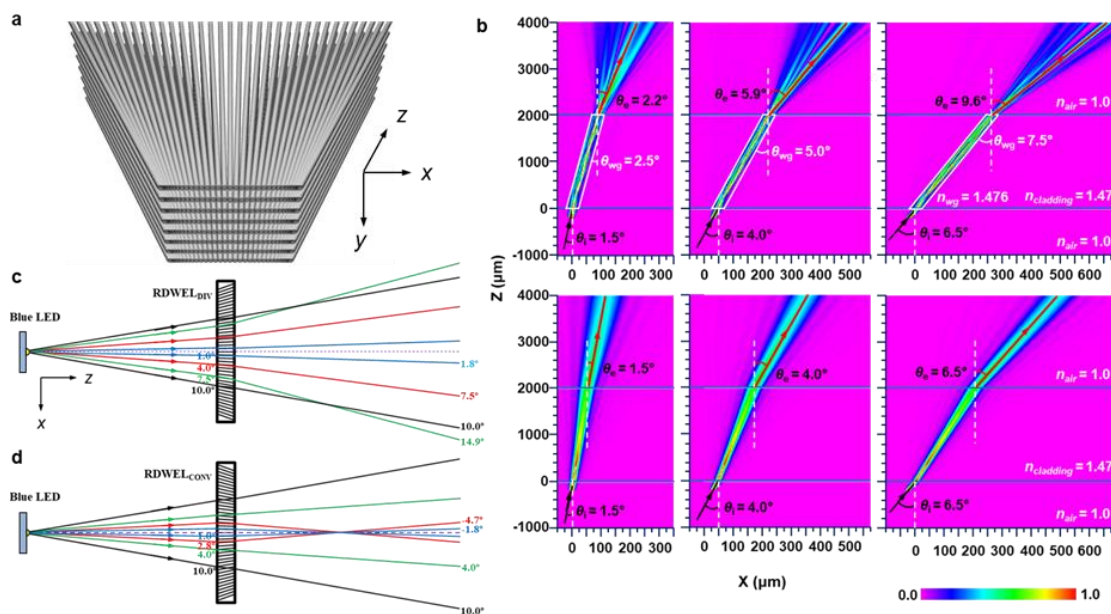


Figure 5.1. Operating principles of the RDWEL (a) Scheme of the RDWEL, which consists of a periodic stack of radially distributed waveguide arrays (b) Beam propagation (BPM) simulations of a laser beam propagating through a waveguide oriented at θ_{wg} with respect to the normal of a 2000 μm -thick film. Control results for the same film without a waveguide are provided in the bottom row. Longitudinal (xz plane) intensity profiles are shown with the corresponding colour intensity scale; refractive indices of the different layers and angles associated with the trajectory of the beam are provided. For clarity, boundaries of the waveguides are indicated in white while the trajectory of the beam upon exiting the film is indicated by a red arrow. Ray tracing diagrams of light propagating through (c) RDWELDIV and (d) RDWELCONV.

5.2.2. Fabrication and structural characterization of RDWEL

Figure 5.2a is a scheme of the optical assembly employed to fabricate the RDWEL.²³ Here, a collimated broad white incandescent beam is first focused by a cylindrical condenser lens ($f. l. = 12.8 \text{ mm}$) and then patterned by an amplitude mask (thickness = 1.75 mm) before being launched into an optically flat, transparent cell (pathlength = 2 mm) containing photopolymerizable acrylate fluid. The amplitude mask imposes a 2-D pattern with square symmetry ($\Lambda = 80 \mu\text{m}$) on the beam, effectively dividing it into a densely packed ($> 15,000 \text{ cm}^{-2}$) square grid of individual

bright spots. Each bright spot initiates free radical polymerization of acrylate moieties and induces corresponding changes in refractive index (Δn) along its propagation path in the photopolymer fluid. This generates a cylindrical waveguide, which entraps the bright spot and guides it as optical modes through the medium without diverging. In this way, the self-trapped beams^{23,29} simultaneously inscribe the RDWEL - radial arrays of waveguides (xz plane) that are periodically stacked along the y axis - within the acrylate film (Figure 5.2b).

Optical micrographs reveal the microstructure of the RDWEL: longitudinal cross-sections (xz plane) show that the top-most layer consists of ~ 160 cylindrical waveguides spanning $\sim \pm 21^\circ$ with respect to z (Figure 5.2c, Figure S5.4 in Supplementary Information), which is consistent with calculations (Supplementary Information Section S5.1). Transverse cross-sections (xy plane) show the square arrays of discrete bright spots, which correspond to the output of individual waveguides (Figure 5.2d left). Waveguide populations at increasing θ_{wg} appear blurred as they deviate from the optic axis of the microscope and can no longer capture and guide the probe beam of the microscope (Figure 5.2d right).

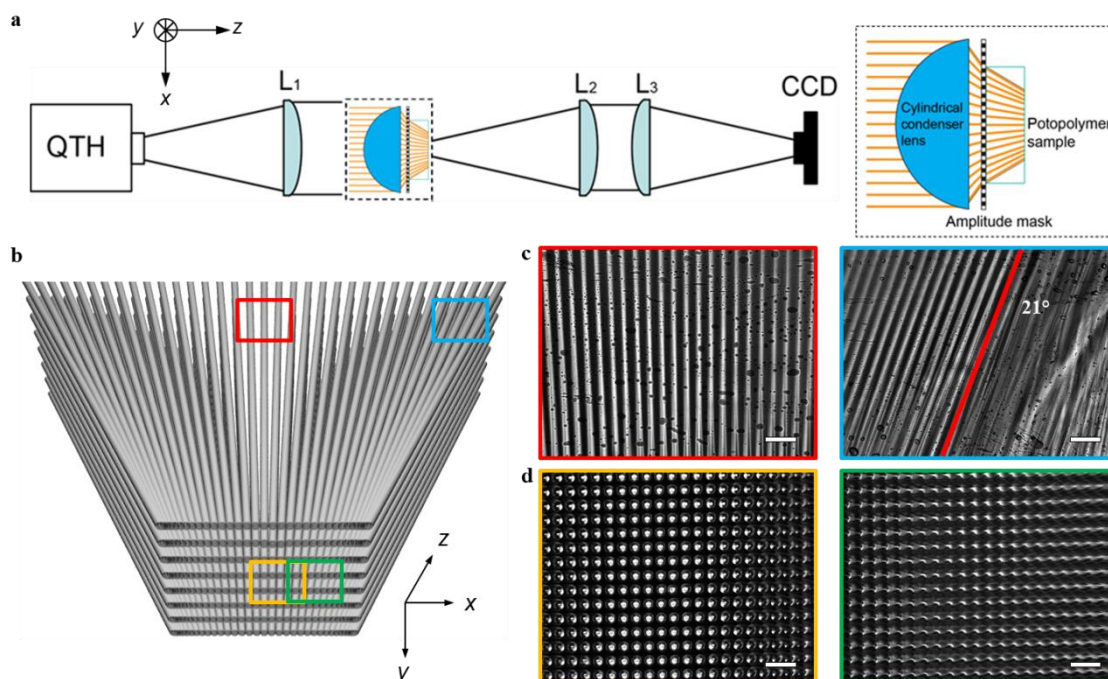


Figure 5.2. The RDWEL was fabricated with (a) incandescent light emitted by a quartz-tungsten-halogen (QTH) lamp, which was collimated by a plano-convex lens (L_1), focused through a cylindrical condenser lens and passed through an amplitude mask and launched onto the optically flat entrance face of a cylindrical cell containing photopolymer fluid. A plano-convex lens pair (L_2 , L_3) imaged the cross-sectional spatial intensity profiles at the sample exit face onto a CCD camera. The inset traces the convergence of the patterned beam of light within the sample. (b) A scheme of the RDWEL containing colour-coded rectangular regions, which were characterized through (c-d) transmission optical microscopy. Scale bar in (c-d) = 200 μm .

5.2.3. Determining the Field of View

We determined the FOV of the fabricated RDWEL to be $\sim 70^\circ$, which corresponds to the sum of the angular acceptance ranges of its constituent waveguides; relative to the control, this corresponds to an enhancement of $\sim 320\%$. We measured the FOV through a previously developed method²³ in which we divided the RDWEL into 13 subpopulations consisting of 9-10 waveguides, each identified by the orientation (θ_{wg}) of its central waveguide. To determine the angular acceptance range of a specific subpopulation, the RDWEL sample was rotated about the y axis so that the θ_{wg} of the

central waveguide coincided with the z axis (**Figure 5.3a**). The incidence angle of the probe beam with respect to the surface normal (z axis) of the RDWEL was then varied over an arc spanning $\pm 10^\circ$ as the output of the waveguide sub-population was imaged onto the CCD camera (further details are provided in Supplementary Information Section S5.4). Figure 5.3b is the sequence of images acquired in this way for a single sub-population of waveguides (where the central waveguide orientation, $\theta_{\text{wg}} = 0^\circ$); corresponding measurements for a control sample – a waveguide-free but otherwise identical acrylate film – are provided and show that light collection occurs over a significantly greater panoramic angular range in the RDWEL. This is quantified in corresponding plots of normalized intensity versus the incident angle of the beam, which yield acceptance ranges ($1/e^2$) of 10.3° and 1.8° for the waveguide subpopulation and control, respectively. This corresponds to an enhancement in the acceptance angular range of $\sim 470\%$. We note that the asymmetry in the plot for the waveguide subpopulation most likely originates from scattering of light by defects in the structure.

Corresponding measurements for the 12 other waveguide sub-populations (control) yielded acceptance angular ranges of 10.3° (2.2 $^\circ$), 8.7° (2.4 $^\circ$), 8.8° (1.9 $^\circ$), 9.0° (2.3 $^\circ$), 9.9° (1.6 $^\circ$), 8.7° (2.3 $^\circ$), 10.3° (1.8 $^\circ$), 9.9° (2.1 $^\circ$), 9.8° (2.3 $^\circ$), 10.9° (2.2 $^\circ$), 9.1° (1.9 $^\circ$), 9.6° (2.4 $^\circ$) and 9.7° (2.0 $^\circ$) for waveguide subpopulations with $\theta_{\text{wg}} = -19.9^\circ, -16.7^\circ, -13.5^\circ, -10.1^\circ, -6.8^\circ, -3.4^\circ, +3.4^\circ, +6.8^\circ, +10.1^\circ, +13.5^\circ, +16.7^\circ$ and $+19.9^\circ$. The average acceptance range of 9.6° is significantly greater than the corresponding value of 5.6° ²⁹ and 6.7° ;²³ which we previously reported for epoxide waveguides. Waveguides with relatively large Δn of up to 0.006 ^{26,30} (and correspondingly increased acceptance ranges) can be induced in acrylate systems whereas a maximum Δn of only 0.001 to 0.002 ^{23,29} is

possible in the epoxide materials. The considerable overlap in acceptance ranges between adjacent waveguide subpopulations imparts a seamless FOV of $\sim 70^\circ$ to the RDWEL.

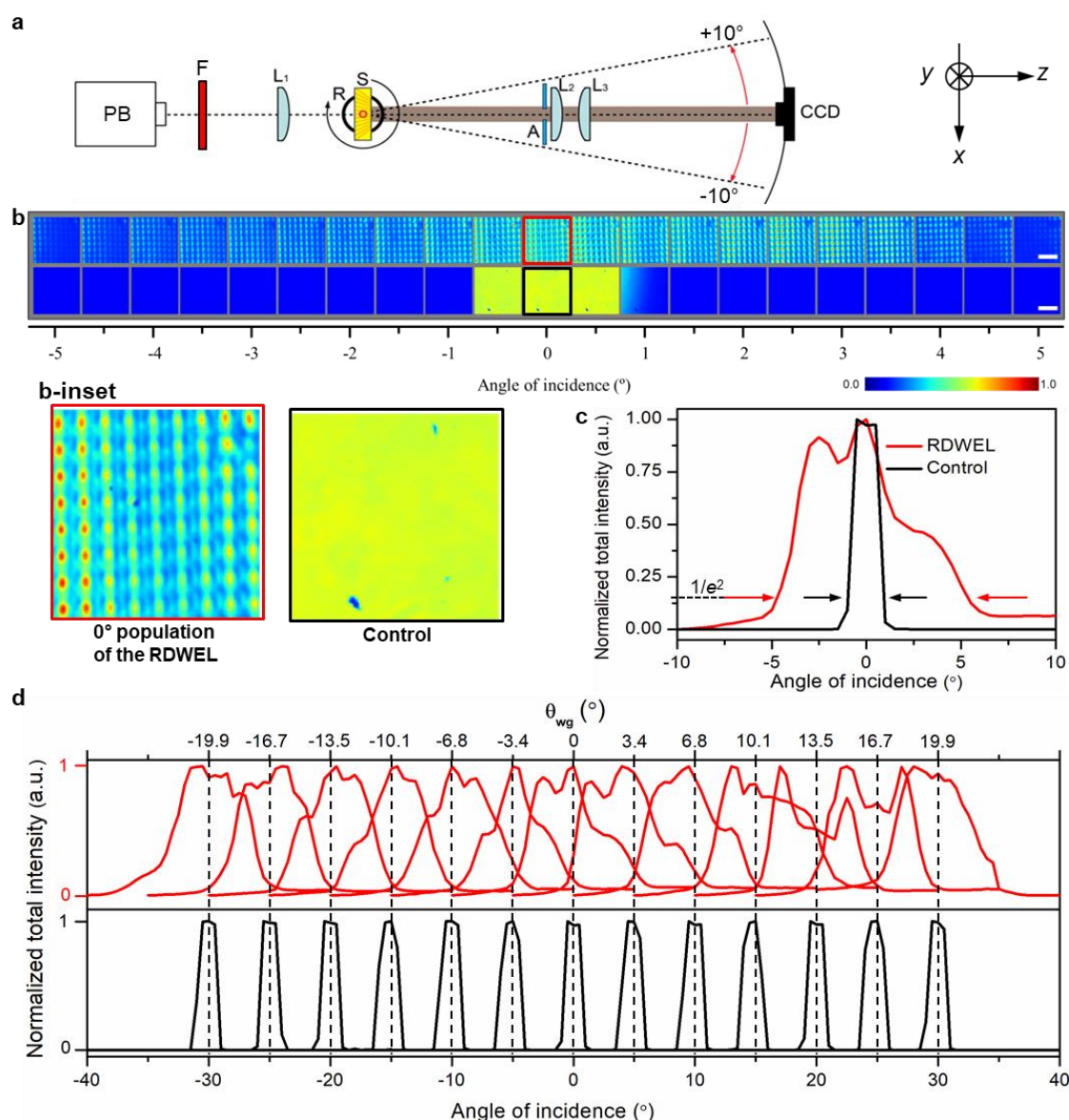


Figure 5.3. Field of view (FOV) of the RDWEL was characterized with (a) probe incandescent beam (PB), which red-filtered (F), collimated (L_1) and launched onto the entrance face of RDWEL_{CONV} (S), which was mounted on a rotatory stage (R). Spatial intensity profiles of a specific waveguide sub-population were imaged by a plano-convex lens pair (L_2 , L_3) equipped with an aperture (A) onto a CCD camera. For each waveguide sub-population, the spatial intensity profile was acquired by varying the incidence angle of the probe beam over $\pm 10^\circ$. (b) Angle-dependent spatial intensity profiles of the $\theta_{wg} = 0^\circ$ waveguide subpopulation (top-row) and control (bottom-row).

Scale bar = 300 μm . A colour intensity scale is provided. Inset shows well-defined, discrete spots corresponding to the output of individual waveguides. (c) Plots of normalized intensity vs. incidence angle of the probe beam for the $\theta_{\text{wg}} = 0^\circ$ waveguide subpopulation (red) and control (black). (d) The seamless FOV of the RDWEL corresponds to the overlapping angular acceptance ranges of all 13 waveguide sub-populations (red). Corresponding measurements for the control are provided in black. θ_{wg} of the central waveguide in each waveguide subpopulation is indicated for each plot.

5.2.4. Shaping LED beams with the RDWEL

We experimentally demonstrate that RDWELs modulate the trajectory and spatial intensity profile of a beam emitted by a commercially available LED ($\lambda_{\text{max}} = 470 \text{ nm}$). Specifically, and consistent with calculations detailed above, the divergence of the LED beam is significantly enhanced by RDWEL_{DIV} while the same beam is focused by RDWEL_{CONV}.

In this experiment, the same beam was launched onto the entrance face of the control, RDWEL_{DIV} and RDWEL_{CONV} samples, respectively. At the entrance face (and consistent with calculations described above), the beam is 9.2 mm wide with a divergence angle of 20° . Its longitudinal intensity profile (along propagation axis z) was projected onto a white screen and imaged with a camera (**Figure 5.4a**). Photographs in Figure 5.4b show that the three samples have strikingly different effects on the trajectory and spatial intensity profile of the beam. 1-D transverse profiles of the LED beam acquired at $z = 2 \text{ cm}$ and $z = 6 \text{ cm}$ from the exit face ($z = 0 \text{ cm}$) of the control yield FWHM widths of 1.9 cm and 3.1 cm, respectively. This in turn corresponds to a divergence of 16.7° , which is commensurate with the divergence angle (20°) of the beam at incidence. Importantly, although the beam diverges upon exit from the control sample, its overall shape – or spatial distribution of intensity - remains effectively the

same.

When propagated through the RDWEL_{DIV} sample, the same beam exhibits significant changes in its spatial profile (Figure 5.4b, bottom). The boundaries ($\theta_i = \pm 10^\circ$) of the 9.2 mm-wide, 20° beam access vicinal waveguides with $\theta_{wg} = \pm 14.6^\circ$ (Figure 5.4b, bottom). In this case, light incident at $\theta_i = \pm 7.5^\circ$ is efficiently guided through waveguides. FWHM values of the beam at 2 cm and 6 cm were 1.9 cm and 3.7 cm, respectively and yield a divergence angle of 24.2° . This corresponds to an increase in divergence of 45 % relative to the control experiment, which is consistent with the calculated value of 48 % (*vide infra*).

Entirely different results were obtained by flipping the film and launching the same LED beam into the RDWEL_{CONV} sample. Here, the central portion ($\sim \pm 1.3$ mm) of the beam with $\theta_i = \pm 2.8^\circ$ couples into vicinal waveguides with $\theta_{wg} = \pm 3.2^\circ$ (see Table S5.2 in the Supporting information) and is ultimately focused by the RDWEL waveguides (Figure 5.1d, Figure 5.4b, bottom). This is observed in the longitudinal profile of the beam upon, which exiting RDWEL_{CONV} contains a significant concentration of intensity along its axial region over a propagation distance of ~ 4 cm, which is accompanied by two distinct streaks of intensity at the beam boundaries. These peripheral streaks correspond to light that is not coupled into waveguides and exits the sample at angles commensurate with their θ_i . Accordingly, the corresponding transverse profiles (Figure 5.4c-d) at short distance (2 cm) contains a saturated peak at the axis accompanied by two peripheral peaks of smaller intensity; the central peak diminishes in intensity at 5 cm, which falls beyond the focal point of the RDWEL_{CONV} (*vide supra*). FWHM widths of the beam of 1.9 cm and 3.0 cm at distances of 2 cm and 6 cm,

respectively yield a divergence of 15.4° , which is comparable to the value of 16.7° observed in the control experiment. This is because the *overall* divergence of the LED beam is determined by the peripheral peaks, which are not waveguided, and therefore exhibit the same trajectory as in the case of the control.

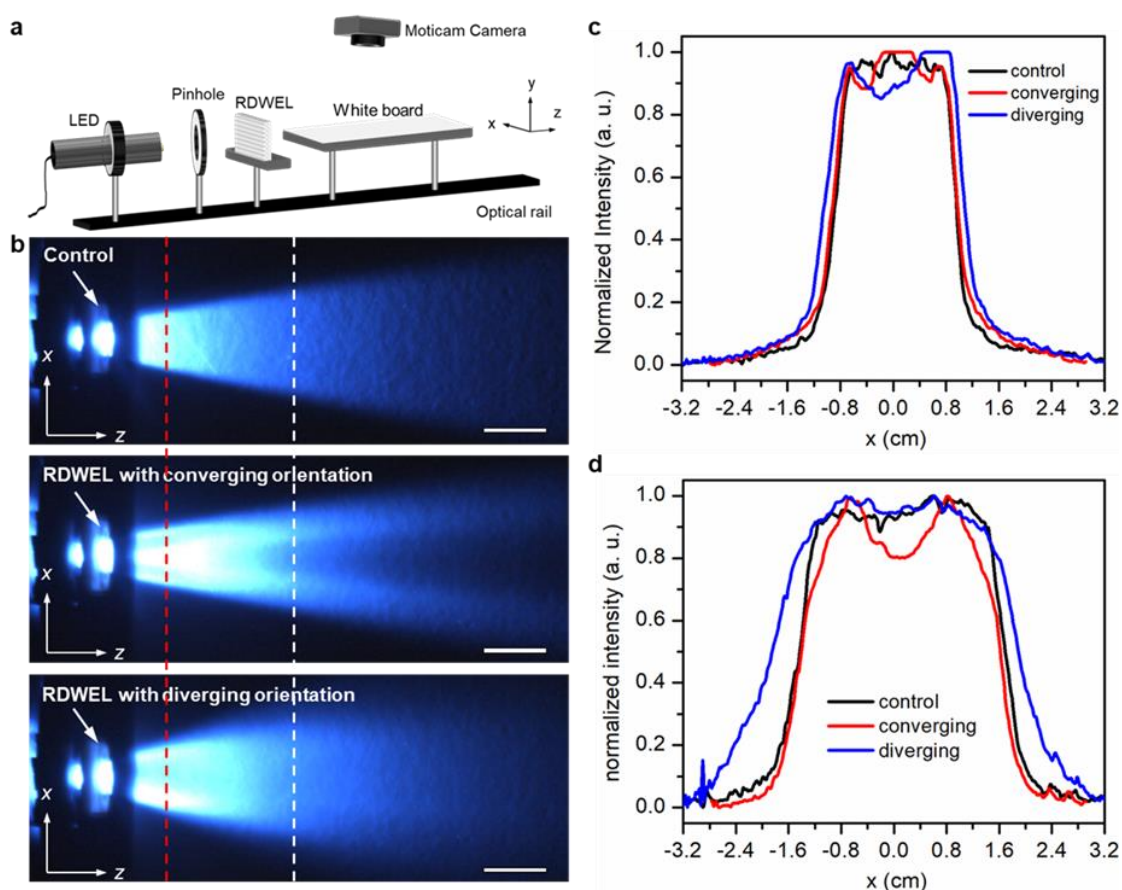


Figure 5.4. Shaping LED beams with RDWEL was demonstrated by (a) launching a blue LED beam, which was first passed through a pinhole onto the entrance face of the $\text{RDWEL}_{\text{DIV}}$ or $\text{RDWEL}_{\text{CONV}}$ sample. The spatial intensity profile of the beam in the xz plane was projected onto a white board and imaged with a camera. Corresponding top-down photographs of the beam after propagating through (b) a control (top), $\text{RDWEL}_{\text{CONV}}$ (central) and $\text{RDWEL}_{\text{DIV}}$ (bottom) samples. Scale bar = 2 cm. (c-d) 1-D transverse intensity profiles of the beam after propagating through the three different samples acquired at 2 cm and 6 cm from the exit face (indicated in (b) by dotted red and white lines, respectively).

5.2.5. Focal length of RDWEL_{CONV}

We further characterized the RDWEL_{CONV} configuration by determining its focal length. Employing the optical assembly shown in **Figure 5.5a**, we launched a LED beam ($\lambda_{\text{max}} = 630 \text{ nm}$) onto the optically flat entrance face of RDWEL_{CONV}, which was positioned $\sim 26 \text{ mm}$ away. A plano-convex lens pair then imaged the cross-sectional profile of the beam at increasing distances from the exit face of the RDWEL_{CONV} ($z = 0 \text{ mm}$) onto a CCD camera. Figure 5.5b contains the sequence of images acquired from $z = 0 \text{ mm}$ to $z = 8 \text{ mm}$. They show that after propagating through RDWEL_{CONV}, the originally uniform LED beam acquires a non-uniform intensity distribution; the pixel-like features in the profiles correspond to the output of individual waveguides in the RDWEL. The profiles consist of an elliptical region of greater intensity in the axial region with weaker wing-like features on either side. The latter correspond to the peripheral streaks observed in longitudinal intensity profiles of the beam after propagation through RDWEL_{CONV}. The central ellipse corresponds to light that is focused by converging waveguides; because of the panoramic arrangement of waveguides in the RDWEL, focusing occurs only along the x direction, giving rise to the elliptical profile. To determine the focal length of RDWEL_{CONV}, we integrated the intensities of the most intense population of waveguides ($320 \text{ }\mu\text{m}$ (x) \times $640 \text{ }\mu\text{m}$ (y)) enclosed in the red rectangle. The resulting power was then plotted as a function of distance (z); the maximum of this plot – corresponding to the greatest power localized within the white rectangle - yields the focal length of RDWEL_{CONV}. We determined this maximum in power occurs at $\sim 2 \text{ mm}$ (Figure 5.5c), which in turn represents the focal length of the RDWEL_{CONV}.

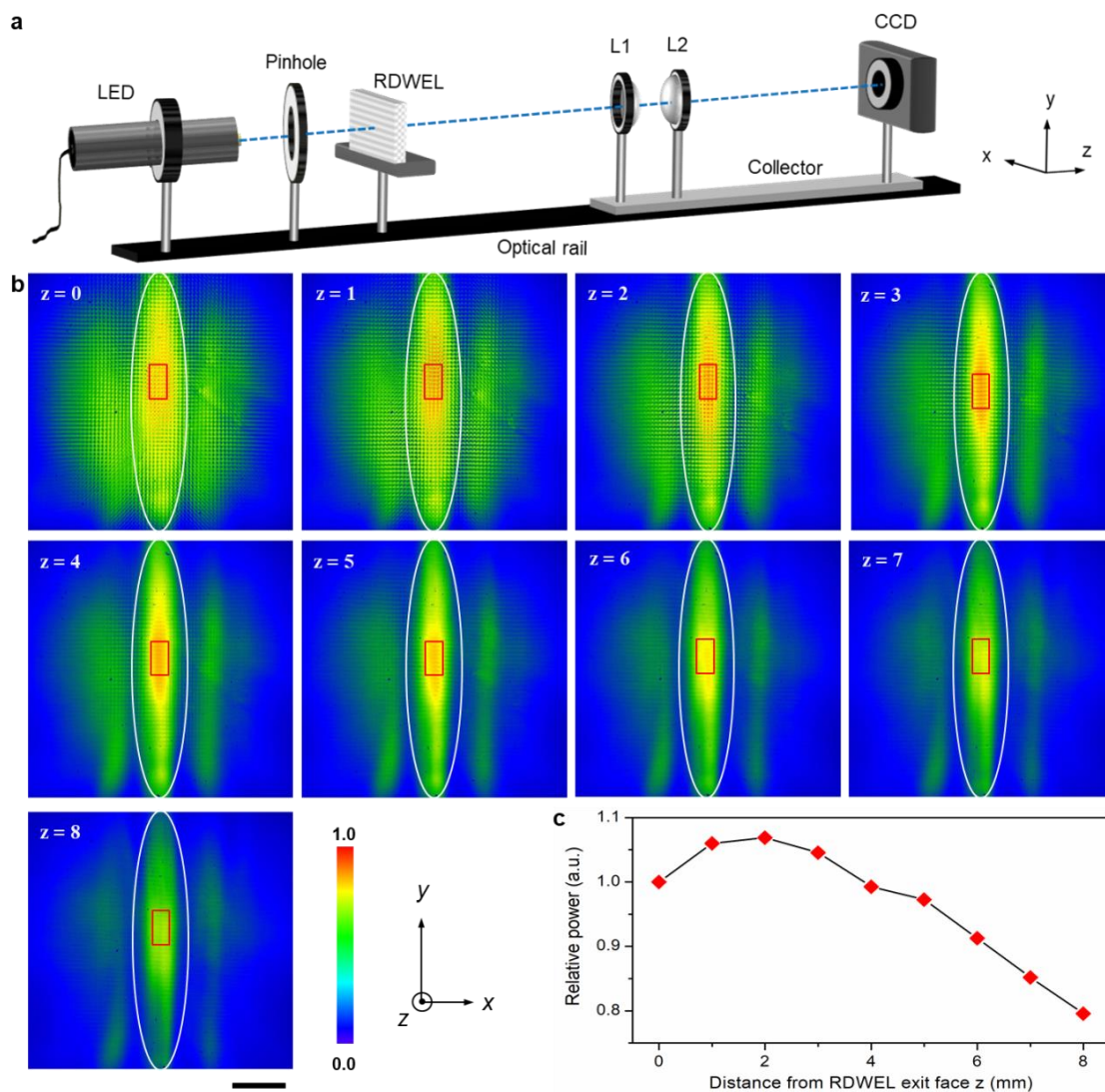


Figure 5.5. The focal length of $\text{RDWEL}_{\text{CONV}}$ was determined by (a) imaging the cross-sectional spatial intensity profile of a red LED beam at different distances from the exit face of the $\text{RDWEL}_{\text{CONV}}$. (b) Corresponding spatial intensity profiles acquired from $z = 0$ mm (exit face) to $z = 8$. Scale bar = 1 mm. Colour intensity scale is provided. The integrated intensity of a sub-population of waveguides contained in red rectangle was (c) plotted against z to determine the focal length of $\text{RDWEL}_{\text{CONV}}$. Measurements were normalized to integrated intensity at $z = 0$.

5.3. Conclusions and Outlook

We demonstrated that the RDWEL - a slim, flexible polymer film imprinted with a radial array of self-induced cylindrical waveguides - can control the spatial intensity distribution and trajectory of a commercially available, visible wavelength LED beam. When employed in the diverging (RDWEL_{DIV}) configuration, the RDWEL construct greatly enhances the divergence of the beam. When flipped to its converging (RDWEL_{CONV}) geometry, the structure now focuses the same beam. The RDWEL possesses a seamless FOV spanning 70° (corresponding to $> 320\%$ enhancement relative to a control; by considering the width and divergence of an incident beam relative to this FOV, it is possible to precisely modulate its shape – or distribution of intensity - and trajectory.

Our proof-of-concept experiments highlight the significant potential of RDWELs as single component, flexible conformal coatings that can precisely modulate the output of LED beams. Through this approach, parameters such as the geometry, refractive index contrast and density of waveguide arrays can be tuned to systematically modulate – and effectively design - the spatial profile and trajectory of incident beams. Because its constituent waveguides are multimoded and guide broadband incandescent light, the RDWEL is operable at all visible wavelengths and therefore applicable to all visible light LEDs. Moreover, its facile, single-step room temperature fabrication technique, which involves only incandescent light and inexpensive photopolymerizable fluid, makes it amenable to large-scale, roll to roll manufacturing processes without disrupting the existing technologies for LED fabrication.

5.4. Materials and Methods

Preparation of the photopolymerizable medium has been described elsewhere.^{26–28} Briefly, 0.3 g (0.015 mmol) of 0.05 N aqueous HCl was added to 4.9 g (19.7 mmol) of 3-(trimethoxysilyl) propyl methacrylate (MAPTMS, Gelest, Inc., USA) to initiate acid-catalyzed hydrolysis and condensation. The mixture was vigorously stirred until it homogenized into a transparent, free-flowing sol, which was then sensitized to visible light through the addition of 0.027 g (0.050 mmol) of photoinitiator bis(eta.5-2,4-cyclopentadien-1-yl)-bis(2,6-difluoro-3-(1H-pyrrol-1-yl)-phenyl) titanium ($\lambda_{\text{max}} = 393 \text{ nm}$ and 460 nm , Ciba Specialty Chemicals, Inc., Canada). The resulting mixture, which was shielded from ambient light, was stirred for six days and filtered through a polytetrafluoroethylene (PTFE) membrane (0.2mm pore size, Pall Corporation, USA) immediately prior to use.

Fabrication of RDWEL: Figure 5.2a is a scheme of the optical assembly employed to fabricate the RDWEL. A broad beam of white incandescent light emitted by a quartz-tungsten-halogen (QTH) lamp (Cole-Parmer, USA) was collimated by a plano-convex lens (f. l. = 250 mm), focused through a cylindrical condenser lens (f. l. = 25.4 mm, CKX025, Newport) and passed through a an amplitude mask with square symmetry ($\Lambda = 80 \mu\text{m}$). The modulated beam was then launched into the optically flat, entrance face of a cylindrical sample cell ($d = 16 \text{ mm}$, pathlength (z) = 2 mm) containing the photopolymerizable sol. The beam irradiated the entire entrance face of sample cell at an intensity of 7.9 mW cm^{-2} . The spatial intensity profile of the beam at the exit face of the sample cell was imaged through a pair of plano-convex lenses onto a

high-resolution, progressive scan, charged-coupled device (CCD) (2040 pixels (H) x 1532 pixels (V)) with a resolution of $3.2 \mu\text{m pixel}^{-1}$ and sensitivity range = 350 nm to 1150 nm (WinCamD™ digital camera, Data Ray Inc., USA).

Microstructural characterization: transmission optical micrographs of longitudinal and transverse cross-sections of the RDWEL were acquired with an Olympus BX51 microscope (X5 magnification) equipped with a digital CCD camera (Q Imaging, RETIGA EXi, Mono 12-bit, non-cooled). The longitudinal micrograph showing a layer containing the entire radial distribution of waveguides of the RDWEL (Figure S5.4) was acquired with a Nikon Eclipse LV100N POL epifluorescence microscope (Nikon Instruments, Mississauga, ON, Canada), equipped with X2 physiological objective lenses and a Retiga2000R cooled CCD camera (QImaging, Mono 12-bit, non-cooled, Surrey, BC, Canada).

FOV of the RDWEL: The FOV of the whole RDWEL was determined through a previously described method.²³ Briefly, a probe white incandescent beam was passed through a red filter ($\lambda_{\text{cut-off}} = 610 \text{ nm}$) and collimated by a plano-convex lens (f. l. = 25 cm) before being launched onto the entrance face of the RDWEL sample, which was mounted on a rotation stage. A high-resolution CCD camera (2040 pixels (H) x 1532 pixels (V), $3.2 \mu\text{m/pixel}$) equipped with a pair of imaging lenses (f. l. = 25 cm) was employed to capture the intensity profiles of the beam at the exit face of the RDWEL. To measure the FOV, we divided the constituent waveguides of the RDWEL into 13 sub-populations and measured their respective angular acceptance ranges. Each waveguide sub-population was centered about a waveguide with $\theta_{\text{wg}} = \pm 19.9^\circ$, $\pm 16.7^\circ$, $\pm 13.5^\circ$, $\pm 10.1^\circ$, $\pm 6.8^\circ$, $\pm 3.4^\circ$, and 0° relative to z axis. For each set of measurements, we

first rotated the RDWEL so that the waveguide subpopulation being sampled coincided with the propagation axis of the probe beam. Accounting for refraction at the air-sample interface, these angles corresponded to $\theta_{\text{rwg}} \pm 30^\circ$, $\pm 25^\circ$, $\pm 20^\circ$, $\pm 15^\circ$, $\pm 10^\circ$, $\pm 5^\circ$, and 0° relative to the RDWEL surface normal. Keeping the probe beam fixed, we then rotated the optical rail bearing the RDWEL, and the imaging optics over an arc spanning $\pm 10^\circ$ about z . we acquired spatial intensity profiles of the RDWEL exit face at 0.5° intervals. In this way, we determined the angular range over which each sub-population collected and waveguided light through the RDWEL. The FOV of the RDWEL corresponded to the sum of the acceptance angular ranges of all 13 waveguide sub-populations.

LED beam shaping: Figure 5.4a is a scheme of the optical assembly employed in beam shaping experiments. A size-controllable pinhole was placed ~ 20 mm in front of a LED (M470L3, Thorlabs), which emitted blue light ($\lambda_{\text{max}} = 470$ nm). The RDWEL sample was positioned at a distance of ~ 6 mm from the pinhole. The intensity distribution of the LED beam along its propagation axis was projected onto a white board and imaged with a “Moticam” camera (1600 pixels (H) x 1200 pixels (V), Motic[®], Hong Kong) was mounted perpendicular to the white board. Spatial intensity profiles of the beam were processed with ImageJ software.

Focal length of RDWEL_{CONV} was determined through the optical assembly pictured in Figure 5.5a. A divergent beam emitted by a red LED ($\lambda_{\text{max}} = 630$ nm) equipped with a 7 mm pinhole is passed through a RDWEL-CO positioned ~ 26 mm from the LED. The 2D intensity profile of the beam at the exit face of the RDWEL is focused by a pairs of imaging lenses ($d = 2.54$ cm, f. l. = 10 mm) on to a CCD camera (2040 pixels (H) x 1532 pixels (V), $3.2 \mu\text{m}/\text{pixel}$). During the experiments, the imaging lenses and

the CCD camera are moved with the same pace away from the exit face of the RDWEL, over a distance of 8 mm, with 1 mm interval.

Simulations of light propagation: Simulation of light transmission in and out of single waveguides were carried out using Beam Propagation Method (BPM),^{31–33} which was implemented through the BeamPROPTM software package (RSoft Products, Synopsys®, USA). The waveguides studied had slanted angle from 2.5 °, 5.0 ° and 7.5 ° (relative to the z-axis). All waveguides were 40 μm wide with graded refractive index ($\Delta n_{\max} = 0.006$). In each case of study, a single Gaussian beam was launched from air with an angle (which is within the acceptance cone of the waveguide) into the waveguides, and the longitudinal (xz plane) profile of the beam propagating in as well as exiting from the waveguides were recorded. Identical simulation was conducted in a continuous homogeneous material with the same refractive index for comparison.

Acknowledgement

HL and KAB contributed equally to this work. We thank Ms. Fariha Mahmood for assisting with part of the simulation. Funding from the Natural Sciences and Engineering Research Council, Canadian Foundation for Innovation and McMaster University is gratefully acknowledged.

References

- (1) Held, G. *Introduction to Light Emitting Diode Technology and Applications*; CRC Press, 2009.
- (2) Pimputkar, S.; Speck, J. S.; DenBaars, S. P.; Nakamura, S. Prospects for LED Lighting. *Nat. Photonics* **2009**, *3* (4), 180–182.
- (3) Sung, W.-T.; Lin, J.-S. Design and Implementation of a Smart LED Lighting System Using a Self Adaptive Weighted Data Fusion Algorithm. *Sensors* **2013**, *13* (12), 16915–16939.
- (4) Li, W.-T.; Jin, J.; Li, Q.; Wu, C.-F.; Lu, H.; Zhou, Q.; Li, A.-M. Developing LED UV Fluorescence Sensors for Online Monitoring DOM and Predicting DBPs Formation Potential during Water Treatment. *Water Res.* **2016**, *93*, 1–9.
- (5) Van Derlofske, J. F. Computer Modeling of LED Light Pipe Systems for Uniform Display Illumination; Ferguson, I. T., Park, Y.-S., Narendran, N., DenBaars, S. P., Eds.; International Society for Optics and Photonics, 2001; Vol. 4445, pp 119–129.
- (6) Svilainis, L. LED Brightness Control for Video Display Application. *Displays* **2008**, *29* (5), 506–511.
- (7) Zeng, L.; O'Brien, D.; Minh, H.; Faulkner, G.; Lee, K.; Jung, D.; Oh, Y.; Won, E. High Data Rate Multiple Input Multiple Output (MIMO) Optical Wireless Communications Using White Led Lighting. *IEEE J. Sel. Areas Commun.* **2009**, *27* (9), 1654–1662.
- (8) Komine, T.; Nakagawa, M. Fundamental Analysis for Visible-Light Communication System Using LED Lights. *IEEE Trans. Consum. Electron.* **2004**, *50* (1), 100–107.
- (9) Buřtner, A.; Zeitner, U. D. Wave Optical Analysis of Light-Emitting Diode Beam Shaping Using Microlens Arrays. *Opt. Eng.* **2002**, *41* (10), 2393.
- (10) Sun, L.; Jin, S.; Cen, S. Design of Free-Form Microlens for LED General Illumination. In *Proc. of SPIE-OSA-IEEE*; Jeon, H., Yang, C.-C., Eds.; Asia Communications and Photonics, 2009; Vol. 7635, p 763509.
- (11) Joo, J. Y.; Kang, C. S.; Park, S. S.; Lee, S.-K. LED Beam Shaping Lens Based on the near-Field Illumination. *Opt. Express* **2009**, *17* (26), 23449–23458.
- (12) Zhou, L.; Bai, G.-L.; Guo, X.; Shen, S.; Ou, Q.-D.; Fan, Y.-Y. Light Beam Shaping for Collimated Emission from White Organic Light-Emitting Diodes Using Customized Lenticular Microlens Arrays Structure. *Appl. Phys. Lett.* **2018**, *112* (20), 201902.
- (13) Suslik, L.; Pudis, D.; Gaso, P.; Lettrichova, I.; Kovac, J.; Hronec, P.; Nolte, R.; Schaaf, P. Far-Field Pattern Modification of LEDs with 2D PhC PDMS Membrane; Popiolek-Masajada, A., Urbanczyk, W., Eds.; 2014; p 944110.
- (14) Cheng, B. S.; Chiu, C. H.; Huang, K. J.; Lai, C. F.; Kuo, H. C.; Lin, C. H.; Lu, T. C.; Wang, S. C.; Yu, C. C. Enhance Light Extraction of InGaN-Based Green LEDs by Nano-Imprinted 2D Photonic Crystal Pattern. *Semicond. Sci. Technol.* **2008**, *23* (5), 055002.
- (15) David, A.; Fujii, T.; Sharma, R.; McGroddy, K.; Nakamura, S.; DenBaars, S. P.;

- Hu, E. L.; Weisbuch, C.; Benisty, H. Photonic-Crystal GaN Light-Emitting Diodes with Tailored Guided Modes Distribution. *Appl. Phys. Lett.* **2006**, *88* (6), 061124.
- (16) Min-An Tsai; Peichen Yu; Chao, C. L.; Chiu, C. H.; Kuo, H. C.; Lin, S. H.; Huang, J. J.; Lu, T. C.; Wang, S. C. Efficiency Enhancement and Beam Shaping of GaN–InGaN Vertical-Injection Light-Emitting Diodes via High-Aspect-Ratio Nanorod Arrays. *IEEE Photonics Technol. Lett.* **2009**, *21* (4), 257–259.
- (17) Tsai, M.-A.; Yu, P.; Chiu, C. H.; Kuo, H. C.; Lu, T. C.; Lin, S. H. Self-Assembled Two-Dimensional Surface Structures for Beam Shaping of GaN-Based Vertical-Injection Light-Emitting Diodes. *IEEE Photonics Technol. Lett.* **2010**, *22* (1), 12–14.
- (18) Pan, J. W.; Tu, S. H.; Sun, W. S.; Wang, C. M.; Chang, J. Y. Integration of Non-Lambertian LED and Reflective Optical Element as Efficient Street Lamp. *Opt. Express* **2010**, *18* (S2), A221.
- (19) Hsu, K.-F.; Lin, C.-W.; Hwang, J.-M. High Efficiency Batwing Thin-Film Design for LED Flat Panel Lighting. In *2014 9th International Microsystems, Packaging, Assembly and Circuits Technology Conference (IMPACT)*; IEEE, 2014; pp 480–483.
- (20) Chang, S.-I.; Yoon, J.-B.; Kim, H.; Kim, J.-J.; Lee, B.-K.; Shin, D. H. Microlens Array Diffuser for a Light-Emitting Diode Backlight System. *Opt. Lett.* **2006**, *31* (20), 3016.
- (21) Fournier, F. R. A Review of Beam Shaping Strategies for LED Lighting; Kidger, T. E., David, S., Eds.; International Society for Optics and Photonics, 2011; Vol. 8170, p 817007.
- (22) Chiang, C.-W.; Hsu, Y.-K.; Pan, J.-W. Design and Demonstration of High Efficiency Anti-Glare LED Luminaires for Indoor Lighting. *Opt. Express* **2015**, *23* (3), A15.
- (23) Lin, H.; Hosein, I. D.; Benicasa, K. A.; Saravanamuttu, K. Slim Films with Seamless Panoramic Fields of View: The Radially Distributed Waveguide Encoded Lattice (RDWEL). *Adv. Opt. Mater.* **2018**, Submitted.
- (24) Mitchell, M.; Segev, M. Self-Trapping of Incoherent White Light. *Nature* **1997**, *387* (6636), 880–883.
- (25) Trillo, S.; Torruellas, W. *Spatial Solitons*; Trillo, S., Torruellas, W., Eds.; Springer Series in Optical Sciences; Springer Berlin Heidelberg: Berlin, Heidelberg, 2001; Vol. 82.
- (26) Zhang, J.; Kasala, K.; Rewari, A.; Saravanamuttu, K. Self-Trapping of Spatially and Temporally Incoherent White Light in a Photochemical Medium. *J. Am. Chem. Soc.* **2006**, *128* (2), 406–407.
- (27) Zhang, J.; Saravanamuttu, K. The Dynamics of Self-Trapped Beams of Incoherent White Light in a Free-Radical Photopolymerizable Medium. *J. Am. Chem. Soc.* **2006**, *128* (46), 14913–14923.
- (28) Kasala, K.; Saravanamuttu, K. Coaxial Self-Trapping of White and Gray Regions of an Incandescent Field: A Bright Core with a Dark Cladding. *Phys. Res. Int.* **2012**, *2012*, 1–5.
- (29) Hosein, I. D.; Lin, H.; Ponte, M. R.; Basker, D. K.; Brook, M. A.; Saravanamuttu,

- K. Waveguide Encoded Lattices (WELs): Slim Polymer Films with Panoramic Fields of View (FOV) and Multiple Imaging Functionality. *Adv. Funct. Mater.* **2017**, *27* (40), 1702242.
- (30) Saravanamuttu, K.; Du, M.; Najafi, S. I.; Andrews, M. P. Photoinduced Structural Relaxation and Densification in Sol-Gel-Derived Nanocomposite Thin Films: Implications for Integrated Optics Device Fabrication. *Can. J. Chem.* **1998**, *76*, 1717–1729.
- (31) Feit, M. D.; Fleck, J. A. Light Propagation in Graded-Index Optical Fibers. *Appl. Opt.* **1978**, *17* (24), 3990–3998.
- (32) Yevick, D. A Guide to Electric Field Propagation Techniques for Guided-Wave Optics. *Opt. Quantum Electron.* **1994**, *26* (3), S185–S197.
- (33) Scarmozzino, R.; Gopinath, A.; Pregla, R.; Helfert, S. Numerical Techniques for Modeling Guided-Wave Photonic Devices. *IEEE J. Sel. Top. Quantum Electron.* **2000**, *6* (1), 150–162.

Supporting Information

Table of Content

S5.1. Determining the angles of waveguides in the RDWEL	192
S5.2. Coupling a diverging LED beam to RDWEL with different orientations	195
S5.3. Top-down micrograph of the entire RDWEL	199
S5.4. Measuring the FOV of a waveguide subpopulation of the RDWEL	200

S5.1. Determining the angles of waveguides in the RDWEL

To find out the angle of each waveguide in the RDWEL, we employed ray tracing as shown in **Figure S5.1**, where a photomask and the polymerisable sol are placed flush with the Cylindrical condenser lens. The normal incident light therefore would refract multiple times at the interfaces (See the blue arrows), each time follows Snell's law.

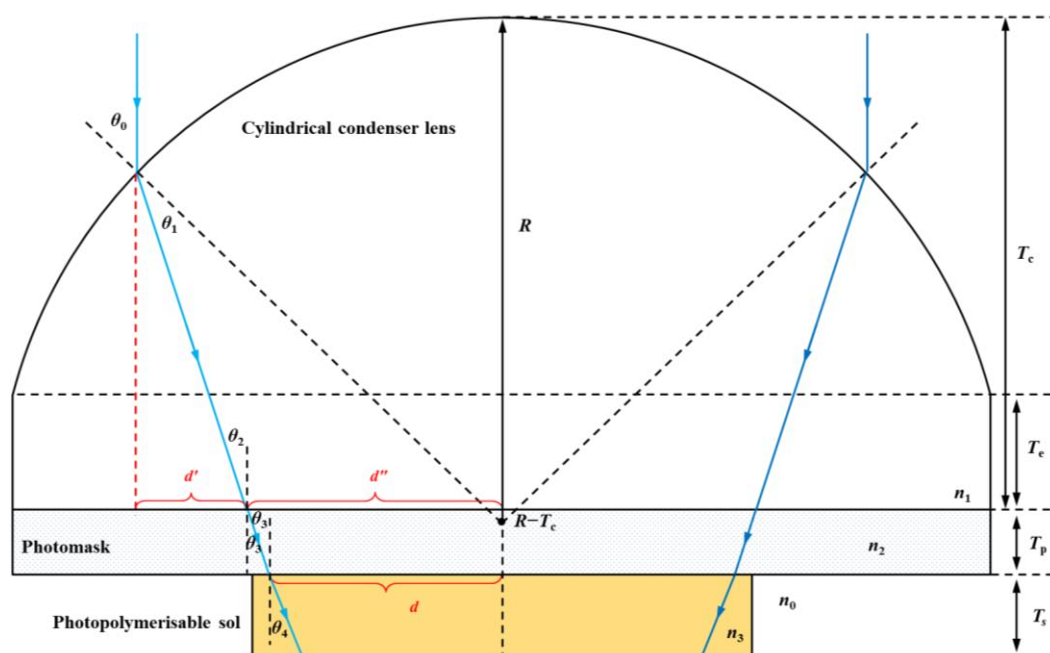


Figure S5.1. Schematic diagram showing the ray tracing method used to determine the angular directions of the waveguides in the RDWEL. Blue lines depict the transmission traces of the normal incident light through the cylindrical condenser lens, the photomask into the photopolymerisable sample.

Based on the schematic diagram and the light rays, we can obtain the following formulas:

$$n_0 \times \sin\theta_0 = n_1 \times \sin\theta_1 \quad [S5.1]$$

$$n_1 \times \sin\theta_2 = n_2 \times \sin\theta_3 = n_3 \times \sin\theta_4 \quad [S5.2]$$

$$R \times \sin\theta_0 = d' + d'' \quad [S5.3]$$

$$d' = [R \times \cos\theta_0 - (R - T_c)] \times \tan(\theta_0 - \theta_1) \quad [\text{S5.4}]$$

$$d = d' - T_p \times \tan\theta_3 \quad [\text{S5.5}]$$

Where θ_0 , θ_1 , θ_2 , θ_3 , and θ_4 refer to the incident angles or refraction angles at the interface of different medium. n_0 , n_1 , n_2 , and n_3 refer to the refractive index of air, the condenser lens, the photomask, and the photopolymerisable medium, respectively. R , T_c , T_e , T_p , and T_s correspond to the radius of the curved plane, the entire thickness of the condenser lens, the edge thickness of the lens, the thickness of the photomask, and the thickness of the sample cell, respectively.

In our case of study, $n_0 = 1.00$, $n_1 = 1.53$, $n_2 = 1.55$, $n_3 = 1.47$, $R = 13.12$ mm, $T_c = 12.8$ mm, and $T_p = 1.5$ mm. By substituting these values into the parameters in the above formulas, we can find out the entrance position (indicated by d) of the beam and the angles of the beam refracting into the photopolymerisable sample (θ_4), for any θ_0 with a given value. We can then plot the calculated refraction angles (θ_4) versus the calculated off-centered position (d), which is shown in **Figure S5.2**.

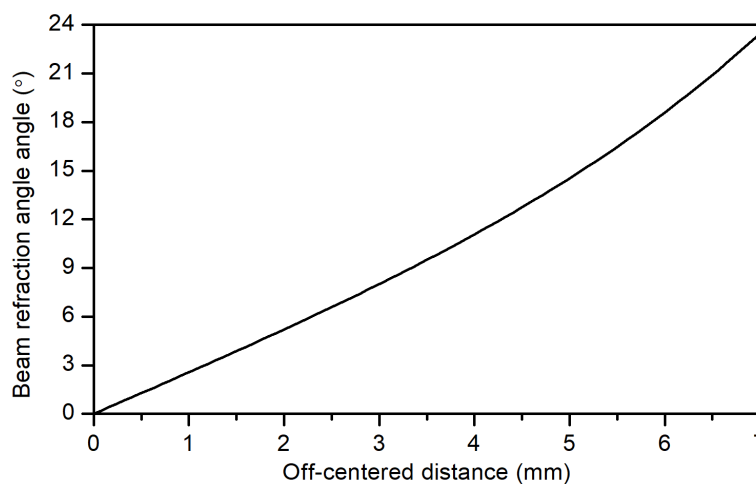


Figure S5.2. Plots showing the refraction angles of the beam into the photopolymer versus the off-centered distance of their starting point at the entrance face of the RDWEL.

Since we place a photomask with light and dark squares in front of the sample cell, the normally incident broad beam would split into discrete microscopic light rays and subsequently inscribe the waveguides. As the photomask has a periodicity of 80 μm , the off-centered positions of waveguides at the entrance face of the RDWEL are located approximately every 80 μm . Therefore, By assigning d (off-centered distance, see Figure S5.1) with values from 0 mm to 6.5 mm (half the width of the region illuminated) with 0.08 mm intervals, we can find out the angles of all the waveguides in the RDWEL, which are listed in **Table S5.1**.

Table S5.1 Summary of the angles of all waveguides in the RDWEL

d' / mm	$\theta_{\text{wg}} / ^\circ$								
0.00	0.00	1.36	3.50	2.72	7.20	4.08	11.33	5.36	15.91
0.08	0.20	1.44	3.71	2.80	7.43	4.16	11.59	5.44	16.23
0.16	0.41	1.52	3.93	2.88	7.66	4.24	11.86	5.52	16.55
0.24	0.61	1.60	4.14	2.96	7.89	4.32	12.12	5.60	16.88
0.32	0.82	1.68	4.35	3.04	8.12	4.40	12.40	5.68	17.21
0.40	1.02	1.76	4.56	3.12	8.36	4.48	12.67	5.76	17.55
0.48	1.23	1.84	4.74	3.20	8.59	4.56	12.95	5.84	17.89
0.56	1.43	1.92	4.99	3.28	8.83	4.64	13.23	5.92	18.23
0.64	1.64	2.00	5.21	3.36	9.07	4.72	13.51	6.00	18.59
0.72	1.84	2.08	5.42	3.44	9.31	4.80	13.80	6.08	18.94
0.80	2.05	2.16	5.64	3.52	9.56	4.88	14.09	6.16	19.31
0.88	2.26	2.24	5.86	3.60	9.80	4.96	14.38	6.24	19.67
0.96	2.46	2.32	6.08	3.68	10.05	5.04	14.68	6.32	20.05
1.04	2.67	2.40	6.30	3.76	10.30	5.12	14.98	6.40	20.43
1.12	2.88	2.48	6.53	3.84	10.55	5.20	15.29	6.48	20.81
1.20	3.09	2.56	6.75	3.92	10.81	5.28	15.60	6.56	21.20
1.28	3.29	2.64	6.97	4.00	11.07				

S5.2. Coupling a diverging LED beam to RDWEL with different orientations

When applying RDWEL with converging orientation (written as RDWEL_{CONV}) to a LED, the diverging LED beam enters the RDWEL from the side with larger waveguide spacing. The off-centered distances and angles of the constituent waveguides are written as d' and θ_{wg} , as shown in **Figure S5.3a**. Whereas when applying RDWEL with diverging orientation (Written as RDWEL_{DIV}) to the LED, the diverging LED beam enters the RDWEL from the side with smaller waveguide spacing. The waveguides with angle of θ_{wg} in this case have off-centered positions (p_d) given by

$$p_c = d' - T \times \tan\theta_{wg} \quad [S5.6]$$

Where d' and θ_{wg} are the parameters given in Table 5.1, and T is the thickness of the film. (Figure S5.3b).

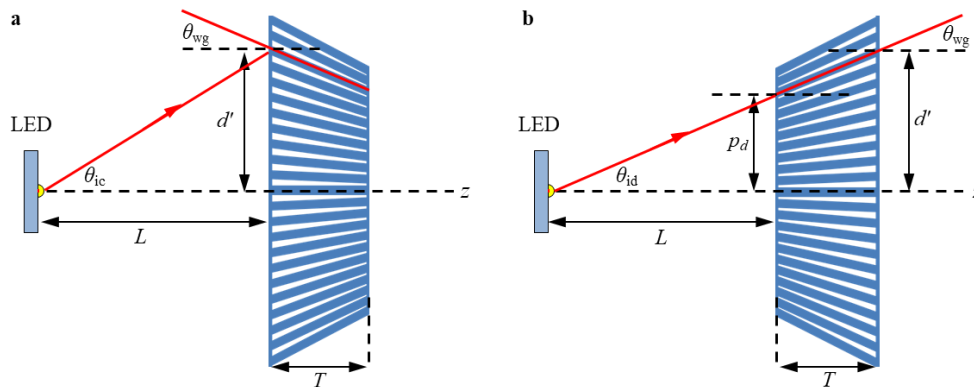


Figure S5.3. Schematic diagram of employing RDWEL with converging orientation (a) and diverging orientation (b) to a LED beam. z is the optical axis, L is the distance between the RDWEL and the LED, and θ_{ic} and θ_{id} refer to refer to the incident angle of the LED when the RDWEL_{CONV} and RDWEL_{DIV} are employed respectively.

Owing to the refractive index contrast between its core and cladding, a waveguide possesses an acceptance cone, light incident within which suffers total internal reflection (TIR). The boundary angles of the acceptance cone θ_1 and θ_2 of the

waveguide can then be calculated using the following formulas:

$$n_{\text{core}} \times \sin\theta_c = n_{\text{cladding}} \times \sin 90^\circ \quad [\text{S5.7}]$$

$$\theta_{r1} = [\theta_{\text{wg}} - (90^\circ - \theta_c)] \quad [\text{S5.8}]$$

$$\theta_{r2} = [\theta_{\text{wg}} + (90^\circ - \theta_c)] \quad [\text{S5.9}]$$

$$n_0 \times \sin\theta_1 = n_{\text{core}} \times \sin\theta_{r1} \quad [\text{S5.10}]$$

$$n_0 \times \sin\theta_2 = n_{\text{core}} \times \sin\theta_{r2} \quad [\text{S5.11}]$$

Where n_{core} and n_{cladding} refer to the refractive index of core and cladding of the waveguide, θ_{wg} is the angle of the waveguide relative to z axis, θ_{r1} and θ_{r2} correspond to the refraction angle of θ_1 and θ_2 into the waveguide core, and n_0 is to the refractive index of air.

The refraction angle of the waveguide (θ_{rwg}) is given by:

$$n_0 \times \sin\theta_{\text{rwg}} = n_{\text{core}} \times \sin\theta_{\text{wg}} \quad [\text{S5.12}]$$

From Figure S5.3, the incident angles (θ_i) of the LED into any waveguides are given by:

$$\tan\theta_{ic} = d'/L \text{ (for RDWEL}_{\text{CONV}}) \quad [\text{S5.13}]$$

$$\tan\theta_{id} = p_d/L \text{ (for RDWEL}_{\text{DIV}}) \quad [\text{S5.14}]$$

Now if we substituent the above formulas with the following parameters: $T = 2$ mm, d' and θ_{wg} are the paramerters given in Table 5.1, $n_{\text{core}} = 1.476$, $n_{\text{cladding}} = 1.470$ (namely $\Delta n = 0.006$), $n_0 = 1.0$, and $L = 26$ mm, we can calculate the rest physical quantities, and understand the relationships between any microscopic threads from the LED and the waveguides the threads access, which provide the theoretical basis for studying the coupling of diverging beam to RDWEL with different orientations.

In the case of employing RDWEL with converging orientation to the LED, we

obtained the following physical quantities summarized in **Table S5.2**.

Table S5.2 Summary of waveguide off-centered distances (d'), waveguide angles (θ_{wg}), waveguide acceptance cones (θ_1 , θ_2), waveguide refraction angles (θ_{rwg}) and incident angle of the LED when employing REWEL_{CONV} (θ_{ic})

d' /mm	θ_{wg} /°	θ_1 /°	θ_2 /°	θ_{rwg} /°	θ_{ic} /°	d' /mm	θ_{wg} /°	θ_1 /°	θ_2 /°	θ_{rwg} /°	θ_{ic} /°
0.00	0.00	-7.64	7.64	0.00	0.00	2.32	-5.93	-16.50	-1.12	-8.76	5.10
0.08	-0.20	-7.94	7.34	-0.29	0.18	2.40	-6.14	-16.82	-1.44	-9.09	5.27
0.16	-0.40	-8.23	7.05	-0.59	0.35	2.48	-6.36	-17.15	-1.76	-9.41	5.45
0.24	-0.60	-8.53	6.75	-0.88	0.53	2.56	-6.58	-17.48	-2.08	-9.73	5.62
0.32	-0.80	-8.82	6.46	-1.18	0.71	2.64	-6.80	-17.82	-2.40	-10.06	5.80
0.40	-1.00	-9.12	6.16	-1.47	0.88	2.72	-7.02	-18.15	-2.73	-10.39	5.97
0.48	-1.20	-9.42	5.87	-1.77	1.06	2.80	-7.24	-18.49	-3.06	-10.72	6.15
0.56	-1.40	-9.71	5.57	-2.06	1.23	2.88	-7.46	-18.83	-3.39	-11.05	6.32
0.64	-1.60	-10.01	5.28	-2.36	1.41	2.96	-7.69	-19.17	-3.72	-11.39	6.49
0.72	-1.80	-10.31	4.98	-2.65	1.59	3.04	-7.91	-19.52	-4.06	-11.73	6.67
0.80	-2.00	-10.61	4.68	-2.95	1.76	3.12	-8.14	-19.87	-4.39	-12.07	6.84
0.88	-2.20	-10.91	4.39	-3.25	1.94	3.20	-8.37	-20.22	-4.73	-12.41	7.02
0.96	-2.40	-11.21	4.09	-3.54	2.11	3.28	-8.61	-20.57	-5.08	-12.76	7.19
1.04	-2.60	-11.51	3.79	-3.84	2.29	3.36	-8.84	-20.93	-5.42	-13.11	7.36
1.12	-2.80	-11.81	3.49	-4.14	2.47	3.44	-9.07	-21.29	-5.77	-13.46	7.54
1.20	-3.01	-12.12	3.19	-4.44	2.64	3.52	-9.31	-21.66	-6.12	-13.82	7.71
1.28	-3.21	-12.42	2.89	-4.74	2.82	3.60	-9.55	-22.03	-6.48	-14.18	7.88
1.36	-3.42	-12.73	2.59	-5.04	2.99	3.68	-9.79	-22.40	-6.84	-14.54	8.06
1.44	-3.62	-13.03	2.29	-5.35	3.17	3.76	-10.04	-22.78	-7.20	-14.91	8.23
1.52	-3.83	-13.34	1.98	-5.65	3.35	3.84	-10.28	-23.16	-7.56	-15.28	8.40
1.60	-4.03	-13.65	1.68	-5.96	3.52	3.92	-10.53	-23.54	-7.93	-15.65	8.57
1.68	-4.24	-13.96	1.37	-6.26	3.70	4.00	-10.78	-23.93	-8.30	-16.03	8.75
1.76	-4.45	-14.27	1.07	-6.57	3.87	4.08	-11.04	-24.32	-8.68	-16.41	8.92
1.84	-4.65	-14.58	0.76	-6.88	4.05	4.16	-11.29	-24.72	-9.06	-16.80	9.09
1.92	-4.86	-14.90	0.45	-7.19	4.22	4.24	-11.55	-25.13	-9.44	-17.19	9.26
2.00	-5.07	-15.22	0.14	-7.50	4.40	4.32	-11.81	-25.53	-9.83	-17.59	9.43
2.08	-5.29	-15.53	-0.17	-7.81	4.57	4.40	-12.08	-25.95	-10.23	-17.99	9.61
2.16	-5.50	-15.85	-0.49	-8.13	4.75	4.48	-12.34	-26.37	-10.62	-18.39	9.78
2.24	-5.71	-16.18	-0.80	-8.45	4.92	4.56	-12.61	-26.79	-11.03	-18.80	9.95

Note: Only the vicinal waveguides accessed by LED with θ_{ic} up to $\sim 10^\circ$ are listed here.

In the case of employing RDWEL with diverging orientation to the LED, we

obtained the following physical quantities summarized in **Table S5.3**.

Table S3 Summary of waveguide off-centered distances (p_d), waveguide angles (θ_{wg}), waveguide acceptance cones (θ_1 , θ_2), waveguide refraction angles (θ_{rwg}) and incident angle of the LED when employing RDWEL_{DIV} (θ_{id})

p_d /mm	θ_{wg} /°	θ_1 /°	θ_2 /°	θ_{rwg} /°	θ_{id} /°	p_d /mm	θ_{wg} /°	θ_1 /°	θ_2 /°	θ_{rwg} /°	θ_{id} /°
0.00	0.00	-7.64	7.64	0.00	0.00	2.40	6.80	2.40	17.82	10.06	5.28
0.07	0.20	-7.34	7.94	0.29	0.16	2.47	7.02	2.73	18.15	10.39	5.44
0.15	0.40	-7.05	8.23	0.59	0.32	2.55	7.24	3.06	18.49	10.72	5.59
0.22	0.60	-6.75	8.53	0.88	0.48	2.62	7.46	3.39	18.83	11.05	5.75
0.29	0.80	-6.46	8.82	1.18	0.64	2.69	7.69	3.72	19.17	11.39	5.91
0.37	1.00	-6.16	9.12	1.47	0.80	2.76	7.91	4.06	19.52	11.73	6.06
0.44	1.20	-5.87	9.42	1.77	0.97	2.83	8.14	4.39	19.87	12.07	6.22
0.51	1.40	-5.57	9.71	2.06	1.13	2.91	8.37	4.73	20.22	12.41	6.38
0.58	1.60	-5.28	10.01	2.36	1.29	2.98	8.61	5.08	20.57	12.76	6.53
0.66	1.80	-4.98	10.31	2.65	1.45	3.05	8.84	5.42	20.93	13.11	6.69
0.73	2.00	-4.68	10.61	2.95	1.61	3.12	9.07	5.77	21.29	13.46	6.84
0.80	2.20	-4.39	10.91	3.25	1.77	3.19	9.31	6.12	21.66	13.82	7.00
0.88	2.40	-4.09	11.21	3.54	1.93	3.26	9.55	6.48	22.03	14.18	7.15
0.95	2.60	-3.79	11.51	3.84	2.09	3.33	9.79	6.84	22.40	14.54	7.31
1.02	2.80	-3.49	11.81	4.14	2.25	3.41	10.04	7.20	22.78	14.91	7.46
1.09	3.01	-3.19	12.12	4.44	2.41	3.48	10.28	7.56	23.16	15.28	7.62
1.17	3.21	-2.89	12.42	4.74	2.57	3.55	10.53	7.93	23.54	15.65	7.77
1.24	3.42	-2.59	12.73	5.04	2.73	3.62	10.78	8.30	23.93	16.03	7.92
1.31	3.62	-2.29	13.03	5.35	2.89	3.69	11.04	8.68	24.32	16.41	8.08
1.39	3.83	-1.98	13.34	5.65	3.05	3.76	11.29	9.06	24.72	16.80	8.23
1.46	4.03	-1.68	13.65	5.96	3.21	3.83	11.55	9.44	25.13	17.19	8.38
1.53	4.24	-1.37	13.96	6.26	3.37	3.90	11.81	9.83	25.53	17.59	8.53
1.60	4.45	-1.07	14.27	6.57	3.53	3.97	12.08	10.23	25.95	17.99	8.69
1.68	4.65	-0.76	14.58	6.88	3.69	4.04	12.34	10.62	26.37	18.39	8.84
1.75	4.86	-0.45	14.90	7.19	3.85	4.11	12.61	11.03	26.79	18.80	8.99
1.82	5.07	-0.14	15.22	7.50	4.01	4.18	12.89	11.43	27.22	19.22	9.14
1.89	5.29	0.17	15.53	7.81	4.17	4.25	13.16	11.85	27.66	19.64	9.29
1.97	5.50	0.49	15.85	8.13	4.33	4.32	13.44	12.26	28.10	20.07	9.44
2.04	5.71	0.80	16.18	8.45	4.49	4.39	13.73	12.69	28.55	20.50	9.59
2.11	5.93	1.12	16.50	8.76	4.64	4.46	14.01	13.12	29.01	20.94	9.74
2.18	6.14	1.44	16.82	9.09	4.80	4.53	14.30	13.55	29.47	21.39	9.88
2.26	6.36	1.76	17.15	9.41	4.96	4.60	14.60	13.99	29.94	21.84	10.03
2.33	6.58	2.08	17.48	9.73	5.12						

Note: Only the vicinal waveguides accessed by LED with θ_{id} up to $\sim 10^\circ$ are listed

here.

In the working principle of the main text, we presented that the acceptance ranges of waveguides with $\theta_{\text{wg}} = 2.5^\circ$, 5.0° and 7.5° were $[-3.9^\circ, 11.4^\circ]$, $[-0.3^\circ, 15.1^\circ]$ and $[3.4^\circ, 18.9^\circ]$, respectively. These values were calculated based on formula [S5.7]–[S5.11], by substituting $n_{\text{core}} = 1.476$, $n_{\text{cladding}} = 1.470$, $n_0 = 1.0$, and the values of θ_{wg} . The corresponding angles θ_1 and θ_2 calculated from the formulas defines the angular acceptance ranges of the waveguides.

S5.3. Top-down micrograph of the entire RDWEL

Optical micrograph of the longitudinal cross-section of the entire RDWEL shows a layer consisting of ~ 160 waveguides which span $\sim \pm 21^\circ$. The region the constituent waveguides of the RDWEL covers is approximately 13 mm, indicating that the boundary waveguides ($\sim \pm 21^\circ$) are located a ~ 6.5 mm away from the center of the RDWEL. The high consistency between the beam angles obtained from experiment and the ones listed in Table S5.1 indicating that the ray tracing calculation in Section S5.1 is quite reliable.



Figure S5.4. Optical transmission micrograph of the longitudinal cross-section of the entire RDWEL. Scale bar = 1 mm.

S5.4. Measuring the FOV of a waveguide subpopulation of the RDWEL

The FOV measurements require the sampling angular range covers the acceptance range of the probing waveguide subpopulation.

From Table S5.3, we can see the refraction angle of a 10.0° (θ_{wg}) waveguide is 14.9° (θ_{rwg}), the corresponding boundary angles are $\theta_1 = 7.2^\circ$ and $\theta_2 = 22.8^\circ$. (All angles are relative to the surface normal of the RDWEL, or the z axis). The acceptance cone of the 10.0° waveguide subpopulation therefore corresponds approximately to $[7.2^\circ, 22.8^\circ]$.

During the FOV measurement, we first rotated the RDWEL by 15° ($\approx \theta_{\text{rwg}} = 14.9^\circ$). In this way, the 15° beam (relative to the surface normal of the RDWEL) refracts into the RDWEL with an angle of 10.14° ($\approx \theta_{\text{wg}} = 10.0^\circ$), and probes the 10.0° waveguide sub-population of the RDWEL.

We then rotated the RDWEL and imaging components simultaneously (they are all mounted on a rotatable optical rail) over an arc of $\pm 10^\circ$, while keeping the light source fixed. In which way, the incident angle of the probe beam spans from 5° to 25° ($15^\circ \pm 10^\circ$) relative to the surface normal of the whole RDWEL sample. Certainly this sampling angular range ($[5^\circ, 25^\circ]$) covers the acceptance range ($[7.2^\circ, 22.8^\circ]$) of the 10.0° waveguide sub-populations.

Chapter 6 Conclusions and Future Directions

6.1 General Conclusions

In this thesis, several slim polymer films encoded with optical waveguides or waveguide lattices were fabricated, and their performances on controlling the flow of light were examined. The main contributions of this thesis are summarized as follows.

The first objective of this thesis is to fabricate a functional waveguide structure with planar geometry as an efficient light collecting and guiding system. We realized this goal by taking inspiration from the collective behavior of ommatidia of arthropods, and developed a polymer thin film comprised multidirectional intersecting waveguide lattices (Chapter 2). We employed a low-cost, single step and room temperature self-written technique to fabricate the waveguide encoded lattices (WELs), which are impossible to construct through conventional, divergence-limited photolithographic techniques. This technique harnesses nonlinear propagation of light, specifically modulation instability and self-trapping of white incandescent light in a cycloaliphatic epoxide based photopolymer system. By launching collimated white incandescent light simultaneously from 5 directions into the photopolymerisable epoxide sol, we encoded a slim polymer film with intersecting waveguide lattices orientating at $\pm 30^\circ$, $\pm 15^\circ$, and 0° . Characterization through optical microscopy and laser transmission provided evidences for the successful inscription and the intersection status of the 5 waveguide lattices. Crosstalk-free transmission of multiple laser beams into this film indicated that the waveguide lattices were mutually independent, although they

intersect each other multiple times in the polymer films. To examine the light collecting and guiding performance of this film, we measured the angular range (or FOV) over which individual waveguide lattices could perceive. Combining the fields of view of the five waveguide lattices endowed the film a discontinuous panoramic FOV of $\sim 94^\circ$, which corresponded to a 66% enhancement over its waveguide-free counterpart. This FOV enhancement originated from the refractive index difference (Δn) between the core and surrounding region of the waveguides, which through comparing with theoretical calculation and simulation, was estimated to be approximately 0.001. Owing to the intersecting arrangement of waveguides, the film exhibited powerful capacity to focus and invert images when employed for preliminary imaging applications. This study paved the way for fabricating compound-eye inspired planar polymer films for light harvesting and wide FOV optical sensing applications.

Since the FOV of the above WELs was discontinuous, another slim polymer film possessing continuous FOV was developed. This film was consisted of a periodical stack of waveguide arrays, each comprising cylindrical polymer waveguides densely packed with radial distribution (Chapter 3). This radially distributed waveguide encoded lattice (RDWEL) was inscribed in the epoxide base photopolymer via mask-assisted self-trapping of a large ($> 15,000 \text{ cm}^{-2}$) converging (only in one direction) population of white light filaments. Optical characterization of the polymerized thin film confirmed the inscription of the RDWEL, with the constituent waveguides spanned $\pm 33^\circ$. Transmitting collimated white incandescent light from different directions (within the estimated FOV of the RDWEL) indicated that part of

the probe beam was always captured and waveguided to the exit face of the structure. This was owing to on one hand, the refractive index difference of the waveguides, which only collect light incident within their acceptance cones; on the other hand, the multimodal, polychromatism of the waveguides, which allow them to guide incandescent light even under passive conditions. We divided the RDWEL into 23 waveguide subpopulations and measured individual angular acceptance ranges. The resulting angular ranges of the waveguide subpopulations exhibited an average enhancement of 83% relative to the angular ranges of the unstructured counterparts. These angular ranges overlapped considerably with each other, indicating the RDWEL could continuously and seamlessly capture light incident over these angular ranges. Stitching up these angular acceptance ranges rendered the RDWEL a seamless FOV of 115° , which to our best knowledge, corresponded to the largest known panoramic FOV for a planar structure. We then employed this thin film for panoramic imaging, and demonstrated that all objects passing through the RDWEL within its FOV formed corresponding images with high clarity and spatial resolution. This study laid the experimental foundation for the fabrication of planar polymer films with up to 180° seamless panoramic FOV and solid-angle FOV, as well as excellent imaging functionalities in terms of the spatial resolution, angular span and wavelength sensitivity, etc.

Another specific objective of this thesis is to develop a waveguide based thin film via straightforward and cost-effective approach to enhance the conversion efficiency of solar cells. This goal was realized with a thin polymer film encoded with slanted slab optical waveguides, which could steer away light beams that would otherwise

impinge on the fingers (metal contacts) of solar cells to reduce the reflection loss (Chapter 4). We conducted beam propagation simulation first to demonstrate the feasibility of using waveguides with different slant angles as light steering elements. We then fabricated periodic arrays of slab waveguides with slanted angles of 0° , 0.66° , 1.33° , 1.99° , and 2.65° using the white-light self-written technique and the epoxide based photopolymer used in the previous projects. The spacing of the waveguide slabs were carefully designed so that they could be accurately aligned with the fingers of solar cells. We monitored the temporal evolution of the fabrication process and characterized the polymerized film with optical microscopy, both of which proved the inscription of the slanted waveguides. We then examined the beam collecting and steering performance experimentally using a 2.65° slab waveguide and a normally incident laser beam as demonstration. It was observed that when incident on and in proximate to the waveguide, the laser beam was collected by the waveguide, and shifted away from its original optical path. Given this, we carefully aligned these waveguide encoded thin films on commercially purchased silicon solar cells, and measured the external quantum efficiency (EQE) and the short circuit currents (J_{SC}). Compared with waveguide-free control samples, all films comprising waveguides exhibited efficiency enhancement of up to 4.42%, in the visible to near infrared region. This study provides a new practical solution to overcome the reflection losses of normal incident light from grid fingers. The advantages such as the straightforward design without changing the solar cell structure, the facile and cost-effective fabrication method, as well as the broadband-operating capability of the polymer slab waveguides would inspire more functional waveguide structures, which would further

increase the conversion efficiency of commercial silicon solar modules.

Controlling the divergence and manipulating the output pattern of diverging beams, such as LED beams, would extend their applications to many fields. In Chapter 5, we present the proof of concept of employing thin films comprising RDWEL to control the divergence angle and far-field intensity distribution of a diverging beam emitted from a blue LED. We conducted beam propagation simulation and ray tracing calculation first to study the interactions between the RDWEL and the light threads with different divergence angles, and predict the possible exiting directions of the beams. This provided us with the theoretical guidance to design the experiments and explain the results observed in the subsequent experiments. We then fabricated the RDWEL using the similar method described in Chapter 3. A photopolymerisable organosiloxane substituted acrylate fluid was selected as the waveguide matrix, owing to the large refractive index change it could be induced during the photo-inscription processes. We then studied the FOV of this RDWEL with the same method described in previous chapters. It was observed that the constituent waveguides of the RDWEL had an average angular acceptance range of $\sim 9.6^\circ$, which corresponded to an approximate FOV enhancement of 320%, as compared to the waveguide-free control medium. The considerable overlap between the acceptance ranges of the probed waveguide subpopulations gave this RDWEL a seamless panoramic FOV of 70° . This value clearly pointed out the angular range the RDWEL could operate with, and the $\sim 9.6^\circ$ FOV of its constituent waveguides offered a high angular capacity the RDWEL could tolerate. We kept the RDWEL at a specific position on the optical path of a blue LED and studied its beam shaping performances.

The results revealed the configuration dependent beam manipulation performances of the RDWEL. Specifically, employing RDWEL with diverging orientation to the LED beam yielded beam expanding along the horizontal direction; whereas applying a RDWEL with converging orientation to the LED beam resulting in slight narrowing of the beam. The intensity distributions of the far-field output of the beam were also changed in both cases. We conducted measurements by varying the divergence angle of the LED beam while keeping other conditions constant to study the behaviours of the light beam coupled and decoupled into the RDWEL. Results revealed that the diverging LED beams falling in the acceptance cones of the constituent waveguide subpopulations of the RDWEL resulted in the beam manipulation in both divergence angle and intensity distribution; whereas the diverging beam falling beyond the acceptance cone of the RDWEL sub-waveguides suffered barely any beam manipulation.

This work opened out a new approach to control the inflow and outflow of diverging light beams. The special characteristics of the RDWEL-derived thin films would have potential application in optical devices including cameras, microscopes and endoscopes, solar panels, LCD and LEDs.

6.2 Future work

Following the work presented in this thesis, further work could proceed in several directions.

Firstly, for the work of employing RDWEL related structures for wide FOV imaging, a few things would need consideration. The fields of view of the ommatidia of arthropods, regardless of their orientation, are always the same. The FOV of the constituent waveguide subpopulations of the RDWEL mentioned in Chapter 3, however, vary significantly, owing to the converging beam, which induces non-identical Δn at different regions. To obtain a uniform Δn , spatial light modulator (SLM) would be needed to modify the intensity distribution of the converging beam. As the film is in planar geometry, the reflectivity of light threads with different incident angles would also need to be considered while designing the SLM.

Another important direction is to further increase the FOV, as the planar RDWEL could only perceive an angular range as large as 115° . To enhance the FOV, waveguide arrays with larger angular span would be needed. Theoretical calculations have shown light beams with incident angle up to 90° could be collected by slanted waveguides with planar surfaces. For instance, a waveguide with slanted angle of $\theta_{wg} \approx 39.4^\circ$ constructed in the epoxide based system ($n = 1.51$, $\Delta n = 0.001$) would give an angular acceptance cone of $[66.2^\circ, 90^\circ]$. A symmetric RDWEL fabricated in the photopolymerisable epoxide medium with its constituent waveguides spanning $\pm 39.4^\circ$ would be able to perceive a panoramic FOV of 180° . To fabricate such RDWEL, a single lens with larger numerical apertures (NA) would be employed, for instance, a high-NA semicylindrical condenser lens or a high NA linear Fresnel lens. Such

structures can also be achieved using multiple lenses with smaller NA, which collectively give a larger converging angular range in the photopolymer systems. Stitching RDWEL with smaller angular spanning together to give a larger angular spanning is also a method which could think, but it would bring a challenge of retaining the planar geometry of the final structure, and reducing the gap between the stitched parts.

All the RDWLEs discussed above have their constituent waveguides radially distributed along the horizontal direction, but periodically stacked in the very direction. Such structures only have panoramic fields of view. One of the importance directions in this research field is to develop planar thin films with other waveguide arrangements, for instance, arranging waveguides omnidirectionally over solid angles. Such waveguide encoded thin films can be realized in polymer medium using the self-written technique and employing light beams converging from two directions (both x and y). Circular lenses with higher NA, for instance, circular Fresnel lens could be used to enlarge the angular span of the waveguides, and thin films with FOV up to $180^\circ \times 180^\circ$ could be achieved.

The refractive index difference between the core and cladding of the waveguides is a very crucial factor that would considerably affect the performances of the waveguide structures. For instance, with $n = 1.51$ and $\Delta n = 0.01$, a waveguide with $\theta_{\text{wg}} \approx 34.6^\circ$ would be able to collect light from 90° , whereas 39.4° (vide supra) is needed. This could make the fabrication process much easier, as multiple lenses and single lens with very large NA may not be needed. Several approaches could be considered to increase the Δn . Firstly, modifying the current photopolymer systems by adjusting

their compositions or introducing other materials, such as nanoparticles.¹⁻³ For instance, Pradana *et al.* reported that doping TiO₂ nanoparticles into a nanoimprint polymer resist yielded a hybrid material with increased refractive index.³ Another direction is to fully change the material, such as changing the single-component photopolymer system into polymer blends, which would go phase separation under the illumination of optical fields. For instance, Biria and Hosein *et al.* reported a photorefractive polymer blend comprised of high refractive-index TMPTA (Trimethylolpropane triacrylate) and low refractive-index PDMS (epoxypropoxypropyl-terminated polydimethylsiloxane oligomer), which polymerized individually and induced refractive index change of 0.034 (measured refractive index for cured TMPTA and PDMS were 1.480 and 1.446, respectively).⁴ Changing the inscribing light source from white light into UV lasers would have some benefits. For instance, Jacobson *et al.* fabricated micro-scale truss structures via UV laser induced self-written approach.⁵⁻⁷ This method is fast, the self-written waveguides all have step index profiles, and the uncured regions can be removed through simple solvent developing processes. Fabricating RDWEL using UV laser inscription would allow us to remove the unpolymerized regions, and backfill curable (either photopolymerizable or thermopolymerizable) medium with much lower refractive index to increase Δn . Opaque materials would be another alternative backfilling materials that would reduce even completely eradicate crosstalk in the imaging applications.

We demonstrated in Chapter 4 the concept of employing thin films encoded with slanted slab waveguides in solar cells. There are a few modifications we can do to further enhance the light harvesting performance of these thin films. Firstly, although

the thin films encoded with slanted slab waveguides led to enhanced conversion efficiency over the unstructured films, the solar cells encapsulated with the epoxide based thin films, regardless waveguide encoded or not, exhibited lower external quantum efficiency (EQE) and short circuit current (J_{SC}) versus non-encapsulated solar cells.⁸ This was mainly attributed to the absorption of the unreacted photosensitive species in this photopolymer system, which can be alleviated by replacing camphorequinone with less colored photosensitizers, and reducing the thickness of the thin films. Bleaching the sample with facile and straight forward methods which don't change the structure of the thin films would also be a good alternative approach.

Another importance direction is to modify the structure of the thin film for wide angle light collection. As we know, the beam steering effect of a slanted waveguide originated from the Δn between its core and surrounding regions. Increasing the Δn would increase the collection range of the waveguide, giving it collection ability to light incident from wide angles. For instance, Biria and Hosein *et al.* reported that a waveguide structure with large Δn exhibited high conversion efficiency even when the incident angle of probe beam reached 40 degree.⁹ Besides, increasing the Δn would also increase the number of modes the waveguide can host,^{10,11} which would reduce the leakage of the light from the wall of the waveguides, as well as increasing the chances of concentrate the light intensities which would lead to enhanced efficiency.^{12–}
¹⁴ Engineering other parameters of the waveguides, for instance, increasing the tilting angle of the slanted slab waveguides (θ_{wg}), or introducing multidirectional waveguide arrays may also enable the waveguide-comprising films the capability of light

harvesting over wide angles, even up to all angles. The advantages of UV-inscription, as mentioned earlier, render it a good fabrication method. Fabricating slanted slab waveguides using UV lasers for enhancing the conversion efficiency of solar cells would be an interesting extension.

In Chapter 5, we presented the proof of concept of using RDWEL-comprising thin films to control the output of light emitted from diverging light sources. To understand the coupling and decoupling of the diverging beam into the RDWEL, we intentionally kept the RDWEL at a specific distance away from the LED, and employed only part of the LED beam and part of the constituent waveguides of the RDWEL for the study. As the ultimate goal is to apply the RDWEL based thin films as conformal coating for LED, several future work remains.

The first thing is to couple diverging light efficiently into all constituent waveguides of the RDWEL. To realize this goal, we would need to calculate the angular acceptance ranges of the all the constituent waveguides of the RDWEL, then design the angles of the microscopic light threads (of the diverging beam) that impinge on the entrance face of the waveguides. By tuning the pinhole size to tune the divergence angles of the probe beam (here refers to only part of the LED beam), and adjusting the position of the RDWEL, the beam could be fully coupled by the RDWEL. The $\sim 9.6^\circ$ angular tolerance capacity of the waveguides would make the calibration easier, because for a beam with constant divergence angle, putting the RDWEL within a certain distance range would lead to full coupling; while putting the RDWEL at a constant position, the beam within a certain divergence angular range would also be fully coupled to the RDWEL.

The second goal is to couple the entire LED beam into the RDWEL. As the LED has very large divergence angle, a RDWEL with its constituent waveguides spanning over large angular range would be needed. Waveguides with large Δn would also be very necessary, as it would increase the angular tolerance capacity. The RDWEL in this case would be placed right on top of the LED, as a huge structure would be needed if put far away from the LED. In this way, employing the RDWEL directly on LED as conformal coating to efficiently couple the entire beam into the corresponding waveguides and manipulate the output of the beam would be realized.

Another interesting direction would be fabricating RDWEL with different shapes (for instance curved surfaces), so that the advantages of the curved surfaces and the good characteristics of waveguides would be combined.

References

- (1) Saravanamuttu, K.; Du, M.; Najafi, S. I.; Andrews, M. P. *Photoinduced Structural Relaxation and Densification in Sol-Gel-Derived Nanocomposite Thin Films: Implications for Integrated Optics Device Fabrication*; 1998; Vol. 76.
- (2) Böhm, J.; Haußelt, J.; Henzi, P.; Litfin, K.; Hanemann, T. Tuning the Refractive Index of Polymers for Polymer Waveguides Using Nanoscaled Ceramics or Organic Dyes. *Adv. Eng. Mater.* **2004**, *6* (12), 52–57.
- (3) Pradana, A.; Kluge, C.; Gerken, M. Tailoring the Refractive Index of Nanoimprint Resist by Blending with TiO₂ Nanoparticles. *Opt. Mater. Express* **2014**, *4* (2), 329–337.
- (4) Biria, S.; Hosein, I. D. Control of Morphology in Polymer Blends through Light Self-Trapping: An *in Situ* Study of Structure Evolution, Reaction Kinetics, and Phase Separation. *Macromolecules* **2017**, *50* (9), 3617–3626.
- (5) Jacobsen, A. J.; Barvosa-Carter, W.; Nutt, S. Shear Behavior of Polymer Micro-Scale Truss Structures Formed from Self-Propagating Polymer Waveguides. *Acta Mater.* **2008**, *56* (6), 1209–1218.
- (6) Jacobsen, A. J.; Barvosa-Carter, W.; Nutt, S. Micro-Scale Truss Structures

- Formed from Self-Propagating Photopolymer Waveguides. *Adv. Mater.* **2007**, *19* (22), 3892–3896.
- (7) Jacobsen, A. J.; Barvosa-Carter, W.; Nutt, S. Compression Behavior of Micro-Scale Truss Structures Formed from Self-Propagating Polymer Waveguides. *Acta Mater.* **2007**, *55* (20), 6724–6733.
 - (8) Chen, F.; Pathreker, S.; Kaur, J.; Hosein, I. D. Increasing Light Capture in Silicon Solar Cells with Encapsulants Incorporating Air Prisms to Reduce Metallic Contact Losses. *Opt. Express* **2016**, *24* (22), A1419–A1430.
 - (9) Biria, S.; Chen, F. H.; Pathreker, S.; Hosein, I. D. Polymer Encapsulants Incorporating Light-Guiding Architectures to Increase Optical Energy Conversion in Solar Cells. *Adv. Mater.* **2018**, *30* (8), 1705382.
 - (10) Crisp, J.; Elliott, B. J. *Introduction to Fiber Optics*; Newnes, 2005.
 - (11) Saleh, B. E. A.; Teich, M. C. *Fundamentals of Photonics*; Wiley-Interscience, 2007.
 - (12) Dalal, V. L.; Moore, A. R. Design Considerations for High-intensity Solar Cells. *J. Appl. Phys.* **1977**, *48* (3), 1244–1251.
 - (13) Chegaar, M.; Hamzaoui, A.; Namoda, A.; Petit, P.; Aillerie, M.; Herguth, A. Effect of Illumination Intensity on Solar Cells Parameters. *Energy Procedia* **2013**, *36*, 722–729.
 - (14) Effect of Light Intensity | PVEducation. https://pveducation.org/es/fotovoltaica/-effect-of-light-intensity#footnoteref1_yfn2d0a (accessed May 22, 2018).